Search for New Phenomena with the mono-jet signature, And a direct measurement of the Z boson invisible width, with the ATLAS Detector at the CERN Large Hadron Collider

by

Reyhaneh Rezvani

A thesis submitted in conformity with the requirements
for the degree of Doctor of Philosophy
Graduate Department of Physics
University of Toronto

Abstract

Search for New Phenomena with the Mono-jet Signature,

and a Direct Measurement of the Z Boson Invisible Width,

with the ATLAS Detector at the CERN Large Hadron Collider

Reyhaneh Rezvani

Doctor of Philosophy

Graduate Department of Physics

University of Toronto

2013

A search for new physics in events with an energetic jet and large missing transverse momentum is performed with the ATLAS detector, using 2011 dataset corresponding to 4.7 fb^{-1} integrated luminosity. A model–independent approach is adopted, making predictions in various kinematic regions sensitive to potentially new physics scenarios. Data–driven background determination methods are developed to obtain robust predictions of the Standard Model expectations of the number of events in each probed kinematic region. No deviation from the Standard Model expectation is observed, and the results are hence interpreted in the context of the ADD scenario of Large Extra Dimensions, and pair production of WIMP dark matter candidates. This results in the world's tightest constraints on the size of the D-dimensional Planck scale as the fundamental parameter of the ADD theory. The constraints obtained on Dark Matter suppression scale are stronger than those obtained from dedicated direct and indirect dark matter experiments for a large range of WIMP masses.

Furthermore, data-driven estimates of various Standard Model processes contributing to the mono-jet final state allows a precise direct measurement of the invisible decay width of the Z boson. This results in a measurement at 5% precision level, comparable to the results of the L3 experiment, and better than all other LEP direct measurements.

To my family

Acknowledgements

This thesis would not have been possible without the guidance and help of several individuals who in one way or another contributed their valuable assistance to the completion of this study.

First and foremost, my sincere gratitude goes to my supervisor Professor Robert Orr, whose knowledge, support, and patience made the whole effort of this thesis possible.

My utmost gratitude goes to Professor Pierre-Hugues Beauchemin, a great friend and adviser, who patiently guided me through all the steps, with whom I spent great moments of my PhD programme, and from whom I learned lessons in physics and life.

I would like to thank Professor Pierre Savard and Professor Richard Teuscher for their support and very helpful advice during my PhD programme.

My special thanks go to my dear friend, Professor Ketevi Assamagan, whose help and fruitful conversations had a great impact on this thesis.

I would like to thank the rest of my committee: Professor Peter Krieger, Professor Micheal Luke, Professor Amanda Peet, and Professor Regina Demina.

Special thanks go to my very good friends for the great moments we shared together, and the help they provided me with throughout my stay at CERN. Thank you Philippe, Richard, Nicola, Nina, Steven, and Joe!

Words cannot express how thankful I am to my parents for supporting me throughout my studies at university and all my life, without whom this entire effort would not have been possible, and to my two sisters, with whom I have had the happiest moments of my life.

Contents

List of Tables

List of Figures

Chapter 1

Introduction

1.1 Standard Model of Particle Physics

The Standard Model of particle physics [1, 2] is a quantum field theory with a $U_Y(1) \times SU_L(2) \times SU_C(3)$ gauge symmetry, describing the interactions among the elementary matter particles via the electromagnetic, weak, and strong gauge bosons arising from the local gauge invariance requirement of the Lagrangian density. It includes 24 fermions (6 quarks, 6 leptons, and their corresponding anti–particles), 12 bosons as force carriers (γ, $W^{\pm}$, Z^0, and 8 gluons), and a scalar field called the Higgs field which generates the masses of the force carrier bosons through the spontaneous symmetry breaking mechanism. All these particles have been observed experimentally, with the possible Higgs boson candidate discovered in year 2012 [3].

1.2 Open Issues of the Standard Model

Although the predictions of the Standard Model (SM) agree extremely well with experimental observations thus far, there are still open issues not explained by this model, among which are:

- The model makes no attempt to describe the gravitational force.

- The Higgs mechanism gives rise to the hierarchy problem: the quantum corrections to the Higgs mass from fermionic loops are:

$$\Delta m_H^2 = -\frac{|\lambda_F|^2}{8\pi^2}[\Lambda_{UV}^2 + ...] \quad (1.1)$$

  where λ_F is the coupling to the Higgs field, and Λ_{UV} is the ultraviolet cutoff scale up to which the Standard Model is valid, taken to be the Planck scale ($\sim 10^{19}$ GeV). The Higgs mass has been recently observed [3] to be $\sim$ 126 GeV, which is orders of magnitude smaller than these quantum corrections. In order to reach a physical mass as small as this value, the bare Higgs mass– a parameter of the Lagrangian– should be set to a large value such that the resulting physical mass stays small, in agreement with observations. The mass parameter is therefore fine tuned to the 17th decimal in order to get the observed mass from a 10^{19} GeV correction. This fine tuning is not natural and is considered as a severe lack of predictability of the Standard Model theory.

- The velocity dispersions of galaxies, galaxy clusters and gravitational lensing indicate that the baryonic matter constitutes only 5% of the energy density of the universe, and the source of the rest of the energy density is unknown, 23% of which is referred to as Dark Matter. No field in the Standard Model can play the role of Dark Matter.

- Current observations indicate that the expansion of the universe is accelerating [4], implying the existence of dark energy as 74% mass–energy content of the universe, with a vacuum energy density, a parameter with dimension of $(length)^{-2}$, of the order of $(10^{-3})^4$ eV. However the value predicted by the Standard model is large and proportional to M_P^4 obtained from the quantum corrections, and thus $\sim$ 120 orders of magnitude larger than the value predicted by observations.

These problems are not addressed by the Standard Model of particle physics, and indicate that fundamental ingredients are still missing in the Standard Model description of the universe. This thesis is dedicated to search for deviations from the Standard Model expectations that could provide crucial hints– if observed– about these missing ingredients. In the case of no observed deviation, the results of this experimental investigation are used to constrain the latest theoretical attempts made to solve these problems. These constraints may guide theorists.

1.3 Mono-jet Topologies

Event topologies with one high transverse momentum jet and large missing transverse energy (mono-jets) are important final states for searches for new phenomena beyond the Standard Model (BSM), and for testing some of the Standard Model predictions, at the LHC. The large missing transverse energy can be a signature of weakly interacting particles not yet discovered. In order to tag events with large missing transverse energy, they are required to be accompanied by jets, giving rise to final states produced by strong interactions and therefore involve the highest production rate for new phenomena. Moreover, requiring a high value of $E_{\mathrm{T}}^{\mathrm{miss}}$ and the particular mono–jet event topology allow for a powerful suppression of the QCD multijet background and accurate prediction of the residual background. The beyond Standard Model scenarios resulting in such final states include Supersymmetry [5], Large Extra Dimensions (LED) scenarios, and a general model of production of dark matter (DM) particles. Mono-jet events have been studied in this thesis [6–8], and found to be consistent with Standard Model expectations. Therefore, constraints are set on the large extra dimensions model of Arkani-Hamed, Dimopoulos, Dvali (ADD) [9], and the pair production of Weakly Interacting Massive Particles (WIMPs) as dark matter candidates [10–12]. Under such consistency with the Standard Model expectations, the data can also be used to study $\mathrm{Z}(\nu\nu)$ events. In particular, a precise measurement of the invisible decay width of the Z boson from mono-jet events, i.e. decay of the Z boson to a pair of weakly interacting particles in association with jets, can be performed, as well as studying the effect of quantum electrodynamic (QED) radiation in typical Z($\ell\ell$) events.

Models with Large extra dimensions provide an important ingredient to a solution of the hierarchy problem in an attempt to explain why gravity is so much weaker than the other forces. According to such models, the fundamental scale of gravity (M_D) is of the order of the weak scale, hence eliminating any hierarchy between the Higgs mass and the size of its quantum correction. The weakness of gravity is then due to its dilution in the large extra dimensions. By postulating the energy scale of the gravitational interaction to be the same as the weak scale, these models also offer a potential opportunity to study gravity in the domain of particle physics and therefore provide crucial hints on how to formalise a quantum description of gravity, one of the important elements missing in the Standard Model. There is no model of quantum gravity thus far. However, an effective field theory valid below the energy scale M_D can be used to study the direct production of a weakly interacting graviton in association with an energetic jet in hadron colliders, in the context of the ADD scenario. Such an effective theory would only constitute a rough approximation to the non-renormalisable gravitational interactions, which can be included in the quantum field theory formalism. This approximate theory that can be formulated to study large extra dimensions model would therefore only apply at an energy regime much smaller than the new energy scale of the gravitational interaction.

In the ADD scenario, gravity propagates in the (4 + n)-dimensional bulk of space-time where n is the number of extra spatial dimensions. In the Standard Model all fields are confined to four dimensions. The apparent large difference between the characteristic mass scale of gravity, the Planck mass, and the electroweak scale as characterised by the W boson mass, is the result of assuming large sizes for the extra dimensions. The connection between effective 4–D Planck scale M_P and the size R of the extra dimensions is $M_P^2 \sim M_D^{2+n} R^n$ (Sec. 2.2). An appropriate choice of R, for a given n, results in a value of M_D close to the electroweak scale. In this way hierarchy of scales, and hence the fine tuning of the scalar Higgs mass is eliminated. However this does not yet give a solution to the hierarchy problem as it introduces a large fine tuning of R, the size of the extra dimension. It may be possible to build models in which the size of the extra dimensions expands in such a way to describe inflation of the observed 4-D world [13], or in which the size of the extra dimensions is stabilised at large values [14].

At hadron colliders, the ADD graviton could be produced in association with a jet via the three production processes, shown in Fig. 2.1, $qg \rightarrow qG$, $gg \rightarrow gG$, and $q\bar{q} \rightarrow gG$, where G stands for a graviton state, q for quark, and g for gluon. Gravitons do not interact with the detector due to the weakness of gravitational force in 4 dimensions, or equivalently due to the propagation of the graviton field into extra spatial dimensions that are much larger than the width of the graviton wave-packet. This would result in missing energy due to the graviton, plus mono-jet signature.

One of the most popular scenarios accounting for the observed dark matter in the universe is the hypothesized existence of Weakly Interacting Massive Particles (WIMPs) which have not been detected so far due to their weak interactions, although they have significant gravitational effects. An example of WIMPs are the neutralinos in SUSY models. Dark matter candidates should be stable and heavy compared to leptons and light quarks, since they have not been observed. Some symmetry, such as R-parity conservation in SUSY [15,16], KK number conservation in large extra dimensions models, etc., is required to prevent WIMPs from rapidly decaying to known Standard Model particles. Such symmetries result in the production of WIMPs in pairs. Effective field theories can be used to make reliable low energy predictions for the production of WIMPs at the LHC. The production of a pair of WIMPs in proton - proton interactions in association with an energetic jet from initial or final state radiation, results in missing energy plus a jet; the mono-jet topology. In these models, [10], [17], WIMPs have masses in the range between a few GeV and a TeV, hence accessible at the LHC.

As mentioned above, if no new physics is observed, the data can be used to measure quantities in the Standard Model. Since the major contribution to mono-jet events within the Standard Model comes from Z($\nu\nu$)+jets events, a direct measurement of the decay width of the Z boson to a pair of weakly interacting neutral particles can be performed. Such a measurement offers the opportunity to probe the weak couplings of the Z to neutrinos and to measure these couplings in hadronic environments. It could also reveal anomalies not necessarily visible in beyond Standard Model searches. For example the measurement is sensitive to any non–standard couplings of the Z boson to the Standard Model neutrinos, or to any additional Z decays to exotic particles beyond the Standard Model expectations, such as supersymmetric partners of the neutrinos. This measurement also provides an opportunity to study large angle QED radiation effects on the hadronic system recoiling against the Z boson. This can be useful in improving the description of QED in particle generators, resulting in a reduction of the corresponding uncertainties in other analyses.

Our knowledge of the Standard Model processes and of the effect of the detector on the measurement of final states from the p–p collisions is not perfect. There are various sources of systematic uncertainties on the cross sections, renormalisation and factorisation scales, parton showers, as well as the detector effects such as jet energy scale and resolution. The largest, and irreducible background, to the mono-jet events is the Z boson production in association with a jet, where the Z boson decays to two neutrinos. Another important reducible contribution is due to the events including a W boson plus a jet, where the charged lepton from the W boson decay is not reconstructed, or in the case of the hadronic decays of the τ lepton from the W decay, results in additional low p_{T} jets. Well–defined W+jets and Z+jets Standard Model processes with fully reconstructed and identified leptons can be used to model with high accuracy the main backgrounds to the mono–jet events. Such techniques which use data to model physics processes are called "data–driven" background determinations. They typically reduce the systematic uncertainties resulting from the simulated–based predictions, and consequently improve the sensitivity to new physics. One of the original features of the work to be presented here is the development and use of such data–driven techniques to estimate with good precision most of the Standard Model contributions to mono-jet events. Such predictions can also be used in precision measurements, such as a measurement of the Z invisible decay width that is competitive with the LEP direct measurement [18–21].

In the following, the details of a search for new physics with the mono-jet signature will be presented, using the total 2011 data corresponding to 4.7 fb^{-1} integrated luminosity. To optimise the sensitivity to all the models, and to avoid biases toward a particular model, the analysis is conducted in a model-independent way, and only the final results will be interpreted in the contexts of the LED and WIMP models.

This thesis is organised as follows: a brief introduction to the effective field theories, as well as the theoretical models considered in this thesis is presented in Chapter 2. The layout of the LHC accelerator and the ATLAS detector are described in Chapter 3. Object reconstruction is presented in Chapter 4. The data and simulated samples used in the analysis are described in Chapter 5, with the mono-jet selection cuts detailed in Chapter 6, while Chapter 7 focuses on the study of the trigger chosen to select the data in the signal regions. The determination of the Standard Model background in the mono–jet signal regions is detailed in Chapter. 8 and 9, before describing the experimental results in Chapter 10. The theoretical interpretations of Graviton emission and pair-production of WIMPs are presented in Chapter 11. Finally, the mono-jet results are used to perform a measurement of the invisible width of the Z boson in Chapter 12, before the concluding remarks in Chapter 13.

Chapter 2

Theoretical Interpretations

2.1 Effective Field Theories

Effective field theories are appropriate theoretical tools to describe physics at energies significantly lower than a given physically meaningful energy scale Λ, in the absence of an explicit knowledge of the microscopic model needed above the scale Λ. The idea is to approximate the unknown theory by an operator expansion containing all possible interactions of all orders including the fields expected to be involved in the new theory, and satisfying all the fundamental symmetries expected in the theory. This is equivalent to the Taylor expansion of a function, where the coefficients of expansion are the derivatives of the function evaluated at some fixed point x_0. If the function is not known, as is the case here, the coefficients of expansion stay undetermined. This therefore introduces a set of free parameters needed to describe the strength of various terms in the expansion of the Lagrangian. Therefore, these effective couplings of the low–energy approximation of the microscopic theory provided by the effective Lagrangian have to be probed in experiments.

The Lagrangian density corresponds to an expansion of powers of $\frac{energy}{\Lambda}$. For energies much lower than Λ, the higher order operators of the expansions are irrelevant, and the microscopic theory can be approximated by a finite sum over the first few terms in the expansion. This has the advantage of limiting the number of free parameters that must be determined in experiments in order to describe the physics properly. However, it limits the validity of the theory to a low energy region. This has impact at the LHC that will be discussed later.

2.2 Models of Large Extra Dimensions

2.2.1 Introduction

One of the physics scenarios beyond the Standard Model that can result in a mono-jet signature involves large extra dimensions (LED) [9]. Models of extra dimensions are inspired by string theory where 10 or 11 dimensions are required for an anomaly–free theory. There is no low–energy equivalence of string theory, but the fundamental features such as extra dimensions can be included in quantum field theories. Theoretical models, such as the Arkani-Hamed, Dimopoulos, Dvali (ADD) scenario [9] considered in this analysis, provide an important ingredient in a solution of the problems caused by the large hierarchy of fundamental scales relevant in high energy physics, by bringing the energy scale associated with gravity close to the electroweak scale. As mentioned in Sec. 1.3, in such scenarios, the fundamental strength of gravity is comparable to the weak scale, but its apparent weakness is due to the propagation of its field into the additional spatial dimensions.

At distances much larger than the size of the extra dimensions R, the world is effectively four-dimensional. The gravitational potential is then given by Gauss' law in 4 dimensions:

$$V(r) \sim \frac{m_1\, m_2}{M_P^2} \frac{1}{r} \quad , \quad r >> R \tag{2.1}$$

where M_P is the effective Planck scale in 4 dimensions ($\sim 10^{19}$ GeV).

At distances much smaller than R, the extra dimensions become effective, and the potential is given by Gauss' law in 3+n spatial dimensions:

$$V(r) \sim \frac{m_1\, m_2}{M_D^{n+2}} \frac{1}{r^{n+1}} \quad , \quad r << R \tag{2.2}$$

Putting $r = R$, the effective 4-dimensional Planck scale M_P and M_D are related via:

$$M_P^2 \sim M_D^{2+n}\, R^n \tag{2.3}$$

From this equation, it becomes clear that by a suitable choice of R, $M_D \sim M_W$, eliminating the hierarchy between the two scales. However, to complete the solution to the hierarchy problem, it has to be explained why these extra dimensions are so large [13, 14]. There is no renormalisable quantum field theory that can involve gravitational couplings to the SM particles as the graviton is already a dimension 1 operator. So any operator coupling a graviton to a Standard Model field would be non-renormalisable. However, a low-energy effective field theory valid below the scale $\Lambda \sim M_D$ can be used to calculate the production cross section of massive spin-two gravitons [22] in a proton-proton collider. The three processes at leading order are: $qg \to qG$, $gg \to gG$, $q\bar{q} \to gG$. G stands for the graviton, and q and g represent the quark and gluon respectively. The emitted graviton carries momentum in the extra dimensions, or couples very weakly to the matter in the 4-dimensions through the gravitational force. So it will be undetected, resulting in an apparent imbalance in transverse momentum or energy ($E_{\mathrm{T}}^{\mathrm{miss}}$). The final state parton will produce a jet through fragmentation and hadronisation. Therefore the signature will be a single energetic jet and high missing E_{T}. Figure 2.1 shows the Feynman diagrams of the three sub-processes.

2.2.2 Cross Section Calculations

Starting from Einstein's equation in general relativity, and assuming that the graviton's momentum carried in the extra dimensions, transverse to the 4–D brane, is much less

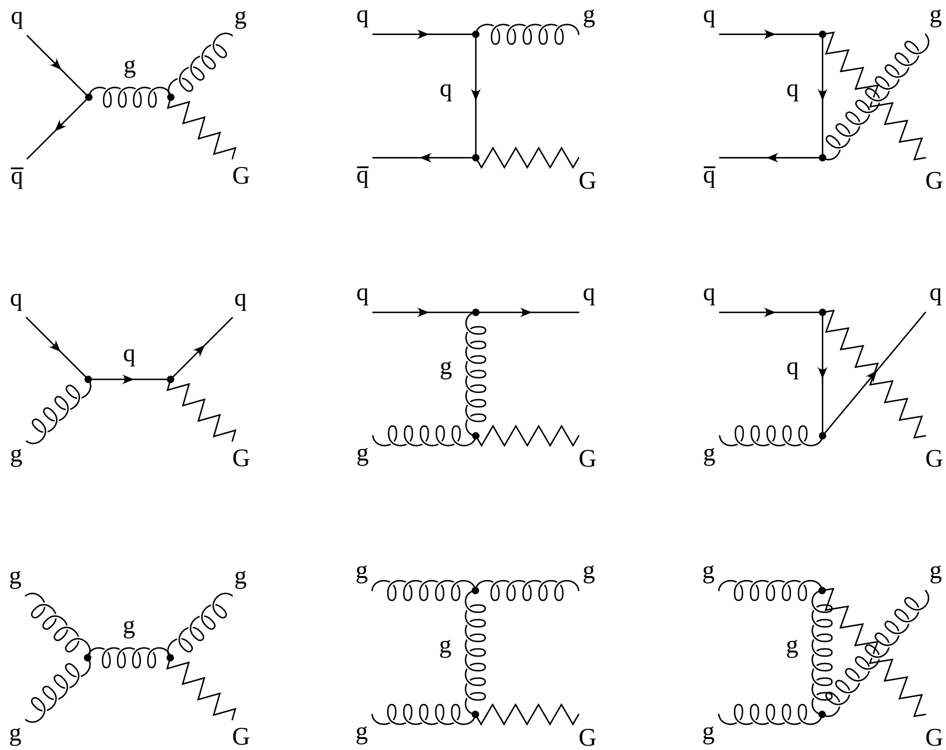

Figure 2.1: Feynman diagrams for emission of a real ADD graviton in a hadron collider.

than the scale of the theory M_D, the metric can be expanded around its flat Minkowski value. Keeping only the first power in the expansion, and requiring the periodicity of the metric under spatial transformations in the compactified extra dimensions, the interaction Lagrangian of a spin–two massive graviton can be written as:

$$\mathcal{L} = -\frac{\sqrt{8\pi}}{M_P} G^{(k)}_{\mu\nu} T^{\mu\nu}, \tag{2.4}$$

where $G^{(k)}_{\mu\nu}$ is the gravitational field of the graviton mode k. If the extra spatial dimensions are compactified and hence unobserved at our energy scale, the momentum of the graviton in these extra dimensions is quantised. This gives rise to a tower of mass terms in the 4–D Lagrangian, referred to as KK modes. The term $T^{\mu\nu}$ is the energy–momentum tensor which is symmetric and conserved. Writing $T^{\mu\nu}$ in terms of the SM fields by taking the derivative of the SM Lagrangian with respect to the metric, the Feynman rules for the graviton–SM fields interactions can be obtained. The amplitude for producing the graviton mode is suppressed by $1/M_P^2$ [22]. However, in the calculation of the total cross section for producing all the Kaluza-Klein excitation modes, a large phase space factor, proportional to M_P^2, offsets this suppression, and the inclusive cross section could be large enough for an observable signal to be produced at the LHC. The total differential cross section is related to M_D via:

$$\frac{\partial^2 \sigma_{tot}}{\partial t \partial m} \sim \frac{m^{n-1}}{M_D^{n+2}} \tag{2.5}$$

where m is the KK graviton mode's mass, n is the number of extra dimensions, and t is one of the Mandelstam variables, corresponding to the 4–momentum transfer. To get the inclusive cross section, a summation over the different masses of the KK excitations is performed. The mass of each successive KK mode is equal to $|k|/R$, where k is an integer corresponding to the k^{th} mode of the quantised graviton momentum in the extra dimension. The mass splitting is therefore of the order of $1/R$ where ([22]) :

$$\frac{1}{R} = M_D \left(\frac{M_D}{M_P/\sqrt{8\pi}}\right)^{2/n} \tag{2.6}$$

This mass splitting is very small compared to the experimental energy resolution for values of n that are not too large (below ~ 10). For example assuming $M_D = 2$ TeV, the splitting is about 0.2×10^{-5} keV, 57 keV, and 20 MeV, for $n = 2, 4, 6$ respectively. Therefore the sum over all mass modes can be replaced by an integral. For larger values of n the cross sections are negligible. The total differential cross section for each of the three sub-processes are:

$$\frac{\partial^2 \sigma_{tot}}{\partial t \partial m}(q\bar{q} \to gG) = \frac{\alpha_s}{36s} \frac{m^{n-1}}{M_D^{n+2}} F_1(t/s, m^2/s) \tag{2.7}$$

$$\frac{\partial^2 \sigma_{tot}}{\partial t \partial m}(qg \to qG) = \frac{1\alpha_s}{96s} \frac{m^{n-1}}{M_D^{n+2}} F_2(t/s, m^2/s) \tag{2.8}$$

$$\frac{\partial^2 \sigma_{tot}}{\partial t \partial m}(gg \to gG) = \frac{3\alpha_s}{16s} \frac{m^{n-1}}{M_D^{n+2}} F_3(t/s, m^2/s), \tag{2.9}$$

Here $t = (p_{parton} - p_G)^2$ and $s = (p_{parton} + p_G)^2$ are the Mandelstam variables, corresponding to the momentum transfer and centre of mass energy, m is the mass of an individual graviton mode, and F_i are the following functions:

$$F_1(x,y) = \frac{1}{x(y-1-x)}[-4x(1+x)(1+2x+2x^2)+y(1+6x+18x^2+16x^3)-6y^2x(1+2x)+y^3(1+4x)] \tag{2.10}$$

$$F_2(x,y) = -(y-1-x)F_1(\frac{x}{y-1-x}, \frac{y}{y-1-x}) \tag{2.11}$$

$$F_3(x,y) = \frac{1}{x(y-1-x)}[1+2x+3x^2+2x^3+x^4-2y(1+x^3)+3y^2(1+x^2)-2y^3(1+x4)+y^4] \tag{2.12}$$

The cross sections in Eq. 2.7- 2.9 were used in the `ExoGraviton` generator (see Appendix. B) for event generation. The two free parameters of the theory, that need to be fixed to some value in the generator to produce simulation event samples, are the scale of the theory M_D, and the generator–level transverse momentum cut off p_{T}^{Cut} of the outgoing parton, for each value of the number of extra dimensions n. A non-zero value of p_{T}^{Cut} is needed to avoid infrared divergences coming from the soft parton radiation. However, choosing a low non-zero p_{T}^{Cut} results in low statistics in the high $- p_{\mathrm{T}}$ region where the signal might be discovered when compared to background. On the other hand, calculations of the effective field theory are not reliable at energies close to the scale of the theory M_D or above, as the finite expansion of the effective Lagrangian considered for the prediction no longer represents a good approximation of the right quantum gravity theory at energies near or above the scale M_D. If, for a specific choice of p_{T}^{Cut}, the chosen M_D is not large enough, the calculation could involve the energy regime close to the scale M_D where events with $\hat{s} \sim M_D$ have a large contribution to the cross–section. Similarly, if for a particular choice of M_D the generator–level p_{T}^{Cut} is not low enough, one would face the same problem. One way to test the impact of the high energy behaviour of the theory on the prediction in the region of interest is to study the truncation of the phase space. Events with $\hat{s} > M_D^2$ are suppressed and not considered in the cross–section calculation, and hence are given a weight of zero in the generator. The contribution of such events can be seen by comparing the curve of the total cross section to that of the truncated cross section as a function of each of the two parameters. Figure 2.2 shows the ADD total and truncated cross sections as functions of the cut on the transverse momentum p_{T}^{Cut} of the recoiling parton, for $M_D = 3$ TeV, and also as functions of M_D for the generator–level $p_{\mathrm{T}}^{Cut} = 250$ GeV, for 2, 4, and 6 extra dimensions. The value of M_D at which the two cross section curves, as functions of M_D, begin to split defines a lower value for M_D below which the cross section calculations of the effective theory are not reliable. Similarly, the value of p_{T}^{Cut} at which the two cross section curves, as functions of p_{T}^{Cut}, begin to split defines a upper value for p_{T}^{Cut} above which the cross section calculations of the effective theory are not reliable. The generator–level p_{T}^{Cut} value used in this analysis was 80 GeV. This choice was made such that it did not bias the p_{T} distribution of the leading jet for a lowest p_{T}^{Cut} of 120 GeV at the reconstruction level, which defines the first signal region of the analysis as explained in Sec. 6. This choice still gave enough statistics in higher energy signal regions, with a p_{T}^{Cut} of 500 GeV on the leading jet. In these high–p_{T} signal regions, the impact of the region where the calculation is not reliable can become large, resulting in as large as a 50% difference between the truncated and complete cross–sections. This is explained in detail in Sec. 11.4 and Table 11.16. In such cases, care has to be taken in the interpretation of the experimental results in this region.

2.3 WIMP Pair Production

If interactions between dark matter and Standard Model particles involve mediators with masses large compared to the typical momentum exchange in the process, they can be described by an effective field theory. In such scenarios, a pair of WIMP particles is produced by the colliding partons and can be described by a contact interaction Lagrangian

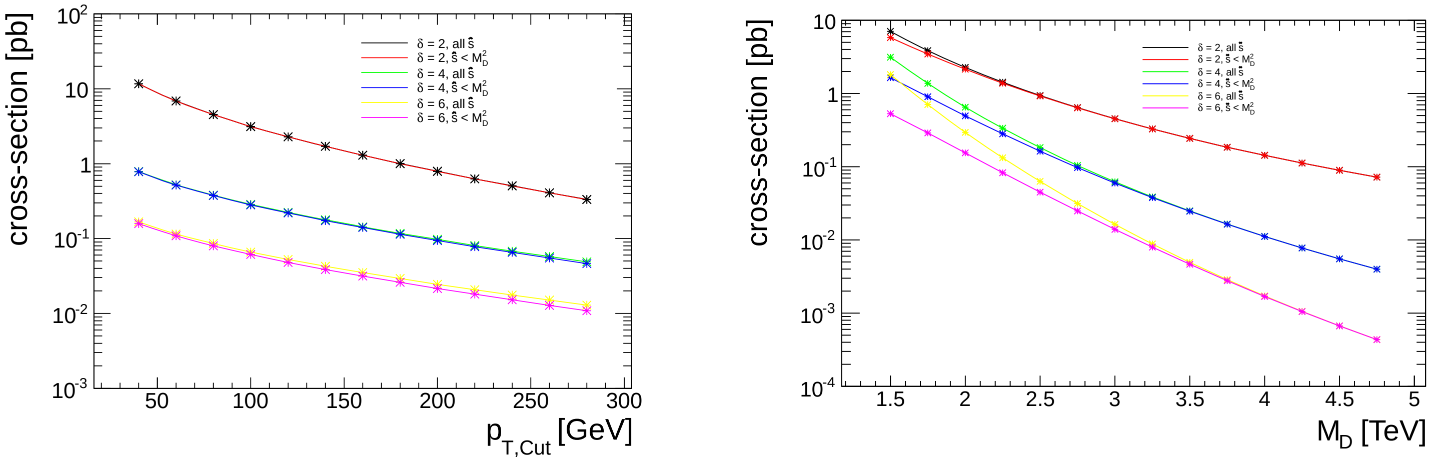

Figure 2.2: Total ADD graviton cross–section as a function of the generator–level p_{T}^{Cut} of the recoiling parton for $M_D = 3.0$ TeV (Left), and as a function of M_D for generator–level $p_{\mathrm{T}}^{Cut} = 250$ GeV (Right). Both complete and truncated cross–sections are shown.

valid below the mass scale of the heavy mediators. Due to the stability of the WIMP particles, and their weak interaction with the material of detector, resulting in their undetectability, one of the leading channels for dark matter searches at hadron colliders is a mono–jet signature, where the jet comes from ISR/FSR [10], [17], [23], as shown in Fig. 2.3. In the model considered here [12], WIMP particles are assumed to be Dirac fermions. Fourteen interactions are considered between them and the SM fields, following the naming scheme of [24], and listed in Table 2.1. These interactions can further be classified into five categories based on their $E_{\mathrm{T}}^{\mathrm{miss}}$ distributions, denoted by operators: D1, D5, D8, D9, D11. Operators D1, D5, D8, and D9 describe different quark couplings (vector, axial vector, and scalar couplings) to WIMPs ($qq \rightarrow \chi\bar{\chi}$), and D11 describes the gluon coupling ($gg \rightarrow \chi\bar{\chi}$). The energy scale of the effective theory is assumed to be equivalent to the suppression parameter M^*, mass of the heavy mediator divided by the couplings to partons and the WIMPs, $M^* = \frac{M}{\sqrt{g_q g_\chi}}$. M^* is the quantity on which a limit is set for various WIMP masses. This is described in more detail in Sec. 11.5.

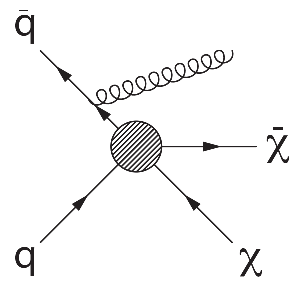

Figure 2.3: Feynman diagram for WIMP pair production, in association with a jet, in a hadron collider.

Name	Operator	Name	Operator
D1	$\frac{m_q}{(M^\star)^3}\bar{\chi}\chi\bar{q}q$	D2	$\frac{m_q}{(M^\star)^3}\bar{\chi}\gamma^5\chi\bar{q}q$
D3	$\frac{m_q}{(M^\star)^3}\bar{\chi}\chi\bar{q}\gamma^5 q$	D4	$\frac{m_q}{(M^\star)^3}\bar{\chi}\gamma^5\chi\bar{q}\gamma^5 q$
D5	$\frac{1}{(M^\star)^2}\bar{\chi}\gamma^\mu\chi\bar{q}\gamma_\mu q$	D6	$\frac{1}{(M^\star)^2}\bar{\chi}\gamma^\mu\gamma^5\chi\bar{q}\gamma_\mu q$
D7	$\frac{1}{(M^\star)^2}\bar{\chi}\gamma^\mu\chi\bar{q}\gamma_\mu\gamma^5 q$	D8	$\frac{1}{(M^\star)^2}\bar{\chi}\gamma^\mu\gamma^5\chi\bar{q}\gamma_\mu\gamma^5 q$
D9	$\frac{1}{(M^\star)^2}\bar{\chi}\sigma^{\mu\nu}\chi\bar{q}\sigma_{\mu\nu}q$	D10	$\frac{1}{(M^\star)^2}\epsilon^{\mu\nu\alpha\beta}\bar{\chi}\sigma^{\mu\nu}\gamma^5 chi\bar{q}\sigma_{\alpha\beta}q$
D11	$\frac{1}{(4M^\star)^3}\bar{\chi}\chi\alpha_s(G^a_{\mu\nu})^2$	D12	$\frac{1}{(4M^\star)^3}\bar{\chi}\gamma^5\chi\alpha_s(G^a_{\mu\nu})^2$
D13	$\frac{1}{(4M^\star)^3}\bar{\chi}\chi\alpha_s G^a_{\mu\nu}\tilde{G}^{a,\mu\nu}$	D14	$\frac{1}{(4M^\star)^3}\bar{\chi}\gamma^5\chi\alpha_s G^a_{\mu\nu}\tilde{G}^{a,\mu\nu}$

Table 2.1: Operators coupling Dirac fermion WIMPs to Standard Model quarks or gluons.

2.4 Decays of the Z Boson

In Standard Model, the neutral gauge boson couplings to the leptons are given by:

$$\mathcal{L} = \ell\bar{\ell}\gamma^\mu eA_\mu - \frac{1}{\sqrt{2}}(\frac{G_F M_Z^2}{\sqrt{2}})^{\frac{1}{2}}\bar{\nu}\gamma^\mu(1-\gamma_5)\nu Z_\mu$$
$$- \frac{1}{\sqrt{2}}(\frac{G_F M_Z^2}{\sqrt{2}})^{\frac{1}{2}}[2\sin^2\theta_W\bar{\ell}\gamma^\mu(1+\gamma_5)\ell Z_\mu + (2\sin^2\theta_W - 1)\bar{\ell}\gamma^\mu(1-\gamma_5)\ell Z_\mu], \quad (2.13)$$

where G_F is the Fermi constant, and θ_W is the weak mixing angle: $\cos^2\theta_W = \frac{M_W^2}{M_Z^2}$. Using the Feynman rules for the elementary vertices obtained from the above Lagrangian density, the decay rate of the Z boson to a pair of $\nu\bar{\nu}$ equals:

$$\Gamma(Z \to \nu\bar{\nu}) = \frac{G_F M_Z^3}{12\pi\sqrt{2}} \sim \frac{11.4[MeV]}{(\sin\theta_W \cos\theta_W)^3} \tag{2.14}$$

and to a pair of $\ell\bar{\ell}$:

$$\Gamma(Z \to \ell\bar{\ell}) = \Gamma(Z \to \nu\bar{\nu})[(2\sin^2\theta_W)^2 + (2\sin^2\theta_W - 1)^2] \tag{2.15}$$

Using $\sin^2\theta_W = 1 - \frac{M_W^2}{M_Z^2}$, $M_W = 80.385$ GeV, and $M_Z = 91.1876$ GeV, the ratio of the widths is:

$$\frac{\Gamma(Z \to \nu\bar{\nu})}{\Gamma(Z \to \ell\bar{\ell})} \sim \frac{1}{(2\sin^2\theta_W)^2 + (2\sin^2\theta_W - 1)^2} \sim 1.977 \tag{2.16}$$

Considering three light neutrino generations in the Standard Model, the ratio equals 5.930 according to the SM expectations. Section. 12 presents the direct measurement of this ratio with the ATLAS detector.

Chapter 3

LHC and the ATLAS Detector

The Large Hadron Collider (LHC) at Conseil Européenne pour la Recherche Nucléaire (CERN) is located 150 meters underground, beneath the France-Suisse border near Genève. LHC is a proton–proton collider, with a circumference of 26.7 km, and a design capacity to reach a centre of mass energy of 14 TeV and an instantaneous luminosity of 10^{34} $cm^{-2}s^{-1}$. The machine reuses the tunnel that was built for CERN's previous big accelerator, the Large Electron-Positron (LEP) accelerator.

The ATLAS (A Toroidal LHC ApparatuS) detector is a general purpose detector [25], [26] designed to detect particles produced from the collision of the two proton beams.

3.1 The Accelerator

The accelerator complex at CERN is a collection of machines, each injecting the beams to the next one while increasing their energies. The beam size (emittance) decreases as the beam energy increases in the chain. This results in higher luminosity, and decreases the probability of magnetic failure of each successive machine. The colliding beams are in two separate vacuum pipes, as they have the same charge but should be accelerated in opposite directions, and hence electric fields in opposite directions are required to accelerate them. The last machine of the accelerator complex is the LHC, which accelerated, in 2011, each beam up to 3.5 TeV. To prevent the possibility of a magnet system failure, a centre of mass energy of 7 TeV is chosen, while the initial design was at 14 TeV. The procedure of accelerating the protons is as follows: protons are obtained by ionisation from the hydrogen atoms, after which they are injected to Linac2, a linear accelerator which accelerates them to 50 MeV. The protons are then injected into the Proton Synchrotron Booster (PSB) and then to PS, which accelerate them up to 1.4 GeV and 25 GeV, respectively. The next in the chain is the Super Proton Synchrotron (SPS) which accelerates the protons up to 450 GeV. Finally the beams are injected in the LHC accelerator, in both the clockwise and anti-clockwise directions. In the LHC they are accelerated to 3.5 TeV. Figure 3.1 shows a view of the machine complex and the injection chain.

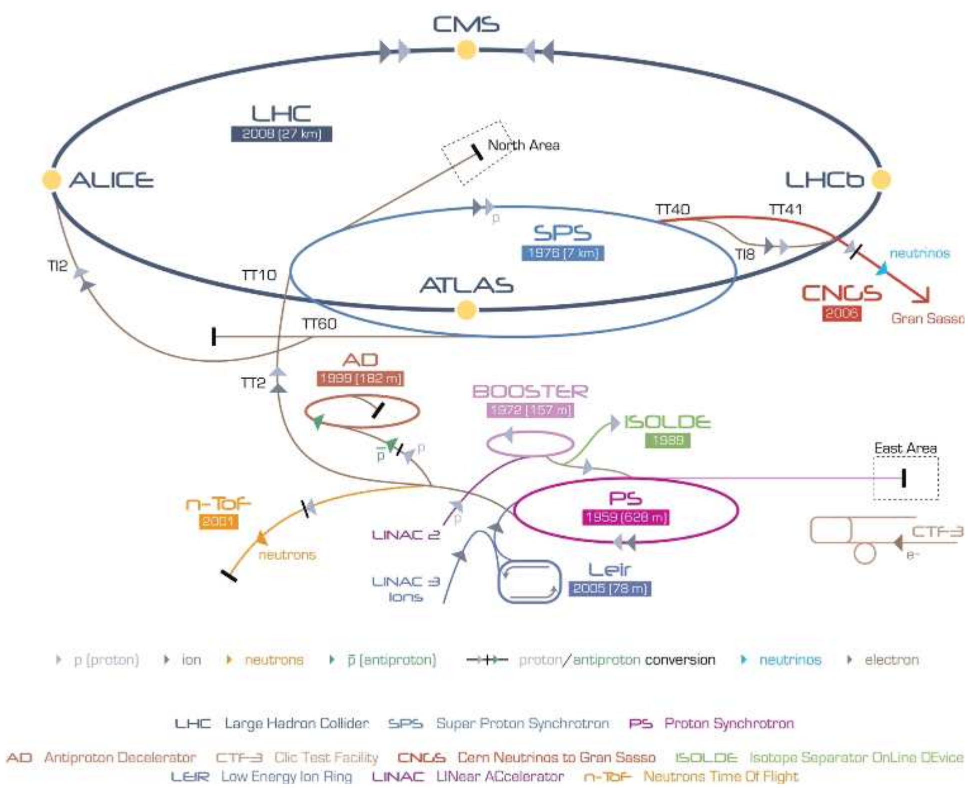

Figure 3.1: The LHC injection complex.

The LHC circle is made of eight arcs and intersection points, one of which is where the ATLAS detector is located. The intersection points are used for either experiments, or for beam injection, beam dumping, and beam cleaning. The beams are circulated in the evacuated beam pipes to avoid collisions with gas molecules. Dipole superconducting magnets are used to keep the protons in a circular orbit, required to bend the beams around the LHC ring. Quadrupole magnets are used to focus the beams to a small size which affects the luminosity and is therefore important in order to maximise the number of collisions produced at the centre of a detector. To accelerate the protons around the ring, the radio frequency (RF) cavities are used.

3.2 The ATLAS Detector

ATLAS detector is designed to cover a wide range of physics searches and SM measurements. It has a 'barrel plus endcaps' design with almost 4π solid angle to maximise the coverage of detectable particles produced in the collisions.

There are two main categories of the ATLAS sub-detectors: tracking devices – Inner Detector described in Sec. 3.2.2 and Muon Chambers described in Sec. 3.2.4, and calorimeters – electromagnetic and hadronic calorimeters described in Sec. 3.2.3. Magnetic fields (Solenoid and Toroid magnets, Sec. 3.2.1) are used to bend charged particles in the tracking devices. The trajectories are reconstructed via the signals generated by matter ionisation resulting from the passage of the charged particles. These reconstructed trajectories are used to obtain the measurement of the particles' momenta. Calorimeters are used to measure the energies of the particles traversing them, by absorbing the total energy of the particles that interact electromagnetically or strongly, and measuring the energy deposited in the calorimeter volume. An overview of the ATLAS detector is shown in Fig. 3.2.

Three types of coordinate systems are used in ATLAS according to the geometry of different sub-detectors. The origin is at the nominal interaction point (IP) in the centre

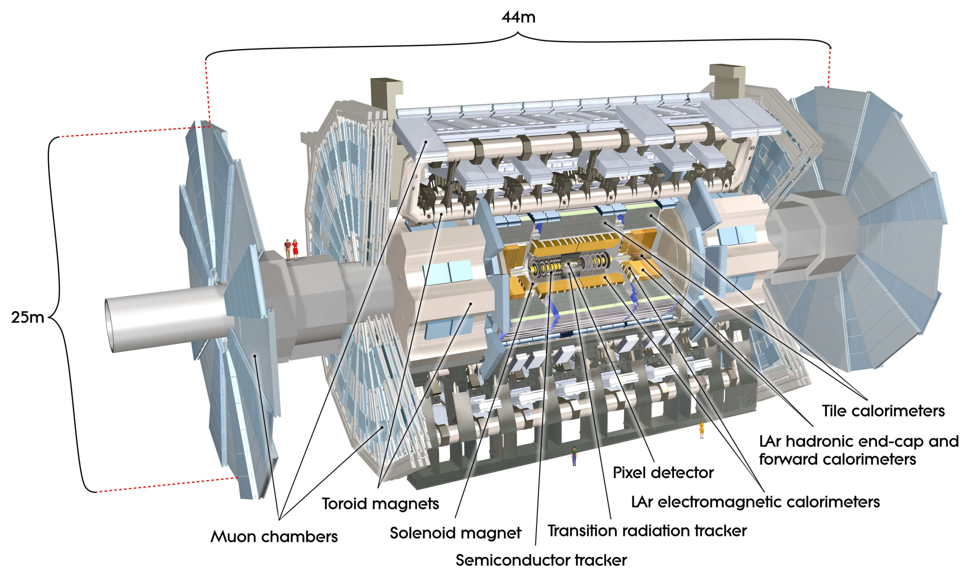

Figure 3.2: The ATLAS detector.

of the detector.

In the Cartesian coordinate system, the z-axis is defined along the beam pipe. The x-axis points from the IP to the centre of the LHC ring, and the y axis points upward.

The cylindrical coordinate system (z, R, ϕ) is mainly used for the tracking systems. The variable R is the perpendicular distance to the z-axis, and ϕ is the azimuthal angle in the x-y plane, around the beam.

The spherical coordinate system is also sometimes used $(p_{\mathrm{T}}, \eta, \phi)$. The variable η is the pseudo-rapidity, defined as $\eta = -\ln(\tan(\frac{\theta}{2}))$, where θ is the polar angle from the beam axis. The pseudo-rapidity is equal to the rapidity $y = \frac{1}{2}\ln(\frac{E+p_z}{E-p_z})$ for massless particles. This is a very useful coordinate system as it is invariant under boosts along the z–axis. Therefore it represents the system equally in its own reference frame and in the lab reference frame.

The relative distance ΔR between two objects in the pseudo-rapidity-azimuthal angle space is defined as:

$$\Delta R = \sqrt{(\phi_1 - \phi_2)^2 + (\eta_1 - \eta_2)^2} \tag{3.1}$$

where ϕ_i and η_i are the azimuthal and polar angles of object i, respectively.

3.2.1 Magnet System

The magnetic system consists of an inner superconducting solenoid providing the inner detector with magnetic field, and a large superconductor barrel toroid and two endcap eight-fold toroids outside the calorimeters, generating the magnetic fields for the muon spectrometer.

The solenoid has a length of 5.3 m, with a bore of 2.46 m. It provides a field of 2 T in the volume of the trackers. Since the solenoid is positioned in front of the calorimeters, the solenoid coil has been made very thin in order to reduce the probability of particles from the collision interacting with the material before reaching the calorimeters.

The barrel toroid consists of eight toroidal magnets symmetrically positioned in ϕ, each extending up to $|z| = 12.7$ m. Their size in R extends from 9.4 m to 20.1 m. Inside this shell, the barrel muon chambers are located. The magnetic field inside the shell is along the ϕ direction, so that the charged particles traversing the muon spectrometer are bent in the η direction.

The two endcap toroids also consist of eight toroidal magnets, symmetrically around the beam axis, and rotated by 22.5° with respect to the barrel toroid coil system. This is to optimise the bending power in the overlap regions of the barrel and endcap coils. The magnets are located at $|z| = 8$ to 12.5 m, with R between 1.7 and 10.7 m. The peak magnetic field on the endcap toroid superconductors is 4.1 T.

Figure 3.3 shows the ATLAS magnet system.

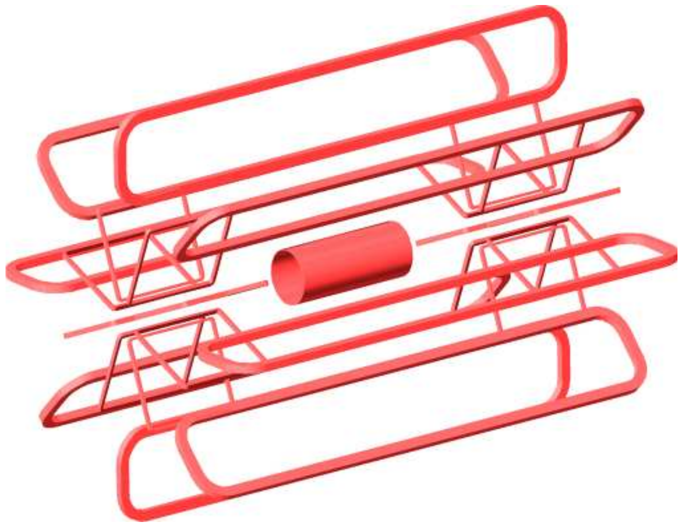

Figure 3.3: The barrel solenoid, barrel toroid, and endcap toroids.

3.2.2 Inner Detectors

The Inner Detector (ID) is composed of three sub-detectors, with the magnetic field produced by the solenoid. Its total length is $|z| = 7$ m, limited by the position of the endcap calorimeters, and its $|\eta|$ coverage goes up to 2.5. It provides the highest granularity nearest to the interaction point by using semi-conductor pixel detectors, with the innermost layer at a radius of 40 cm from the beam pipe. Charged particles ionise the material of the detectors, allowing the reconstruction of their trajectories as well as the positions of the primary and secondary vertices.

3.2.2.1 Pixel Detector

The pixel detector has the highest spatial granularity and is closest to the interaction point. This provides the best resolution closest to the beam pipe, in order to get a precise location of the vertices. The detector consists of three barrel layers at average radii of 5, 8.8, and 13 cm, and a $|z|$ distance of 4 cm, and four endcap disks on each side in order to complete the η coverage. The pixel sensors are segmented in two dimensions making a total of 140 million elements, with a size of 50×300 μm in the $R\phi - z$ space. Each barrel pixel module is 62.4 mm long and 22.4 mm wide, with 61440 pixel elements.

The pixel sensors are reverse biased silicon p–n junctions. The reverse bias produces a depletion layer which extends through the whole depth of the junction. The depletion layer has no carriers, and hence no current flows. When a charged particle passes through the depletion layer, it ionises the silicon, and thus produces carriers. The resulting current is what allows the detection of the charged particles.

3.2.2.2 SCT

The Semi-Conductor Tracker (SCT) contributes to the measurement of the particle momentum, track impact parameter (the transverse distance to the beam axis at the point of the closest approach), and the vertex position. The SCT also uses silicon p–n junction sensors. However, they are in the forms of strips, which is possible due to the lower occupancy at the radii where the SCT layers are located, and allows the cost of the system to be reduced compared to the use of pixels. It has nine endcap disk-shaped layers, and four cylindrical barrel layers of silicon detectors, with radii 30., 37.3, 44.7, and 52. cm, respectively. The spatial resolution of the modules is 16×580 μm in $R\phi -$ z space. Small angle (40 mrad) stereo strips are used to measure both coordinates.

3.2.2.3 TRT

The Transition Radiation Tracker (TRT) consists of straw detectors, parallel to the beam pipe in the barrel region, and arranged radially in the endcaps. Consequently, only the R and ϕ coordinates can be determined from each straw hit in the barrel, and the ϕ and z coordinates in the endcaps. The two endcaps consist of 18 wheels each. Each straw is 4 mm in diameter filled with the xenon gas, and with a 30 μm diameter wire acting as the anode at the centre of the straw. Each straw is a proportional ionisation detector. As a charged particle traverses a straw, it ionises the gas medium, and due to a potential difference between the wire (anode) and the the straw wall (cathode), the detected signal is caused by gas cascade amplification which produces enough ionisation to be detected. As well as being a tracking detector, the TRT also allows discrimination between electron and pion on the basis of transition radiation. The multiple di–electric interfaces are formed by filling the space between the straw tubes with polypropylene fibres. When a charged particle passes through multiple interactions between di–electric media, it produces coherent electromagnetic radiation, in the X–ray region. Since the probability of particle transition radiation increases with the relativistic γ factor of the particle ($\gamma = \frac{E}{mc^2}$), this allows a discrimination between a lighter particle (with a higher γ) and a heavier particle, and plays an important role in differentiating electrons from pions.

The momentum resolution of the inner detector can be parametrised as follows:

$$\frac{\sigma(p)}{p} = a \oplus b.p_{\mathrm{T}} \qquad \mathrm{for}|\eta| < 1.9 \tag{3.2}$$

$$\frac{\sigma(p)}{p} = a \oplus b.p_{\mathrm{T}}.\frac{1}{\tan^2\theta} \qquad \mathrm{for}|\eta| > 1.9, \tag{3.3}$$

where a and b are the multiple scattering and the intrinsic resolution terms, respectively, with the designed values listed in Table 3.1, and θ is track's polar angle.

η region	a (%)	b (TeV^{-1})
barrel	1.55 ± 0.01	0.417 ± 0.011
transition	2.55 ± 0.01	0.801 ± 0.567
end–caps	3.32 ± 0.02	0.985 ± 0.019

Table 3.1: Momentum resolution in the Inner Detector.

The layout of the inner detector is shown in Fig. 3.4.

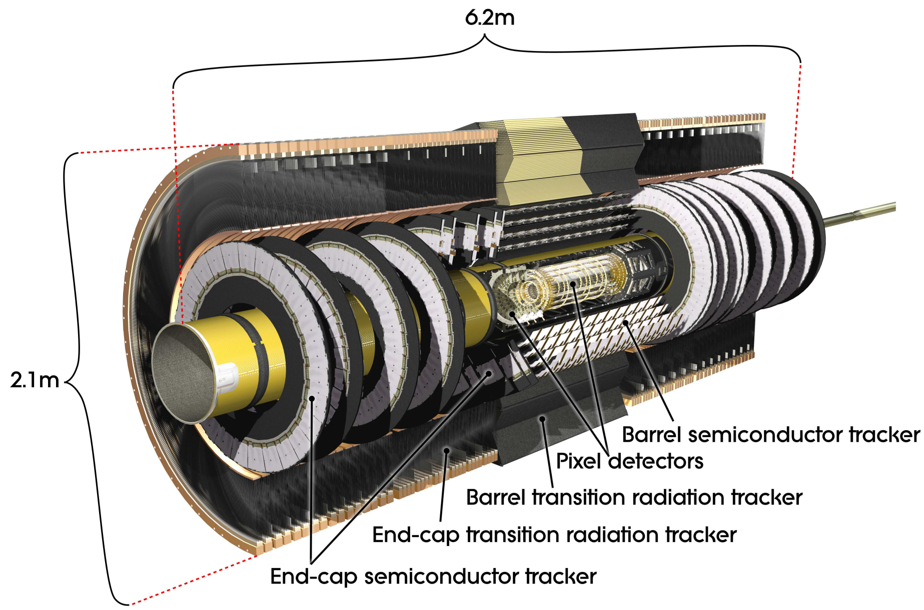

Figure 3.4: The ATLAS inner detector.

3.2.3 Calorimeters

The ATLAS calorimetry consists of an electromagnetic (EM) calorimeter up to $|\eta|$ of 3.2, hadronic barrel and endcaps with coverage of $|\eta| < 1.7$ and $1.5 < |\eta| < 3.2$, respectively, and the forward calorimeters covering $3.1 < |\eta| < 4.9$. All these sub-detectors use the sampling technology to measure the energy loss of the particles: absorbing and active layers of different materials are used to produce the particle shower and to measure the deposited energy, respectively. The absorber, usually made of a very dense material, is to develop the particle shower or to stop the particles. Electromagnetic calorimeters use absorbers where the radiation length is much less than the nuclear interaction length. In hadronic calorimeters, the radiation and interaction lengths of the absorber are comparable. The active medium is used to measure the energy deposited by the particle through reading the signal from the ionisation electrons.

3.2.3.1 EM Calorimeter

The EM calorimeter has lead as the absorber, and Liquid Argon (LAr) as the sensitive medium, with an accordion geometry. The accordion geometry is chosen to ensure azimuthal uniformity (no cracks). Up to the $|\eta|$ coverage of 1.8, there is an active presampler layer of LAr liquid 11 mm in thickness, located between the EM calorimeter and the cryostat wall, in order to provide a first sampling of the particle showers in front of the calorimeter, and correct for their energy loss in the dead material, cryostat, and the solenoid, upstream. It has a coarser granularity , 0.025×0.1 in $\Delta\eta \times \Delta\phi$, compared to EM calorimeter.

The barrel includes two identical half-barrels, each with three layers, separated by a gap of 6 mm at z = 0. Their coverage is $|\eta| < 1.475$. The granularity of the barrel layers in $\Delta\eta \times \Delta\phi$ is 0.003×0.1, 0.025×0.025, and 0.05×0.025, respectively, as is shown in Figure 3.5. This fine granularity allows for the electron/Π_0 distinction. The longitudinal segmentation allows for reconstructing the direction of photons, a feature very important in $H \to \gamma\gamma$ searches. The total thickness of the barrel calorimeter is ~ 24 radiation length (X_0). Each endcap EM calorimeter consists of two wheels that are coaxial, with a coverage of $1.375 < |\eta| < 2.5$ and $2.5 < |\eta| < 3.2$ for the outer and inner wheels, respectively. The total thickness of the endcap calorimeters is $\sim 26X_0$.

The signals from the EM calorimeters (with triangular shape) are sent to preamplifiers located outside the cryostats. The output of the preamplifiers are shaped and then sampled 5 times every 25 ns, corresponding to a total of 5 LHC bunch–crossings. The triangular signal has a rise time of ~ 1 ns, and a decay time of several hundreds of ns (~ 460 ns in the barrel, and a bit less in the endcaps due to their smaller gaps). This makes the LAr response time of the order of a few bunch–crossings, affecting the level of the out–of–time pile–up.

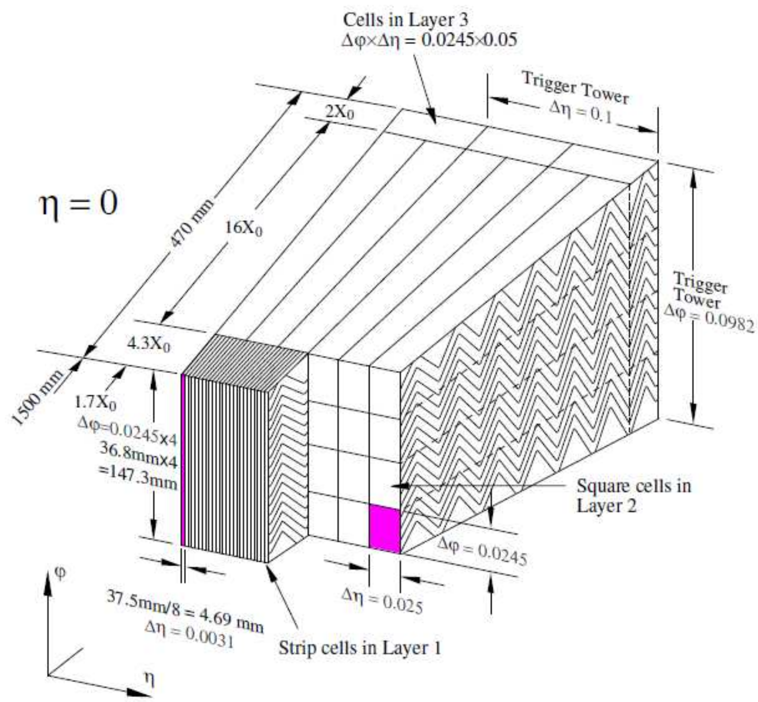

Figure 3.5: Structure of the three EM barrel layers.

3.2.3.2 Tile Calorimeter

Tile calorimeter with a coverage of $|\eta| < 1.7$ is a sampling calorimeter, using the scintillating tiles as the active material as it results in a better resolution and time of response compared to LAr, and iron as the absorber. Each tile is read out on both outer sides into two separate photo–multipliers. It has one barrel and two extended barrels, extending in R from an inner radius of 2.28 m to an outer radius of 4.25 m. The barrel is longitudinally segmented in three layers, with radiation lengths of 1.4, 4.0, and 1.8 X_0, respectively.

3.2.3.3 Hadronic Endcap Calorimeters

The Hadronic EndCap (HEC) calorimeters extend up to $|\eta| = 3.2$. Each endcap consists of two independent wheels with an outer radius of 2.03 m. The HEC is a sampling calorimeter using LAr for the active material, and copper as the absorber.

The thickness of the hadronic calorimeters are optimised in order to contain most of the hadronic showers, and minimise their punch-through into the muon system.

3.2.3.4 Forward Calorimeters

The Forward CALorimter (FCAL) covers the range $3.1 < |\eta| < 4.9$, with a front face 4.7 m away from the interaction point in the z direction. It completes the η coverage of the ATLAS calorimetry systems, as well as reducing the level of radiation entering the muon spectrometer. It is a sampling calorimeter, consisting of three layers. The active material is LAr, and the absorber is copper in the first layer and tungsten in the next two layers. In each layer, it consists of the concentric rods and tubes filled with LAr, parallel to the beam pipe. The rods are at positive high voltage and the tube walls (acting as the cathode) are grounded.

The energy resolution of the calorimeter can be parametrised as follows:

$$\frac{\sigma(E)}{E} = \frac{a}{\sqrt{E(\mathrm{GeV})}} \oplus b \oplus \frac{c}{E(\mathrm{GeV})} \tag{3.4}$$

The first term is the sampling term, which corresponds to the Poisson fluctuations of the particles in the shower[1], depending on the choice of absorber and the active material, as well as the thickness of the sampling layers. The constant term is due to the detector non-uniformities, crack regions, and presence of dead material. The last term corresponds to the electronic noise. Table 3.2 lists the designed values of different terms for the EM and hadronic calorimeters.

The better resolution of the EM calorimeter compared to the hadronic calorimeter is due to the fact that part of the energy of the hadronic shower remains invisible, through interaction of particles with the nuclei and producing neutrinos and nuclear fragments. The better resolutions of both compared to FCAL is due to a poor stochastic term of the energy resolution in FCAL due to the small sampling fraction of the shower.

The layout of the ATLAS calorimeter system is shown in Fig. 3.6.

[1] The number of particles in a shower is proportional to the energy of the initial particle.

calorimeter	a	b	c
EM	10%	0.7%	0.2%
Hadronic	50%	3%	–
FCAL	100%	10%	–

Table 3.2: Energy resolution in the calorimeter sub-detectors.

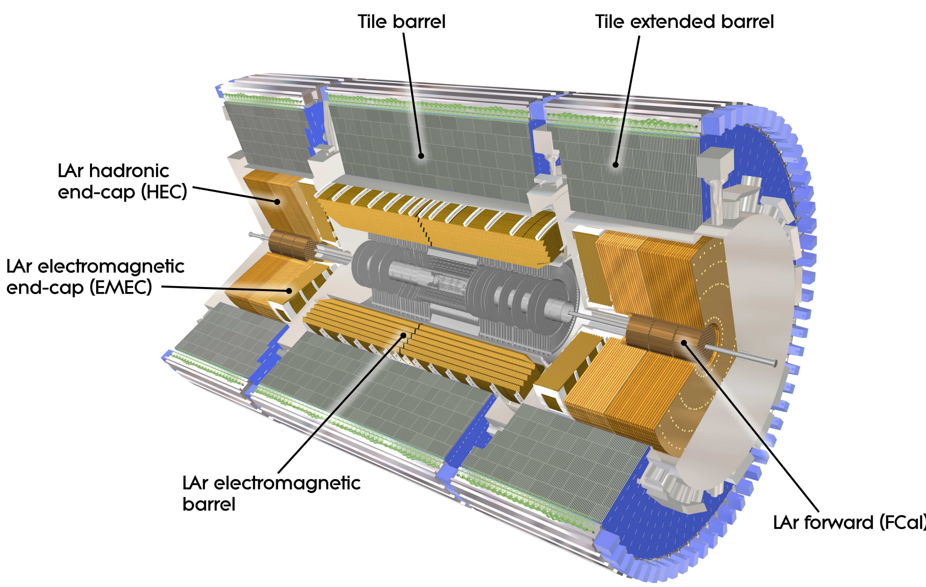

Figure 3.6: The ATLAS calorimetry.

3.2.4 Muon Chambers

The muon chambers are located outside the calorimeters, and are used to measure the momenta of the muons traversing them, based on the magnetic deflection of the muon tracks in the magnetic field provided by the barrel toroid over the range $|\eta| < 1.0$, and by the endcap toroids for $1.4 \leq |\eta| \leq 2.7$. In the transition region, $1. \leq |\eta| \leq 1.4$, a combined magnetic field of the barrel and endcap toroids is present.

The muon spectrometer consists of two types of detectors in both barrel and endcap regions: the high-precision tracking chambers (MDT and CSC) measuring the position of the muon tracks up to $|\eta|$ of 2.7, and the trigger chambers (RPC and TGC) for event triggering purposes, with a total coverage of $|\eta| < 2.4$. The momentum resolution of the spectrometer is $\alpha.p_{\mathrm{T}}$, with α being 4% for tracks with $p_{\mathrm{T}} < 500$ GeV, and 10% for transverse momenta up to 1 TeV.

3.2.4.1 MDT

The Monitored Drift Tubes (MDT) are precision tracking chambers, covering up to 2.7 in $|\eta|$. In the barrel region, there are three concentric cylinders, at radii of 5., 7.5, and 10. m, respectively, covering up to $|\eta|$ of 1. There are four endcap wheels on each side, located at $|z|$ of 7, 10, 14, and 21 – 23 m from the interaction point. MDT consists of aluminium drift tubes 30 mm in diameter with a 50 μm diameter central wire. The tubes are filled with a non-flammable mixture of Ar and CO_2.

3.2.4.2 CSC

The Cathode Strip Chambers (CSC) cover the range $2 < |\eta| < 2.7$, and are equipped with cathode strip readouts. They use a gas mixture of Ar, CO_2, and CF_4. The two coordinates of the muon track are obtained by measuring the induced charge on the two orthogonal cathode strips, one orthogonal to the anode, and one parallel to it.

3.2.4.3 RPC

The Resistive Plate Chambers (RPC) are gaseous detectors covering $|\eta| < 1.05$, used for trigger purposes. The basic unit consists of a gas gap formed by two parallel high voltage plates, creating a uniform electric field. As the ionising particle passes through the gas, the signal due to the electron avalanche is read out by two sets of orthogonal strips on each side of the gas gap.

3.2.4.4 TGC

The Thin Gap Chambers (TGC) are located in the endcap regions, covering a range of $1.05 < |\eta| < 2.4$. Their functionality is similar to the CSCs. The signals from the anode wire and the orthogonal readout cathode strips are used to provide the trigger information, as well as the measurement of the two coordinates (R and ϕ).

The momentum resolution of the muon chamber can be parametrised as follows:

$$\frac{\sigma(p)}{p} = \frac{a}{\sqrt{p_{\mathrm{T}}}} \oplus b \oplus c.p_{\mathrm{T}}, \tag{3.5}$$

where a, b, and c are coefficients related to the energy loss in the calorimeter material, multiple scattering and intrinsic resolution terms, respectively, with the designed values listed in Table 3.3.

η region	a (TeV)	b (%)	c (TeV^{-1})
barrel	0.25 ± 0.01	3.27 ± 0.05	0.168 ± 0.016
transition	0	6.49 ± 0.26	0.336 ± 0.072
end–caps	0	3.79 ± 0.11	0.196 ± 0.069

Table 3.3: Momentum resolution in the Muon Spectrometer.

The layout of the ATLAS muon spectrometer is shown in Fig. 3.7.

3.2.5 Trigger

Considering the LHC bunch spacing of 25 ns, and high luminosities of the bunches, a trigger system is required to select rare physics processes of interest. The ATLAS trigger and Data AQuisition (DAQ) system has a three-level online event selection procedure. This makes the trigger having no dead time, as events are stored in a pipeline for the first level trigger to make its decision. Each level applies further selection criteria with

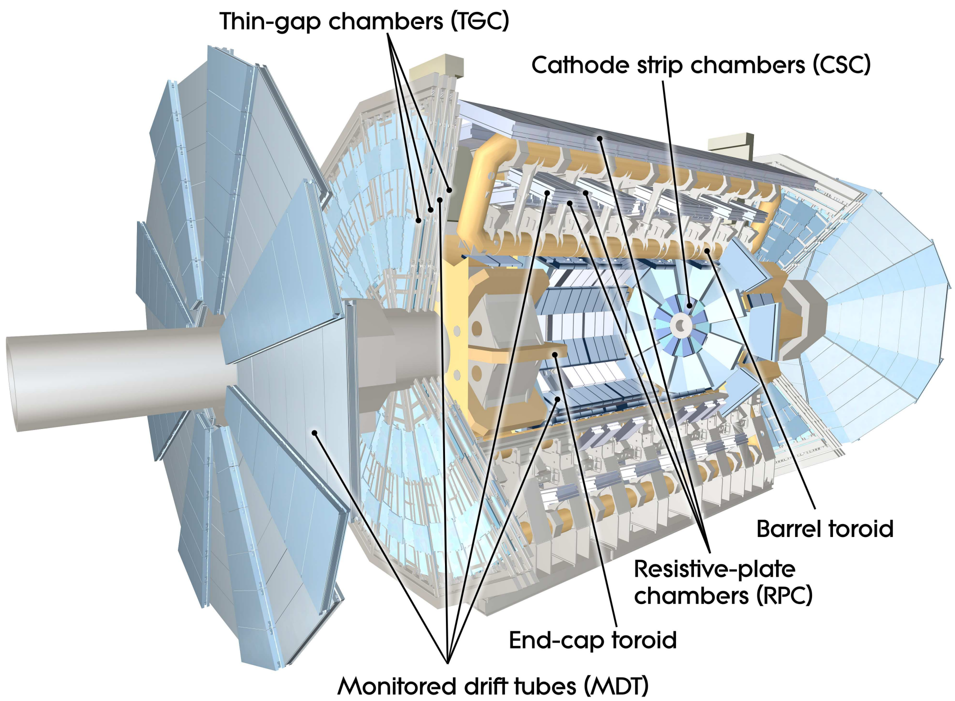

Figure 3.7: The ATLAS muon spectrometer.

respect to the the previous level to reduce the amount of data to be stored. The final rate for permanent storage is ~ 400 Hz.

3.2.5.1 L1

The first-level (L1) trigger makes a decision based on a subset of information from the calorimeter or muon detectors (RPC and TGC). It searches for high $p_{\rm T}$ muons traversing RPC or TGC, or high $p_{\rm T}$ electrons, photons, jets, and hadronically decaying τs in the calorimeter, as well as large missing transverse and total energies, by summing over the energies of the trigger towers – regions in the EM or hadronic calorimeters with a granularity of 0.1×0.1 in $\Delta\eta \times \Delta\phi$, and 800,000 channels in the RPCs (Barrel) and TGCs Endcaps. It then forms the Region Of Interests (ROI), corresponding to limited regions centred around these objects, and it includes information about the $p_{\rm T}$, η, and ϕ of these candidate objects. L1 trigger requires about 2 μs to make a decision (the L1 latency), limited by the length of the pipeline for event storage. All the information from the detector is stored in pipeline memories until this decision is made. The output rate of LVL1 is about 75 kHz, and can be controlled by changing the L1 trigger thresholds. All the information accepted by L1 is stored in ReadOut Buffers (ROB), to be used by the L2 trigger.

3.2.5.2 L2

The L2 trigger is a software–based trigger that uses the ROI information provided by L1. It has access to the full detector granularity if necessary. However, it usually uses the data from a small fraction of the detector corresponding to the ROIs provided by LVL1. It has a time latency of 1 – 10 ms, and a final output rate of about 5 kHz.

3.2.5.3 EF

The last stage of the online event selection is done at the Event Filter (EF) level. It uses the offline algorithms along with the latest calibration information, to fully reconstruct the events that have passed the L2 trigger. The output event rate of EF is about 400 Hz. Selected events are stored permanently in storage disks for offline analyses, and in different data streams: `EGamma` for events with electron candidates, `JetTauEtmiss` for events with jets or τ candidates, or high $E_{\mathrm{T}}^{\mathrm{miss}}$, and `MUON` including events with muon candidates. An event can belong to more than one data stream.

At each trigger level, many different triggers run in parallel. A trigger chain is a set of the three trigger levels with specific thresholds. As an example, the $E_{\mathrm{T}}^{\mathrm{miss}}$ trigger `EF_xe60_verytight_noMu` used in this analysis to select events in the signal regions has the following triggers in the chain: `L1_xe50_noMu`, `L2_xe55_noMu`, and `EF_xe60_noMu`. "`noMu`" indicates that no muon information is used to calculate the $E_{\mathrm{T}}^{\mathrm{miss}}$, and the number after "`xe`" indicates the lower threshold applied on the $E_{\mathrm{T}}^{\mathrm{miss}}$ at each trigger level.

Chapter 4

Object Reconstruction

In this section, the reconstruction methods of various objects (jets, $E_{\mathrm{T}}^{\mathrm{miss}}$, and leptons) used in this analysis are explained.

4.1 Jet Reconstruction

Final state partons from the hard scattering processes in a proton-proton collision are colour states which undergo fragmentation and hadronisation processes before reaching the detector. During fragmentation, the initial parton radiates extra partons, which will form the final state hadrons during the hadronisation process. The collection of these hadrons will then form a jet of particles moving in the direction highly correlated to that of the initial boosted parton. These jets of hadrons are what are observed in the detector. Since they carry the information about the initial partons, understanding the properties of jets is extremely important. Jet finding algorithms can be run on various physical objects in the calorimeter (particles, topological calorimeter clusters, calorimeter towers). Each of them can give different estimates of the initial parton properties.

In the following sub-sections, first various jet finding algorithms and different types of inputs are explained. Then the methods used to calibrate jets are detailed, and finally jet cleaning procedure to recognise poorly reconstructed or non–physical jets is described.

4.1.1 Jet Algorithms

Jet algorithms are used to combine spatially related energy deposits into a jet. A jet reconstruction algorithm clusters groups of energy deposits into a single jet. This process is governed by a distance parameter R; the distance in η–ϕ space between two energy depositions. In physical terms, R governs how far a soft parton can be from the primary jet axis, and still be included in the jet. The jet reconstruction algorithms must have the following properties:

- Infrared safety: the emission of soft partons in the final state should not affect the topology and number of jets found by the algorithm.
- Collinear safety: a jet should be reconstructed independent of the fact that a particle carrying a certain fraction of the jet p_{T} is split into two collinear particles or not.
- Order independence: the algorithm should result in the same jet final states regardless of the type of the input (parton, particle, or detector level inputs such as towers or topological clusters).
- Detector effects such as electronic noise, dead material regions, and crack sections should have a minimum effect on the results of the jet finding algorithm.
- The algorithm should be robust in the presence of pile-up and underlying event in the collision.

The procedure used to combine the jet inputs in ATLAS is based on the four-vector sum of the inputs:

$$(\vec{p}, E)_{\mathrm{jet}} = \sum_{i}^{N_{\mathrm{inputs}}} (\vec{p_i}, E_i) \tag{4.1}$$

In the following, two main ATLAS jet algorithms are described: the fixed cone and the sequential recombination algorithm.

4.1.1.1 Cone Algorithm

This is based on an iterative seeded fixed-cone procedure, combining the inputs based on their geometrical proximity in the detector. First a seed among the constituents is chosen, providing that the constituent is the highest in p_{T} and above the seed threshold of 1 GeV. Then, all the inputs within a cone of radius R_{cone} are combined with the seed, $\Delta R = \sqrt{\Delta\eta^2 + \Delta\phi^2} < R_{\mathrm{cone}}$, where R_{cone} is 0.4 or 0.6 in ATLAS, corresponding to a narrow or wide cone jet. The sum of the four-momenta of all the constituents inside this cone results in a new direction, around which a new cone is centred. Inputs are then re-combined with respect to this new direction, and a new cone is formed. The procedure continues until the direction of the cone stays stable and does not change with the recombination. This stable cone is called a jet. Once this jet is formed, the procedure is repeated for the next seed candidate.

Such an algorithm is not infrared safe in the sense that in the presence of soft radiation in between two jets, the algorithm can result in the reconstruction of a single jet rather than two. It can also result in some constituents being included in two different cones. In order to avoid such double counting, a "split/merge" process is performed: jets are merged if they share constituents with more than a specific p_{T} fraction of the less energetic jet. And they are split if this fraction is less than f_{sm}. In ATLAS f_{sm} is chosen to be 0.5.

A second deficiency of this algorithm is that the seed might be lost from the jet in the process of recalculation of the cone direction, resulting in high energy constituents being absent from any of the final state jets (the dark tower problem [27]).

4.1.1.2 Sequential Recombination Algorithm

This algorithm is based on the combination of pairs of inputs into a single constituent if they satisfy a minimum distance criterion. Pair merging is repeated till no further such combination is possible. The ATLAS recombination jet finder is known as the "k_{T}

algorithm". In this algorithm the combination of a pair of inputs ij, depends on the value of the parameter d_{ij}, where:

$$d_{ij} = \min(p_{\mathrm{T},i}^2, p_{\mathrm{T},j}^2)\frac{\Delta\eta_{ij}^2 + \Delta\phi_{ij}^2}{R^2} \tag{4.2}$$

where p_{T} is the transverse momentum of each constituent, and R is the distance parameter, controlling the size of the jet. As in the cone algorithm $R = 0.4$ and 0.6 for narrow and wide jets. The transverse momentum squared of constituent i relative to the beam is set to be $p_{\mathrm{T},i}^2 = d_i$, and the constituents are merged if:

$$d_{ij} < d_i \tag{4.3}$$

The merged pair is then removed from the list of inputs, and is replaced by the new combined constituent. The above condition ensures that the low p_{T} inputs are likely to be merged with the closest higher p_{T} ones. This procedure is infrared safe since it does not use seeds.

However, the method becomes problematic in the high pile up environment. This algorithm depends on combining low p_{T} constituents. If there is pile up, there are many random constituents not associated with the real jet. This could result in different jets being found, depending on the details of the random pile up.

Another approach, the anti-k_{T} algorithm, behaves oppositely to the k_{T} algorithm in that high p_{T} inputs are merged first. In this approach, d_{ij} is defined as:

$$d_{ij} = min(p_{T,i}^{-2}, p_{T,j}^{-2})\frac{\Delta\eta_{ij}^2 + \Delta\phi_{ij}^2}{R^2} \tag{4.4}$$

and $p_{T,i}^{-2} = d_i$. This algorithm is much less affected by pile up, as it starts building the jet from the hard constituents. It also gives the jets a regular area. Figure 4.1 shows the jet areas created by the two algorithms.

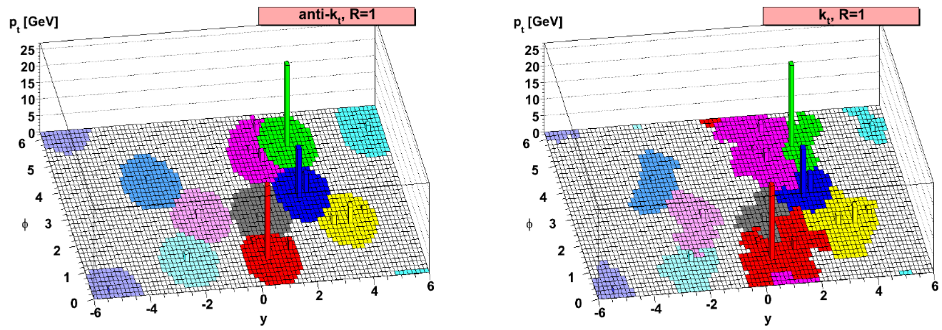

Figure 4.1: Jet shapes created by the Anti-k_{T} and k_{T} algorithms.

4.1.2 Jet Inputs

The input constituents used to build a jet should reflect the energy deposition of the hadrons forming the jet. In the following, two types of inputs are discussed: calorimeter towers, and topological calorimeter clusters.

4.1.2.1 Calorimeter Towers

The calorimeter towers have a bin size of $\Delta\eta \times \Delta\phi = 0.1 \times 0.1$ in the region $|\eta| < 4.9$ and $-\pi < \phi < \pi$. This gives a total of 6400 towers in the calorimeter. The energy deposition in the towers is assumed to represent massless particles. The total energy of each tower is the sum of the energies of the calorimeter cell constituents in the tower. These can be negative due to noise in the calorimeter electronics. Simply ignoring these towers results in an enhancement of the contribution of positive noise fluctuations. To avoid this problem noise suppression is done: towers with negative energy are combined with nearby positive–energy towers, such that the combined four–momentum has $E > 0$.

4.1.2.2 Topoclusters

Another type of jet input constituents are the calorimeter topological clusters which constitute the best estimator of the shower of a particle in the calorimeter. A cluster is seeded by a cell with a signal to noise ratio ($\Gamma = \frac{|E_{\text{cell}}|}{\sigma_{\text{noise, cell}}}$) above a threshold of $\Gamma > 4$. All direct neighbours of the seed in all three dimensions are added to the cluster. Neighbours of the neighbours are added only if they have $\Gamma > 2$. Finally, a ring of border of cells with $\Gamma > 0$ are added to the cluster. Once all such clusters are formed, a cluster is split in the case where more than one local energy maximum is found within it. Topoclusters are the preferred jet input constituents in ATLAS as the calorimeter towers do not make best use of the fine granularity of the calorimeter. Moreover, topoclustering automatically applies the noise suppression, and includes fewer cells in each jet, resulting in less noise contribution to the jet. However, topoclusters are sensitive to the noise modelling in the calorimeter.

4.1.3 Jet Calibration

The ATLAS calorimeters have a lower response to the hadronic energy deposits compared to electromagnetic. The lower response of the hadronic showers compared to electromagnetic ones is due to:

- Possibility of hadron-nucleon strong interactions, resulting in "invisible" energy loss such as binding energy, nuclear fragments, and production of slow neutrinos, which is not the case for electrons and photons.
- Leakage of the hadronic shower energy outside the detector because the nuclear interaction length is large, compared to the radiation length.

Due to this non-compensating behaviour, the energy of hadronic jets must be calibrated back to the particle level. Low energy density ($\frac{\text{Energy}}{\text{Volume}}$) cells are likely to be from hadronic showers, and are weighted by the order of electron/pion signal ratio. High density cells are more likely to be from electromagnetic showers, and need no additional weights. The calibration can be done at two levels: particle and parton levels. The particle level calibration corrects the jet energy back to the energy of the particles inside the jet, while the parton level corrections correct the jet energy back to the energy of the parton from the hard scattering which makes the jet. The official ATLAS calibrations are done at the particle level. The parton level corrections could depend on the specific physics signature under study.

Three calibration procedures are used in ATLAS as explained in the following subsections.

4.1.3.1 Electromagnetic Jet Energy Scale (EMJES)

This calibration scheme is a jet–based calibration, correcting for the missing part of the hadronic energy of the jets. Therefore, it depends on the correct description of hadrons in the ATLAS calorimeter simulation. The corresponding Jet Energy Scale (JES) correction factors depend on the p_{T} and η of the jets. Simulation samples are used to derive these JES factors by comparing the p_{T} of a reconstructed jet matched to a truth[1] jet ($\Delta R < 0.3$), and are binned in bins of truth p_{T} and η. This map is then re-binned in bins of the reconstructed p_{T}; this is known as the "numerical Inversion" procedure. In–situ measurements of γ+jets or Z+jets and single hadron response can also be used to get the JES factors, and to constrain the systematic uncertainties on the calibration constants extracted from simulation. This calibration scheme does not improve the jet energy resolution, and only calibrates the average jet energy and p_{T}. This is the method used for calibrating jets in this analysis.

4.1.3.2 Global Cell Weighting (GCW)

The GCW calibration scheme calibrates the energy of the cells in a jet based on their position in the calorimeter, and their energy density $\rho_i = \frac{E_i}{V_i}$, where E_i is the electromagnetic energy of the cell, and V_i its volume. The cell calibration constants are obtained from QCD di–jet simulation samples by fitting the energy of reconstructed tower jets to the energy of the corresponding truth particles, and then optimising in order to im-

[1]The generator level information.

prove the jet energy resolution. Once the cells are calibrated, the jet four-momentum is re-calculated according to:

$$(\vec{p}, E)_{\mathrm{jet}} = \sum_{i}^{N_{\mathrm{cells}}} w(\rho_i, \vec{X}_i)(\vec{p_i}, E_i), \tag{4.5}$$

where $w(\rho_i, \vec{X}_i)$ is the calibration weight for cell i. These weights depend on the jet shower profiles, as different profiles result in different energy densities.

4.1.3.3 Local Hadronic (LC)

In this scheme, the calibration is applied to the clusters after classifying them as electromagnetic or hadronic. This classification is done based on the properties of the topocluster energy, using distinguishing characteristics between electromagnetic and hadronic clusters, such as energy density. The energy of the hadronic topoclusters will be corrected for the non-compensation, out-of-cluster energy depositions, and the presence of dead material in the detector, by applying multiplicative calibration weights to their constituent cells. These weights are derived using simulated samples or test beam data.

4.1.4 Jet Data Quality and Cleaning

Jets in the calorimeters that are not associated with real energy depositions of particles from collisions can be either due to calorimeter electronic noise or from non-collision events such as energetic cosmic muons showering in the calorimeter, or beam – halo events. In order to remove such jets, the jet cleaning cuts are applied to all the jets with $p_{\mathrm{T}} > 20$ GeV. The following variables are used for the jet cleaning:

- emf: jet energy fraction in the electromagnetic calorimeter.
- fmax: maximum jet energy fraction (in a calorimeter layer).
- HECf: jet energy fraction in the Hadronic End–Caps (HEC).

- LArQ (LArQuality): the jet energy fraction corresponding to LAr cells with a cell Q-factor[2] greater than 4000.

- HECQ: jet energy fraction corresponding to HEC cells with a cell Quality factor greater than 4000.

- NegativeE: amount of negative energy in the jet.

- t (Timing): jet time computed as the energy–weighted sum of the mean time of its cell constituents.

- chf (jet charged fraction): ratio of the sum of the p_{T} of all the tracks associated to the jet divided by the calibrated jet p_{T}.

A jet is considered a bad jet if it satisfies at least one of the criteria below:

- **HEC spikes** : Huge noise bursts of hundreds of GeV generate energetic jets, but the quality of the fit of the signal pulse shape is poor, resulting in a large jet quality factor.

  (HECf > 0.5 and $|$HECQ$| > 0.5$) or NegativeE > 60 GeV or HECf $> 1 - |$HECQ$|$

- **EM coherent noise** :

  emf > 0.90 and $|$LArQ$| > 0.8$ and $|\eta_{jet}| < 2.8$

- **non-collision and cosmic background** : Appendix C for more details.

  $|t| > 10$ ns

  or (emf < 0.05 and chf < 0.10 and $|\eta_{jet}| < 2$)

  or (emf > 0.95 and chf < 0.10 and $|\eta_{jet}| < 2$)

  or (emf < 0.05 and $|\eta_{jet}| \geq 2$)

  or (fmax > 0.99 and $|\eta_{jet}| < 2$)

[2]The cell quality factor measures the difference between the measured pulse shape (a_i^{meas}) and the predicted pulse shape (a_i^{pred}) that is used to reconstruct the cell energy, and is defined as: $\sum\limits_{samples} (a_i^{meas} - a_i^{pred})^2$.

In this analysis, the event is removed if it contains at least one bad jet above 20 GeV in p_{T}.

4.2 Missing Transverse Energy Reconstruction

The vector sum of the momenta of final state particles in the x – y plane should be zero as the two incoming partons collide along the z axis. A non-zero sum could indicate the presence of a weakly interacting particle crossing the detector such as a neutrino, or could be due to an energy mis–measurement of a visible particle, and is referred to as the missing transverse energy $E_{\mathrm{T}}^{\mathrm{miss}}$ in the event. Missing transverse energy is an important component in this analysis. It could be due to, e.g. the graviton p_{T}, or the Z boson p_{T}.

The ingredients to reconstruct $E_{\mathrm{T}}^{\mathrm{miss}}$ are the energy deposits in the calorimeter cells and the muon tracks in the muon chambers. Also a correction is applied for the energy lost in the cryostat. There are two main methods to reconstruct $E_{\mathrm{T}}^{\mathrm{miss}}$.

The first approach (MET_LocHadTopo) is based on the total energy deposition in the calorimeter topoclusters. Topocluster energies are first calibrated using the LC calibration scheme, as described in Sec. 4.1.3.3. This calibration scheme also corrects for the energy loss in the detector dead material regions, such as the cryostat. So no further correction is made for the energy loss in the cryostat. The magnitude of the vector sum of all the cells in these calibrated topoclusters is the value of the MET_LocHadTopo,

$$E_{x,y}^{\mathrm{miss}} = - \sum_{\mathrm{TopoCells}} E_{x,y}^{\mathrm{Cell}} . \tag{4.6}$$

The second approach (MET_RefFinal) is based on the sum of transverse momenta of reconstructed calibrated objects. The objects are electrons, photons, hadronically decaying tau-leptons, jets and muons.

The main differences between the two approaches to calculate $E_{\mathrm{T}}^{\mathrm{miss}}$ are the muon contribution which is not included in the first approach, and the calibration schemes.

Since events with mono-jet topologies have no isolated lepton in the final state, the first approach to calculate $E_{\mathrm{T}}^{\mathrm{miss}}$ is used in this analysis.

4.3 Lepton Reconstruction

Electrons and muons are used in this analysis to construct the lepton control regions for determination of the main electroweak backgrounds to the signal regions. They are also used in the lepton vetoes in the signal regions where no lepton may be present in the final state. In the following two sections, brief descriptions of the muon and electron reconstruction methods are provided.

4.3.1 Muon Reconstruction

Muon reconstruction is based on the combined use of data from Inner Detector (ID), Calorimeters, and the Muon Spectrometer (MS). There are four main strategies to reconstruct the muons in ATLAS:

- the standalone strategy, which finds the tracks in the muon spectrometer and extrapolates them to the beam line.
- the combined strategy, which pairs the MS tracks to the Inner Detector tracks and combines the two measurements.
- the tagged muon strategy, which extrapolates Inner Detector tracks above a certain threshold to the first station of the MS and searches for nearby segments.
- the calorimeter tagging strategy to tag ID tracks using the calorimeter cell signals.

The standalone strategies have a slightly larger η coverage, but with a much lower muon momentum resolution compared to the combined algorithms. In this analysis, muons in data Control Regions (CR) are required to be combined muons; i.e muons reconstructed using the combined strategy. The muons used to veto have a looser requirement, i.e. a more stringent veto of being either combined or segment-tagged muons.

For each strategy, two main reconstruction algorithms can be used: Staco, and Muid [26]. Staco is an algorithm which combines an ID and an MS track that can be matched in η and ϕ. The principle of this method is the statistical combination of the parameters of these two independent measurements by means of their covariance matrices. Muid uses a global fit to combines an ID track with an MS track. The algorithm used in this analysis for both CR and veto muons is Staco, which is the current default for physics analyses in ATLAS.

4.3.2 Electron Reconstruction

Clusters in the electromagnetic calorimeter are reconstructed using the sliding window algorithm [28], which constructs rectangular clusters of a fixed size, with a position chosen such that the cluster energy is maximised. The cluster window size is larger for electrons compared to photons, as electrons interact more with the detector material, and also emit soft photons when bending in the magnetic fields. For each reconstructed cluster, the algorithm searches for a track matched to a window of size 0.05×0.10 in $\Delta\eta \times \Delta\phi$, with a track momentum compatible with the energy of the cluster: $\frac{E}{p} < 10$. If no associated conversion - no association to a conversion vertex from a converted photon - is found for this track, it is considered to be an electron candidate, otherwise a photon candidate. For electrons, based on the shower shapes, tracking parameters, and matching quality, three levels of electron quality are defined in decreasing order of efficiency and increasing order of purity: loose, medium++, and tight++. Each quality criterion is a combination of various cuts related to the $\eta - \phi$ position of the electron, number of associated hits in different ID sub-detectors, and shower shape variables.

In this analysis, tight++ electrons are used in the W($e\nu$)+jets control regions defined in Sec. 8.2, due to the large purity of tight++ algorithm in order to reject the QCD multi–jet background in W($e\nu$)+jets control regions. For the Z(ee)+jets control regions, due to lower statistics and also lower QCD multi–jet background, medium++ algorithm is used. Finally, for the electron veto requirements, medium++ electrons are used.

Chapter 5

Data and Simulation Event Samples

The data and simulated event samples used in this analysis are the Standard Model D3PDs made from the official ATLAS AOD[1] samples, and are much reduced in size compared to AODs.

The data samples correspond to the data-taking periods B to M, corresponding to the data taken from 22$^{\text{nd}}$ of March 2011 to 30$^{\text{th}}$ of October 2011. They correspond to an integrated luminosity of 4.7 fb^{-1} with an uncertainty of 3.9%. The samples include only events for which the whole ATLAS detector was fully operational[2]. The `JetTauEtmiss` data stream is used for this analysis[3], after selecting events with a calorimeter-based missing transverse energy ($E_{\mathrm{T}}^{\mathrm{miss}}$) trigger. Table 5.1 lists the corresponding integrated luminosity for each period, along with the trigger used to select events in that period.

Simulated samples are produced with the ATLAS software, Athena release 17. The distribution of the average number of interactions per bunch-crossing (μ) in data is used to model the pile-up in simulation. Hence no additional pile-up re-weighting procedure[4] is needed for simulated events in this analysis.

[1] Analysis Object Data (AOD) is a summary of the reconstructed Event Summary Data (ESD).

[2] By using the Good Run Lists (GRL).

[3] For the electron control regions the `EGamma` stream is used, and for the study of the trigger efficiency the `Muon` stream is used, as explained in later sections.

[4] Assigning pile-up weights to each event based on the number of reconstructed vertices in the event, in order to reproduce the μ distribution obtained from data.

Period	Run range	Luminosity (pb^{-1})	Trigger considered
B	178044 - 178109	11.73	EF_xe60_noMu
D	179710 - 180481	166.33	EF_xe60_noMu
E	180614 - 180776	48.65	EF_xe60_noMu
F	182013 - 182519	132.35	EF_xe60_noMu
G	182726 - 183462	507.53	EF_xe60_noMu
H	183544 - 184169	259.50	EF_xe60_noMu
I	185353 - 186493	338.39	EF_xe60_noMu
J	186516 - 186533	20.76	EF_xe60_tight_noMu
J	186669 - 186755	204.90	EF_xe60_verytight_noMu
K	186873 - 187815	590.10	EF_xe60_verytight_noMu
L	188921 - 190343	1403.68	EF_xe60_verytight_noMu
M	190608 - 191933	1019.73	EF_xe60_verytight_noMu
Total	178044 - 191933	4703.65	

Table 5.1: Integrated luminosity and the corresponding trigger for different data periods. For the three runs of period J, EF_xe60_noMu was prescaled and EF_xe60_verytight_noMu was not active. A total integrated luminosity of 4.7 pb^{-1} is calculated for the complete dataset, using the data for which the ATLAS detector was fully operational.

The W and Z bosons decaying leptonically in association with jets are generated with ALPGEN [29] interfaced with HERWIG [30, 31], for the parton shower and fragmentation processes, and with JIMMY [32] for the underlying event process. The parton density functions (PDF) used for these samples are CTEQ6L1 [33]. The events are generated with different parton multiplicities from zero to five. The overall normalisation of these samples are on the next–to–next–to–leading order (NNLO) cross sections calculated with FEWZ [34, 35].

The $t\bar{t}$ samples are generated with MC@NLO [36, 37], interfaced with HERWIG for the parton shower and fragmentation processes, and with JIMMY for the underlying event process. The cross–sections are given at the NLO with a next-to-next-leading logarithmic correction (NNLL). The CTEQ6.6 [38] NLO PDF set is used for the matrix element, parton showering and the underlying event process.

Appendix. A includes all the simulation event samples used in this analysis, along with their corresponding cross sections and the generator used to produce them, in Tables A.1, A.2, A.3, A.4, A.5, and A.6.

Signal samples were generated using the ExoGraviton generator [39] (more details in Appendix. B) and passed to the fast detector simulation (AtlFast II [40]) and reconstruction. Parton showering and hadronisation were performed by PYTHIA [41] with the ATLAS MC11c tuning and MRST LO** PDF set [42]. The PDF re-weighting tool is then used to get the corresponding CTEQ6.6 signal acceptances and cross sections. Table A.7 in Appendix. A shows the production cross sections of signal samples for different (n, M_D) phase space points[5] with a cut of 80 GeV at the generator level on the transverse momentum of the outgoing parton. The M_D values chosen to generate the samples are the ones nearest to the latest published M_D limits presented in [6] and [43]. Additional samples with a modification in the level of Initial and Final State Radiations (ISR/FSR), different Parton Distribution Function sets, and choices of normalisation and

[5]The complete table of cross sections can be found at: https://twiki.cern.ch/twiki/bin/viewauth/Atlas/ADDGraviton

factorisation scales Q^2, have also been generated at truth level for the signal systematic uncertainties studies.

Chapter 6

Object Definition and Event Selection

The `JetTauEtmiss` data stream (as mentioned in Sec. 3.2.5) is used to select events in the signal regions. Such events satisfy the following event preselection criteria:

- The data is collected with the ATLAS detector being fully operational. This requires the use of the ATLAS official Good Run Lists (GRL).
- To select events with a high $E_{\mathrm{T}}^{\mathrm{miss}}$, the calorimeter-based $E_{\mathrm{T}}^{\mathrm{miss}}$ trigger `EF_xe60_verytight_noMu` is used as will be explained in Chapter 7.
- To make sure the events are coming from a hard collision, the presence of at least one reconstructed primary vertex with at least two associated tracks is required.
- Jets are reconstructed using the anti-k_{T} algorithm as explained in Sec. 4.1.1, with a cone radius of 0.4, and calibrated to the electromagnetic level, using the EMJES coefficients as explained in Sec. 4.1.3. The leading jet is required to be central with $|\eta| < 2.0$, and with $emf > 0.1$ and $chf > 0.02$ (defined in Sec. 4.1.4). All the jets are required to be above 30 GeV in p_{T} and with $|\eta| < 4.5$. The ATLAS official jet cleaning cuts, as presented in Sec. 4.1.4 are applied on all the jets above

20 GeV in p_{T} to remove calorimeter electronic noise, non-collision, and beam halo backgrounds.

- The $E_{\mathrm{T}}^{\mathrm{miss}}$ is calculated from the topoclusters in the calorimeter (MET_LocHadTopo, as defined is Sec. 4.2), up to $|\eta|$ of 4.5. As the events only include jets and no leptons in the final state, this type of $E_{\mathrm{T}}^{\mathrm{miss}}$ is a good estimate of the transverse momentum of the new particle recoiling the parton from the hard scattering.

The main objects in a mono-jet final state are jets and $E_{\mathrm{T}}^{\mathrm{miss}}$, and there should not be any charged leptons (e, μ). Hence events are rejected if they contain at least one electron or muon with the requirements as described below:

Loose electrons:

- $p_T > 20$ GeV and $|\eta_{\mathrm{cluster}}| < 2.47$, where η_{cluster} is the η of the calorimeter cluster associated with the electron
- Medium++ requirements (Sec. 4.3.2)
- author $\in \{1, 3\}$. This means that the object is reconstructed by the standard cluster–based and track–based algorithms.
- exclude electrons with clusters that include cells with a dead High Voltage, or with missed FEBs[a]
- keep electrons in crack regions
- No overlap removal with jets

Loose muons:

- $p_T > 7$ GeV and $|\eta| < 2.5$
- StacoCombined or Segment-tagged requirements (Sec. 4.3.1)
(equivalent to author $\in \{6, 7\}$)
- Isolated p_T-cone20 < 1.8 GeV
- Matched to inner detector track fulfilling quality cuts

[a]Front End Board

Although the signature of interest has a mono-jet topology, the presence of a 2$^{\text{nd}}$ jet in the event is tolerated since it could be due to the radiation of the high p_{T} leading jet. Allowing a second jet also reduces the signal systematic uncertainties due to ISR/FSR, and increases the signal acceptance. Events with a 3rd jet above 30 GeV are rejected. Furthermore, to reduce the multi-jet background to the mono-jet events where the 2$^{\text{nd}}$ jet is aligned with the direction of $E_{\text{T}}^{\text{miss}}$ and is mis-measured, a lower $\Delta\phi$ cut between the 2$^{\text{nd}}$ jet and the $E_{\text{T}}^{\text{miss}}$ is applied: $|\Delta\phi(E_{\text{T}}^{\text{miss}}, \text{jet}_2)| > 0.5$.

Finally, four Signal Regions (SR) are defined by symmetric cuts on the leading jet p_{T} and the $E_{\text{T}}^{\text{miss}}$, with the following lower thresholds (in GeV): 120, 220, 350, and 500. Table 6.1 summarises these four inclusive signal regions. The lowest signal region is chosen so that it is in the plateau of the $E_{\text{T}}^{\text{miss}}$ trigger (Chapter 7). The highest signal region is defined such that there are still enough statistics in the highest control region for the data–driven background determination (Chapter 8).

Signal regions	SR 1	SR 2	SR 3	SR 4
Common cuts	Preselection cuts + lepton veto + $\|\Delta\phi(E_{\text{T}}^{\text{miss}}, \text{jet}_2)\| > 0.5$ + $N_{\text{jets}} < 3$			
Dedicated cuts	$p_{\text{T}}^{\text{jet}_1} > 120$ GeV $E_{\text{T}}^{\text{miss}} > 120$ GeV	$p_{\text{T}}^{\text{jet}_1} > 220$ GeV $E_{\text{T}}^{\text{miss}} > 220$ GeV	$p_{\text{T}}^{\text{jet}_1} > 350$ GeV $E_{\text{T}}^{\text{miss}} > 350$ GeV	$p_{\text{T}}^{\text{jet}_1} > 500$ GeV $E_{\text{T}}^{\text{miss}} > 500$ GeV

Table 6.1: Definition of the four inclusive signal regions of the analysis.

Chapter 7

Trigger

To select events with high $E_{\mathrm{T}}^{\mathrm{miss}}$, the lowest unprescaled calorimeter-based $E_{\mathrm{T}}^{\mathrm{miss}}$ trigger active for the 2011 data-taking is used: the `EF_xe60_verytight_noMu` trigger (more details in Sec. 3.2.5), with lower calorimeter-based $E_{\mathrm{T}}^{\mathrm{miss}}$ thresholds of 50, 55, and 60 GeV at the L1, L2, and EF levels, respectively. Since this trigger was not active for the first data periods (B-I), the `EF_xe60_noMu` trigger was used instead, with an additional lower cut of 55 GeV on the L2 $E_{\mathrm{T}}^{\mathrm{miss}}$, in order to emulate the `EF_xe60_verytight_noMu` trigger. Also for the first three runs of period J, the `EF_xe60_tight_noMu` trigger was used along with a lower cut of 55 GeV on the L2 $E_{\mathrm{T}}^{\mathrm{miss}}$, as `EF_xe60_noMu` was prescaled and `EF_xe60_verytight_noMu` was not active. Table 7.1 summarises the triggers considered in each period, with the associated integrated luminosities listed in Table 5.1.

Period	Trigger and requirement
B to I	`EF_xe60_noMu` and L2 $E_{\mathrm{T}}^{\mathrm{miss}} > 55$ GeV
J (186516, 186532, 186533)	`EF_xe60_tight_noMu` and L2 $E_{\mathrm{T}}^{\mathrm{miss}} > 55$ GeV
J (from 186533) to M	`EF_xe60_verytight_noMu`

Table 7.1: Trigger and additional requirements considered for different data periods.

The efficiency of the `EF_xe60_verytight_noMu` trigger is estimated using a data control region selected from the `MUON` data stream, and triggered by an orthogonal[1] muon trigger (`EF_mu18_medium`). This control region mainly consists of the electroweak $W(\mu\nu)$+jets events, selected using the standard selection cuts except the muon veto (Sec. 8.2.3). Figure 7.1 shows the efficiency as a function of the offline reconstructed $E_{\mathrm{T}}^{\mathrm{miss}}$. This efficiency is compared to the one obtained from the pile-up re-weighted simulated $W(\mu\nu)$+jets samples, and a difference of $\sim 1\%$ is found between the two. For predictions fully based on simulation, which include signal yields, $t\bar{t}$+single t, and di-boson background determinations, the trigger should be emulated in a way that has an efficiency equal to that in the data. However, instead of applying a scale factor, which is ratio of data trigger efficiency to that from simulation, to the simulation to correct for this difference, an uncertainty of $\sim 1\%$ is assigned to the signal yield or to any background determined from simulation.

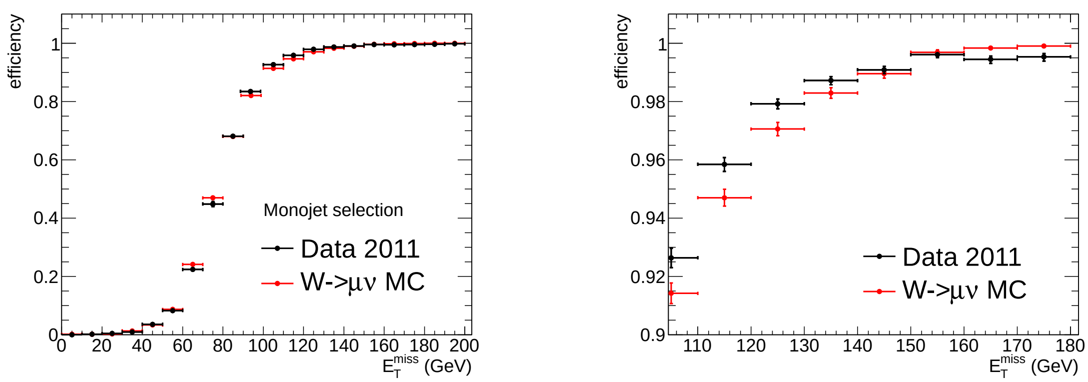

Figure 7.1: `EF_xe60_verytight_noMu` trigger efficiency as a function of the offline reconstructed $E_{\mathrm{T}}^{\mathrm{miss}}$ using $W(\mu\nu)$+jets data (black) and simulated (red) events.

The combined jet+$E_{\mathrm{T}}^{\mathrm{miss}}$ trigger is not used, mainly due to the fact that it has the same $E_{\mathrm{T}}^{\mathrm{miss}}$ threshold as the one used in this analysis, but with additional tight jet requirements which reduce the trigger efficiency with respect to the single object trigger. Moreover, there is a difference between calibrations of the trigger-based $E_{\mathrm{T}}^{\mathrm{miss}}$ using the LC calibration scheme and the offline reconstructed jets using the EMJES calibration

[1]It is orthogonal to the $E_{\mathrm{T}}^{\mathrm{miss}}$ trigger as the latter only uses the calorimeter information, and not the muons.

(Sec. 4.1.3) in 2011 data-taking, and also an additional contribution to the systematic uncertainty due to the Jet Energy Scale.

The effect of in-time pile–up (multiple interactions occurring in the same bunch crossing, due to the large number of protons in each beam) on the trigger efficiency is studied by comparing the efficiency estimated using control region events with different number of reconstructed vertices in the event. The difference among resulting trigger efficiencies is $\sim 1\%$ from the in-time pile–up effect. The effect of the neighbouring bunch crossings due to the longer response of the various detector electronics compared to the time spacing of the bunches (out-of-time pile–up) on the trigger efficiency is studied using the bunch position information: bunch crossings with different positions in the bunch trains, each consists of up to 36 proton bunches with a time spacing of 50 ns, are used to estimate the trigger efficiency. This results in less than 1% difference among the resulting trigger efficiencies. Since data control regions are used to estimate the trigger efficiency, the in–time and out–of–time pile–up effects are automatically included in this estimation, and hence no systematic uncertainty is attributed to it.

Chapter 8

Determination of Electroweak Backgrounds

This chapter describes the method used to determine the main backgrounds present in this analysis. The overall data–driven strategy to determine the background is explained in Sec. 8.1. The procedure for applying this strategy to get the background determination from muon control regions is explained in detail in Sec. 8.2. Electron control regions, and finally estimation of systematic uncertainties are presented in Sec. 8.3 and 8.4.

8.1 Introduction and Strategy

The largest background to mono-jet events in the kinematic regions defined in Sec. 6 is the Standard Model electroweak background. The main process is the irreducible background Z($\nu\nu$)+jets. The next largest, reducible, background is W($\tau\nu$)+jets, where the τ decays either leptonically or hadronically. Finally there are the contributions from Z($\tau\tau$)+jets, W($\ell\nu$)+jets, and Z($\ell\ell$)+jets with $\ell = \mu, e$.

The determination of all the electroweak backgrounds is done using exclusive data Control Regions (CR), consisting of W($\ell\nu$)+jets, or Z($\ell\ell$)+jets Standard Model processes. The method is based on a “pseudo” cross section measurement. The data control regions are corrected for the lepton–related selection cuts that are used to define these control regions, but the jets kinematics are kept at the detector level. This gives the rate of events corresponding to the full lepton phase space, and is referred to as the pseudo cross section; i.e. the cross section after full correction of the lepton cuts, but with no jet unfolding[1]. An additional set of transfer factors is applied to these full lepton phase space regions to account for the differences in jet and $E_{\mathrm{T}}^{\mathrm{miss}}$ distributions between control and signal regions. The jet kinematics are the same in $\mathrm{Z}(\ell\ell)$ and $\mathrm{Z}(\nu\nu)$ events, or in $\mathrm{W}(\ell\nu)$ and $\mathrm{W}(\ell_{\mathrm{missing}}\nu)$ events where the lepton is missed, so one process can be used to model another. Simulation is only used to obtain corrections for lepton acceptance and QED radiation effects, in order to normalise the jet distributions obtained from data control regions to those in signal regions. The impact on the background prediction is small, since such corrections are obtained only through ratios where the same jets and $E_{\mathrm{T}}^{\mathrm{miss}}$ selection cuts are applied to both numerator and denominator of the simulation–based factor, and jet effects cancel. The advantage of such a method is that it removes the presence of large systematic uncertainties – both experimental uncertainties on jet modelling such as the jet energy scale, as well as the theoretical uncertainties on the cross sections such as renormalisation and factorisation scales, and parton distribution functions – associated with an approach based on only simulation.

A drawback of this method is that the available statistics of $\mathrm{Z}(\ell\ell)$ in the control region is about an order of magnitude smaller than the statistics of the process $\mathrm{Z}(\nu\nu)$ it is being used to model. However, in W+jets control regions, which are used to determine W+jets background in signal regions, the jet kinematics are close to those in Z+jets events, and the differences have been carefully studied, with a small systematic uncertainty, in the Rjets[2] precision measurement [44]. So W+jets control regions can also be used to model $\mathrm{Z}(\nu\nu)$+jets events in signal regions. In addition, they have much

[1] Measured distributions are distorted by the finite resolution and limited acceptance of the detector. The transformation to the true distribution is called unfolding.

[2] A measurement of the ratio of the W + 1 jet to Z + 1 jet cross sections.

larger statistics compared to Z($\ell\ell$) control regions, therefore do not limit the precision of the determination. Both electron and muon channels can be used for this purpose, resulting in four orthogonal control regions: W($\mu\nu$)+jets, W($e\nu$)+jets, Z($\mu\mu$)+jets, and Z(ee)+jets.

As mentioned before, this background prediction method is essentially equivalent to a W/Z+jets cross section measurement, where the jet quantities are left at the detector level, i.e. unfolded. Selection cuts on lepton kinematics used in previous ATLAS precision Standard Model measurements [45,46] have been used here to select events for W/Z+jets control regions. However, the same jet cuts as in the signal regions defined in Sec. 6 are applied to the jets in these control regions, so that they model the signal region properly.

One difficulty in applying the mono-jet selection cuts to control regions is the definition of $E_{\mathrm{T}}^{\mathrm{miss}}$. In Z($\nu\nu$)+jets events in signal regions, the calorimeter–based $E_{\mathrm{T}}^{\mathrm{miss}}$ represents the p_{T} of the Z. This is also almost the case in muon control regions, as muons deposit negligible energy in the calorimeter. However, in electron control regions the calorimeter energy deposited by the electrons from the boson decay is not negligible, and must be removed from the calorimeter–based $E_{\mathrm{T}}^{\mathrm{miss}}$ to give the correct Z p_{T}, equivalent to $|\vec{E}_{\mathrm{T}}^{\mathrm{miss}} + \vec{p_{\mathrm{T}}}^{\mathrm{electron}}|$. This yields missing transverse momentum which, as in Z invisible decays, does not take into account the contribution from the decay products of W or Z bosons. However, for W($e\nu$) control region used to estimate the W($e\nu$) background in signal regions, the cut is directly applied on the calorimeter–based $E_{\mathrm{T}}^{\mathrm{miss}}$ without removing the deposited energy from the electron. This is due to the fact that the W($e\nu$) background in signal regions consists of events with electrons passing the electron veto, hence contributing to the calorimeter–based $E_{\mathrm{T}}^{\mathrm{miss}}$. To model the $E_{\mathrm{T}}^{\mathrm{miss}}$ distribution of such events in the control region, the same calorimeter–based $E_{\mathrm{T}}^{\mathrm{miss}}$ is used, i.e. without removing the electron contribution.

The presence of reconstructed leptons in the control regions affects the shape of the $E_{\mathrm{T}}^{\mathrm{miss}}$ and number of jets distributions, compared to those of the signal regions. For example, removing jets associated with electrons in the electron control regions removes part of the available jet phase space in these control regions compared to that in Z($\nu\nu$)+jets events. Similarly, additional radiation from muons and electrons in the control regions can produce extra jets that would not be present in the Z($\nu\nu$)+jets events. Correction factors based on simulation are used to correct for these differences between control and signal regions. The precision of this method relies on how well these differences due to the impact of the lepton between the signal and the control regions, as well as the background to W+jets and Z+jets control regions are modelled.

In summary, the method can be described in four steps:

- Selection of data control regions, and subtraction of background (N_{bkg}) in these regions. Using previous Standard Model precision measurements, the electroweak background contributions to the W/Z+jets events can be modelled well by simulations. However this is not the case for QCD multi–jet background to the W/Z+jets events. Hence, these precision measurements use data–driven techniques to estimate this background [45, 46], which is used in this analysis also.

- Correction for lepton acceptance and efficiency, and the acceptance of W/Z specific cuts– symbolised by C in equations below– which provides the pseudo cross sections mentioned above.

- Using a transfer factor, T, to account for the possible differences between signal and control regions due to the presence of the leptons in the control regions.

- Applying the efficiency ratio of the triggers used in the signal and control regions ($R_{trig} = \frac{\epsilon^{SR}_{trig}}{\epsilon^{CR}_{trig}}$), as well as the ratio of the corresponding luminosities of data streams used to select events in signal and control regions ($\frac{\mathcal{L}_{E_{\mathrm{T}}^{\mathrm{miss}}}}{\mathcal{L}_{\ell}}$) . This only applies to the electron control regions (Sec. 8.3) for which a different trigger and data stream than that of the signal regions is used to select events, while a dedicated electron trigger is required to get the electron data control region sample. This need not be the case for muon control regions. Since no muon correction is applied to the calorimeter–based $E_{\mathrm{T}}^{\mathrm{miss}}$ trigger (Sec. 7), the same $E_{\mathrm{T}}^{\mathrm{miss}}$ trigger can be used to select events in both signal and non–overlapping muon control regions. In this case, the trigger efficiency ratio is equal to 1 with no uncertainty.

As an example, the determination of Z($\nu\nu$)+jets from the Z($\ell\ell$) control region is done as follows:

$$N^{SR}_{\mathrm{Z}(\rightarrow\nu\nu)+jets} = (N^{Data}_{\mathrm{Z}(\rightarrow\ell\ell)+jets} - N_{bkg}) \times C \times T \times R_{trig} \times \frac{\mathcal{L}_{E_{\mathrm{T}}^{\mathrm{miss}}}}{\mathcal{L}_{\ell}} \tag{8.1}$$

All correction factors are computed in bins of $E_{\mathrm{T}}^{\mathrm{miss}}$, and for each of the four regions. So the full kinematic distribution is corrected, and not only its integral. This is due to the fact that the acceptance and efficiencies of the leptons, the background contamination in the control regions, and the distortion of the $E_{\mathrm{T}}^{\mathrm{miss}}$ distribution due to the presence of the lepton in the control regions compared to the signal regions, can vary as a function of the vector boson transverse momentum. Binning in terms of the calorimeter-based $E_{\mathrm{T}}^{\mathrm{miss}}$ hence corrects both the normalisation and the shape of the $E_{\mathrm{T}}^{\mathrm{miss}}$ distribution in the control regions to be similar to that of the signal regions.

Not all the correction factors are based on simulation. The lepton identification efficiencies are derived from data by applying data-driven scale factors [47] corresponding to the ratio of data to simulation based identification efficiencies to the simulation-based efficiency maps. Also, the multi-jet QCD background in the control regions (N_{QCD}) is estimated using the data-driven approach mentioned above.

The complete procedure of obtaining the data–driven determination of process X in a mono–jet signal region, $N_X^{SR,\mathrm{predicted}}$, is as follows:

$$N^{SR,\text{predicted}}_{\mathrm{Z}(\rightarrow\nu\nu)+jets} = \frac{(N^{Data}_{\mathrm{Z}(\rightarrow\ell\ell)+jets} - N_{QCD}) \times (1-f_{EW})}{A_\ell \times \epsilon_\ell \times \epsilon^{trig}_\ell \times \mathcal{L}_\ell} \times \frac{N^{SR}_{\mathrm{Z}(\rightarrow\nu\nu)+jets}}{N_{\mathrm{Z}(\rightarrow\ell\ell)+jets}} \times \epsilon^{trig}_{E_{\mathrm{T}}^{\mathrm{miss}}} \times \mathcal{L}_{E_{\mathrm{T}}^{\mathrm{miss}}} \quad (8.2)$$

$$N^{SR,\text{predicted}}_{\mathrm{Z}(\rightarrow\nu\nu)+jets} = \frac{(N^{Data}_{\mathrm{W}(\rightarrow\ell\nu)+jets} - N_{QCD}) \times (1-f_{EW})}{A_\ell \times \epsilon_\ell \times \epsilon_W \times \epsilon^{trig}_\ell \times \mathcal{L}_\ell} \times \frac{N^{SR}_{\mathrm{Z}(\rightarrow\nu\nu)+jets}}{N_{\mathrm{W}(\rightarrow\ell\nu)+jets}} \times \epsilon^{trig}_{E_{\mathrm{T}}^{\mathrm{miss}}} \times \mathcal{L}_{E_{\mathrm{T}}^{\mathrm{miss}}} \quad (8.3)$$

$$N^{SR,\text{predicted}}_{\mathrm{Z}(\rightarrow\ell\ell)+jets} = \frac{(N^{Data}_{\mathrm{Z}(\rightarrow\ell\ell)+jets} - N_{QCD}) \times (1-f_{EW})}{A_\ell \times \epsilon_\ell \times \epsilon^{trig}_\ell \times \mathcal{L}_\ell} \times \epsilon^{trig}_{E_{\mathrm{T}}^{\mathrm{miss}}} \times \mathcal{L}_{E_{\mathrm{T}}^{\mathrm{miss}}} \times T(\not{\ell}) \quad (8.4)$$

$$N^{SR,\text{predicted}}_{\mathrm{W}(\rightarrow\ell\nu)+jets} = \frac{(N^{Data}_{\mathrm{W}(\rightarrow\ell\nu)+jets} - N_{QCD}) \times (1-f_{EW})}{A_\ell \times \epsilon_\ell \times \epsilon_W \times \epsilon^{trig}_\ell \times \mathcal{L}_\ell} \times \epsilon^{trig}_{E_{\mathrm{T}}^{\mathrm{miss}}} \times \mathcal{L}_{E_{\mathrm{T}}^{\mathrm{miss}}} \times T(\not{\ell}) \quad (8.5)$$

where:

N^{Data}_X and N_{QCD} are the number of data events in the control region of process X, and the corresponding QCD multi-jet background estimated with data–driven techniques.

A_ℓ and ϵ_ℓ are the lepton acceptance and identification efficiency.

ϵ^{trig}_ℓ and $\mathcal{L}_\ell$ are the lepton trigger efficiency and the corresponding luminosity, for the lepton control region. This is needed only for the background determinations based on the electron control regions.

$\epsilon^{trig}_{E_{\mathrm{T}}^{\mathrm{miss}}}$ and $\mathcal{L}_{E_{\mathrm{T}}^{\mathrm{miss}}}$ are the $E_{\mathrm{T}}^{\mathrm{miss}}$ trigger efficiency and the corresponding luminosity, for the signal region. This is needed only for the background determinations based on the electron control regions.

ϵ_W is the efficiency for the W boson specific selection cuts: the transverse mass cut, and the cut on the corrected $E_{\mathrm{T}}^{\mathrm{miss}}$.

f_{EW} is the electroweak background fraction. It is defined as the ratio of simulated electroweak events, including single top, $t\bar{t}$, and di-boson events as well, excluding the electroweak process corresponding to the control region to all simulated electroweak events. To remove this background, the factor $(1 - f_{EW})$ can be used instead of directly subtracting the number of electroweak background events in control regions. This procedure has the advantage that it reduces the associated uncertainties in the background ratio, since it is expected that variations due to both the generator model and detector simulation will contribute in a similar way to each process if the same generator and detector simulation are used. Furthermore, such an estimate does not depend on the knowledge of the absolute luminosity in data.

$\frac{N^{SR}_{Z(\to\nu\nu)+jets}}{N_{Z(\to\ell\ell)+jets}}$ is the ratio of simulated Z($\nu\nu$)+$jets$ events in the signal region to simulated Z($\ell\ell$)+jets events in the full lepton phase space. This term includes the ratio of branching fractions $\frac{\mathrm{Br}(Z\to\nu\nu)}{\mathrm{Br}(Z\to\ell\ell)}$, and the difference in event topology between the decays Z($\nu\nu$) + $jets$ and Z($\ell\ell$)+jets due to the presence of the leptons in the Z($\ell\ell$) control region.

$\frac{N^{SR}_{Z(\to\nu\nu)+jets}}{N_{W(\to\ell\nu)+jets}}$ is the ratio of simulated Z($\nu\nu$)+jets events in the signal region to the simulated W($\ell\nu$)+jets events in the full lepton phase space. This term includes the ratio of branching fractions $\frac{\mathrm{Br}(Z\to\nu\nu)}{\mathrm{Br}(Z\to\ell\ell)}$, the ratio $R^{\sigma}_{W/Z+jets}$ of the W($\ell\nu$)+jets cross section over that of Z($\ell\ell$)+jets, and the difference in event topology between the decays Z($\nu\nu$)+jets and W($\ell\nu$)+jets due to the presence of the lepton in the W($\ell\nu$) control region.

$T(\ell)$ is a transfer factor that includes the probability of losing the leptons in the W($\ell\nu$)+jets or Z($\ell\ell$)+jets events in the signal region (i.e. probability of surviving the lepton veto requirements), as well as the difference in phase space between the target process and the full lepton phase space of W($\ell\nu$)+jets or Z($\ell\ell$)+jets events, after the mono-jet cut on the jets and $E_{\mathrm{T}}^{\mathrm{miss}}$. This difference in phase space is due to the fact that the W/Z+jets backgrounds with missed leptons are determined from W/Z+jets events with leptons being in the acceptance and reconstructed.

8.2 Muon Control Regions

8.2.1 Introduction

As explained in Sec. 8.1, the determination of the electroweak background can be summarised in the following steps: selecting data control regions and removing the other Standard Model backgrounds in them, then applying a set of correction and transfer factors to get an accurate prediction for W/Z+jets events in the signal region. In the following subsections, each of the two muon control regions, Z($\mu\mu$) and W($\mu\nu$), are defined, and corrections required to get back to the full muon phase space and then to a specific process in the signal region are explained.

The Z control region is employed to separately determine the contribution of Z($\nu\nu$)+jets, Z($\tau\tau$)+jets, and Z($\mu\mu$)+jets processes in the signal region. The W control region is used to determine the rate of Z($\nu\nu$)+jets, W($\tau\nu$)+jets, and W($\mu\nu$)+jets events in the signal region.

The same $E_{\mathrm{T}}^{\mathrm{miss}}$ trigger as that of the signal regions is used to select events in the muon control regions. Hence no additional correction for the difference in the trigger efficiencies between control and signal regions is required. A set of correction factors is applied to the events in each control region to recover the full lepton phase space. Then another set of correction factors is applied to get the final determination of number of events of each electroweak background in a mono-jet signal region. In order to check the validity of the simulation-based correction factors, a set of closure tests are performed. For each process, these tests compare the kinematic distributions of that process in the signal regions obtained directly from the corresponding simulated samples to the ones obtained using the simulated samples of the control regions after applying the required corrections. As mentioned before, all correction factors are applied bin-by-bin to the control regions (as functions of the variable of interest, such as the calorimeter-based $E_{\mathrm{T}}^{\mathrm{miss}}$ or leading jet p_{T}), in order to get a good description of the shape and the normalisation of the Standard Model contribution to the mono-jet signal regions.

8.2.2 Z($\mu\mu$) Control Region

In muon control regions, a "good" muon is defined to be one fulfilling the following criteria:

- Staco combined as mentioned in Sec. 4.3.1.
- $p_{\mathrm{T}} > 20$ GeV and $|\eta| < 2.4$

- Isolation cut : ptcone20 < 1.8 GeV, where ptcone20 is the sum of the p_{T} of all the inner detector tracks in a cone of radius 0.2 around the muon track.

- z distance (z_0) of the muon track with respect to the primary vertex should be less than 10 mm.

- The inner detector track to which the MS track is matched should fulfil a set of quality criteria related to the number of hits in the inner detector [48].

Events in the Z($\mu\mu$) control region satisfy the following criteria:

- Have exactly two good muons as defined above.

- Pass all the signal region cuts on the jets and calorimeter–based $E_{\mathrm{T}}^{\mathrm{miss}}$ as explained in Sec. 4.2, as well as the lepton veto.

- 66 GeV $< m_{\mu\mu} <$ 116 GeV, where $m_{\mu\mu}$ is the invariant mass computed from the four vectors of the two selected muons, in order to limit the contamination from $\gamma^*(\ell\ell)$+jets.

Table 8.1 summarises the Z($\ell\ell$) control regions definition.

Control regions	region 1	region 2	region 3	region 4
Common cuts	Preselection cuts (Sec. 6) + $\Delta\phi(E_{\mathrm{T}}^{\mathrm{miss}}, \mathrm{jet}_2) > 0.5$ + $N_{\mathrm{jets}} < 3$ + exactly 2 good muons + lepton veto (except on good muons) + 66 GeV $< m_{\mu\mu} <$ 116 GeV			
Dedicated cuts	$p_T^{\mathrm{jet}_1} > 120$ GeV $E_{\mathrm{T}}^{\mathrm{miss}} > 120$ GeV	$p_T^{\mathrm{jet}_1} > 220$ GeV $E_{\mathrm{T}}^{\mathrm{miss}} > 220$ GeV	$p_T^{\mathrm{jet}_1} > 350$ GeV $E_{\mathrm{T}}^{\mathrm{miss}} > 350$ GeV	$p_T^{\mathrm{jet}_1} > 500$ GeV $E_{\mathrm{T}}^{\mathrm{miss}} > 500$ GeV

Table 8.1: Definition of the four Z($\mu\mu$)+jets exclusive control regions.

These four Z($\mu\mu$)+jets control regions are used to determine the contribution of Z($\nu\nu$)+jets, Z($\tau\tau$)+jets, and Z($\mu\mu$)+jets in the signal regions. To summarise:

$$N^{SR,\text{predicted}}_{\mathrm{Z}(\to\nu\nu)+jets} = \frac{(N^{Data}_{\mathrm{Z}(\to\mu\mu)+jets}) \times (1 - f_{EW})}{A_\mu \times \epsilon_{\mu_1} \times \epsilon_{\mu_2}} \times \frac{N^{SR}_{\mathrm{Z}(\to\nu\nu)+jets}}{N_{\mathrm{Z}(\to\mu\mu)+jets}} \tag{8.6}$$

$$N^{SR,\text{predicted}}_{\mathrm{Z}(\to\tau\tau)+jets} = \frac{(N^{Data}_{\mathrm{Z}(\to\mu\mu)+jets}) \times (1 - f_{EW})}{A_\mu \times \epsilon_{\mu_1} \times \epsilon_{\mu_2}} \times T(\not\tau) \tag{8.7}$$

$$N^{SR,\text{predicted}}_{\mathrm{Z}(\to\mu\mu)+jets} = \frac{(N^{Data}_{\mathrm{Z}(\to\mu\mu)+jets}) \times (1 - f_{EW})}{A_\mu \times \epsilon_{\mu_1} \times \epsilon_{\mu_2}} \times T(\not\mu) \tag{8.8}$$

Table 8.2 lists the total number of data events, before background subtraction or applying any correction, in each Z($\mu\mu$) control region.

Control regions	$N^{Data}_{\mathrm{Z}(\to\mu\mu)+jets}$
region 1	4816
region 2	445
region 3	45
region 4	6

Table 8.2: Total number of data events in each Z($\mu\nu$) control region, before background subtraction or applying any correction.

The values of f_{EW}, A_μ, and $T(\ell)$, $\ell = e, \mu$ are obtained from simulation, using the fraction of events that pass the jet and $E_{\mathrm{T}}^{\mathrm{miss}}$ mono–jet cuts. The uncertainties affecting jet and $E_{\mathrm{T}}^{\mathrm{miss}}$ quantities will be a small contribution to the overall prediction. However, since simulation is used to correct the control regions for the cuts applied on the muon p_{T}, η, and ϕ by applying the muon acceptance and the invariant mass cuts, the *shape* of these kinematic distributions in the Z($\mu\mu$) control regions should be in good agreement between simulation and data. Figure 8.1 shows this comparison. The distribution of the sum of all simulated Electroweak events including both simulated Z($\mu\mu$) and all the Electroweak background, is normalised to that of data in the control region since only the shape comparison matters here. Good agreement is observed for bulk of the events in each distribution, making it possible to use simulation in calculating some of the lepton–related correction factors. Shown are also the leading jet p_{T} and $E_{\mathrm{T}}^{\mathrm{miss}}$ distributions in

Fig. 8.2. No agreement is required for the latter kinematic distributions, as their shapes are directly taken from the Z($\mu\mu$) data control regions. However, good agreement is nevertheless achieved.

8.2.2.1 Electroweak background f_{EW}

The QCD multi-jet background in the Z($\mu\mu$) control region is estimated to be negligible. The ratio of other backgrounds f_{EW} is estimated using simulated samples, and is defined as:

$$f_{EW} = \frac{\sum_i N_i^{CR}}{N_{Z(\mu\mu)}^{CR} + \sum_i N_i^{CR}}, \tag{8.9}$$

where N_i^{CR} is the number of events of electroweak process i excluding Z($\mu\mu$), passing the Z($\mu\mu$) control region cuts. These backgrounds include $t\bar{t}$ + single top (1.5%), di-bosons (0.3%), Z($\tau\tau$) (0.1%), and W($\ell\nu$) (0.01%) events. The value of $1 - f_{EW}$ in each of the control regions is listed in Tab. 8.3, and is shown in Fig. 8.3 for the first control region, as a function of the calorimeter–based $E_{\mathrm{T}}^{\mathrm{miss}}$ which is equivalent to the p_{T} of the Z. As can be seen from the plot, there is no dependence of f_{EW} on the kinematics of the event; these background processes are all known electroweak processes with no fake leptons, and having a more boosted lepton from the boson decay will not change the probability of the event passing the control region cuts.

8.2.2.2 Muon Acceptance

Muon acceptance corrects for the cuts applied to the muon p_{T} and η. It is defined at muon truth level, as the muon identification efficiency applies the p_{T} and η cuts at the truth level. The only remaining factor to be corrected for is the difference between the reconstructed and the truth muon p_{T} and η distributions, as the former is cut on in data control regions, while the latter is used in getting the identification efficiency maps. This difference is calculated and found to be almost unity, as shown in Fig. 8.4.

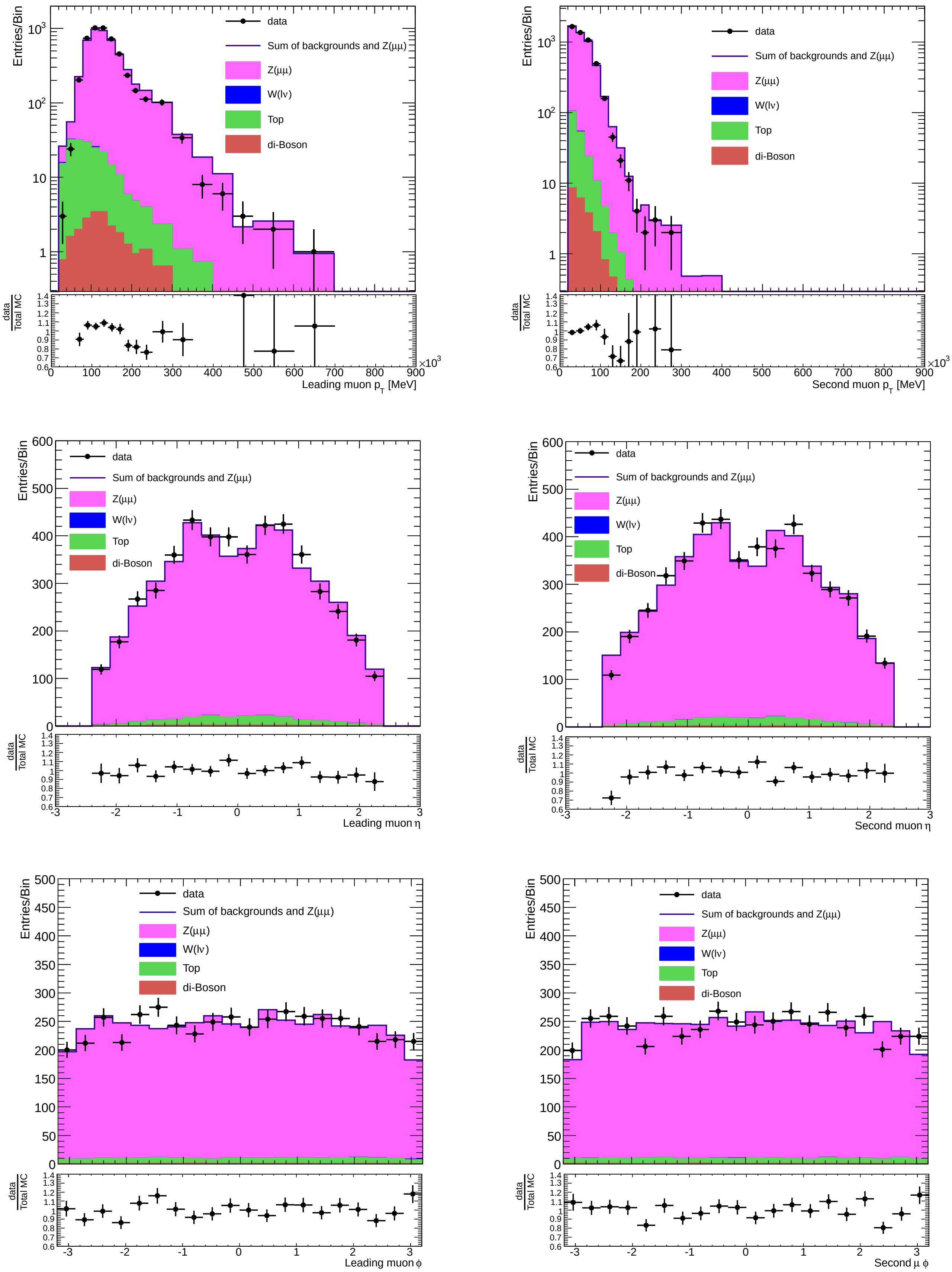

Figure 8.1: Distributions of the leading and second muons p_{T}, η, and ϕ in the first $\mathrm{Z}(\mu\mu)$+jets control region.

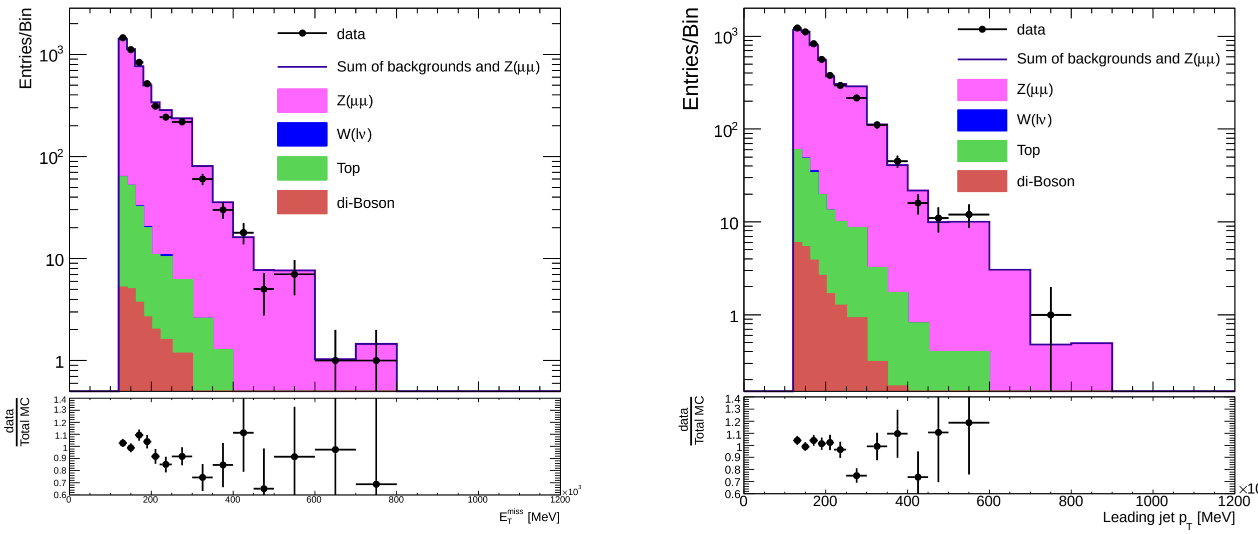

Figure 8.2: Distributions of the calorimeter-based $E_{\mathrm{T}}^{\mathrm{miss}}$ and leading jet p_{T} in the first Z($\mu\mu$)+jets control region.

Control regions	$1 - f_{EW}$ (%)
region 1	98.05 $\pm$ 0.06
region 2	98.14 $\pm$ 0.24
region 3	97.48 $\pm$ 1.02
region 4	94.20 $\pm$ 5.46

Table 8.3: (1-f_{EW}) in each Z($\mu\mu$) control region, calculated as ratio of integrals. Uncertainties are statistical only.

The acceptance is calculated in bins of the calorimeter-based $E_{\mathrm{T}}^{\mathrm{miss}}$, and is defined as the fraction of events with the two "truth" muons from the Z decay having $p_{\mathrm{T}} > 20$ GeV and $|\eta| < 2.4$. This fraction is calculated after applying all the mono-jet cuts related to the jets, $E_{\mathrm{T}}^{\mathrm{miss}}$, and lepton vetoes with muon veto not applied on the 2 selected truth muons, but on any additional ones, as well as the cut on the invariant mass of the muon pair at the reconstruction level for events entering the numerator of the acceptance

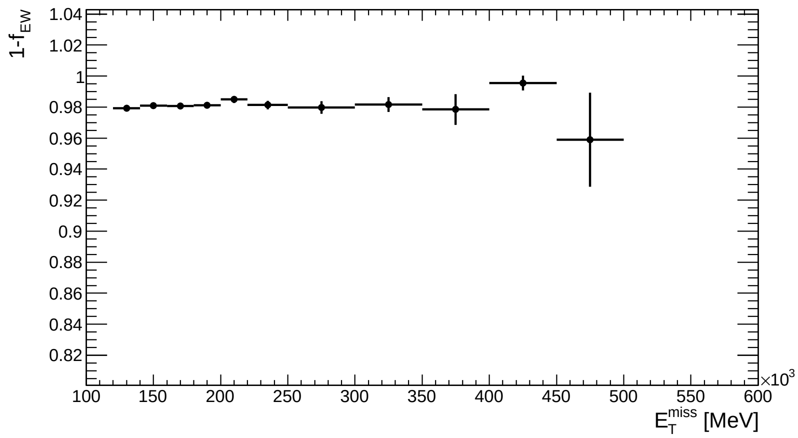

Figure 8.3: Distribution of $(1 - f_{EW})$ in the first Z($\mu\mu$)+jets control region.

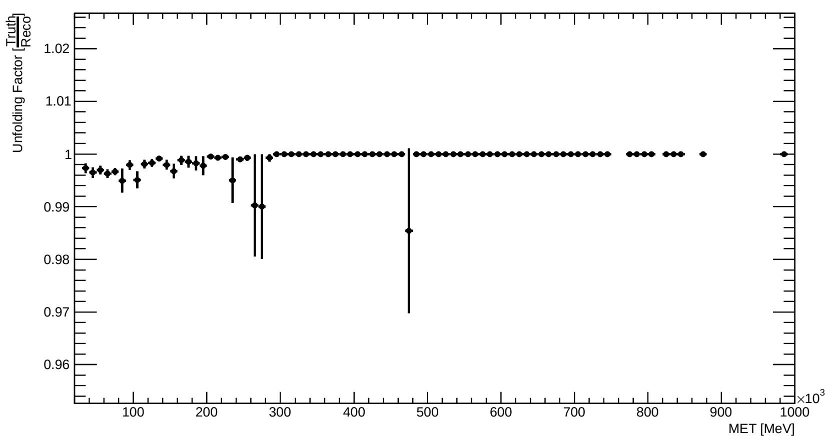

Figure 8.4: Difference between reconstructed and truth muon p_{T}.

definition, and at the truth level for the events entering the denominator. In other words, this acceptance only corrects for the muon p_{T} and η cuts, given the other cuts are passed. Figure 8.5 shows this acceptance in the first control region, and Table 8.4 summarises its value in different control regions.

The reconstruction efficiency of the invariant mass cut is corrected for by applying the cut at the reconstructed level in the numerator of the acceptance, and at truth level in the denominator. The γ^* contamination in the mass range 66 - 116 GeV is almost the same as the contamination from Z($\mu\mu$) outside that window, such that the rate of

Z($\mu\mu$) events in the window matches that of Z($\nu\nu$) which has no γ^* contamination. A very small correction of ~ 1.01 is later applied to ensure that this equality holds.

Control regions	Acceptance (%)
region 1	64.75 $\pm$ 0.37
region 2	78.84 $\pm$ 1.08
region 3	86.76 $\pm$ 2.99
region 4	84.95 $\pm$ 8.01

Table 8.4: Muon acceptance corrections in each Z($\mu\mu$) control region, calculated as ratio of integrals. The uncertainties are statistical only.

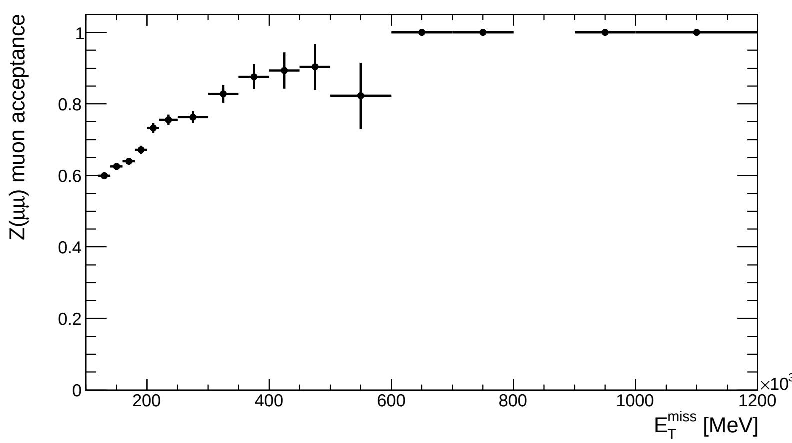

Figure 8.5: Z($\mu\mu$) muon acceptance in the first Z($\mu\mu$)+jets control region.

8.2.2.3 Muon identification efficiency

The muon reconstruction efficiency, corresponding to the Staco combined criteria as mentioned in Sec. 4.3.1, z distance with respect to the primary vertex, and the track quality cuts, is binned in bins of muon $\eta - \phi$. However, the muon isolation efficiency, corresponding to the ptcone20 cut, has a slight dependency on the muon p_{T} up to 40 GeV after which it becomes flat, as is shown in Fig. 8.6.

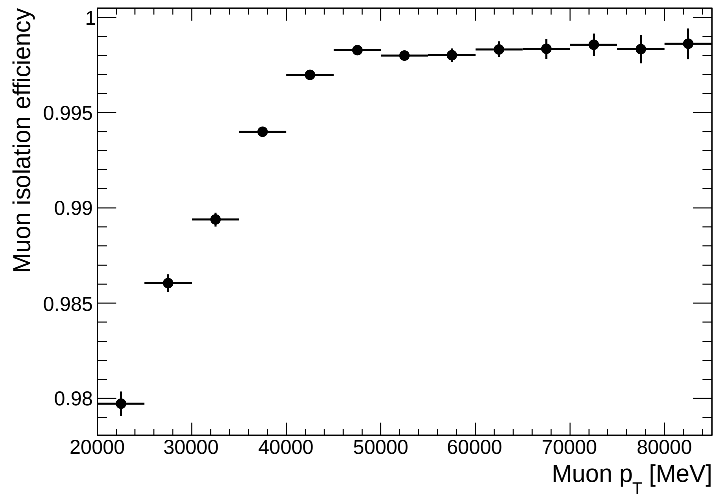

Figure 8.6: Muon isolation efficiency as a function of the reconstructed muon p_{T}.

The identification efficiency map is data-driven in the sense that it is estimated from simulation ($\epsilon_{\mu}^{Simulation}$), and is then multiplied by data scale factors (SF) defined as:

$$SF = \frac{\epsilon_{\mu}^{data}}{\epsilon_{\mu}^{MC}} \tag{8.10}$$

The same method (tag and probe [48]) is used to estimate the efficiencies from data and simulation in scale factors.

The identification efficiency from simulation ($\epsilon_{\mu}^{Simulation}$) is the efficiency of identifying a muon from the boson decay. In other words, knowing that the muon is from the boson decay, it is the probability of passing all the identification criteria mentioned above. The simulated Z($\mu\mu$)+jets `PYTHIA` sample (Chapter 5) is used to estimate $\epsilon_{\mu}^{Simulation}$. To ensure that the muon under consideration comes from the boson decay, it is considered in the efficiency estimation only if it can be matched to a muon at the truth level coming from the decay of the Z[3], with a matching criterion of: $\Delta R = \sqrt{\eta^2 + \phi^2} < 0.05$. In this matching, the truth muons with $p_{\mathrm{T}} > 20$ GeV and $|\eta| < 2.4$ are considered, as the

[3]The pdgId and number of parents information of the truth muon is used to make sure it is coming from the decay of the Z boson.

same cuts are used in the definition of the muon acceptance at truth level. However the reconstructed muon matched to the truth is considered to have $p_T > 15$ GeV and $|\eta| < 2.4$, since the reconstructed p_{T} is lower than the truth p_{T} due to the detector resolution effects.

The muon identification efficiency definition can be summarised as follows:

$$\epsilon_{\mu}^{Simulation} = \frac{\text{Number of events with a matched-to-truth reconstructed } \mu \text{ passing the identification criteria}}{\text{Number of events with a matched-to-truth reconstructed } \mu} \tag{8.11}$$

where the truth muon satisfies $p_T^{\mathrm{truth}} > 20$ GeV and $|\eta^{\mathrm{truth}}| < 2.4$.

Due to the fact that the p_{T} and η cuts are applied to the muon at truth level in the definition of $\epsilon_{\mu}^{Simulation}$ and at the reconstruction level in the data control regions, an additional correction factor is required which accounts for the differences between truth and reconstructed muon p_{T} and η distributions. Such a factor has been estimated and shown to be near unity (Fig. 8.4).

Figures 8.7 and 8.8 show the simulation–based $\eta - \phi$ efficiency maps, before applying the scale factors. The efficiency drops at $\eta \sim 0$ due to the crack in the muon chambers for the services.

8.2.3 W($\mu\nu$) Control Region

Events in the W($\mu\nu$) control region satisfy the following criteria:

- Exactly one good muon (as defined in Sec. 8.2.2)
- Pass all the signal region cuts on the jets and $E_{\mathrm{T}}^{\mathrm{miss}}$, as well as the lepton vetoes.
- $E_{\mathrm{T}}^{\mathrm{miss}}$ corrected for the selected muon should be larger than 25 GeV. This is approximately equivalent to the p_{T} of the neutrino from the W decay, and is calculated as: $|\vec{E}_{\mathrm{T}}^{\mathrm{miss}} - \vec{p_{\mathrm{T}}}^{\mu}|$.

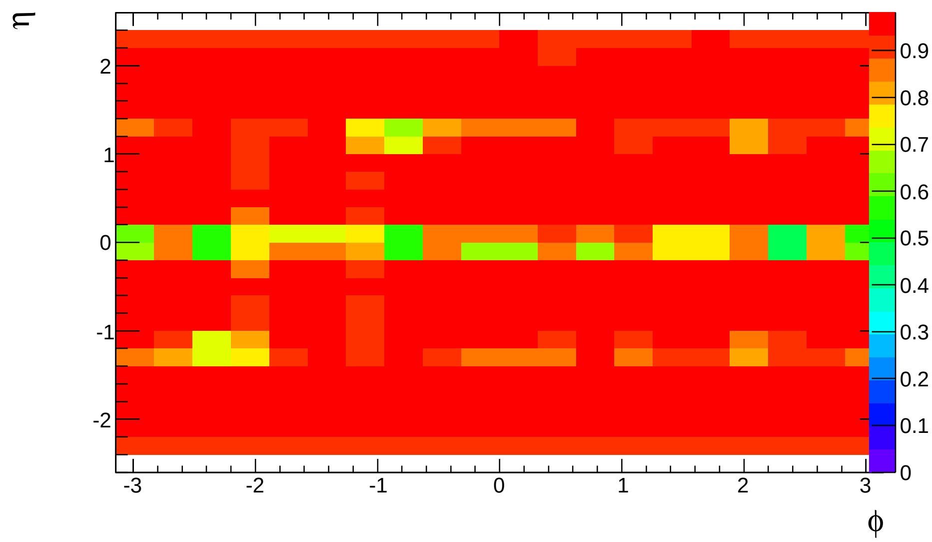

Figure 8.7: Simulation–based muon identification efficiency as function of the muon $\eta - \phi$ without applying the scale factors.

- A transverse mass m_{T} above 40 GeV, with
  $m_{\mathrm{T}} = \sqrt{2 \times p_T^{\mu} \times E_{\mathrm{T}}^{\mathrm{miss}} \times [1 - \cos\Delta\phi(\mu, E_{\mathrm{T}}^{\mathrm{miss}})]}$

The last two cuts are applied to purify the W control region, based on studies done for the Standard Model measurements of the W/Z cross sections [45, 46].

Table 8.5 summarises the W($\mu\nu$) control region definition.

Control regions	region 1	region 2	region 3	region 4
Common cuts	Preselection cuts (Sec. 6) + $\Delta\phi(E_{\mathrm{T}}^{\mathrm{miss}}, \mathrm{jet}_2) > 0.5$ + $N_{\mathrm{jets}} < 3$ + exactly 1 good muon + lepton veto (except on the good muon) + $m_{\mathrm{T}} > 40$ GeV			
Dedicated cuts	$p_{\mathrm{T}}^{\mathrm{jet}_1} > 120$ GeV $E_{\mathrm{T}}^{\mathrm{miss}} > 120$ GeV	$p_{\mathrm{T}}^{\mathrm{jet}_1} > 220$ GeV $E_{\mathrm{T}}^{\mathrm{miss}} > 220$ GeV	$p_{\mathrm{T}}^{\mathrm{jet}_1} > 350$ GeV $E_{\mathrm{T}}^{\mathrm{miss}} > 350$ GeV	$p_{\mathrm{T}}^{\mathrm{jet}_1} > 500$ GeV $E_{\mathrm{T}}^{\mathrm{miss}} > 500$ GeV

Table 8.5: Definition of the four W($\mu\nu$)+jets exclusive control regions.

These four W($\mu\nu$)+jets control regions are used to determine the contributions of Z($\nu\nu$)+jets, W($\tau\nu$)+jets, and W($\mu\nu$)+jets in the signal regions. To summarise:

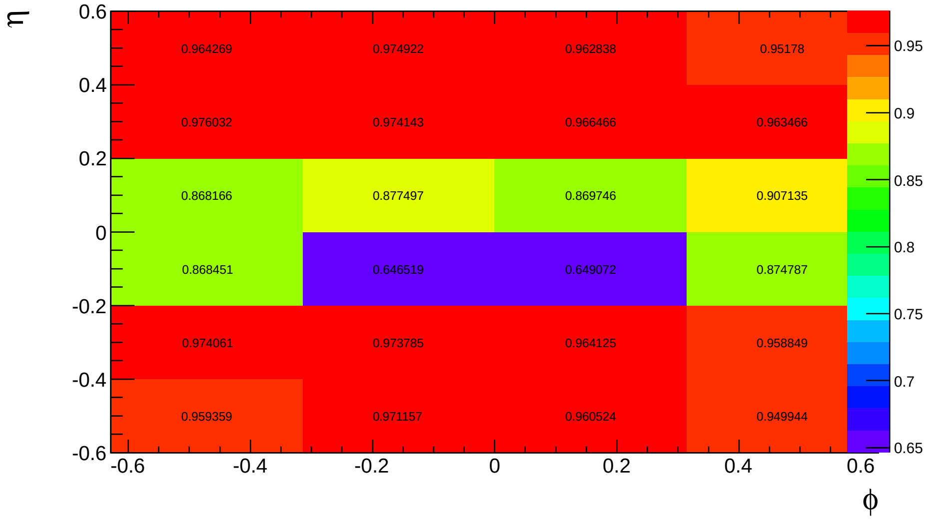

Figure 8.8: Simulation–based muon identification efficiency as function of the muon $\eta - \phi$ without applying the scale factors (zoomed).

$$N^{SR,\text{predicted}}_{\text{Z}(\to\nu\nu)+jets} = \frac{(N^{Data}_{\text{W}(\to\mu\nu)+jets}) \times (1 - f_{EW})}{A_\mu \times \epsilon_\mu \times \epsilon_W} \times \frac{N^{SR}_{\text{Z}(\to\nu\nu)+jets}}{N_{\text{W}(\to\mu\nu)+jets}} \tag{8.12}$$

$$N^{SR,\text{predicted}}_{\text{W}(\to\tau\nu)+jets} = \frac{(N^{Data}_{\text{W}(\to\mu\nu)+jets}) \times (1 - f_{EW})}{A_\mu \times \epsilon_\mu \times \epsilon_W} \times T(\not\tau) \tag{8.13}$$

$$N^{SR,\text{predicted}}_{\text{W}(\to\mu\nu)+jets} = \frac{(N^{Data}_{\text{W}(\to\mu\nu)+jets}) \times (1 - f_{EW})}{A_\mu \times \epsilon_\mu \times \epsilon_W} \times T(\not\mu) \tag{8.14}$$

Table 8.6 lists the total number of data events in each W($\mu\nu$) control region before background subtraction or applying any correction factor.

As in the Z($\mu\mu$) control regions, f_{EW}, A_μ, and $T(\not\ell)$ are obtained from simulation, using the fraction of events that pass the jet and $E_{\text{T}}^{\text{miss}}$ mono–jet cuts. However, the shape of the muon's kinematic distributions in the W($\mu\nu$) control regions should show good agreement between simulation and data, since the modelling of some of the correction factors are based on the simulated muon kinematics, namely, muon acceptance, the transverse mass, and the corrected $E_{\text{T}}^{\text{miss}}$ cuts. Figure 8.9 shows this comparison, with W and Z simulated

Control regions	$N^{Data}_{\mathrm{W}(\rightarrow\mu\nu)+jets}$
region 1	40427
region 2	3596
region 3	364
region 4	49

Table 8.6: Total number of data events in each W($\mu\nu$) control region, before background subtraction or applying any correction factor.

events scaled by[4] 0.88 to match the total normalisation of data, as only shape comparison is important here. Good agreement is observed for bulk of the events in each distribution, justifying the use of simulation to calculate some of the lepton–related correction factors. Shown are also the leading jet p_{T} and calorimeter-based $E_{\mathrm{T}}^{\mathrm{miss}}$ distributions in Fig. 8.10. No agreement is required for these two kinematic distributions, as their shapes are directly taken from the W($\mu\nu$) data control regions. Nevertheless, good agreement is achieved.

8.2.3.1 Electroweak background f_{EW}

The electroweak backgrounds in the W($\mu\nu$) control region include $t\bar{t}$ + single top (2.9%), di-bosons (0.5%), Z($\ell\ell$) (4.3%), and W($\tau\nu$) (2.2%) events. The ratio of these backgrounds to each of the control regions is listed in Table 8.7, and the distribution of (1-f_{EW}) for the first control region is shown in Fig 8.11, with no dependence on $E_{\mathrm{T}}^{\mathrm{miss}}$. The contribution of QCD multi-jet events is estimated using data–driven techniques [49], and is found to be negligible, $\sim 0.2\%$.

[4]This scale factor is calculated as: $\frac{N^{CR}_{Data} - N^{Top,t\bar{t},di-Boson}_{MC}}{N^{Electroweak}_{MC}}$. The number of top, $t\bar{t}$, and di-boson events is first subtracted from data as their corresponding simulated samples have been generated with NLO generators. Whereas the Electroweak simulated samples have been generated with the `ALPGEN` generator which is a Leading Order (LO) generator.

Control regions	(1-f_{EW}) (%)
region 1	90.1 $\pm$ 0.1
region 2	91.6 $\pm$ 0.4
region 3	92.0 $\pm$ 1.1
region 4	88.0 $\pm$ 3.9

Table 8.7: f_{EW} in each W($\mu\nu$) control region, calculated as ratio of integrals. Uncertainties are statistical only.

8.2.3.2 Muon Acceptance

The acceptance is calculated in bins of the calorimeter-based $E_{\mathrm{T}}^{\mathrm{miss}}$, and is defined as the fraction of events with the truth muon from the W decay having $p_{\mathrm{T}} > 20$ GeV and $|\eta| < 2.4$. This fraction is calculated after applying all the mono-jet cuts related to the jets, $E_{\mathrm{T}}^{\mathrm{miss}}$, and lepton vetoes, as well as the cuts on the transverse mass and the corrected $E_{\mathrm{T}}^{\mathrm{miss}}$. All these mono-jet related cuts are applied at the reconstruction level. In summary, the acceptance only corrects for the muon p_{T} and η cuts, given the other cuts are passed. An additional factor corrects for the acceptance of the cuts on the transverse mass and the corrected $E_{\mathrm{T}}^{\mathrm{miss}}$, which corresponds to the neutrino p_{T}, and is defined as fraction of simulated events passing the cuts on the m_{T} and corrected $E_{\mathrm{T}}^{\mathrm{miss}}$ at the reconstructed level given the event has a good identified muon and satisfies all signal selection cuts. Another factor, the identification efficiency map, will correct for the probability of identifying the muon. Figure 8.12 shows the muon acceptance in the first control region, and Table 8.8 summarises the value of this acceptance in different control regions, while Figure 8.13 and Table 8.9 show the distribution and values of the efficiency of the m_{T} and corrected $E_{\mathrm{T}}^{\mathrm{miss}}$ cuts, respectively.

Control regions	Acceptance (%)
region 1	78.31 ± 0.18
region 2	87.17 ± 0.47
region 3	91.36 ± 1.12
region 4	89.41 ± 3.47

Table 8.8: Muon acceptance corrections in each W($\mu\nu$) control region, calculated as ratio of integrals. Uncertainties are statistical only.

Control regions	ϵ_W (%)
region 1	64.06 ± 0.25
region 2	64.23 ± 0.75
region 3	69.49 ± 2.00
region 4	75.11 ± 4.66

Table 8.9: Values of ϵ_W in each of the W($\mu\nu$) control regions, calculated as ratio of integrals. Uncertainties are statistical only. ϵ_W is the efficiency of the control region cut on m_{T} and the corrected $E_{\mathrm{T}}^{\mathrm{miss}}$ (corrected for the selected muon).

8.2.3.3 Muon identification efficiency

The muon identification efficiency is explained in Sec. 8.2.2.3 in detail. As for the Z($\mu\mu$) control regions, it is used as one of the factors needed to recover the full muon phase space. However, there is also an identification efficiency map needed for the determination of the W($\mu\nu$)+jets background in the signal regions, when the muon has passed the muon veto criteria. This efficiency is defined as:

$$\epsilon_{\ell,veto}^{Simulation} = \frac{\text{Number of events with a matched-to-Truth reconstructed } \mu \text{ passing the } \mu \text{ veto criteria}}{\text{Number of events with a matched-to-Truth reconstructed } \mu} \tag{8.15}$$

Here, the truth muon satisfies $p_{\mathrm{T}} > 7$ GeV and $|\eta| < 2.5$ to match the p_{T} and η cuts used in the muon veto.

Figures 8.14 and 8.15 show the efficiency map for the veto muon, without any scaling with the W($\mu\nu$) simulated events with the full lepton phase space (more explanation in Sec. 8.2.6).

8.2.4 Determination of Z($\nu\nu$)

Two independent predictions of Z($\nu\nu$) can be obtained: one from Z($\mu\mu$) and one from W($\mu\nu$) control regions.

8.2.4.1 Determination of Z($\nu\nu$) from Z($\mu\mu$) Control Region

As mentioned before, the determination of Z($\nu\nu$) from Z($\mu\mu$) control regions can be done according to:

$$N^{SR,\text{predicted}}_{\mathrm{Z}(\to\nu\nu)+jets} = \frac{(N^{Data}_{\mathrm{Z}(\to\mu\mu)+jets}) \times (1 - f_{EW})}{A_\mu \times \epsilon_{\mu_1} \times \epsilon_{\mu_2}} \times \frac{N^{SR}_{\mathrm{Z}(\to\nu\nu)+jets}}{N_{\mathrm{Z}(\to\mu\mu)+jets}} \tag{8.16}$$

Once the full lepton phase space is recovered, the determination of Z($\nu\nu$)+jets background in the signal region is done by applying the following factor, based on simulation, which corrects for the branching ratio of Z($\nu\nu$) to Z($\mu\mu$) after mono-jet cuts, and also the difference in the event topologies due to the presence of the muons in the control regions:

$$\frac{N^{SR}_{\mathrm{Z}(\to\nu\nu)+jets}}{N_{\mathrm{Z}(\to\mu\mu)+jets}} \tag{8.17}$$

where $N_{\mathrm{Z}(\to\mu\mu)+jets}$ is the number of Z($\mu\mu$) events in the control region being corrected to the full muon phase space.

Table 8.10 summarises the value of this correction factor for each control region (defined as the ratio of the integrals of the two histograms used in the definition above), and Figure 8.16 shows its distribution in the first control region. The ratio of the branching ratios of Z($\nu\nu$) to Z($\mu\mu$) is ~ 5.93, as explained in Sec. 2.4. However, there is an additional phase space difference due to the impact of photon radiation from the muons, resulting in extra energy contribution to $E_{\mathrm{T}}^{\mathrm{miss}}$, and also a different jet phase space. This additional correction is $\sim 25\%$, Table 8.10. For higher values of $E_{\mathrm{T}}^{\mathrm{miss}}$, and consequently higher leading jet p_{T}, the lepton is harder. Therefore, there is a higher chance that the radiated photons from the lepton are at higher p_{T}, resulting in a higher correction factor as the Z p_{T} increases, as can be seen in Fig. 8.16.

Control regions	$\frac{N^{SR}_{\mathrm{Z}(\to\nu\nu)+jets}}{N_{\mathrm{Z}(\to\mu\mu)+jets}}$
region 1	7.46 ± 0.06
region 2	8.32 ± 0.23
region 3	9.44 ± 0.88
region 4	7.32 ± 1.66

Table 8.10: $\frac{N^{SR}_{\mathrm{Z}(\to\nu\nu)+jets}}{N_{\mathrm{Z}(\to\mu\mu)+jets}}$, calculated as ratio of integrals, in each Z($\mu\mu$) control region. Uncertainties are statistical only.

8.2.4.2 Determination of Z($\nu\nu$) from W($\mu\nu$) Control Region

As mentioned before, determination of Z($\nu\nu$) from W($\mu\nu$) control regions can be done according to:

$$N^{SR,\mathrm{predicted}}_{\mathrm{Z}(\to\nu\nu)+jets} = \frac{(N^{Data}_{\mathrm{W}(\to\mu\nu)+jets}) \times (1 - f_{EW})}{A_\mu \times \epsilon_\mu \times \epsilon_W} \times \frac{N^{SR}_{\mathrm{Z}(\to\nu\nu)+jets}}{N_{\mathrm{W}(\to\mu\nu)+jets}}, \tag{8.18}$$

which means by applying the following factor to the W($\mu\nu$) data control region corrected back to the full lepton phase space:

$$\frac{N^{SR}_{\mathrm{Z}(\to\nu\nu)+jets}}{N_{\mathrm{W}(\to\mu\nu)+jets}} \tag{8.19}$$

where $N_{\mathrm{W}(\to\mu\nu)+jets}$ is the number of W($\mu\nu$) events in the data control region after being corrected for the identification efficiency, muon acceptance, and ϵ_W.

This factor accounts for the ratio of branching ratios of Z($\nu\nu$) to Z($\mu\mu$) which is ~ 5.93, the ratio of the cross sections of Z($\mu\mu$) to W($\mu\nu$) after the mono-jet cuts which is $\sim \frac{1}{8.49}$ [44, 49], and the differences in the event topologies between Z($\nu\nu$) and W($\mu\nu$) events which is of the order of $\sim 11\%$ as can be inferred from Table 8.11 for each control region. This correction factor is smaller than the one obtained for the Z($\mu\mu$) control region ($\sim$ 25%), due to the fact that there is only one lepton here, resulting in less radiation, and less phase space difference with Z($\nu\nu$). Figure 8.17 shows the distribution of this factor in the first control region.

Control regions	$\frac{N^{SR}_{\mathrm{Z}(\to\nu\nu)+jets}}{N_{\mathrm{W}(\to\mu\nu)+jets}}$
region 1	0.783 $\pm$ 0.004
region 2	0.853 $\pm$ 0.012
region 3	0.822 $\pm$ 0.036
region 4	0.691 $\pm$ 0.077

Table 8.11: $\frac{N^{SR}_{\mathrm{Z}(\to\nu\nu)+jets}}{N_{\mathrm{W}(\to\mu\nu)+jets}}$, calculated as ratio of integrals, in each W($\mu\nu$) control regions. Uncertainties are statistical only.

8.2.5 Determination of W($\tau\nu$) from W($\mu\nu$) Control Region

The following factor, which corrects for the difference in event topologies between W($\mu\nu$) and W($\tau\nu$) events, is used to determine the contribution of W($\tau\nu$)+jets in signal regions:

$$T(\not\tau) = \frac{N^{SR}_{\mathrm{W}(\to\tau\nu)+jets}}{N_{\mathrm{W}(\to\mu\nu)+jets}} \tag{8.20}$$

where $N_{\mathrm{W}(\to\mu\nu)+jets}$ is the number of W($\mu\nu$) events in the data control region after being corrected to the full muon phase space.

Table 8.12 summarises the value of this correction factor for each control region. It is defined as the ratio of the integrals of the two histograms used in the definition above, and Figure 8.18 shows its distribution in the first control region. As $E_{\mathrm{T}}^{\mathrm{miss}}$ increases, the probability of losing W($\tau\nu$)+jets events gets smaller since it is more difficult to lose the more boosted τs.

Control regions	$\frac{N^{SR}_{\mathrm{W}(\to\tau\nu)+jets}}{N_{\mathrm{W}(\to\mu\nu)+jets}}$
region 1	0.386 ± 0.003
region 2	0.277 ± 0.009
region 3	0.206 ± 0.021
region 4	0.153 ± 0.048

Table 8.12: $\frac{N^{SR}_{\mathrm{W}(\to\tau\nu)+jets}}{N_{\mathrm{W}(\to\mu\nu)+jets}}$, calculated as ratio of integrals, in each W($\mu\nu$)+jets control region. Uncertainties are statistical only.

8.2.6 Determination of W($\mu\nu$) from W($\mu\nu$) Control Region

W($\mu\nu$)+jets events can pass the mono-jet signal selection cuts when the muon from the W decay is either out of muon veto acceptance as defined in Sec. 8.2.3.2, $P(\mu \notin A_\mu)$, or not identified, $P(\mu \in A_\mu \wedge \mu \notin \epsilon_\mu)$, according to:

$$P(\not{\mu}) = P(\mu \notin A_\mu) + P(\mu \in A_\mu \wedge \mu \notin \epsilon_\mu) \tag{8.21}$$

where P stands for the probability of an event. The loss of the lepton affects the real $E_{\mathrm{T}}^{\mathrm{miss}}$ in the event compared to $E_{\mathrm{T}}^{\mathrm{miss}}$ in the control region or in the full lepton phase space. This effect must also be included in the factor used to determine this background. Both effects can be written as:

$$T(\not{\mu}) = T(1 - A^{veto}) + T(A^{veto} \times (1 - \epsilon^{veto}_{reco})) \tag{8.22}$$

where $T(1 - A^{veto})$ is the factor corresponding to the fraction of simulated events after mono-jet cuts with the truth muon from the W decay not in the p_{T}-η veto acceptance, as shown in Fig. 8.19 with the corresponding values listed in Tab. 8.13. As $E_{\mathrm{T}}^{\mathrm{miss}}$ increases, the value of this factor decreases since there is a less chance of the lepton being out of acceptance when the system is more boosted. The factor $T(A^{veto} \times (1 - \epsilon^{veto}_{reco}))$ represents the fraction of simulated events after mono-jet cuts with the muon from the W decay in the p_{T}-η veto acceptance but not identified, as shown in Fig. 8.20 with the corresponding values listed in Tab. 8.14. The distribution is almost flat, as the identification efficiency varies mainly as a function of only η and ϕ of the muon for boosted muons, as shown in Fig. 8.6. To determine the W($\mu\nu$) background in the signal regions, these two transfer factors, $T(1-A^{veto})$ and $T(A^{veto}\times(1-\epsilon^{veto}_{reco}))$, should be applied to W($\mu\nu$) data control regions. These control regions do not include any selected muon below 20 GeV in p_{T} or outside $|\eta|$ of 2.4. However, in the definition of the muon veto, the muon p_{T} and η thresholds are 7 GeV and 2.5, respectively. Hence W($\mu\nu$) simulated events in the full muon phase space are used to obtain $T(1-A^{veto})$ and $A^{veto}\times(1-\epsilon^{veto}_{reco})$, in order to take into account the contribution from the low-p_{T} muons as well, which are absent in the W($\mu\nu$) data control regions by definition. The factors are weighted in bins of $E_{\mathrm{T}}^{\mathrm{miss}}$ by simulated W($\mu\nu$) events in the full muon phase space. To summarise, the value of the transfer factor $T(\not\mu)$ in bin i of $E_{\mathrm{T}}^{\mathrm{miss}}$, $T_i(\not\mu)$, would be:

$$T_i(\not\mu)=\frac{\Sigma_{p_{\mathrm{T}},\eta}[T(1-A^{veto}(p_{\mathrm{T}},\eta))\times n_i(p_{\mathrm{T}},\eta)]+\Sigma_{p_{\mathrm{T}},\eta,\phi}[T(A^{veto}(p_{\mathrm{T}},\eta)\times(1-\epsilon^{veto}_{reco}(\eta,\phi)))\times m_i(p_{\mathrm{T}},\eta,\phi)]}{\Sigma_{p_{\mathrm{T}},\eta,\phi}N_i(p_{\mathrm{T}},\eta,\phi)} \tag{8.23}$$

where $N_i(p_{\mathrm{T}},\eta,\phi)$ is the number of W($\mu\nu$) events with the full muon phase space, in bin i of $E_{\mathrm{T}}^{\mathrm{miss}}$ with the selected muon having $(p_{\mathrm{T}},\eta,\phi)$ kinematics, and $\Sigma_{p_{\mathrm{T}},\eta,\phi}N_i(p_{\mathrm{T}},\eta,\phi)$ is the total number of W($\mu\nu$) events with the full muon phase space in bin i of $E_{\mathrm{T}}^{\mathrm{miss}}$.

Figure 8.21 shows T($\not\mu$) in bins of $E_{\mathrm{T}}^{\mathrm{miss}}$ in the first control region, obtained by summing the two distributions of Fig. 8.19 and 8.20. Table 8.15 lists its values in the different W($\mu\nu$) control regions.

8.2.7 Determination of Z($\tau\tau$) from Z($\mu\mu$) Control Region

Z($\tau\tau$)+jets events can pass the mono-jet signal selection cuts when the τ lepton decays either hadronically, resulting in additional jets, or leptonically, with the lepton being missed, either being out of lepton acceptance or not being reconstructed. The following

Control regions	$T(1 - A^{veto})$
region 1	0.0868 ± 0.0005
region 2	0.049 ± 0.001
region 3	0.044 ± 0.004
region 4	0.072 ± 0.021

Table 8.13: $T(1 - A^{veto})$, calculated as ratio of integrals, in each W($\mu\nu$) control region, weighted with W($\mu\nu$) events in the full muon phase space. Uncertainties are statistical only.

Control regions	$T(A^{veto} \times (1 - \epsilon^{veto}_{reco}))$
region 1	0.0553 ± 0.0004
region 2	0.058 ± 0.001
region 3	0.058 ± 0.004
region 4	0.062 ± 0.013

Table 8.14: $T(A^{veto} \times (1 - \epsilon^{veto}_{reco}))$, calculated as ratio of integrals, in each W($\mu\nu$) control region, weighted with W($\mu\nu$) events in the full muon phase space. Data-driven scale factors are applied to the muon identification map. Uncertainties are statistical only.

Control regions	$T(\not\mu)$
region 1	0.1420 ± 0.0008
region 2	0.107 ± 0.002
region 3	0.102 ± 0.006
region 4	0.134 ± 0.025

Table 8.15: $T(\not\mu)$, calculated as ratio of integrals, in each W($\mu\nu$) control region, weighted with W($\mu\nu$) events in the full muon phase space. Uncertainties are statistical only.

factor, being applied to the full lepton phase space of the control region, corrects for the difference in event topologies between Z($\mu\mu$) and Z($\tau\tau$) events:

$$T(\not\tau) = \frac{N^{SR}_{\mathrm{Z}(\to\tau\tau)+jets)}}{N_{\mathrm{Z}(\to\mu\mu)+jets}} \tag{8.24}$$

where $N_{\mathrm{Z}(\to\mu\mu)+jets}$ is the number of Z($\mu\mu$) events in the control region being corrected to the full muon phase space. This factor includes, in the denominator, the cross section for producing Z($\mu\mu$)+jets, with $E_{\mathrm{T}}^{\mathrm{miss}}$ representing the Z p_{T} and jets passing the signal region cuts, while the numerator accounts for the probability that the decay of the Z to a pair of τ leptons survive the lepton veto cuts and the cut on the number of jets.

Table 8.16 summarises the value of this correction factor for each control region. These numbers are smaller than the ones listed in Table. 8.12 for $\frac{N^{SR}_{\mathrm{W}(\to\tau\nu)+jets}}{N_{\mathrm{W}(\to\mu\nu)+jets}}$. This is due to the fact that the probability of missing both τs in a Z($\tau\tau$) event is smaller than the probability of losing the τ in a W($\tau\nu$) event.

Figure 8.22 shows the distribution of $T(\not\tau)$ in the first control region. The probability of losing Z($\tau\tau$)+jets events gets smaller as $E_{\mathrm{T}}^{\mathrm{miss}}$ increases, since it is more difficult to lose the more boosted τs.

Control regions	$\frac{N^{SR}_{\mathrm{Z}(\to\tau\tau)+jets}}{N_{\mathrm{Z}(\to\mu\mu)+jets}}$
region 1	0.054 ± 0.001
region 2	0.024 ± 0.003
region 3	0.022 ± 0.008
region 4	0.010 ± 0.010

Table 8.16: $\frac{N^{SR}_{\mathrm{Z}(\to\tau\tau)+jets}}{N_{\mathrm{Z}(\to\mu\mu)+jets}}$, calculated as ratio of integrals, in each Z($\mu\mu$) control region. Uncertainties are statistical only.

8.2.8 Determination of Z($\mu\mu$) from Z($\mu\mu$) Control Region

Z($\mu\mu$)+jets events can pass the mono-jet signal selection cuts when each of the two muons from the Z decay are both out of acceptance, or both not identified, or one is out of acceptance and one not identified. Therefore the corresponding probability P includes four different terms as follows:

$$P(\not\mu_{1,2}) = P[(\mu_1 \notin A_\mu) \wedge (\mu_2 \notin A_\mu)] + P[(\mu_1 \in A_\mu \wedge \mu_1 \notin \epsilon_\mu) \wedge (\mu_2 \in A_\mu \wedge \mu_2 \notin \epsilon_\mu)] + \\ P[(\mu_1 \notin A_\mu) \wedge (\mu_2 \in A_\mu \wedge \mu_2 \notin \epsilon_\mu)] + P[(\mu_1 \in A_\mu \wedge \mu_1 \notin \epsilon_\mu) \wedge (\mu_2 \notin A_\mu)] \quad (8.25)$$

The distribution of each term in Eq. 8.25 is shown in Fig. 8.23. It can be seen that the term corresponding to the leptons being out of acceptance is the dominant term in the probability (top left plot).

However, due to the fact that some of the terms in the above equation suffer from very low statistics in the simulated samples, the following global factor is used instead:

$$T(\not{\mu}_{1,2}) = \frac{N^{SR}_{\mathrm{Z}(\to\mu\mu)+jets)}}{N_{\mathrm{Z}(\to\mu\mu)+jets}} \tag{8.26}$$

where $N_{\mathrm{Z}(\to\mu\mu)+jets}$ is the number of Z($\mu\mu$) events in the control region being corrected to the full muon phase space.

The values of this factor in various control regions are listed in Table 8.17, and its distribution for the first control region is shown in Fig. 8.24. As $E_{\mathrm{T}}^{\mathrm{miss}}$ increases, the probability of losing Z($\mu\mu$)+jets events gets smaller as it is more difficult to lose the more boosted muons.

Control regions	$\frac{N^{SR}_{\mathrm{Z}(\to\mu\mu)+jets}}{N_{\mathrm{Z}(\to\mu\mu)+jets}}$
region 1	0.0250 ± 0.0012
region 2	0.0127 ± 0.0031
region 3	0.0085 ± 0.0084
region 4	0.0501 ± 0.0488

Table 8.17: $\frac{N^{SR}_{\mathrm{Z}(\to\mu\mu)+jets}}{N_{\mathrm{Z}(\to\mu\mu)+jets}}$, calculated as ratio of integrals, in each Z($\mu\mu$) control region. Uncertainties are statistical only.

8.2.9 Closure Tests

8.2.9.1 Closure tests for Z($\mu\mu$) Control Regions

To validate the performance and the validity of decomposition of the factors calculated from simulation, a set of closure tests are performed. For each process, these tests compare the kinematic distributions of that process in the signal regions obtained directly from the corresponding simulated samples to the ones obtained using the simulated $\mathrm{Z}(\mu\mu)$ control region and the correction and transfer factors required to determine the contribution of that process. Figure 8.25 shows the closure tests for the three background determinations from the $\mathrm{Z}(\mu\mu)$ control region, as well as the closure test for the simulation-based correction factors used to recover the full lepton phase space. For the latter, the simulated $\mathrm{Z}(\mu\mu)$ in the control region after being corrected to the full lepton phase space is compared to the simulated $\mathrm{Z}(\mu\mu)$ in the full lepton phase space obtained by applying only the mono-jet specific cuts (cuts on jets, $E_{\mathrm{T}}^{\mathrm{miss}}$, electron veto, and muon veto on any additional muons). The identification efficiency map used in these closure tests is only based on simulation, as the two distributions being compared are both obtained from simulated samples.

8.2.9.2 Closure tests for W($\mu\nu$) Control Regions

As was done for the $\mathrm{Z}(\mu\mu)$ control region simulation-based correction factors, a set of closure tests is done to validate the performance of each of the transfer factors that is based on simulation. For the muon acceptance, m_{T} and corrected $E_{\mathrm{T}}^{\mathrm{miss}}$ efficiency, and identification efficiency, the $\mathrm{W}(\mu\nu)$ simulated sample in the control region after being corrected to the full lepton phase space is compared to $\mathrm{W}(\mu\nu)$ in the full lepton phase space. The $\mathrm{Z}(\nu\nu)$ closure test compares the $\mathrm{Z}(\nu\nu)$ distribution in the signal region obtained directly from $\mathrm{Z}(\nu\nu)$ simulated samples to the one obtained from Equation 8.12, using the simulated $\mathrm{W}(\mu\nu)$ samples. The closure test for $\mathrm{W}(\mu\nu)$ background compares the $\mathrm{W}(\mu\nu)$ distribution in the signal region using the $\mathrm{W}(\mu\nu)$ simulated samples to the one obtained from Equation 8.14. And finally $\mathrm{W}(\tau\nu)$ events in the signal region obtained from simulated $\mathrm{W}(\tau\nu)$ samples are compared to $\mathrm{W}(\mu\nu)$ events in the full lepton phase space after correcting them using Equation 8.20, for the $\mathrm{W}(\tau\nu)$ closure test. All the closure tests are shown in Fig. 8.26. Good agreement is observed between the distribution obtained directly from the simulation event sample of a background and that obtained from the W($\mu\nu$) simulated sample in the control region corrected by the correction factors.

8.3 Electron Control Regions

The strategy to determine electroweak backgrounds from the electron control regions, Z(ee) and W($e\nu$), is the same as the one used for the muon control regions. However there are a few differences as explained below:

- The electron control regions are selected using electron triggers and a different data stream (the `EGamma` stream). This requires applying an additional correction factor to the electron control regions when determining the electroweak backgrounds in signal regions: $\frac{\epsilon^{trig}_{E_{\mathrm{T}}^{\mathrm{miss}}}}{\epsilon^{trig}_{\ell}} \times \frac{\mathcal{L}_{E_{\mathrm{T}}^{\mathrm{miss}}}}{\mathcal{L}_{\ell}}$ (these factors are defined in Sec. 8.1). The calorimeter-based $E_{\mathrm{T}}^{\mathrm{miss}}$ trigger cannot be used here due to the electron energy deposition in the calorimeter which affects the $E_{\mathrm{T}}^{\mathrm{miss}}$ calculated from the energy of the calorimeter topo-clusters.

- An electron-jet overlap removal criterion is applied before selecting good electrons in the control regions. This is due to the fact that some electrons are reconstructed as jets and these electron-jets must be removed from the jet counting. The cone radius used for the removal is 0.2. The jet closest to the reconstructed electron is removed provided that $\Delta R(\mathrm{electron}, jet) < 0.2$.

- An upper cut of 100 GeV is applied on the transverse mass in the W($e\nu$) control regions (and not in the W($\mu\nu$) control regions). This is mainly to remove the QCD background which has a larger contribution in the W($e\nu$) control regions compared to the W($\mu\nu$) control regions, due to the higher probability for QCD jets to mimic the experimental signature of electrons.

- The $E_{\mathrm{T}}^{\mathrm{miss}}$ variable used to model p_{T} of W or Z is not equivalent to the calorimeter-based $E_{\mathrm{T}}^{\mathrm{miss}}$, since the electrons from the boson decay can deposit a non-negligible amount of energy in the calorimeter. Hence the electron's p_{T} is first removed from the calorimeter-based $E_{\mathrm{T}}^{\mathrm{miss}}$ to make it resemble the boson p_T, equivalent to $|\vec{E}_{\mathrm{T}}^{\mathrm{miss}} + \vec{p_{\mathrm{T}}}^{\mathrm{electron}}|$. However, this will not be the case for the W($e\nu$) control regions used to determine the W($e\nu$) background in signal regions. In this case, the calorimeter-based $E_{\mathrm{T}}^{\mathrm{miss}}$ variable is used for the signal $E_{\mathrm{T}}^{\mathrm{miss}}$ cut. This is to make it resemble the W($e\nu$) background in signal regions where the electron is not identified, but neverthless deposits its energy in the calorimeter and is therefore not contributing to the invisible energy of the event. To summarise, the $E_{\mathrm{T}}^{\mathrm{miss}}$ cut is applied to $|\vec{E}_{\mathrm{T}}^{\mathrm{miss}} + \vec{p_{\mathrm{T}}}^{\mathrm{electron}}|$ in all the electron control regions except the one used to determine the W($e\nu$) background in the signal region, for which the calorimeter-based $E_{\mathrm{T}}^{\mathrm{miss}}$ is used: $|\vec{E}_{\mathrm{T}}^{\mathrm{miss}}|$.

- The electron identification map is p_{T}-dependent since the probability that the electron passes the medium++ or tight++ criteria, as mentioned in Sec. 4.3.2, depends on the electron p_{T}. Therefore it is binned as a function of the electron η and p_{T}.

- The correction and transfer factors are binned as functions of $|\vec{E}_{\mathrm{T}}^{\mathrm{miss}} + \vec{p_{\mathrm{T}}}^{\mathrm{electron}}|$, as the calorimeter-based $E_{\mathrm{T}}^{\mathrm{miss}}$ cannot be regarded as the boson p_{T} in the electron control regions, due to the energy deposition of the electron in the calorimeter.

- The QCD multi-jet background in the W($e\nu$) and Z(ee) control regions is not negligible as it is the case in the muon control regions, and is estimated using a data-driven way based on the matrix method[5]. This introduces an additional source of systematic uncertainty on the predictions based on the electron control regions.

[5]The matrix method estimates the fraction of events with a fake electron by using QCD enriched samples defined by loosing electron identification criteria [50].

The determination of the Z($\nu\nu$) background in the signal regions is done using both the W($e\nu$) and Z(ee) control regions. The W($e\nu$) background is determined from the W($e\nu$) control region, and the Z(ee) background from the Z(ee) control region.

8.4 Systematic Uncertainties

Various sources of systematic uncertainty affect the correction factors obtained from simulation. These include uncertainties on the following: the Jet Energy Scale and Resolution[6] (JES/JER), $E_{\mathrm{T}}^{\mathrm{miss}}$ (due to the uncertainty on the topo-clusters energies), muon and electron energy scale and resolution, data-driven efficiency scale factors, different parton showering and underlying event modellings in simulated samples used to derive some of the correction factors, and the QCD background estimation in the electron control regions, as well as the limited statistics in the simulation event samples used to derive some of the factors.

JES, and $E_{\mathrm{T}}^{\mathrm{miss}}$ uncertainties This uncertainty is calculated by varying the p_T-η–dependent jet energy calibration constants (jet energy scale) of all the jets above 20 GeV in the event up and down by one standard deviation on these calibration constants, and propagating the vector sum of the changes to $E_{\mathrm{T}}^{\mathrm{miss}}$. This will modify both the value and direction of $E_{\mathrm{T}}^{\mathrm{miss}}$. The mono-jet kinematic cuts, and the transverse mass cut in case of W control regions, are applied using the new jets and $E_{\mathrm{T}}^{\mathrm{miss}}$. In the case of asymmetric errors when varying the jet energy scale up and down, the maximum deviation is considered, and the uncertainty is symmetrised around the central value.

Lepton energy scale and resolution uncertainties To get the Z mass correct [46], scaling is applied to the muon p_{T} and η. This correction has uncertainties that affect

[6]The resulting uncertainties are small. The method of background determination used here does not suffer from these errors. However, there is a potential residual small uncertainty; e.g JES can affect the amount of the Z boost, and consequently the lepton acceptance and corrections.

simulation[7].

Uncertainty on the scale factors The total uncertainty on the muon reconstruction efficiency scale factors is due to the uncertainties on the background contributions to the data control regions used to get these factors, and also the finite resolution of the detector [48]. It includes both the statistical and systematic uncertainties. The total uncertainty expressed as the quadratic sum of the statistical and systematic uncertainties, affects the muon reconstruction efficiency map. The same holds for the electron efficiency maps.

MC modelling Parton showering and hadronisation affect the hadronic recoil of the system, and thus the reconstructed p_{T} of the vector boson. This will consequently affect the acceptance and correction factors that are $E_{\mathrm{T}}^{\mathrm{miss}}$–dependent and thus W and Z p_{T}–dependent, as was shown in previous sections. The uncertainty due to various parton showering models, represented by "MC modelling" in the tables below, can be estimated by applying the factors derived from a different generator (e.g. `SHERPA`) than the one used for the central values (`ALPGEN` interfaced with `HERWIG`) to the W or Z data control regions, and comparing the predictions for each background channel to those predicted by applying the `ALPGEN`-based correction factors to the same data control regions. In order to investigate the significance of such comparisons, the Monte Carlo statistical fluctuations on the difference between the two predictions are estimated; in some regions these statistical fluctuations are large compared to the central value of the difference, showing that this difference is not a good representation of such uncertainty in these kinematic regions.

To avoid having such large fluctuations due to the limited statistics in the `SHERPA`

[7]The uncertainty on the muon p_{T} resolution is estimated using the official muon smearing class provided by the ATLAS collaboration. The uncertainty on the muon energy scale is derived by re-scaling the muon p_{T} and comparing the results to the ones obtained without re-scaling [51].

samples, ALPGEN samples are re-weighted with event weights based on the difference in the W p_{T} distributions between the two generators [52]. These weights are then applied to all the ALPGEN-based correction factors by which the data in the control region is corrected to obtain predictions in different background channels. The impact on the overall correction factors applied to get Z($\nu\nu$) from Z or W control regions varies between 0.5% and 3% in the first signal region. A conservative uncertainty of 3% in all regions is assigned to the prediction of each background channel. This is typically lower than the statistical uncertainty in all regions but the first one, for which this is the biggest source of error.

MC statistical uncertainty The limited statistics of various ALPGEN simulation event samples used to obtain some of the correction factors is taken into account. To get the statistical uncertainty on the correction factors on the prediction of each background channel, the statistical fluctuation of the overall factor is considered. As an example, the statistical error of the factor $\frac{N^{SR}_{\mathrm{Z}(\to\nu\nu)+jets}}{N^{CR}_{\mathrm{Z}(\to\mu\mu)+jets}}$ is taken as the simulation statistical uncertainty on the Z($\nu\nu$) + $jets$ prediction from the Z($\mu\mu$) + $jets$ control region (the denominator is the Z($\mu\mu$) with all the control region cuts applied, not with the full lepton phase space). This is due to the fact that the same simulation event samples are used in many of the decomposed correction factors.

Trigger efficiency No systematic uncertainty is assumed for the trigger efficiency on the background predictions that are based on the muon control regions, as the same trigger is used for selecting events in both signal and muon control regions. For the electron control regions, the systematic uncertainty on the efficiency ratio $\frac{\epsilon^{trig}_{E_{\mathrm{T}}^{\mathrm{miss}}}}{\epsilon^{trig}_{\ell}}$, is estimated to be negligible.

Uncertainty on f_{EW} Based on the studies done for the measurement of the ratio of W+jet to Z+jet cross sections [44], a maximum of 1% total uncertainty is considered on (1-f_{EW}). It is dominated by the uncertainty due to the difference between ALPGEN and

PYTHIA.

Uncertainty on the QCD multi–jet background As mentioned before, the contribution of the QCD multi–jet background in the muon channels is negligible. In the electron channels, the uncertainty is estimated to be $\sim 1-3\%$ (Sec. 8.3) on the Z($\nu\nu$) determination from W($e\nu$) control regions, and negligible in the Z(ee) control regions.

As an example, Table 8.18 summarises the systematic uncertainties in the first region, on some of the correction factors used in the muon control regions. These uncertainties are quoted on correction factors calculated as ratios of integrals, and are only used to get the final uncertainties in signal region 4, where there are not enough statistics to apply the bin-by-bin correction factors.

To get the total uncertainty on the final background predictions due to a source of systematic uncertainty, all the correction factors affected by that source of uncertainty are varied, and then applied simultaneously to the data control region. This is done bin by bin, except for the fourth signal region due to limited statistics, to study the effect on the final number of predicted events in each background channel; the contribution of each background channel is re-determined by applying all the varied correction factors to the data control regions. Tables 8.19, 8.20, 8.21, 8.22, 8.24, and 8.23 summarise the total relative uncertainty from each source on different background channels determined from the muon control regions, in each of the 4 signal regions. In case of asymmetric errors, the largest error is considered, and the error is symmetrised. The total uncertainty in each background channel is the quadratic sum of all the different uncertainties, including the 1% total uncertainty on (1-f_{EW}). In some signal regions, some of the systematic uncertainties are mainly due to statistical fluctuations of the simulation event samples used to derive them, as can been seen in various tables where the uncertainties from some sources are smaller than the simulation statistical uncertainty.

To get the total uncertainty, correlations among different background channels have been taken into account. As an example, for the muon control regions the uncertainties on the jet energy scale, $E_{\mathrm{T}}^{\mathrm{miss}}$, muon energy scale and resolution, muon efficiency scale factors, 1-f_{EW}, and MC modelling are considered fully correlated among different background channels predictions. This is due to the fact that for all the predictions the same tool is used to get the JES/$E_{\mathrm{T}}^{\mathrm{miss}}$, muon energy scale and resolution, and SFs uncertainties, the MC modelling uncertainty is conservatively taken to be 3%, and f_{EW} is obtained using the same simulation samples for all various control regions. The MC statistical error is only partly correlated whenever the correction factors use the same simulated sample. For example the MC statistical uncertainties on the denominators of the overall correction factors used to determine the three different background channels based on the W($\mu\nu$) control region are considered to be fully correlated, as they all include the same simulated W($\mu\nu$) samples.

Tables 8.25 and 8.26 summarise the systematic uncertainties on the total number of events for each signal region determined from the muon control regions, due to each source of systematic uncertainty. The two tables correspond to when W or Z control regions are used respectively, to determine the Z($\nu\nu$) contribution in the signal regions.

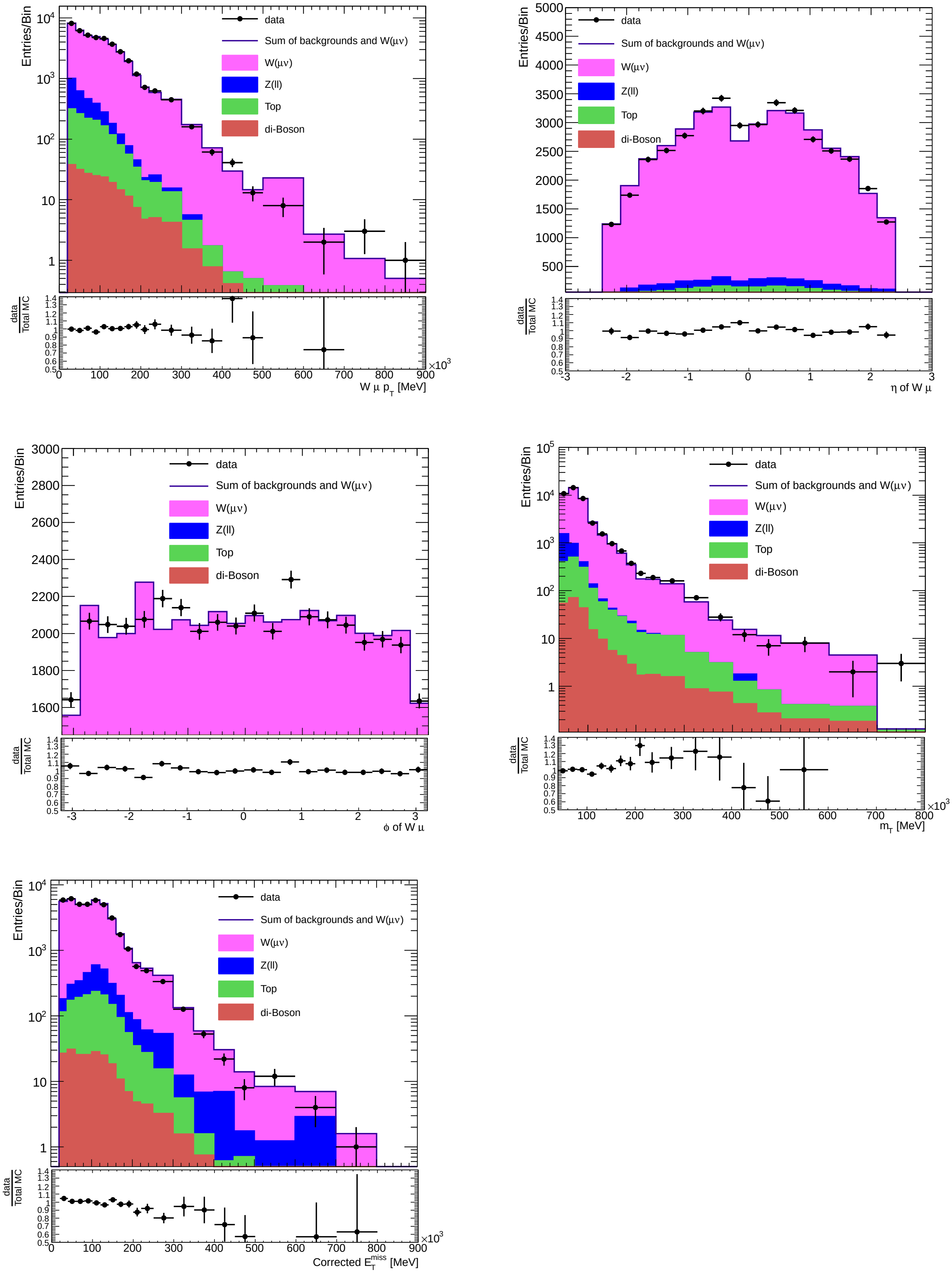

Figure 8.9: Distributions of the leading muon p_{T}, η, and ϕ, m_{T}, and $E_{\mathrm{T}}^{\mathrm{miss}}$ corrected for the selected muon, in the first W($\mu\nu$)+jets control region.

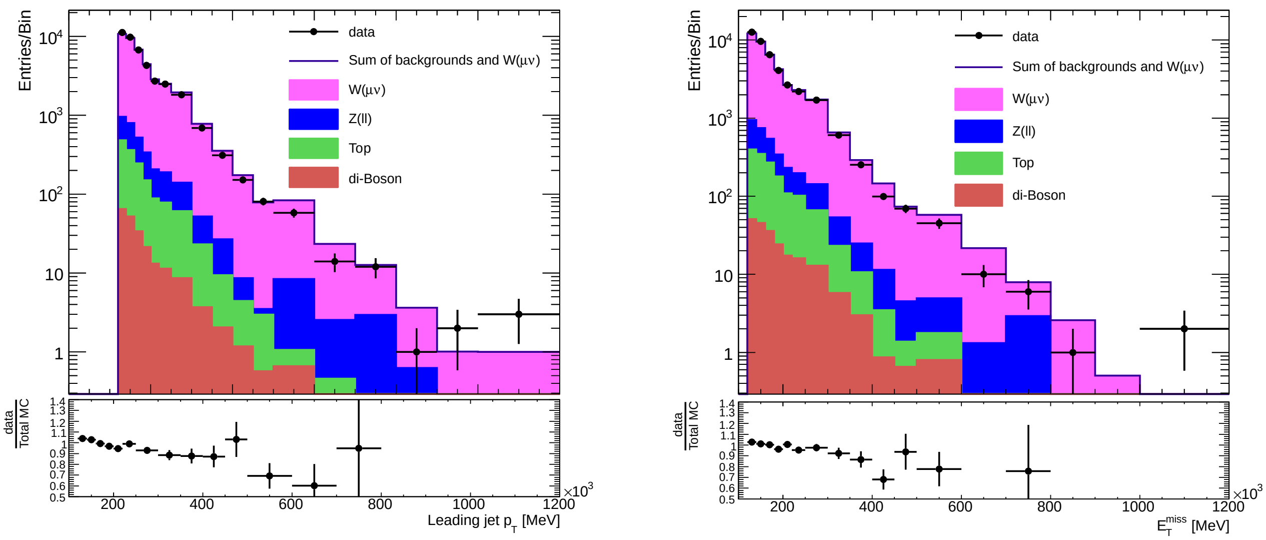

Figure 8.10: Distributions of the leading jet p_{T}, and calorimeter-based $E_{\mathrm{T}}^{\mathrm{miss}}$ in the first W($\mu\nu$)+jets control region.

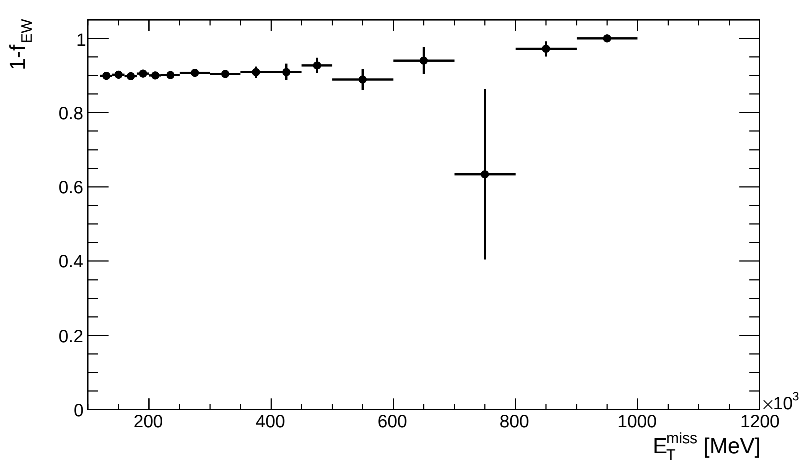

Figure 8.11: Distribution of $(1 - f_{EW})$ in the first W($\mu\nu$)+jets control region.

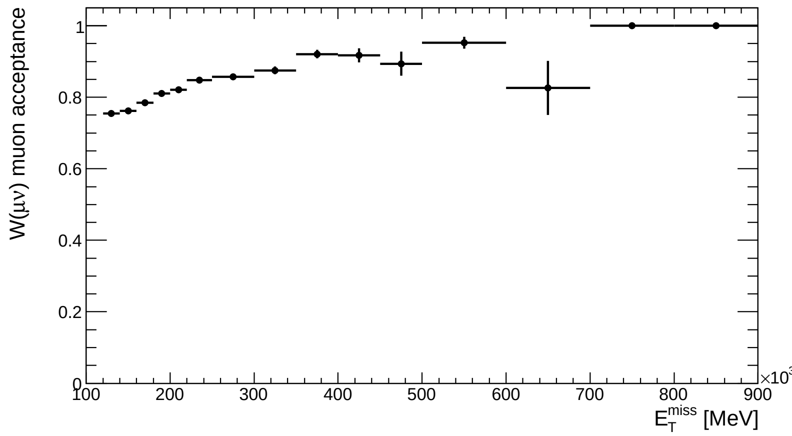

Figure 8.12: W($\mu\nu$) muon acceptance in the first control region.

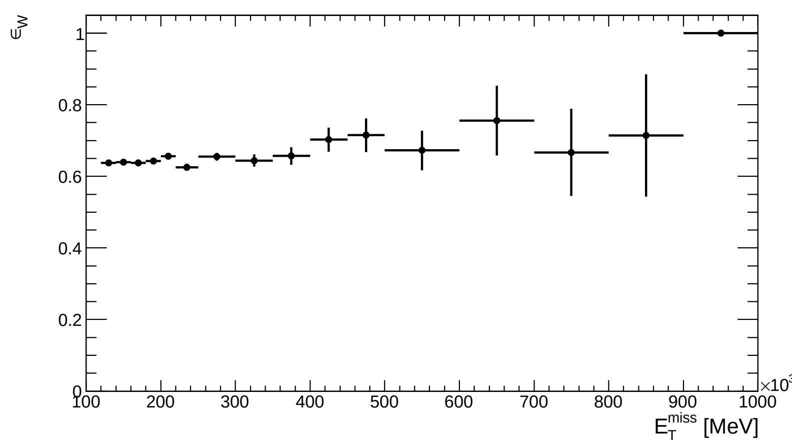

Figure 8.13: Distribution of ϵ_W in the first W($\mu\nu$)+jets control region. Uncertainties are statistical only. ϵ_W is the efficiency of the cuts on m_T and $E_\mathrm{T}^\mathrm{miss}$ (corrected for the selected muon).

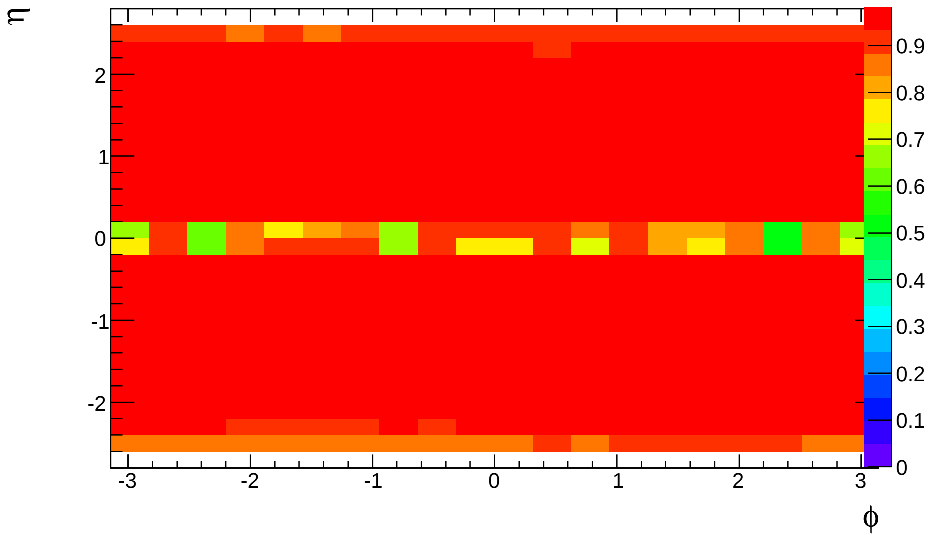

Figure 8.14: Simulation–based veto muon identification efficiency in simulation as function of the muon $\eta - \phi$ without applying the scale factors.

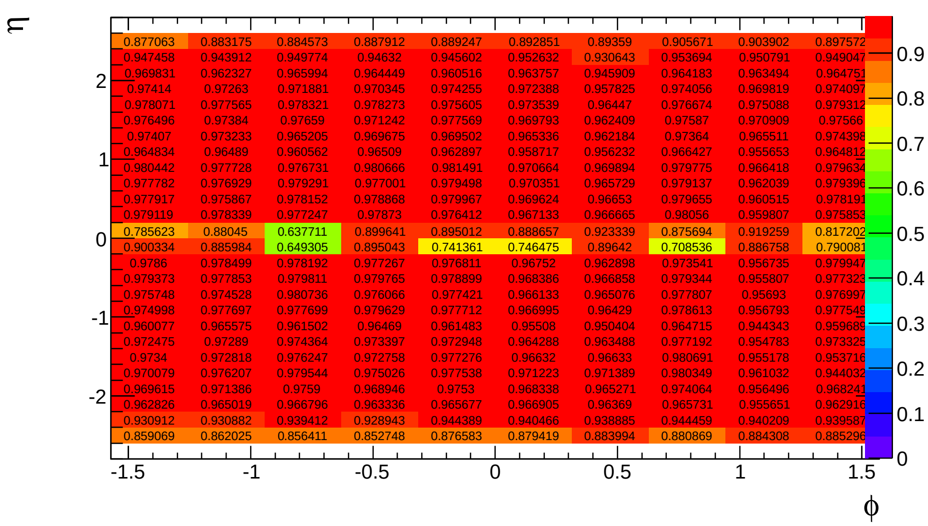

Figure 8.15: Simulation–based veto muon identification efficiency in simulation as function of the muon $\eta - \phi$ without applying the scale factors (zoomed).

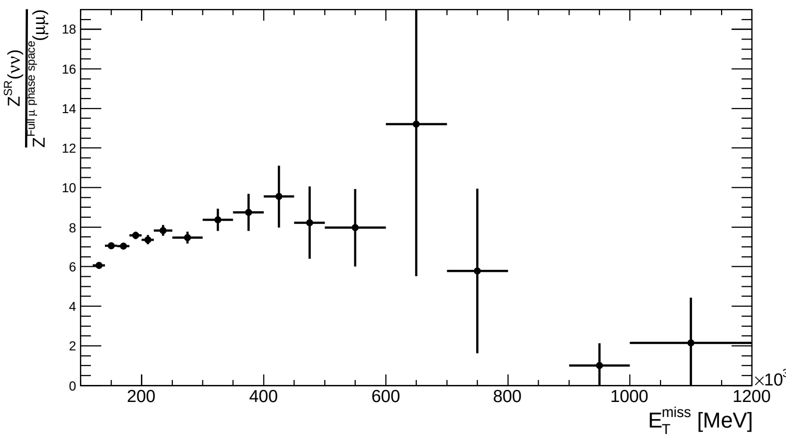

Figure 8.16: Correction factor $\frac{N^{SR}_{\mathrm{Z}(\to\nu\nu)+jets}}{N_{\mathrm{Z}(\to\mu\mu)+jets}}$ in the first Z($\mu\mu$)+jets control region.

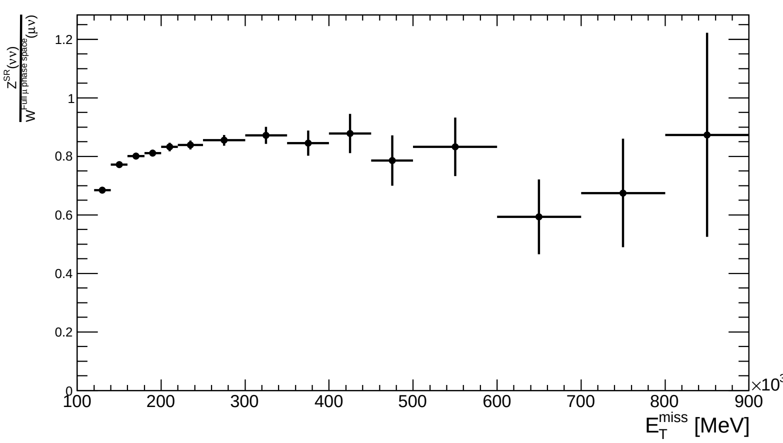

Figure 8.17: Correction factor $\frac{N^{SR}_{\mathrm{Z}(\to\nu\nu)+jets}}{N_{\mathrm{W}(\to\mu\nu)+jets}}$ in the first W($\mu\nu$)+jets control region.

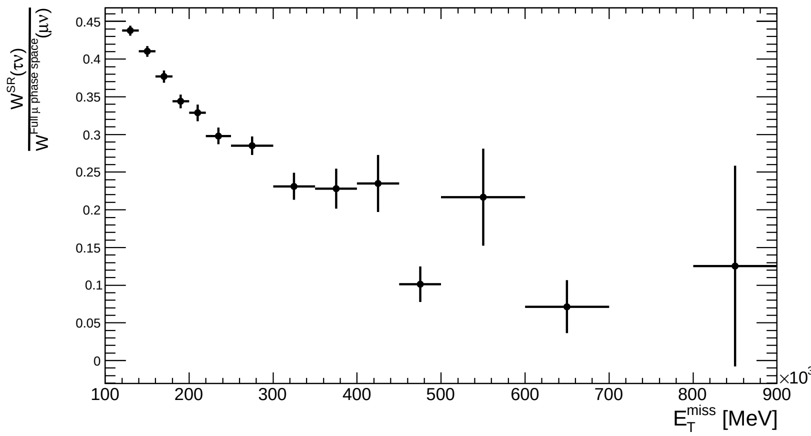

Figure 8.18: Correction factor $\frac{N^{SR}_{\mathrm{W}(\to\tau\nu)+jets}}{N_{\mathrm{W}(\to\mu\nu)+jets}}$ in the first W($\mu\nu$) control region.

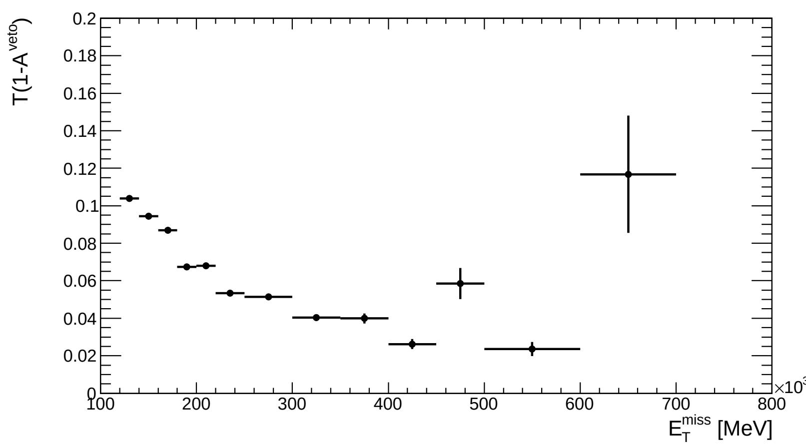

Figure 8.19: Distribution of $T(1-A^{veto})$ in bins of $E_{\mathrm{T}}^{\mathrm{miss}}$, after being weighted with W($\mu\nu$) simulated events in the full muon phase space.

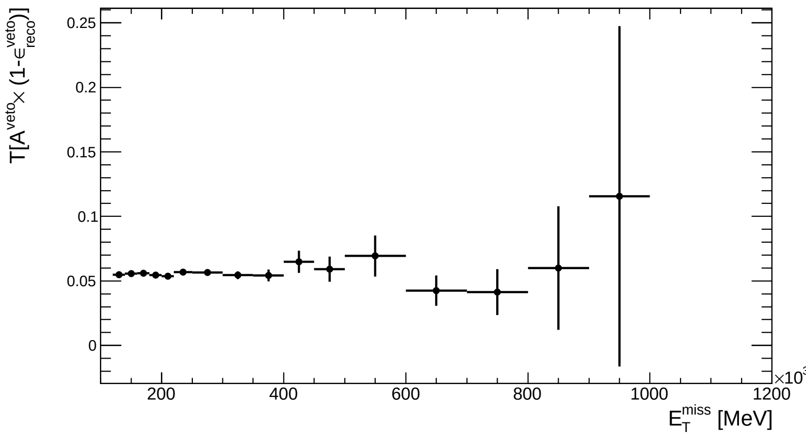

Figure 8.20: Distribution of $T(A^{veto} \times (1 - \epsilon_{reco}^{veto}))$ in bins of $E_{\mathrm{T}}^{\mathrm{miss}}$, after being weighted with W($\mu\nu$) simulated events in the full muon phase space. Data-driven scale factors are applied to the muon identification map.

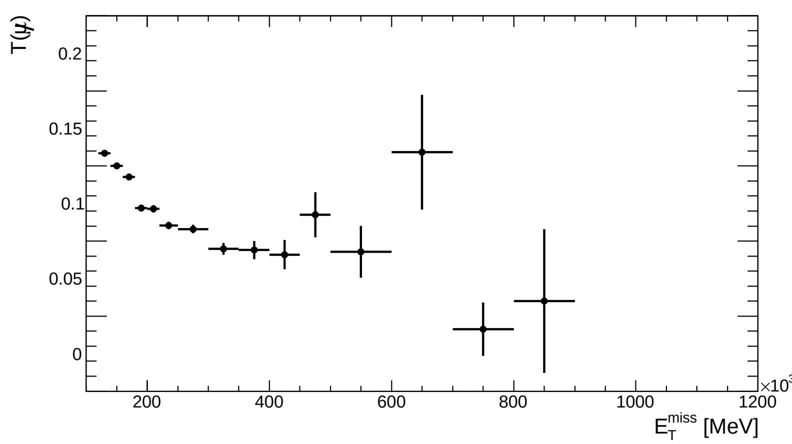

Figure 8.21: Distribution of $T(\not\mu)$ in bins of $E_{\mathrm{T}}^{\mathrm{miss}}$, after being weighted with W($\mu\nu$) simulated events in the full muon phase space.

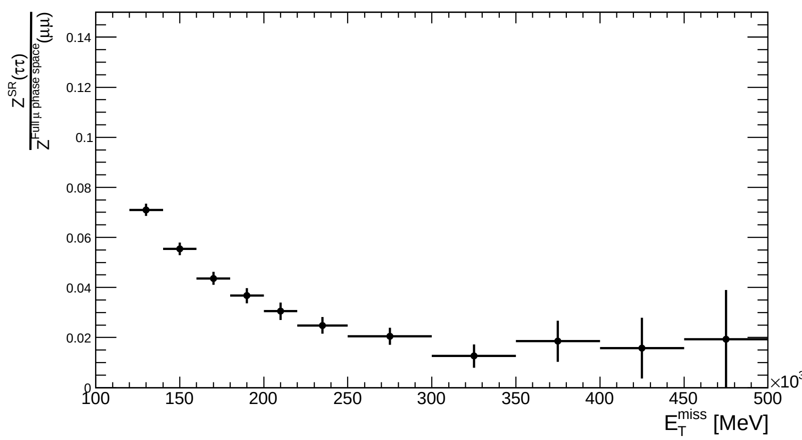

Figure 8.22: Correction factor $\frac{N^{SR}_{Z(\to\tau\tau)+jets}}{N_{Z(\to\mu\mu)+jets}}$ in the first Z($\mu\mu$)+jets control region.

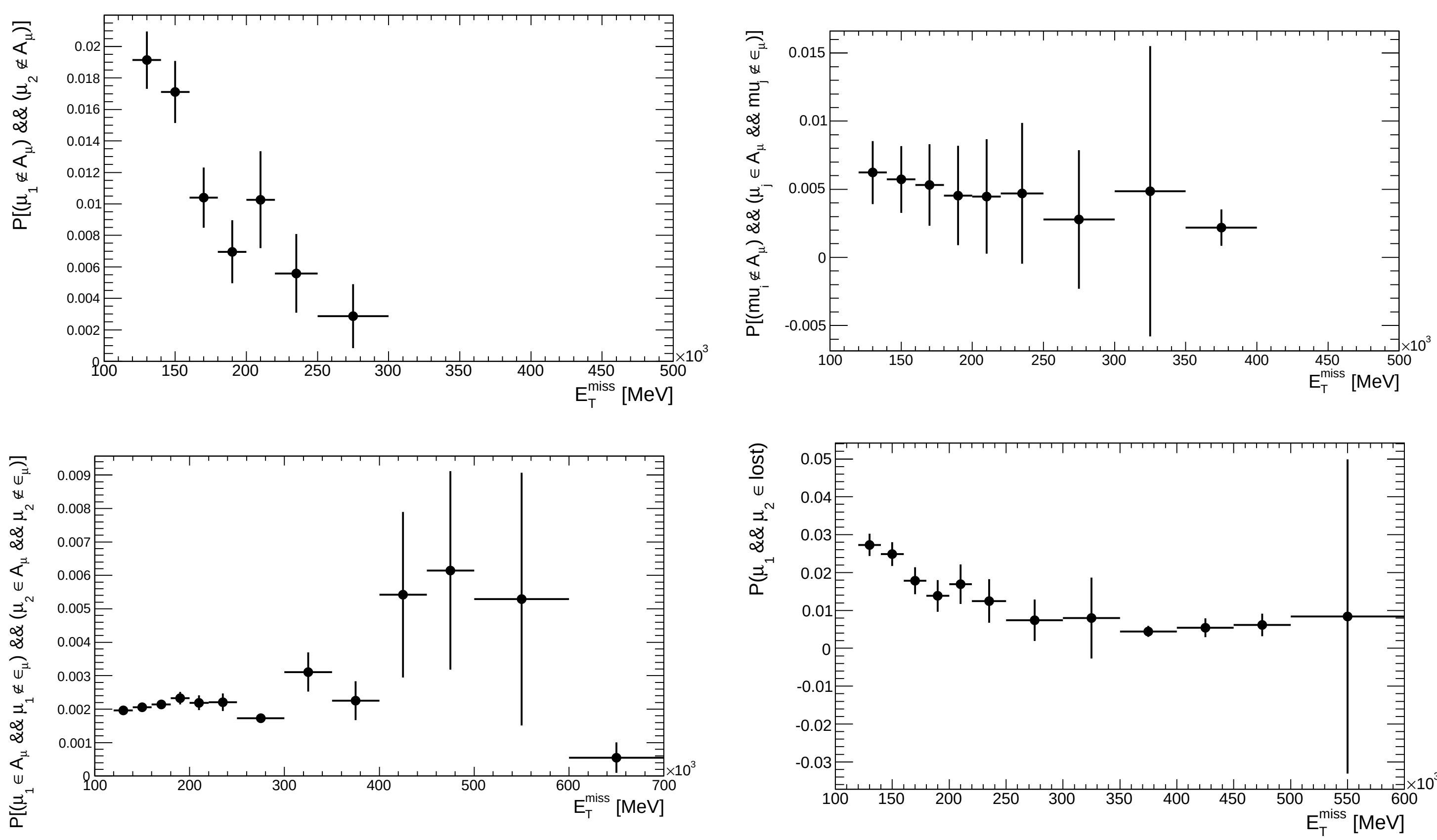

Figure 8.23: Distribution of each term in the probability of losing the two muons in Z($\mu\mu$) events: both muons out of acceptance (top left), one moun out of acceptance and one in acceptance but not reconstructed (top right), both muons in acceptance and not reconstructed (bottom left), and the total probability (bottom right).

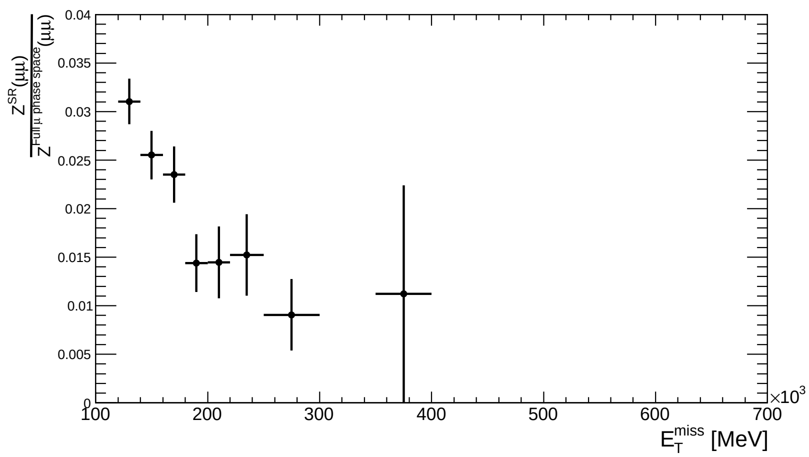

Figure 8.24: Correction factor $\frac{N^{SR}_{Z(\to\mu\mu)+jets}}{N_{Z(\to\mu\mu)+jets}}$ in the first Z($\mu\mu$)+jets control region.

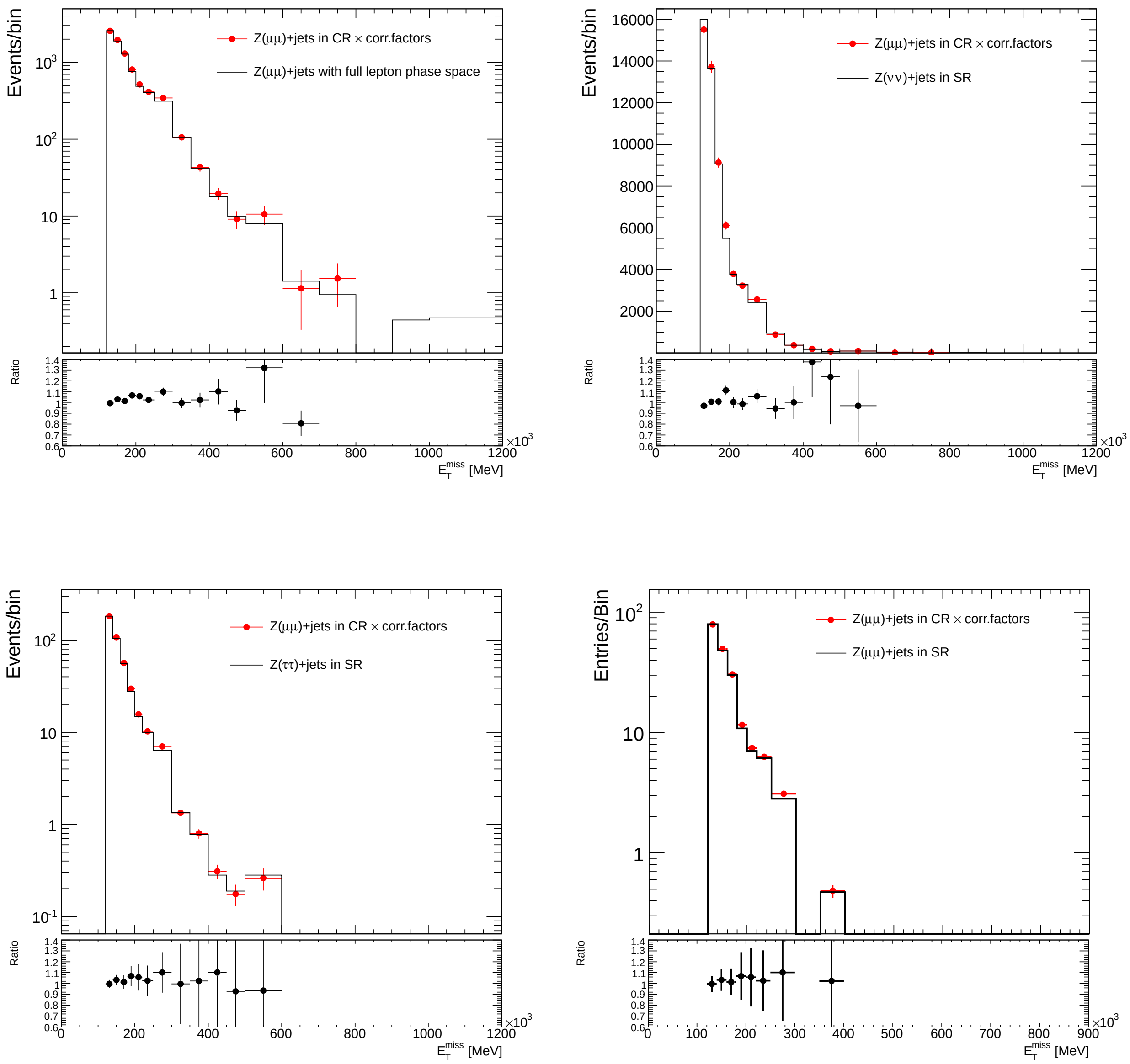

Figure 8.25: Closure tests for: Z($\mu\mu$)+jets in the full muons phase space after the first region cuts on the jets and $E_{\mathrm{T}}^{\mathrm{miss}}$ (top left), Z($\nu\nu$)+jets in signal region 1 (top right), Z($\tau\tau$)+jets in signal region 1 (bottom left), and Z($\mu\mu$)+jets in signal region 1 (bottom right).

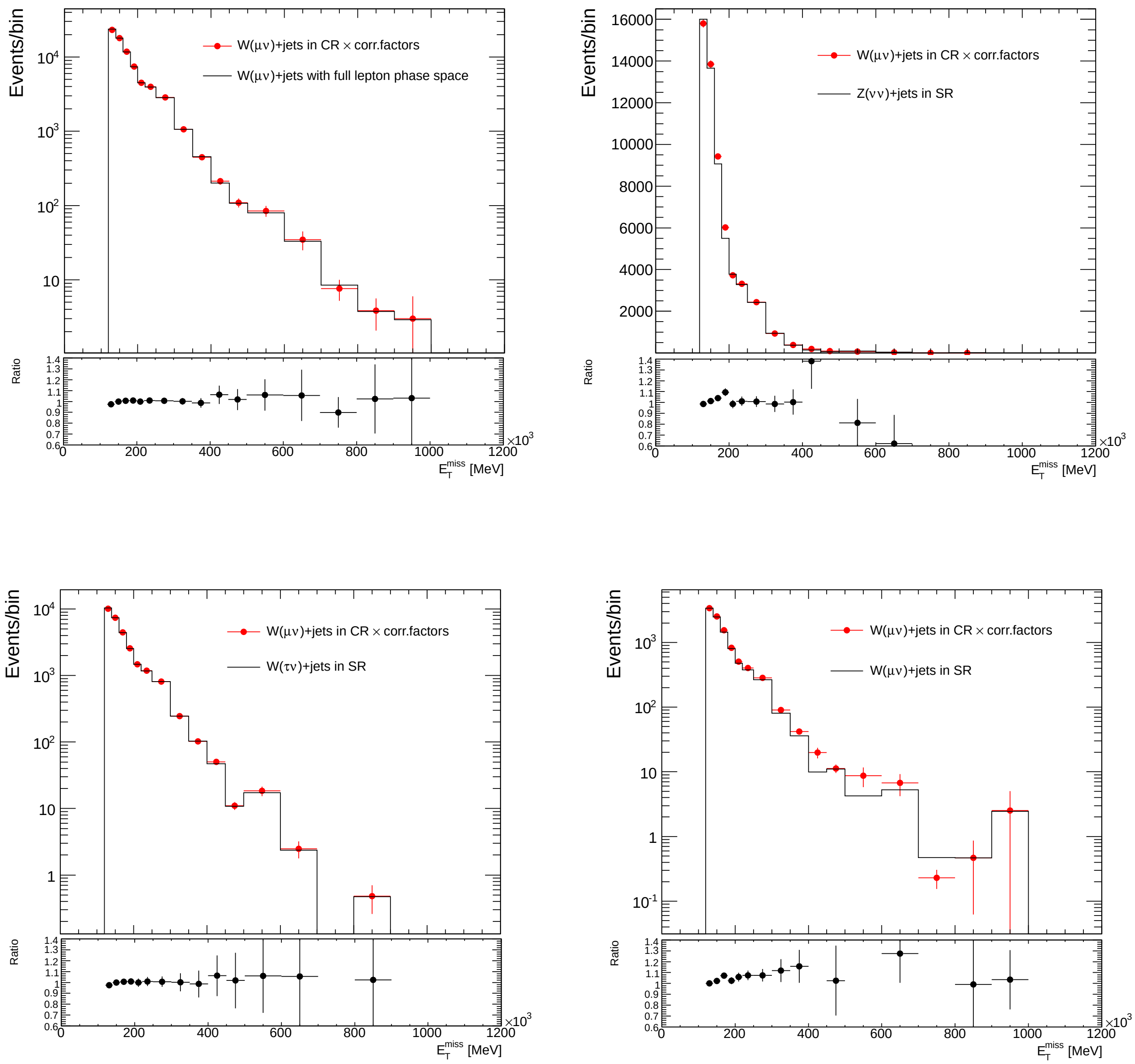

Figure 8.26: Closure tests for: W($\mu\nu$)+jets in the full muons phase space after the first signal region cuts on the jets and $E_{\mathrm{T}}^{\mathrm{miss}}$ (top left), Z($\nu\nu$)+jets in signal region 1 (top right), W($\tau\nu$)+jets in signal region 1 (bottom left), and W($\mu\nu$)+jets in signal region 1 (bottom right).

factor	JES-$E_{\mathrm{T}}^{\mathrm{miss}}$	MC stat uncertainty	SF	μ energy scale and resolution
A_{μ}(W)	0.55	0.23	-	-
ϵ_{W}	0.67	0.39	-	0.12
A_{μ}(Z)	1.25	0.57	-	-
ϵ_{μ}	-	0.01	0.25	-
ϵ_{μ}^{Veto}	-	0.11	0.29	-
$\frac{N^{SR}_{\mathrm{Z}(\to\nu\nu)+jets}}{N_{\mathrm{Z}(\to\mu\mu)+jets}}$	1.03	1.10	-	-
$\frac{N^{SR}_{\mathrm{Z}(\to\mu\mu)+jets}}{N_{\mathrm{Z}(\to\mu\mu)+jets}}$	0.66	0.32	-	-
f_{EW}	0.89	0.12	-	0.22

Table 8.18: Relative systematic uncertainties on different correction factors (in %) due to various sources of uncertainty, in the first signal region. A dash means that the uncertainty does not apply to this correction factor.

source of systematic	Region1	Region2	Region3	Region4
JES-$E_{\mathrm{T}}^{\mathrm{miss}}$	0.73	2.68	5.58	7.28
lepton energy scale and resolution	0.04	0.02	0.13	0.84
SF	0.31	0.33	0.36	0.37
MC modelling	3	3	3	3
MC stat uncertainty (from ALPGEN)	0.55	1.36	3.77	10.93
Total	3.31	4.38	7.45	13.54

Table 8.19: Relative systematic uncertainty (in %) on the Z($\nu\nu$)+jets determination from the W($\mu\nu$)+jets control regions, in the 4 signal regions.

source of systematic	Region1	Region2	Region3	Region4
JES-$E_{\mathrm{T}}^{\mathrm{miss}}$	0.98	4.28	8.51	6.58
SF	0.80	2.97	0.36	0.75
MC modelling	3	3	3	3
MC stat uncertainty (from ALPGEN)	0.86	2.48	7.12	21.62
Total	3.51	6.58	11.54	22.83

Table 8.20: Relative systematic uncertainty (in %) on the Z($\nu\nu$)+kets determination from the Z($\mu\mu$)+jets control regions, in the 4 signal regions.

source of systematic	Region1	Region2	Region3	Region4
JES-$E_{\mathrm{T}}^{\mathrm{miss}}$	1.08	1.82	3.97	8.40
lepton energy scale and resolution	0.04	0.002	0.12	-
SF	0.30	0.33	0.35	0.35
MC modelling	3	3	3	3
MC stat uncertainty (from `ALPGEN`)	0.62	1.81	5.06	15.11
Total	3.41	4.09	7.18	17.58

Table 8.21: Relative systematic uncertainty (in %) on the W($\tau\nu$)+jets determination in the 4 signal regions.

source of systematic	Region1	Region2	Region3	Region4
JES-$E_{\mathrm{T}}^{\mathrm{miss}}$	3.53	6.78	6.29	11.76
lepton energy scale and resolution	0.04	0.04	0.08	4.14
SF	2.10	3.08	3.37	3.79
MC modelling	3	3	3	3
MC stat uncertainty (from `ALPGEN`)	0.73	2.17	6.31	19.17
Total	5.24	8.38	10.04	23.39

Table 8.22: Relative systematic uncertainty (in %) on the W($\mu\nu$)+jets determination in the 4 signal regions.

source of systematic	Region1	Region2	Region3	Region4
JES-$E_{\mathrm{T}}^{\mathrm{miss}}$	4.37	6.19	46.52	-
SF	0.59	3.19	42.75	0.74
MC modelling	3	3	3	3
MC stat uncertainty (from `ALPGEN`)	2.25	10.80	37.76	-
Total	5.87	13.23	73.67	-

Table 8.23: Relative systematic uncertainty (in %) on the Z($\tau\tau$)+jets determination in the 4 signal regions.

source of systematic	Region1	Region2	Region3	Region4
JES-$E_{\mathrm{T}}^{\mathrm{miss}}$	5.18	16.17	-	-
SF	0.60	0.65	-	-
MC modelling	3	3	3	3
MC stat uncertainty (from `ALPGEN`)	5.09	24.40	-	-
Total	7.94	29.45	-	-

Table 8.24: Relative systematic uncertainty (in %) on the Z($\mu\mu$)+jets determination in the 4 signal regions.

source of systematic	Region1	Region2	Region3	Region4
JES-$E_{\mathrm{T}}^{\mathrm{miss}}$	1.10	2.83	5.05	6.22
lepton energy scale and resolution	0.15	0.02	0.12	0.96
SF	0.45	0.53	0.57	0.61
MC modelling	3	3	3	3
Total	3.38	4.28	5.99	7.07

Table 8.25: Relative systematic uncertainty (in %) on the total electroweak background (except W$e\nu$) in the 4 signal regions, with Z($\nu\nu$)+jets determination from the W($\mu\nu$)+jets control regions.

source of systematic	Region1	Region2	Region3	Region4
JES-$E_{\mathrm{T}}^{\mathrm{miss}}$	0.89	3.01	6.38	5.26
lepton energy scale and resolution	0.15	0.02	0.12	0.96
SF	0.53	2.01	0.44	0.65
MC modelling	3	3	3	3
Total	3.33	4.81	7.14	6.25

Table 8.26: Relative systematic uncertainty (in %) on the total electroweak background (except W$e\nu$) in the 4 signal regions, with Z($\nu\nu$)+jets determination from the Z($\mu\mu$)+jets control regions.

Chapter 9

Determination of Non–Electroweak Backgrounds

This chapter presents the description of the method used for determination of the QCD multi-jet and non-collision backgrounds.

9.1 QCD Multi-jet Background

QCD multi-jet events contribute to the signal regions when one or more jets are badly mis-measured such that the jet is lost, and large fake $E_{\mathrm{T}}^{\mathrm{miss}}$ is produced. Two dominant topologies are di-jet and tri-jet events where the second or the third jet is mis-measured. The contribution of multi-jet events with at least one jet lost is a subset of one of the two topologies mentioned above, as explained later. Data–driven techniques are used to determine the contribution of such events. Two types of data control regions are defined to estimate this background. For both types, all the signal selection cuts are applied except that the second jet, above 30 GeV in p_{T}, is required to be along the direction of the $E_{\mathrm{T}}^{\mathrm{miss}}$ direction in the first type, and a third jet, above 30 GeV in p_{T}, is tolerated along the $E_{\mathrm{T}}^{\mathrm{miss}}$ in the second type. This is due to the fact that the contribution of QCD multi–jet events to mono-jet signal regions comes from those events for which the energy of a jet is badly measured such that the p_{T} of the jet falls below the 30 GeV jet definition threshold, hence passing all the signal selection cuts. By studying the transverse energy of jets that point in the direction of $E_{\mathrm{T}}^{\mathrm{miss}}$ which includes the contributions from these mis–measured jets, and by extrapolating the p_{T} distribution of these jets below the 30 GeV jet definition threshold, a data control region is used to get an estimate of the QCD multi–jet background in the signal region. The contribution of events with both the second and the third jets being above 30 GeV in p_{T} and at least one mis-measured and along the $E_{\mathrm{T}}^{\mathrm{miss}}$ direction is a subset of the di-jet or the tri-jet extrapolated regions, and is therefore already taken into account. The contribution of events with a lost second or third jet not along the $E_{\mathrm{T}}^{\mathrm{miss}}$ direction is not estimated, and is considered in the final systematic uncertainties.

This method only provides the number of QCD multi–jet events in the signal regions. It does not allow the prediction of the $E_{\mathrm{T}}^{\mathrm{miss}}$ shape for these events.

9.1.1 Di–jet Control Region

The di-jet control region is obtained by applying all the signal region selection cuts, but inverting the $\Delta\phi$ cut: requiring a second jet with $p_{\mathrm{T}} > 30$ GeV and $|\Delta\phi(2^{\mathrm{nd}}\mathrm{jet}, E_{\mathrm{T}}^{\mathrm{miss}})| \leq 0.5$. Figure 9.1 shows the distributions of the leading jet and the second jet p_{T}, $E_{\mathrm{T}}^{\mathrm{miss}}$, and $\Delta\phi(2^{\mathrm{nd}}\mathrm{jet}, E_{\mathrm{T}}^{\mathrm{miss}})$ in this control region, corresponding to the first signal region: $E_{\mathrm{T}}^{\mathrm{miss}} > 120$ GeV, leading jet $p_{\mathrm{T}} > 120$ GeV.

Standard Model non–QCD contamination to this control region is estimated and removed. The main backgrounds to this control region consist of Z($\nu\nu$)+jets, W($\ell\nu$)+jets, and Z($\ell\ell$)+jets. They are estimated using simulated events and then normalised by applying a set of scale factors obtained from the ratio of the data to simulation in W/Z electroweak control regions presented above. Figure 9.2 shows the p_{T} distribution of the second jet in this di–jet control region after subtracting the backgrounds, along with a linear fit used to extrapolate the distribution down to the region below 30 GeV. The background prediction is obtained from the area under this extrapolation curve, in the region $p_{\mathrm{T}} < 30$ GeV. It corresponds, in the first signal region, to a prediction of ~ 757 events.

9.1.2 Tri-jet Control Region

The tri-jet control region is obtained by applying all the signal region selection cuts, but inverting the third jet veto by requiring exactly 3 jets in the events, with the third jet having $p_{\mathrm{T}} > 30$ GeV. In addition, a $\Delta\phi$ is required: $|\Delta\phi(3^{\mathrm{rd}}\mathrm{jet}, E_{\mathrm{T}}^{\mathrm{miss}})| \leq 0.5$. In this case, the second jet is above 30 GeV in p_{T}, and with $|\Delta\phi(2^{\mathrm{nd}}\mathrm{jet}, E_{\mathrm{T}}^{\mathrm{miss}})| > 0.5$. Figure 9.3 shows the distributions of the leading and third jets p_{T}, $E_{\mathrm{T}}^{\mathrm{miss}}$, and $\Delta\phi(3^{\mathrm{rd}}\mathrm{jet}, E_{\mathrm{T}}^{\mathrm{miss}})$ in this control region, corresponding to the first signal region ($E_{\mathrm{T}}^{\mathrm{miss}} > 120$ GeV, leading jet $p_{\mathrm{T}} > 120$ GeV).

As for the case of the di–jet control region, Standard Model non–QCD contamination to the tri–jet control region is removed before the extrapolation is made. The main backgrounds to this control region consist of Z($\nu\nu$)+jets, W($\ell\nu$)+jets, and Z($\ell\ell$)+jets, and are estimated using simulated events. Figure 9.4 shows the p_{T} distribution of the third jet in the control region, after subtracting the backgrounds, along with a linear fit used to extrapolate the distribution down to the region below 30 GeV. This gives an estimation of ~ 350 events in the first signal region.

Systematic uncertainties in both types of control regions are obtained by varying the range of the fit used to determine the extrapolation curve.

Table 9.1 lists the number of events in each of the QCD data control regions before background subtraction.

Table 9.2 shows the estimation of QCD multi-jet events in each of the four signal regions, along with their uncertainties.

Control Region	region 1	region 2	region 3	region 4
di-jet	84047	3373	224	21
tri-jet	25846	1372	115	11

Table 9.1: Number of data events in each QCD multi-jet control region.

Signal Region	region 1	region 2	region 3	region 4
di-jet background	$757 \pm 28 \pm 643$	$64 \pm 8 \pm 64$	$8 \pm 3 \pm 8$	-
tri-jet background	$350 \pm 18 \pm 296$	-	-	-
total multi-jet	$1107 \pm 33 \pm 940$	$64 \pm 8 \pm 64$	$8 \pm 3 \pm 8$	-

Table 9.2: QCD multi-jet background estimation. Listed are the statistical and systematic uncertainties, respectively. QCD contribution in the fourth signal region is found to be negligible.

9.2 Non-collision Background

The data–driven technique of Beam Background Identification Method [53] is used to determine the rate of non-collision background in the signal regions. This method combines the information from the LAr and Tile calorimeters, and the CSC and inner MDT end-cap muon chambers in order to identify beam halo muons traversing the detector along the beam pipe. The tagging efficiency of the method is $\epsilon = 16\%$, estimated using the unpaired bunch crossings where only one beam is present, and a mis-identification probability of $\sim 10^{-5}$. The non-collision background estimate in each signal region can then be obtained as $N_{\text{ncb}} = N_{\text{tagged}}/\epsilon$, where N_{tagged} is the number of events in the data signal region that have been tagged by the tool.

It is assumed that this method also accounts for the background from cosmic-ray muons. This is due to the fact that the rate of cosmic events in the paired bunch crossings is the same as that in the unpaired bunch crossings that are used to evaluate the tagging efficiency of the method. Therefore, the efficiency already accounts for such events due to their contribution to the denominator of the efficiency definition.

The systematic uncertainty of the method is mainly due to the effect of out-of-time pile-up, and is estimated to be $\sim 10\%$ [53] on the number of tagged events. This is done by estimating the difference between the beam halo rates in two different samples collected from unpaired isolated and unpaired non-isolated bunches, with time spacing of more and less than 75 ns away from the last bunch in the other beam, respectively. Further studies on the rejection of cosmic background events is presented in Appendix. C.

Table 9.3 shows the estimation of the number of tagged and non-collision background events in each signal region, using the method described above.

SR	$N_{\text{tagged}}^{\text{data}}$	$N_{\text{ncb}} \pm \text{stat} \pm \text{sys}$
1	92	$575 \pm 60 \pm 57$
2	4	$25 \pm 13 \pm 3$
3	0	-
4	0	-

Table 9.3: Number of tagged and non-collision background events in each signal region.

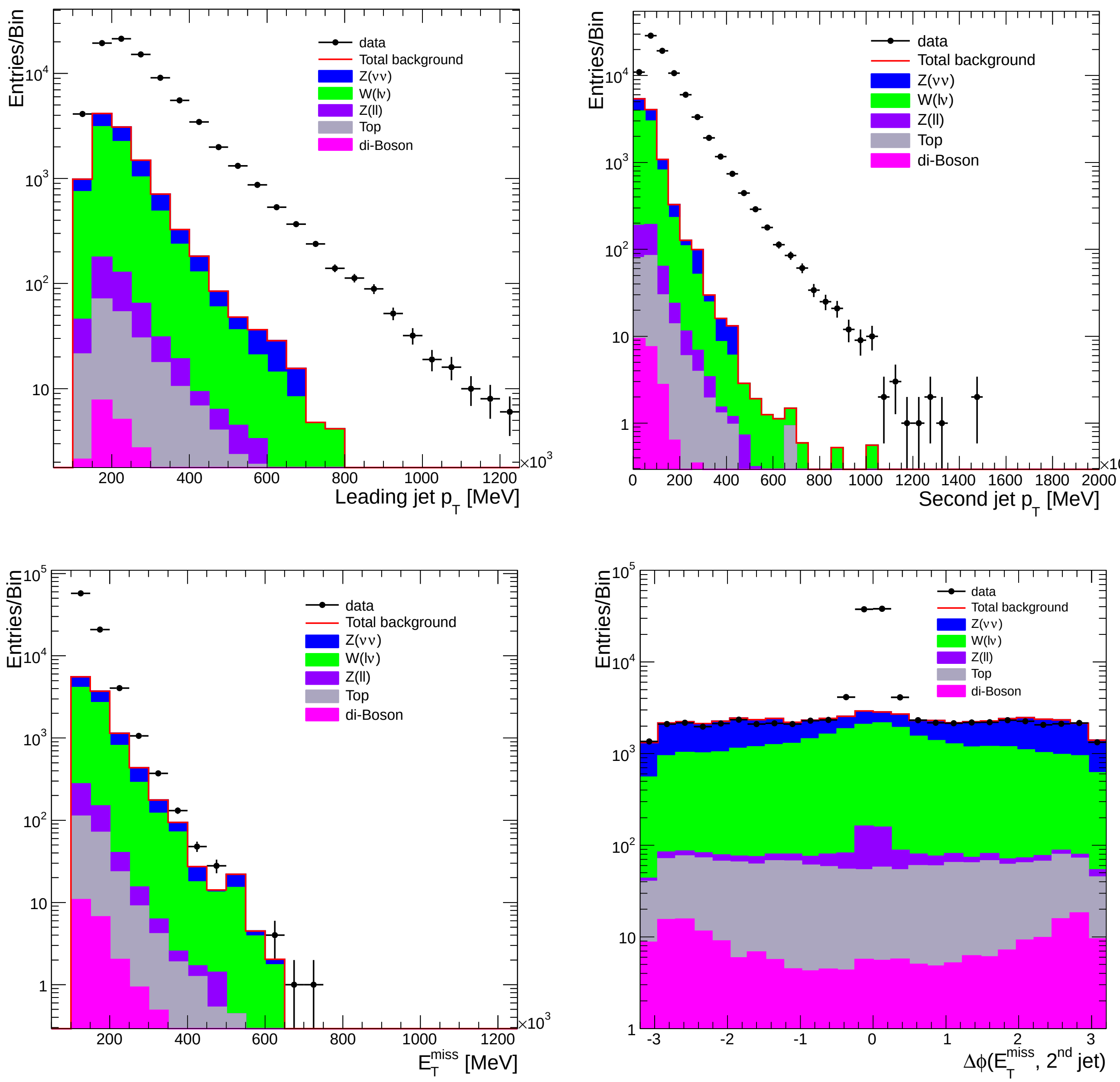

Figure 9.1: Distributions of the leading and second jets p_{T}, $E_{\mathrm{T}}^{\mathrm{miss}}$, and $\Delta\phi(2^{\mathrm{nd}}\mathrm{jet}, E_{\mathrm{T}}^{\mathrm{miss}})$ in the first QCD di-jet control region. All plots are after all the cuts, except the $\Delta\phi$ plot which is without the upper $\Delta\phi$ cut. Shown are also the backgrounds, based on simulation.

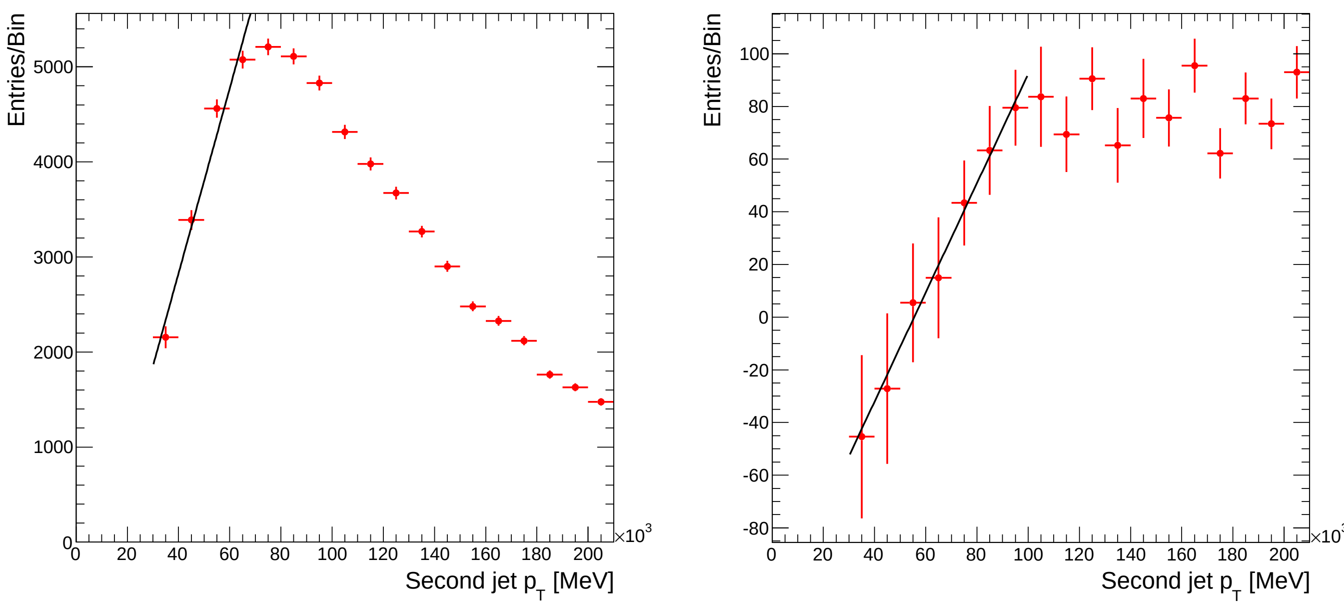

Figure 9.2: Distributions of the second jet p_{T} in the first (left) and second (right) QCD di-jet data control regions after background subtraction. Shown are also examples of the fits.

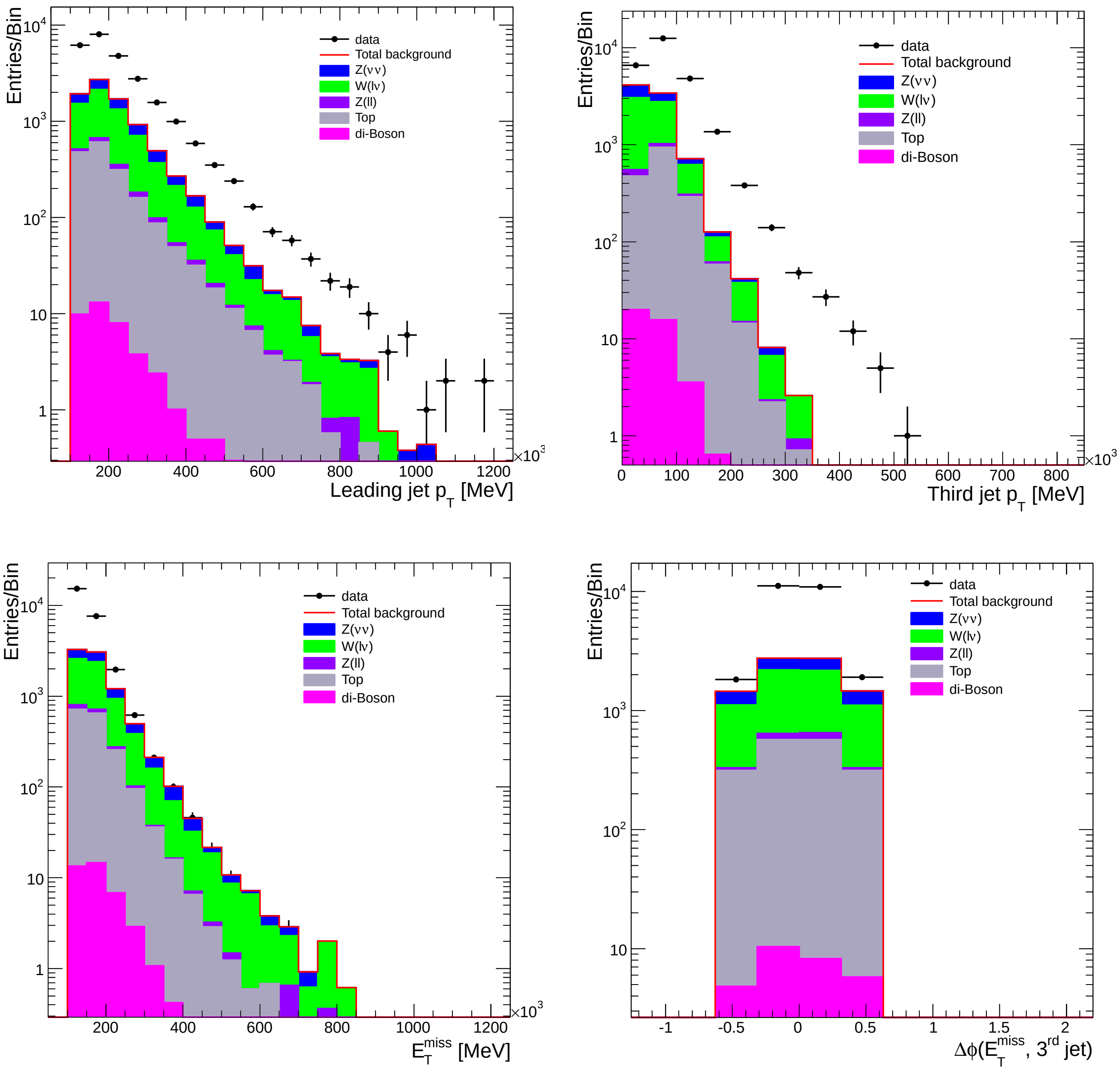

Figure 9.3: Distributions of the leading, and third jets p_{T}, $E_{\mathrm{T}}^{\mathrm{miss}}$, and $\Delta\phi(3^{\mathrm{rd}}\mathrm{jet}, E_{\mathrm{T}}^{\mathrm{miss}})$ in the first QCD tri-jet control region. Shown are also the backgrounds, based on simulation.

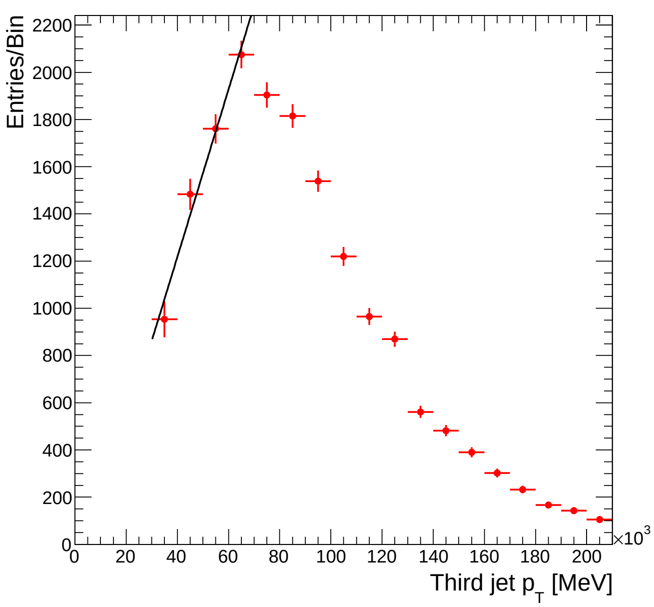

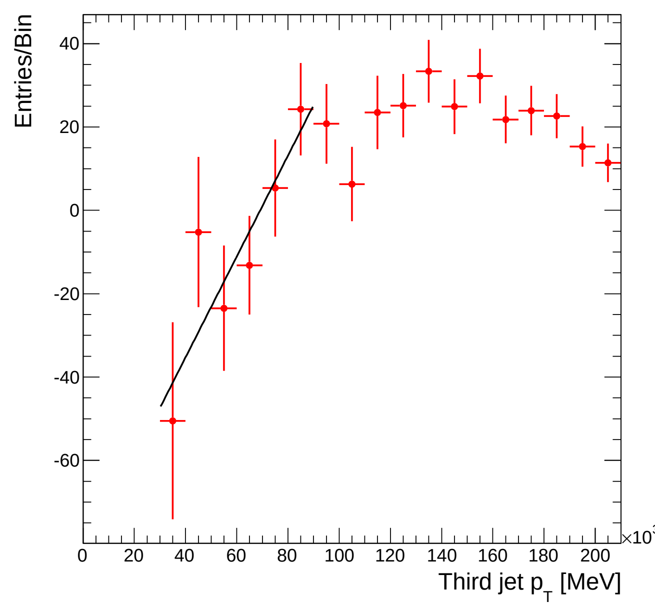

Figure 9.4: Distributions of the third jet p_{T} in the first (left) and second (right) QCD tri-jet data control regions, after background subtraction. Shown are also examples of the fits.

Chapter 10

Experimental Results

Table 10.1 summarises the total number of events for each background channel in the 4 signal regions, with the corresponding statistical and total systematic uncertainties. The statistical errors also include those arising from the simulation samples. The total systematic uncertainty on the total number of events in each region is calculated after taking into account the correlations between different background channels. Presented are also the four predictions for Z($\nu\nu$)+jets from the 2 electron and muon channels, as well as their combinations (Sec. 10.1).

Tables 10.2 - 10.5 list the contributions of individual sources of systematic uncertainty to the total number of background events in each signal region, corresponding to BG (1) - BG (4) presented in Table 10.1, and detailed in Sec. 10.1.

Figure 10.1 provides the comparisons between selected data and all the predicted backgrounds, as function of $E_{\mathrm{T}}^{\mathrm{miss}}$, in each of the four signal regions. In these plots, Z($\nu\nu$)+jets is determined using W($\mu\nu$)+jets events, due to the lower data statistical uncertainty of W control regions compared to Z control regions. As an example of what the data would look like if the ADD model reflected reality, the result is also shown for an excluded ADD point n=2 and M_D = 3.5 TeV. The contribution of the QCD multi-jet background is not shown, as the data-driven method used to determine this background does not provide its shape. Consequently there are more data events in the first few bins of the $E_{\mathrm{T}}^{\mathrm{miss}}$ distribution compared to the Standard Model expectation as can be seen in the ratio plot, as the main contribution of the QCD background is in the low $E_{\mathrm{T}}^{\mathrm{miss}}$ region. The non-collision background is also not shown on the plots, resulting in the deviation observed in the first bin in the first signal region between the prediction and the observation. Figures 10.2 - 10.4 include similar comparisons between data and background, as function of the leading and second jets p_{T} and $|\Delta\phi(E_{\mathrm{T}}^{\mathrm{miss}}, 2^{\mathrm{nd}}\mathrm{jet})|$. In these plots, the correction and transfer factors are determined in bins of the plotted variable[1]. While QCD multi-jet background only significantly affects the first bin of $E_{\mathrm{T}}^{\mathrm{miss}}$ distribution, as its distribution falls rapidly with $E_{\mathrm{T}}^{\mathrm{miss}}$, it does not fall as rapidly as a function of the leading jet p_{T}. Therefore, it results in smaller discrepancies in the first bin of leading jet p_{T} distribution between prediction and observation compared to the $E_{\mathrm{T}}^{\mathrm{miss}}$ distribution, and it has deviations over a larger number of jet p_{T} bins. For the same reason – omission of QCD background from the plots – the $\Delta\phi(E_{\mathrm{T}}^{\mathrm{miss}}, 2^{\mathrm{nd}}\mathrm{jet})$ distribution also has a discrepancy between prediction and observation in the region immediately outside the QCD veto cut, $\Delta\phi(E_{\mathrm{T}}^{\mathrm{miss}}, 2^{\mathrm{nd}}\mathrm{jet}) < 0.5$. Allowing for the above discrepancies, these distributions do not feature any significant deviations between predictions and observations.

There is no need for the shapes of $E_{\mathrm{T}}^{\mathrm{miss}}$ and the jet kinematic distributions in the total background to match those in data, as these are in the signal regions, sensitive to new signatures beyond the Standard Model expectation. The plots of Fig. 10.1– 10.4 however indicate that no new physics is visible from this analysis.

10.1 Combination of Z($\nu\nu$) Determinations

Four predictions for the contribution of the Z($\nu\nu$)+jets background to the signal regions are available; two from the muon W($\mu\nu$)+jets, Z($\mu\mu$)+jets, and two from the electron

[1] The results as quoted in Table 10.1 are derived by using the transfer factors in bins of $E_{\mathrm{T}}^{\mathrm{miss}}$.

Background Predictions ± (data stat.) ± (MC stat.) ± (syst.)				
	Region 1	Region 2	Region 3	Region 4
$Z\nu\nu$ ($W\mu\nu$)	63166 ± 351 ± 347 ± 2059	5405 ± 99 ± 74 ± 225	505 ± 30 ± 19 ± 32	59 ± 9 ± 6 ± 5
$Z\nu\nu$ ($Z\mu\mu$)	63055 ± 931 ± 542 ± 2150	5137 ± 248 ± 127 ± 313	544 ± 83 ± 39 ± 49	75 ± 32 ± 16 ± 6
$Z\nu\nu$ [BLUE, $W\mu\nu$, $Z\mu\mu$]	63158 ± 332 ± 329 ± 2064	5399 ± 97 ± 72 ± 226	508 ± 28 ± 18 ± 34	60 ± 9 ± 6 ± 5
$Z\nu\nu$ [Simple, $W\mu\nu$, $Z\mu\mu$]	63110 ± 502 ± 334 ± 2097	5268 ± 136 ± 79 ± 262	528 ± 50 ± 23 ± 42	72 ± 27 ± 11 ± 5
$Z\nu\nu$ ($We\nu$)	62331 ± 386 ± 505 ± 3989	5299 ± 119 ± 85 ± 311	508 ± 31 ± 34 ± 30	53 ± 10 ± 8 ± 4
$Z\nu\nu$ (Zee)	63220 ± 899 ± 518 ± 3256	5312 ± 232 ± 118 ± 396	453 ± 64 ± 28 ± 34	72 ± 26 ± 10 ± 5
$Z\nu\nu$ [BLUE, $We\nu$, Zee]	63049 ± 729 ± 434 ± 3287	5299 ± 103 ± 117 ± 313	493 ± 29 ± 26 ± 31	56 ± 10 ± 7 ± 4
$Z\nu\nu$ [Simple, $We\nu$, Zee]	62836 ± 537 ± 375 ± 3367	5306 ± 128 ± 86 ± 351	467 ± 48 ± 23 ± 33	70 ± 23 ± 9 ± 5
$Z\nu\nu$ [BLUE, All]	63247 ± 348 ± 336 ± 2050	5400 ± 101 ± 74 ± 220	500 ± 20 ± 17 ± 31	58 ± 7 ± 5 ± 4
$Z\nu\nu$ [Simple, All]	63033 ± 357 ± 261 ± 2258	5322 ± 73 ± 56 ± 268	501 ± 21 ± 16 ± 32	58 ± 7 ± 5 ± 4
$W\tau\nu$	31442 ± 177 ± 195 ± 1006	1853 ± 35 ± 34 ± 65	133 ± 8 ± 7 ± 7	13 ± 2 ± 2 ± 1
$W\mu\nu$	11071 ± 62 ± 81 ± 563	704 ± 13 ± 15 ± 57	55 ± 3 ± 3 ± 4	6 ± 1 ± 1 ± -
$We\nu$	14611 ± 168 ± 121 ± 479	679 ± 28 ± 20 ± 25	40 ± 6 ± 4 ± 3	5 ± 2 ± 1 ± 1
$Z\tau\tau$	421 ± 7 ± 9 ± 22	15 ± 1 ± 2 ± 1	2 ± - ± 1 ± 1	-
$Z\mu\mu$	204 ± 3 ± 10 ± 16	8 ± - ± 2 ± 3	-	-
Multi-jets	1100 ± 33 ± - ± 940	64 ± 8 ± - ± 64	8 ± 3 ± - ± 8	-
$t\bar{t}$+single t	1237 ± - ± 11 ± 247	57 ± - ± 3 ± 12	4 ± - ± 1 ± 1	-
Di-bosons	302 ± - ± 5 ± 61	29 ± - ± 1 ± 5	5 ± - ± 1 ± 1	1 ± - ± - ± -
NCB	575 ± 60 ± - ± 57	25 ± 13 ± - ± 3	-	-
BG (1) [$W\mu\nu$]	124129 ± 617 ± 633 ± 4184	8839 ± 150 ± 118 ± 372	752 ± 41 ± 28 ± 45	84 ± 12 ± 9 ± 6
BG (2) [$Z\mu\mu$]	124018 ± 987 ± 576 ± 4126	8571 ± 255 ± 133 ± 399	791 ± 85 ± 40 ± 56	100 ± 33 ± 16 ± 6
BG (3) [BLUE]	124121 ± 598 ± 612 ± 4185	8833 ± 148 ± 116 ± 373	755 ± 39 ± 27 ± 46	85 ± 12 ± 9 ± 6
BG (3) [Simple]	124073 ± 659 ± 553 ± 4258	8702 ± 163 ± 110 ± 422	775 ± 55 ± 28 ± 61	97 ± 27 ± 11 ± 13
BG (4) [BLUE]	124210 ± 618 ± 626 ± 4152	8834 ± 153 ± 120 ± 367	747 ± 32 ± 25 ± 44	83 ± 10 ± 7 ± 6
BG(4) [Simple]	123996 ± 555 ± 509 ± 4377	8756 ± 120 ± 99 ± 412	748 ± 31 ± 24 ± 45	83 ± 10 ± 7 ± 6
Data	124703	8631	785	77

Table 10.1: Background contributions and number of observed data events in each of the 4 signal regions. Background (1) - (4) refer to the total background in the case where $Z(\nu\nu)$+jets is determined using $W(\mu\nu)$+jets control region events, $Z(\mu\mu)$+jets control region events, the combination of the two, and the combination of the 4 available predictions from $W(\mu\nu)$+jets, $Z(\mu\mu)$+jets, $W(e\nu)$+jets, and $Z(ee)$+jets control regions, respectively. The first, second, and third uncertainties correspond to the data statistical, simulation statistical, and systematic uncertainties, respectively. Shown are the results of combinations using both the BLUE and the Simple weights, defined in Sec. 10.1.

Systematic	Region 1	Region 2	Region 3	Region 4
JES-$E_{\mathrm{T}}^{\mathrm{miss}}$	1.07%	2.71%	4.99%	6.52%
μ energy scale and resolution	0.13%	0.02%	0.11%	0.90%
lepton SF	0.39%	0.48%	0.53%	0.57%
MC modelling	2.92%	2.94%	2.94%	2.99%
$1 - f_{EW}$	0.95%	0.96%	0.97%	0.99%
non-EW systematics	0.79%	0.74%	1.08%	0.24%
MC stat uncertainty	0.51%	1.33%	3.71%	10.88%
Total systematic uncertainty	3.41%	4.42%	7.05%	13.12%
data stat uncertainty	0.50%	1.70%	5.45%	14.78%

Table 10.2: Relative contribution of different sources of uncertainties to BG (1).

Systematic	Region 1	Region 2	Region 3	Region 4
JES-$E_{\mathrm{T}}^{\mathrm{miss}}$	0.89%	2.87%	6.23%	5.56%
μ energy scale and resolution	0.13%	0.02%	0.11%	0.91%
lepton SF	0.45%	0.18%	0.41%	0.62%
MC modelling	2.92%	2.94%	2.94%	2.99%
$1 - f_{EW}$	0.95%	0.96%	0.97%	0.99%
non-EW systematics	0.79%	0.76%	1.02%	0.20%
MC stat uncertainty	0.46%	1.56%	5.01%	16.50%
Total systematic uncertainty	3.36%	4.91%	8.64%	17.73%
data stat uncertainty	0.80%	2.98%	10.69%	32.68%

Table 10.3: Relative contribution of different sources of uncertainties to BG (2).

Systematic	Region 1	Region 2	Region 3	Region 4
JES-$E_{\mathrm{T}}^{\mathrm{miss}}$	1.14%	3.20%	6.21%	6.17%
μ energy scale and resolution	0.02%	0.009%	0.06%	0.37%
lepton SF	0.49%	1.25%	0.49%	0.80%
MC modelling	2.92%	2.94%	3.62%	3.04%
$1 - f_{EW}$	0.95%	0.96%	0.97%	0.99%
non-EW systematics	0.79%	0.75%	1.05%	0.21%
MC stat uncertainty	0.45%	1.26%	3.62%	11.85%
Total systematic uncertainty	3.43%	4.85%	7.91%	13.76%
data stat uncertainty	0.53%	1.87%	7.04	27.98%

Table 10.4: Relative contribution of different sources of uncertainties to BG (3) using Simple weights.

Systematic	Region 1	Region 2	Region 3	Region 4
JES-$E_{\mathrm{T}}^{\mathrm{miss}}$	1.55%	2.44%	5.02%	5.86%
μ energy scale and resolution	0.02%	0.02%	0.07%	0.60%
lepton SF	0.49%	0.77%	0.68%	0.70%
MC modelling	2.92%	2.94%	2.93%	3.04%
$1 - f_{EW}$	0.81%	0.73%	0.65%	0.66%
non-EW systematics	0.79%	0.75%	1.08%	0.25%
MC stat uncertainty	0.41%	1.13%	3.23%	8.80%
Multi-jet BG in electron CR	0.1%	0.1%	0.3%	0.6%
Total systematic uncertainty	3.55%	4.84%	6.82%	11.10%
data stat uncertainty	0.45%	1.37%	4.17%	11.78%

Table 10.5: Relative contribution of different sources of uncertainties to BG (4) using Simple weights.

W($e\nu$)+jets, Z(ee)+jets control regions. In order to benefit from the higher statistics in some of these control regions, or the lower systematic uncertainties in some others, we investigate the gain of combining the 4 measurements. The general formula used for the combination is as follows:

$$x = \vec{w}^T.\vec{x} \tag{10.1}$$

$$(\sigma_x^a)^2 = \Sigma_{i,j}(w_i.w_j.V_a^{ij}) \tag{10.2}$$

$$(\sigma_x^{total})^2 = \Sigma_a\Sigma_{i,j}(w_i.w_j.V_a^{ij}) = \Sigma_{i,j}(w_i.w_j.V^{ij}) \tag{10.3}$$

where $\vec{x}$ is the vector with components equal to the various measurements, $\vec{w}$ is the vector of weights, assigning weights to various measurements according to their relative total uncertainties, V_a is the symmetric matrix of uncertainties corresponding to systematic source a, σ_x^a is the systematic uncertainty on the combined value due to systematic source a, and V is the symmetric matrix of the total uncertainties, i.e. the covariance matrix, equivalent to the sum of all V_a matrices. In the case of four measurements, V_a is:

$$V_a = \begin{pmatrix} \sigma_{1a}^2 & \rho_{12a}\sigma_{1a}\sigma_{2a} & \rho_{13a}\sigma_{1a}\sigma_{3a} & \rho_{14a}\sigma_{1a}\sigma_{4a} \\ \rho_{12a}\sigma_{1a}\sigma_{2a} & \sigma_{2a}^2 & \rho_{23a}\sigma_{2a}\sigma_{3a} & \rho_{24a}\sigma_{2a}\sigma_{4a} \\ \rho_{13a}\sigma_{1a}\sigma_{3a} & \rho_{23a}\sigma_{2a}\sigma_{3a} & \sigma_{3a}^2 & \rho_{34a}\sigma_{3a}\sigma_{4a} \\ \rho_{14a}\sigma_{1a}\sigma_{4a} & \rho_{24a}\sigma_{2a}\sigma_{4a} & \rho_{34a}\sigma_{3a}\sigma_{4a} & \sigma_{4a}^2 \end{pmatrix}, \tag{10.4}$$

where σ_{ia} is the systematic uncertainty on measurement i due to systematic source a, and ρ_{ija} is the correlation between uncertainties of source a on measurements i and j.

The uncertainties related to JES/$E_{\mathrm{T}}^{\mathrm{miss}}$, MC modelling, and f_{EW} are considered fully correlated among the four predictions for the following reasons: for all the predictions the same tool is used to get the JES/$E_{\mathrm{T}}^{\mathrm{miss}}$ uncertainty, the MC modelling uncertainty is conservatively taken to be 3% (Sec. 8.4), and f_{EW} is obtained using the same simulation samples for all various control regions. The uncertainties on the scale factors, and lepton energy scale and resolution are assumed to be fully correlated between the two predictions from Z($\mu\mu$)+jets and W($\mu\nu$)+jets, or from Z(ee)+jets and W($e\nu$)+jets, and fully uncorrelated among the predictions from the electron and muon channels. The data statistical uncertainties are assumed to be uncorrelated among all the four predictions, as the four control regions are orthogonal. When treating correlations among the simulation statistical uncertainties, these uncertainties are further decomposed to the uncertainties on the numerators and denominators of various simulation-based correction factors, due to the fact that the correlations among different channels are sometimes only on the denominator of the correction factor, and sometimes only on the numerator. For example correlations between W($\tau\nu$)+jets and Z($\nu\nu$)+jets background predictions from the W($\mu\nu$)+jets control region are only on the denominators of the corresponding correction factors, as they both use the same W($\mu\nu$)+jets simulation samples for the denominator. This is the case for correlations between the two Z($\nu\nu$)+jets predictions from the W and Z control regions, as they both use the same Z($\nu\nu$)+jets simulation samples for the numerator.

The combination is first done using the Best Linear Unbiased Estimator (BLUE) method [54]. The method is based on the minimisation of the χ^2 defined[2] as:

$$\chi^2 = \left\{ x \begin{pmatrix} 1 \\ 1 \\ ... \\ 1 \end{pmatrix} - \begin{pmatrix} x_1 \\ x_2 \\ ... \\ x_N \end{pmatrix} \right\}^T V^{-1}(\vec{x}) \left\{ x \begin{pmatrix} 1 \\ 1 \\ ... \\ 1 \end{pmatrix} - \begin{pmatrix} x_1 \\ x_2 \\ ... \\ x_N \end{pmatrix} \right\} = [x\vec{e} - \vec{x}]^T . V^{-1}(\vec{x}) . [x\vec{e} - \vec{x}], \tag{10.5}$$

where $\vec{e}$ is a vector with all the components equal to unity, x_i, $(i = 1, ..., N)$ are the N available predictions (4 here), and V is the covariance matrix.

The minimisation of the χ^2 results in the following solution:

[2]This is the generalisation of the following definition of χ^2 for N independent measurements and one random variable: $\chi^2 = \sum\limits_{i=1}^{N} (\frac{x - x_i}{\sigma_i})^2$.

$$x = \frac{\vec{e}^T.(V^{-1}.\vec{x})}{\vec{e}^T.(V^{-1}.\vec{e})} \quad (10.6)$$

$$\sigma_x = \sqrt{\frac{1}{\vec{e}^T.(V^{-1}.\vec{e})}} \quad (10.7)$$

This equation can also be written in the following form, where $\vec{w}$ is the vector of weights:

$$\vec{w} = \frac{V^{-1}.\vec{e}}{\vec{e}^T.(V^{-1}.\vec{e})} \quad (10.8)$$

$$x = \vec{w}^T.\vec{x} \quad (10.9)$$

$$\sigma_x = \sqrt{\vec{w}^T.V.\vec{w}} \quad (10.10)$$

However, the vector of weights as obtained from the BLUE method (Eq. 10.8) can sometimes have negative components for some of the contributions if they have large uncertainties compared to the other available predictions. As an example, in the current analysis the total uncertainties on the predictions from electron channels are higher than those from muon channels, due to a slight difference in the way the correction factors and their variations are applied to each of the control regions. This consequently gives a combined value for x that can be outside the range of the available measurements. In order to avoid such negative weights, another set of weights are defined that are always positive by construction:

$$w_i = \frac{\frac{1}{(\sigma_i^{total})^2}}{\Sigma_j \frac{1}{(\sigma_j^{total})^2}} \quad (10.11)$$

where σ_i^{total} is the total sum in quadrature of statistical and systematic uncertainties on prediction i.

The resulting uncertainties are of course higher than those when using the BLUE weights, as the latter are designed to minimise the χ^2 in Eq. 10.5.

The results of the combination using these two different set of weights are shown in

Table 10.1. The ones derived from simple weights are used as the final results, in order to avoid the problem of negative weights as discussed above.

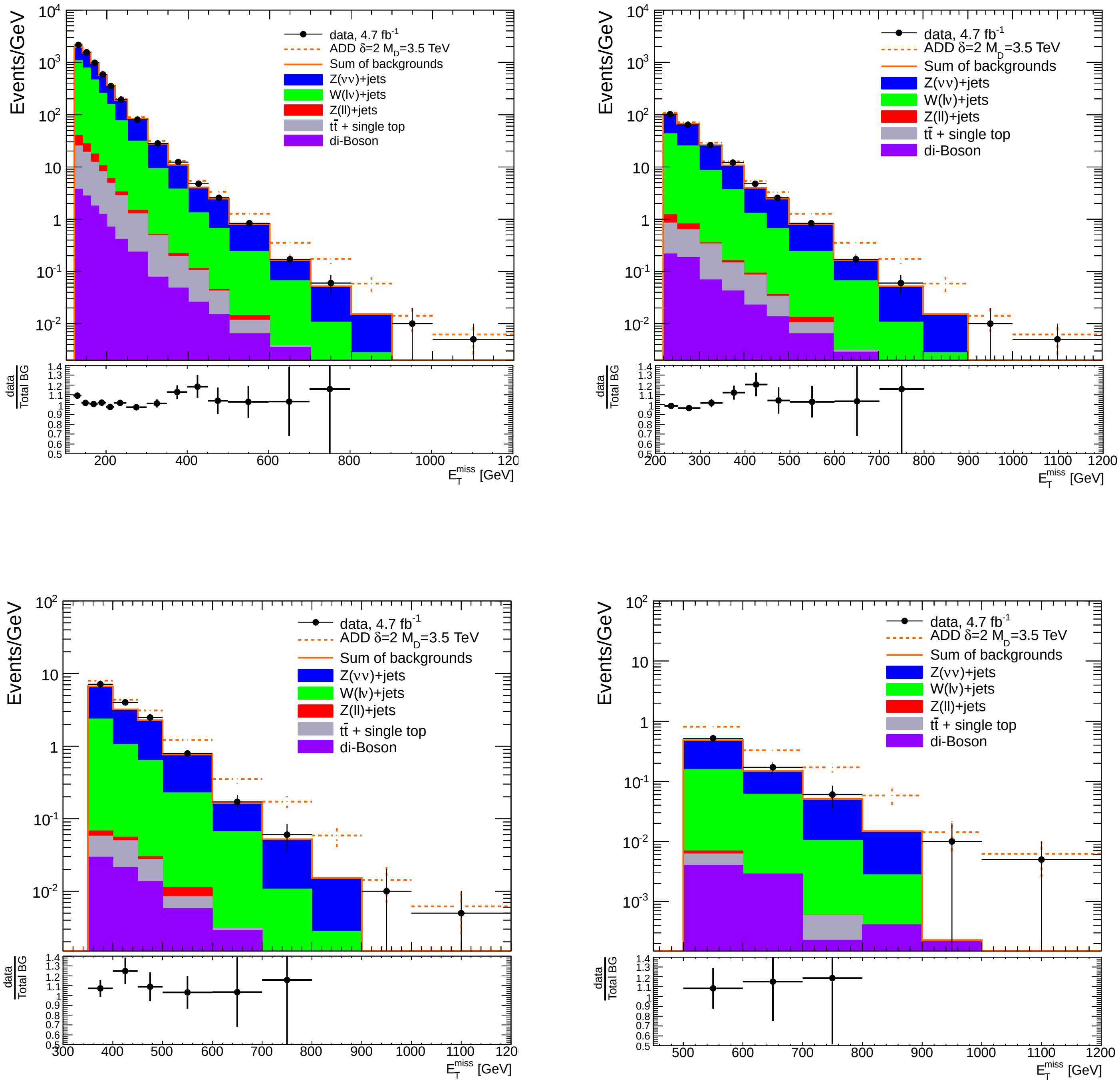

Figure 10.1: Comparisons between observed data and the total expected background, as function of $E_{\mathrm{T}}^{\mathrm{miss}}$, in signal region 1 (upper left), 2 (upper right), 3 (lower left) and 4 (lower right). An excluded ADD signal for n=2 and M_D = 3.5 TeV is also shown. The contribution of the QCD multi-jet and non-collision backgrounds are not included. Excess of data events in the first few bins is due to the contribution of multi-jet QCD events. Events in each bin are divided by the bin width. The errors are statistical only.

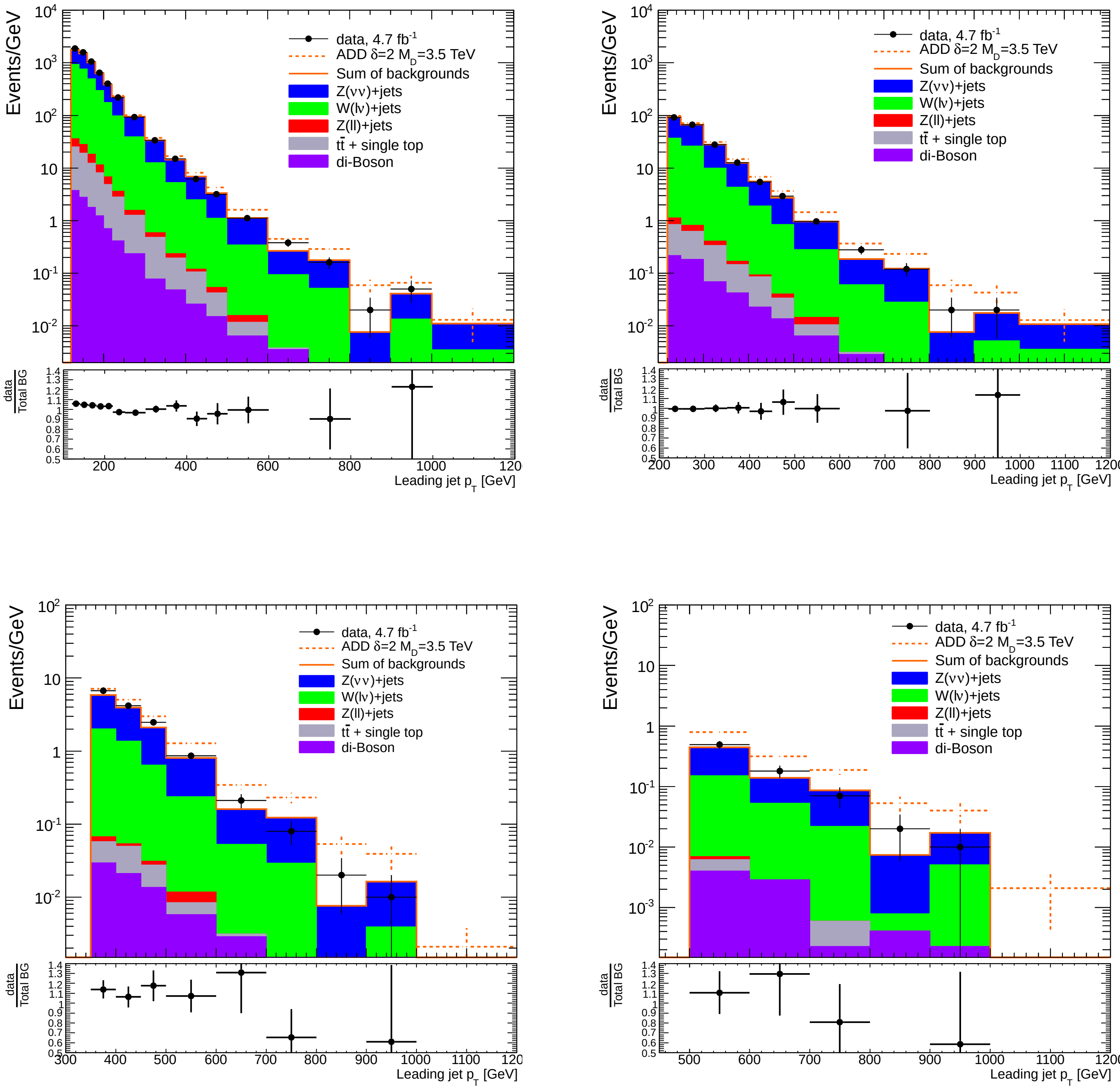

Figure 10.2: Comparisons between observed data and the total expected background, as function of the leading jet p_{T}, in signal region 1 (upper left), 2 (upper right), 3 (lower left) and 4 (lower right). An excluded ADD signal for n=2 and $M_D = 3.5$ TeV is also shown. The contribution of the QCD multi-jet and non-collision backgrounds are not included. Events in each bin are divided by the bin width. The errors are statistical only.

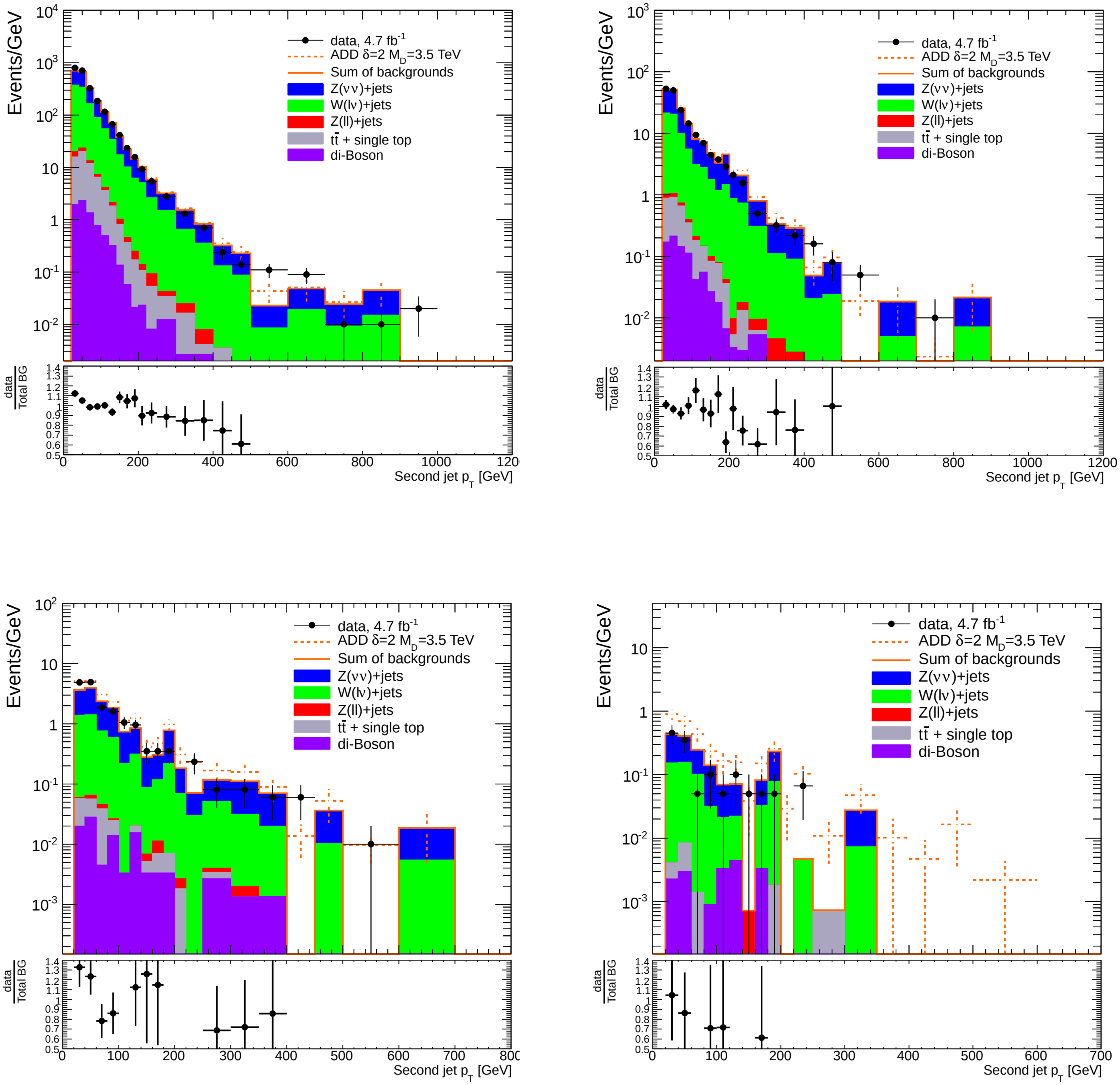

Figure 10.3: Comparisons between observed data and the total expected background, as function of the second jet p_{T}, in signal region 1 (upper left), 2 (upper right), 3 (lower left) and 4 (lower right). An excluded ADD signal for n=2 and $M_D = 3.5$ TeV is also shown. The contribution of the QCD multi-jet and non-collision backgrounds are not included. Events in each bin are divided by the bin width. The errors are statistical only.

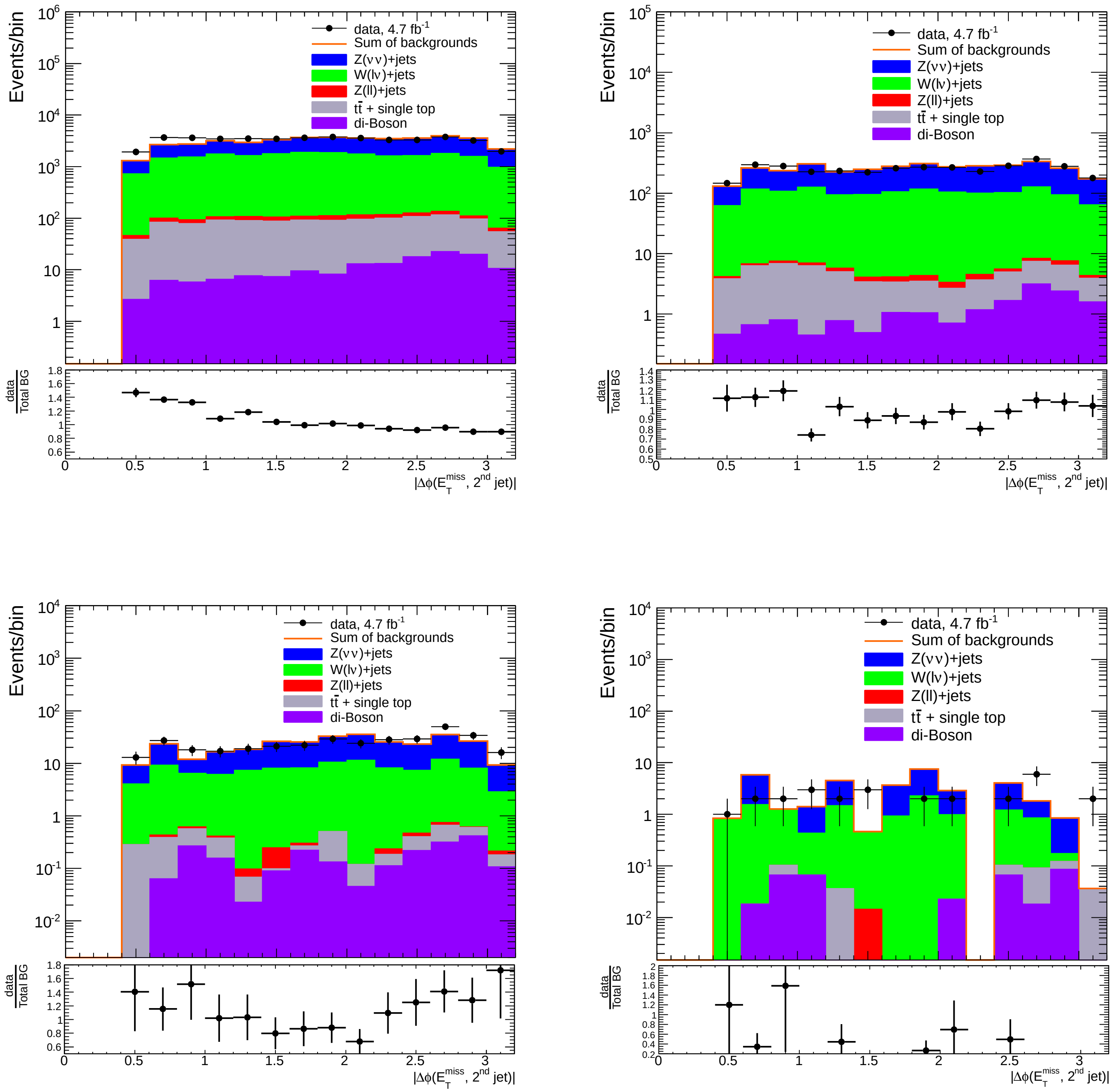

Figure 10.4: Comparisons between observed data and the total expected background, as function of the $|\Delta\phi|$ between the second jet and the $E_{\mathrm{T}}^{\mathrm{miss}}$, in signal region 1 (upper left), 2 (upper right), 3 (lower left) and 4 (lower right). The contribution of the QCD multi-jet and non-collision backgrounds are not included. Events in each bin are not divided by the bin width. The errors are statistical only.

Chapter 11

Theoretical Interpretations

In the absence of any excess of events beyond the Standard Model expectations (Table 10.1), the results are interpreted in the context of the Large Extra Dimensions ADD scenario, and the pair production of WIMPs as dark matter candidates.

11.1 ADD Signal Acceptance

The signal acceptance is shown in Table 11.1 for various numbers of extra dimensions. It includes the acceptance at truth level, reconstruction efficiency, and detector resolution all in one factor. This acceptance is based on the signal samples with a p_{T} cut of 80 GeV at the generator level. Since M_D is a multiplicative factor in the cross section calculations, it can be factored out of the cross section, and is thus cancelled in the acceptance calculation. This is shown in Fig. 11.1 for the p_{T} and $E_{\mathrm{T}}^{\mathrm{miss}}$ distributions of two different values of M_D for n=2. The kinematic distributions do not depend on M_D, within statistical fluctuations. Hence, for each value of number of extra dimensions n, the same signal acceptance is used for different values of M_D. However, there is a residual dependency due to the fact that the graviton mass phase space is constrained to be below the scale M_D, above which the calculations of the effective field theory are not reliable.

The signal acceptance also depends on the number of extra dimensions, and is slightly

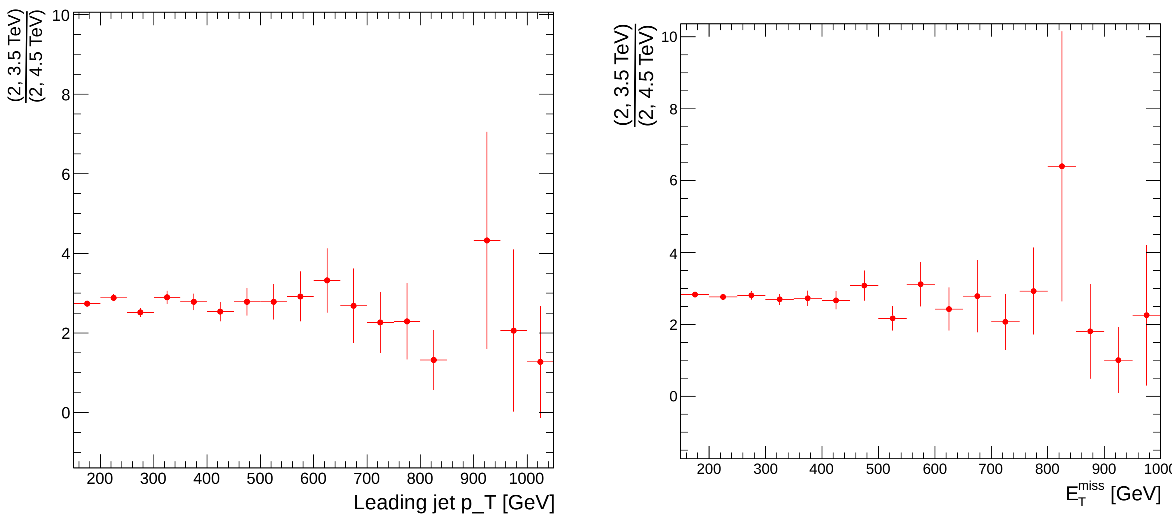

Figure 11.1: Ratio of the leading jet p_{T} (left) and $E_{\mathrm{T}}^{\mathrm{miss}}$ (right) distributions of the two ADD signal points (2, 3.5 TeV) and (2, 4.5 TeV) in (n, M_{D}). The ratio plots are flat within statistical fluctuations, showing that the kinematic distributions are almost M_D − independent for each value of n.

higher for larger numbers of extra dimensions. This is explained by the fact that for larger numbers of extra dimensions, the graviton mass distribution has more entries at high mass values, as shown on the left distribution of Fig. 11.2. This is equivalent to more graviton p_{T} dilution in the extra dimensions, which results in softer graviton p_{T} or leading jet p_{T} in 4 dimensions. However, the $\hat{s}$ of the process becomes larger for higher number of extra dimension, as shown on the right distribution of Fig. 11.2, which is not completely cancelled by the former effect. As a result, the final signal acceptance slightly increases for higher values of number of extra dimension, as can be seen in Fig. 11.3 from the ratio of number of events with n=6 over number of events with n=3 extra dimensions, in bins of the leading jet p_{T}. A slight increase is observed for higher leading jet p_{T} values.

Figure 11.4 shows the distributions of the leading jet p_{T} and $E_{\mathrm{T}}^{\mathrm{miss}}$ for 2-6 extra dimensions after the selection cuts of the first signal region.

$(n,\, M_D)$	Region1	Region2	Region3	Region4
(2, 3.5)	0.288 ± 0.002	0.084 ± 0.001	0.0236 ± 0.0006	0.0067 ± 0.0003
(2, 4.5)	0.288 ± 0.002	0.085 ± 0.001	0.0242 ± 0.0006	0.0071 ± 0.0003
(3, 2.5)	0.312 ± 0.002	0.109 ± 0.001	0.0362 ± 0.0008	0.0111 ± 0.0004
(4, 2.5)	0.321 ± 0.002	0.127 ± 0.001	0.0456 ± 0.0009	0.0151 ± 0.0005
(5, 2.5)	0.326 ± 0.002	0.134 ± 0.001	0.0502 ± 0.0009	0.0179 ± 0.0005
(6, 2.5)	0.325 ± 0.002	0.137 ± 0.001	0.0544 ± 0.0009	0.0198 ± 0.0005

Table 11.1: ADD signal acceptance, using CTEQ6.6 PDF set, for the four signal regions. The errors are statistical only.

11.2 Signal Systematic Uncertainties

Theoretical systematic uncertainties consisting of uncertainties on the choice of Parton Distribution Functions (PDF), Initial and Final State Radiation (ISR/FSR), and choice of the renormalisation and factorisation scale, as well as experimental systematic uncertainties, including uncertainties on JES/$E_{\mathrm{T}}^{\mathrm{miss}}$,luminosity, and trigger are considered, as explained in the following paragraphs. The effect of each source is investigated for different numbers of extra dimensions.

Parton distribution functions The default PDF set used in simulation signal samples is MRST LO**. To study the PDF uncertainties, CTEQ6.6 and its 44 error sets are used[1]. Tables 11.2 and 11.3 list the PDF uncertainties on the ADD signal acceptance and cross section for various number of extra dimensions. The final uncertainty is estimated using the Hessian method as shown in Eq. 11.1 - 11.3, and is divided by 1.645 to convert the 90% CL uncertainties adopted by the CTEQ collaboration to the 68%CL corresponding to a 1σ deviation. The maximum of the up and down variations is then

[1] The PDF re-weighting tool is used to get the signal yields corresponding to this PDF set and its error eigenvectors. They correspond to `mstp(51) = 10550-10594` in `PYTHIA`.

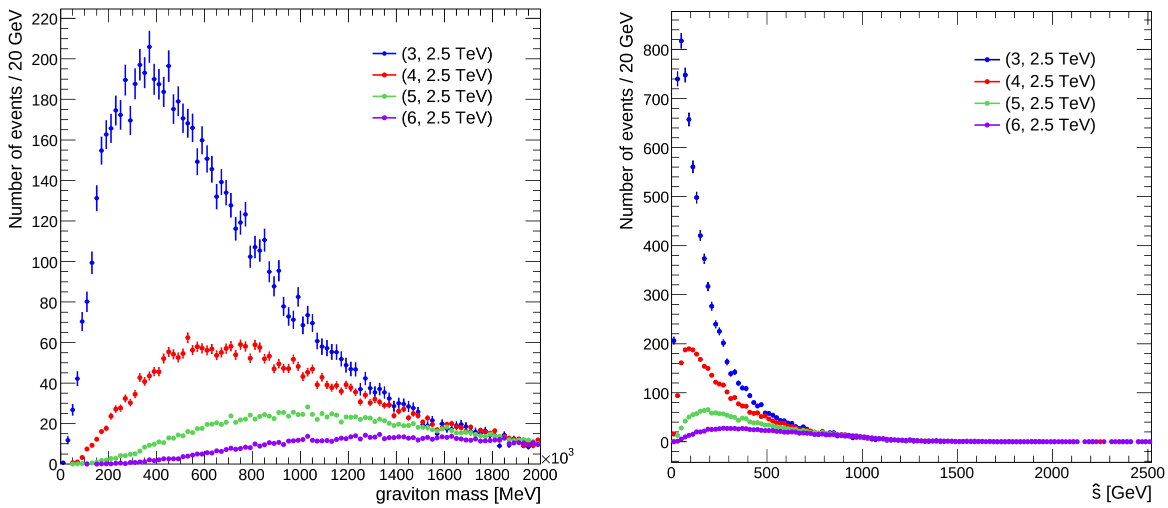

Figure 11.2: Graviton mass distributions (Left), and $\hat{s}$ distributions (Right), for n = 3 - 6 extra dimensions, and $M_D = 2.5$ TeV, normalised to 4.7 fb^{-1} integrated luminosity. The samples have p_{T}^{Cut} at the generator level of 80 GeV, and with the centre of mass energy of 7 TeV.

quoted as the final uncertainty for each signal region. In summary:

$$\Delta^{up}_{\mathrm{PDF}} = \sqrt{\sum_{i=1}^{i=22} (max\left\{x_i^+ - x^0, x_i^- - x^0, 0\right\})^2} \tag{11.1}$$

$$\Delta^{down}_{\mathrm{PDF}} = \sqrt{\sum_{i=1}^{i=22} (max\left\{x^0 - x_i^+, x^0 - x_i^-, 0\right\})^2} \tag{11.2}$$

$$\Delta_{\mathrm{PDF}} = max\left\{\Delta^{up}_{\mathrm{PDF}}, \Delta^{down}_{\mathrm{PDF}}\right\}, \tag{11.3}$$

where the sum is over all the PDF error pairs (22 pairs for CTEQ6.6), x_i^+ is the up variation of error pair i, x_i^- its down variation, and x^0 the central value (x is the variable of interest, such as signal yield or cross section).

Initial and final state radiation To investigate the effect of QCD ISR/FSR on signal acceptance, Monte Carlo samples with more or less ISR/FSR have been generated and used at truth level. This is done by varying the values of `parp64`, `parp67` for ISR and `parp72`, `parj82` for FSR in the `ExoGraviton` generator through the jobOption file

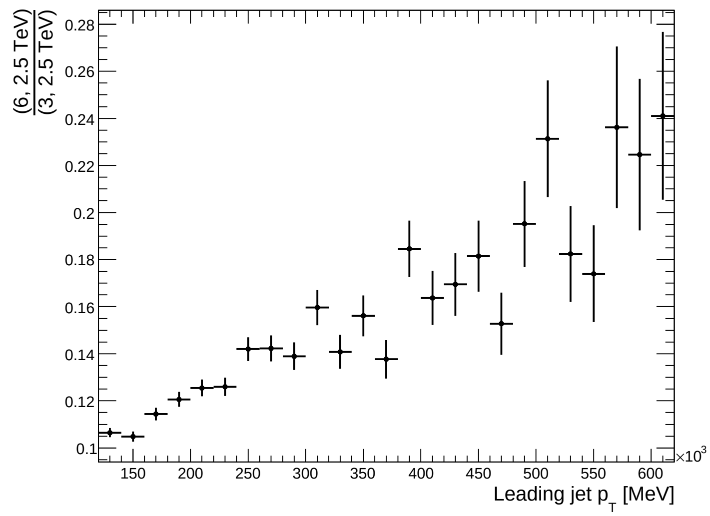

Figure 11.3: Ratio of number of events with n=6 over number of events with n = 3 extra dimensions, normalised to 4.7 fb^{-1} integrated luminosity, in bins of the leading jet p_{T}. No signal selection cut is applied. The samples have p_{T}^{Cut} at the generator level of 80 GeV, with a centre of mass energy of 7 TeV, and $M_D = 2.5$ TeV.

(Appendix. B), as listed in Table 11.4. ISR/FSR can affect the acceptance mainly due to the third jet veto. Tables 11.5 and 11.6 list the relative uncertainties on the signal yield due to less and more level of ISR/FSR, respectively. The maximum deviation is considered for the final uncertainty due to ISR/FSR.

Renormalisation and factorisation scales The renormalisation and factorisation scales enter in the matrix elements, and also the parton distribution functions[2]. At the leading order, they enter the cross section calculations via the running strong coupling constant α_S, and the PDF set. The value used for both scales in the `ExoGraviton` package is $\sqrt{\frac{1}{2}m_{kk}^2 + p_T^2}$, where m_{kk} is the mass of the graviton mode, and p_{T} is the transverse momentum of the recoiling parton. To investigate the relative uncertainty due to the choice of the scales, this value is changed to half and two times its central value, and the

[2]Via `PYPDFU(2212,X1,Q2,XP1)` in the generator.

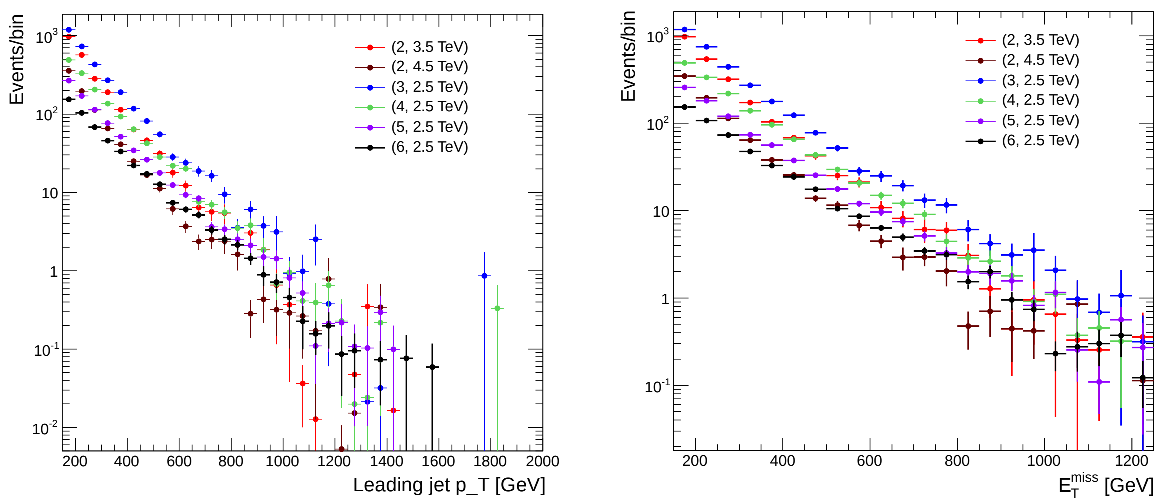

Figure 11.4: Distributions of the leading jet p_{T} and $E_{\mathrm{T}}^{\mathrm{miss}}$ for various $(n,\ M_D)$ ADD phase space points, after the selection cuts of the first signal region, normalised to 4.7 fb^{-1} integrated luminosity. Signal cross sections at LO are used, with the CTEQ6.6 PDF set.

resulting signal yield is compared to the central value at truth, after being normalised to the new cross sections, corresponding to the new choice of the scales. This will take into account the impact on both the signal acceptance and cross section. The maximum deviation is considered for the final uncertainty. Table 11.7 lists the corresponding relative uncertainties on the signal yield.

$(n,\ M_D)$	Region1	Region2	Region3	Region4
(2, 3.5)	0.47	1.52	2.67	3.88
(3, 2.5)	1.29	0.79	1.50	2.58
(4, 2.5)	2.65	1.73	1.33	1.75
(5, 2.5)	4.17	3.22	2.26	1.82
(6, 2.5)	5.42	4.58	3.54	2.75

Table 11.2: PDF uncertainty on the ADD signal acceptance, in %.

(n, M_D)	up variation	down variation
(2, 3.5)	4.00	3.55
(3, 2.5)	6.71	5.51
(4, 2.5)	9.30	7.26
(5, 2.5)	11.43	8.61
(6, 2.5)	13.17	9.64

Table 11.3: Asymmetric PDF uncertainties on the ADD signal cross section, in %.

parameter	less ISR/FSR	more ISR/FSR
`parp64`	4.08	1.02
`parp67`	0.75	1.75
`parp72`	0.2635	0.7905
`parj82`	1.66	0.5

Table 11.4: Values of ISR/FSR parameters used for uncertainty studies.

Jet energy scale, and $E_{\mathrm{T}}^{\mathrm{miss}}$ The uncertainty on the JES and $E_{\mathrm{T}}^{\mathrm{miss}}$ is calculated by varying the p_{T} of all the jets above 20 GeV in p_{T} in the event up and down by one standard deviation on the jet energy scale, and propagating the vector sum of this change to $E_{\mathrm{T}}^{\mathrm{miss}}$. This will change both the value and direction of $E_{\mathrm{T}}^{\mathrm{miss}}$. The mono-jet kinematic cuts are then applied to the new jets and $E_{\mathrm{T}}^{\mathrm{miss}}$. In the case of asymmetric errors, the maximum deviation is considered. Table 11.8 shows the resulting relative uncertainties on the ADD signal yield.

Luminosity There is a 3.9% uncertainty on the total integrated luminosity [55], [56].

Trigger efficiency There is an average difference of 0.66% between the trigger efficiencies obtained from data and simulation (Chapter 7), considered as a source of systematic

(n, M_D)	Region1	Region2	Region3	Region4
(2, 3.5)	5.99	2.73	6.70	8.68
(3, 2.5)	7.62	7.89	7.11	11.70
(4, 2.5)	6.87	3.30	2.76	6.00
(5, 2.5)	5.38	4.81	6.19	7.74
(6, 3.5)	4.84	3.20	2.84	6.40

Table 11.5: Uncertainties on the ADD signal yield due to less ISR/FSR, in %.

(n, M_D)	Region1	Region2	Region3	Region4
(2, 3.5)	2.95	1.21	3.09	6.52
(3, 2.5)	4.07	0.87	1.09	7.68
(4, 2.5)	3.09	2.97	0.54	3.72
(5, 2.5)	2.52	5.31	4.12	13.78
(6, 3.5)	3.18	3.13	0.44	9.61

Table 11.6: Uncertainties on the ADD signal yield due to more ISR/FSR, in %.

uncertainty on the signal yield.

PileUp The effect of pile-up is studied by re-weighting the signal samples using the `PileupReweighting` tool[3]. This results in $\sim 0.15\%$ uncertainty on the signal yield. Hence this uncertainty is neglected. Figure 11.5 shows signal acceptance as a function of the average number of interactions per bunch-crossing, and number of good vertices in the event. The two distributions are flat within statistical fluctuations.

Tables 11.9 – 11.12 list the total uncertainty on the ADD signal yield in the 4 signal regions, due to various sources explained above, as well as the statistical uncertainty due

[3] https://twiki.cern.ch/twiki/bin/viewauth/AtlasProtected/PileupReweighting

(n, M_D)	Region1		Region2		Region3		Region4	
(2, 3.5)	19.06	23.67	15.66	29.65	18.44	30.28	22.51	40.15
(3, 2.5)	19.03	25.25	20.44	25.18	31.36	11.07	31.22	18.18
(4, 2.5)	20.59	25.74	22.50	25.85	23.89	24.08	23.74	68.09
(5, 2.5)	20.44	25.88	19.72	30.23	17.91	36.25	35.52	47.26
(6, 2.5)	20.44	25.13	20.53	26.96	18.90	33.77	8.11	48.97

Table 11.7: Relative scale uncertainty (in %) on the ADD signal yield in each region, when changing the scale up and down, respectively.

(n, M_D)	Region1	Region2	Region3	Region4
(2, 3.5)	4.13	7.42	9.83	12.30
(3, 2.5)	3.11	5.92	8.02	9.43
(4, 2.5)	2.39	4.63	7.68	8.68
(5, 2.5)	4.88	4.49	6.92	10.43
(6, 2.5)	6.65	3.96	5.60	9.45

Table 11.8: Relative uncertainty in %, due to the jet energy scale and $E_{\mathrm{T}}^{\mathrm{miss}}$ on the ADD signal yield.

to the limited statistics of the simulation signal samples.

11.3 The CL$_{\mathrm{S}}$ Method

Upper limits are set on $\sigma \times A \times \epsilon$, where A is the acceptance of the signal selection cuts at the truth level, and ϵ is the reconstruction efficiency of the mono-jet cuts, defined as:

$$A = \frac{\text{Number of events passing the jets and } E_{\mathrm{T}}^{\mathrm{miss}} \text{ cuts at the truth level}}{\text{Total number of events in the phase space generated for the sample}} \tag{11.4}$$

$$\epsilon = \frac{\text{Number of events passing all the mono jet cuts at the reconstructed level}}{\text{Number of events passing the jets and } E_{\mathrm{T}}^{\mathrm{miss}} \text{ cuts at the truth level}} \sim 83\% \tag{11.5}$$

$A \times \epsilon$ as defined in this way is equivalent to the acceptance at the reconstruction

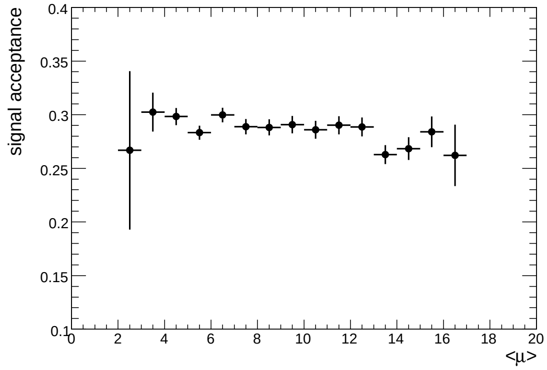

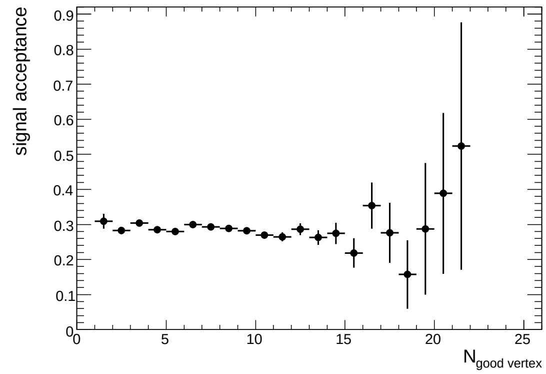

Figure 11.5: ADD signal acceptance as a function of the average number of interactions per bunch-crossing (Left), and the number of good vertices in the event (Right).

n	PDF	ISR/FSR	Scale	JES/$E_{\mathrm{T}}^{\mathrm{miss}}$	Luminosity	Trigger	Total (syst.)	MC (stat.)
2	4.00	5.99	23.67	4.13	3.9	0.66	25.39	0.79
3	6.71	7.62	25.25	3.11	3.9	0.66	27.68	0.73
4	9.30	6.87	25.74	2.39	3.9	0.66	28.59	0.72
5	11.43	5.38	25.88	4.88	3.9	0.66	29.48	0.71
6	13.17	4.84	25.13	6.65	3.9	0.66	29.80	0.72

Table 11.9: Relative systematic uncertainties from each source, along with the total relative systematic and statistical uncertainties, (in %), on the ADD signal yield, $\sigma \times A \times \epsilon$, in the first signal region.

level listed in Table 11.1. To calculate the upper limits on the signal yield, RooStats $\mathrm{CL_S}$ prescription [57] is used [4]. This produces probability density functions which can be used to derive confidence intervals.

The $\mathrm{CL_S}$ method uses the ratio of confidence levels of two hypotheses of interest: the null, or background only hypothesis, and the alternative hypothesis which is favoured when the null hypothesis has been rejected to a sufficient degree. It normalises the confidence level of signal + background hypothesis, $\mathrm{CL_{S+B}}$, to the confidence level for the background only hypothesis, $\mathrm{CL_B}$. This approach is used to deal with situations where the presence of background in data can result in an unphysical estimation of the

[4]Via the `HistFitter` package: https://twiki.cern.ch/twiki/bin/viewauth/AtlasProtected/SusyFitter

n	PDF	ISR/FSR	Scale	JES/$E_{\mathrm{T}}^{\mathrm{miss}}$	Luminosity	Trigger	Total (.syst)	MC (stat.)
2	4.00	2.73	29.65	7.42	3.9	0.66	31.20	1.47
3	6.71	7.89	25.18	5.92	3.9	0.66	28.14	1.25
4	9.30	3.30	25.85	4.63	3.9	0.66	28.33	1.18
5	11.43	5.31	30.23	4.49	3.9	0.66	33.29	1.15
6	13.17	3.20	26.96	3.96	3.9	0.66	30.69	1.13

Table 11.10: Relative systematic uncertainties from each source, along with the total relative systematic and statistical uncertainties, (in %), on the ADD signal yield, $\sigma \times A \times \epsilon$, in the second signal region.

n	PDF	ISR/FSR	Scale	JES/$E_{\mathrm{T}}^{\mathrm{miss}}$	Luminosity	Trigger	Total (.syst)	MC (stat.)
2	4.00	6.70	30.28	9.83	3.9	0.66	33.02	2.82
3	6.71	7.11	31.36	8.02	3.9	0.66	34.04	2.20
4	9.30	2.76	24.08	7.68	3.9	0.66	27.36	2.03
5	11.43	6.19	36.25	6.92	3.9	0.66	39.33	1.93
6	13.17	2.84	33.77	5.60	3.9	0.66	36.40	1.85

Table 11.11: Relative systematic uncertainties from each source, along with the total relative systematic and statistical uncertainties, (in %), on the ADD signal yield, $\sigma \times A \times \epsilon$, in the third signal region.

model parameter, for example, when the rate of observed data events is much lower than the expected number of background events.

In summary, $\mathrm{CL_S}$ is defined as:

$$\begin{aligned}
\mathrm{CL_s} &= \frac{\int_{-\infty}^{t_{Obs}} f(t_\mu|\mu)dt}{\int_{-\infty}^{u_{Obs}} g(u_\mu|\mu)du} && (11.6)\\
t_\mu &= -2\ln Q_1(\mu) && (11.7)\\
u_\mu &= -2\ln Q_2(\mu) && (11.8)\\
Q_1(\mu) &= \frac{\mathrm{L_{S+B}}(\mu, \hat{\hat{\theta}})}{\mathrm{L_{S+B}}(\hat{\mu}, \hat{\theta})} && (11.9)\\
Q_2(\mu) &= \frac{\mathrm{L_B}(\mu, \hat{\hat{\beta}})}{\mathrm{L_B}(\hat{\mu}', \hat{\beta})}, && (11.10)
\end{aligned}$$

n	PDF	ISR/FSR	Scale	JES/$E_{\mathrm{T}}^{\mathrm{miss}}$	Luminosity	Trigger	Total (.syst)	MC (stat.)
2	4.00	8.68	30.28	12.30	3.9	0.66	34.28	5.24
3	6.71	11.70	31.36	9.43	3.9	0.66	35.64	4.01
4	9.30	6.00	24.08	8.68	3.9	0.66	28.17	3.56
5	11.43	13.78	36.25	10.43	3.9	0.66	41.94	3.27
6	13.17	9.61	33.77	9.45	3.9	0.66	38.87	3.13

Table 11.12: Relative systematic uncertainties from each source, along with the total relative systematic and statistical uncertainties, (in %), on the ADD signal yield, $\sigma \times A \times \epsilon$, in the fourth signal region.

where f and g are the probability distribution functions of t_μ and u_μ under the assumption of the signal strength μ, and are obtained by doing pseudo-experiments as explained later. The quantity μ is the signal strength on which the upper limit will be set, and θ and β represent the nuisance parameters of the S+B and B hypotheses. Here $\hat{\hat{\theta}}$ and $\hat{\hat{\beta}}$ denote the values of θ and β that maximise $\mathrm{L}_{\mathrm{S+B}}$ and L_{B}, respectively, for a specified $\mu = 1$. The denominators of Q_1 and Q_2 are unconditional maximised likelihood functions, i.e., $\hat{\mu}$ and $\hat{\theta}$ maximise $\mathrm{L}_{\mathrm{S+B}}$, and $\hat{\mu}'$ and $\hat{\beta}$ maximise L_{B}. Considering the way Q_1 and Q_2 are defined , t_μ and u_μ each express how consistent the model with a variable μ is with the $\mu = 1$ model.

We consider the simple case of a single channel with one type of signal with S events and total background with B events. For a counting experiment such as the present analysis, the shapes of the signal and background distributions are not used to set exclusion limits. The parameter of interest on which the limit will be set is the signal strength μ, with $\mu = 0$ corresponding to the background–only hypothesis, and $\mu = 1$ being the nominal signal + background hypothesis. The corresponding signal yield is $\mu \times \sigma \times A \times \epsilon \times \mathcal{L}$, where σ is the signal cross section, and $\mathcal{L}$ is the integrated luminosity. In the following, the procedure of calculating $\mathrm{L}_{\mathrm{S+B}}$ is presented as an example. The term L_{B} can be obtained similarly.

The probability of observing n events in data when the expected number of events is

$\mu\mathrm{S} + \mathrm{B}$ is :

$$P(n, \theta|\mu, \alpha) = P(\theta|\alpha) \star Pois(n|\mu\mathrm{S} + \mathrm{B}) = P(\theta|\alpha) \star \frac{(\mu\mathrm{S} + \mathrm{B})^n e^{-(\mu\mathrm{S} + \mathrm{B})}}{n!}, \qquad (11.11)$$

where $Pois$ is the Poisson distribution, α is the uncertain (nuisance) parameter with a probability distribution $P(\theta|\alpha)$ with variable θ whose value is specified from a pseudo–experiment. The product, $\star$, represents a convolution. The term $(\mu\mathrm{S} + \mathrm{B})$ is the value of signal + background after taking into account the effect of uncertainties, θ. Assuming a Gaussian distribution for θ, centred at zero with a standard deviation equal to unity:

$$P(n, \theta|\mu, \alpha) = \frac{1}{\sqrt{2\pi}} e^{-\theta^2} \star \frac{(\mu\mathrm{S} + \mathrm{B})^n e^{-(\mu\mathrm{S} + \mathrm{B})}}{n!}. \qquad (11.12)$$

Assuming the number of observed data events to be fixed, this equation depends on μ and is called the likelihood function, $L_{\mathrm{S+B}}(\mu)$. The value of θ is obtained according to its Gaussian probability distribution function from each pseudo-experiment, and is then used to fluctuate each μS+B or B . The fits of Eq. 11.9 and 11.10 are performed for each pseudo-experiment. By performing several pseudo-experiments, the distributions of t_μ and u_μ in Eq. 11.7 and 11.8 are obtained. These are the f and g in Eq. 11.6.

A signal hypothesis is considered excluded at the confidence level γ if:

$$1 - \mathrm{CL_S} \leq \gamma \qquad (11.13)$$

or:

$$1 - \mathrm{CL_S} = 1 - \frac{\int_{-\infty}^{t_{Obs}} f(t_\mu|\mu) dt}{\int_{-\infty}^{u_{Obs}} g(u_\mu|\mu) du} \leq \gamma. \qquad (11.14)$$

Solving the inequality gives an upper limit on the signal strength, μ, above which the signal is excluded at γ confidence level. This upper limit gives an upper bound on the signal yield, which is then used to set limits on theory parameters.

11.4 Limits on M_D

Table 11.13 summarises the 95% CL model-independent upper limits on $\sigma \times A \times \epsilon$ for each of the 4 signal regions, using the Z($\nu\nu$)+jets determined from the combination of the predictions based on W($\mu\nu$)+jets, Z($\mu\mu$)+jets, W($e\nu$)+jets, and Z(ee)+jets control regions, using simple weights, corresponding to BG (4) in Table 10.1. The 95% CL limits refer to the fact that there is a 95% probability that the number of new physics events contained in the observed data is below the obtained limit, in order for the background + signal hypothesis to be consistent with the observed data. For these model-independent limits, only the luminosity uncertainty on the signal strength is considered. No correlation for the JES and $E_{\mathrm{T}}^{\mathrm{miss}}$ uncertainties between signal and background is assumed, and the simulation statistical uncertainty of the signal yield has been set to zero. To get the observed and expected lower limits on the fundamental gravity scale of the model, M_D, correlations of the JES and $E_{\mathrm{T}}^{\mathrm{miss}}$ uncertainties between signal and background, as well as luminosity, trigger, and simulation statistical uncertainties on the signal yield (as presented in Tables 11.9 - 11.12) are accounted for. The resulting upper limit on $\sigma \times A \times \epsilon$ is then used to set the lower limits on M_D. For each value of number of extra dimensions, a central value for the observed lower limit on M_D is computed ignoring signal theoretical uncertainties (PDF, ISR/FSR, Q Scale). As shown in Figure 11.6, this refers to the intersection of the red horizontal line with each of the signal central theoretical curves. The red horizontal line representing the 95% CL observed upper limit on $\sigma \times A \times \epsilon$ is obtained after taking into account the JES and $E_{\mathrm{T}}^{\mathrm{miss}}$ uncertainties correlations between signal and background, as well as luminosity, trigger, and simulation statistical uncertainties on the signal yield for each n. Shown on the plot is only the horizontal line corresponding to n=2. There are 5 such lines in total, for n = 2 to 6. The upper and lower bands on this central value are then computed considering the total signal theoretical uncertainties. These are the intersections of the red horizontal line with the edges of the error bands around each of the theoretical curves for an M_D value. The expected lower limits on M_D are calculated without considering any signal theoretical uncertainty. They are the intersection of the dark blue horizontal line with each of the signal theoretical curves. The $\pm 1\sigma_{BG}$ error bands on the expected limits are the variations expected from statistical fluctuations and experimental systematic uncertainties on the Standard Model background and signal processes, and the corresponding limits are the intersection of the upper and lower edges of the grey shaded area with each of the central lines of the signal theoretical curves. The resulting 95% CL expected and observed lower limits on M_D are shown in Figure 11.7, and the values are quoted in Table 11.14, using the signal cross sections at Leading Order (LO).

Assuming compactification of the extra spatial dimensions on a torus, M_D can be related to the size of the extra dimensions via [22]:

$$R = \frac{1}{M_D}.[\frac{M_P}{\sqrt{8\pi}M_D}]^{\frac{2}{n}} \tag{11.15}$$

The 95% CL observed upper limits at LO on the size of the extra dimensions are listed in Table 11.15, using the M_D values corresponding to the central line of the observed limits.

The limits are based on the calculations of an effective theory, which is not valid for $\hat{s} > M_D^2$ (Sec. 2.2.2). The difference in signal cross section between the complete and the truncated (where events with $\hat{s} > M_D^2$ are suppressed) samples is listed in Table 11.16 for different number of extra dimensions and for the fourth signal region. To mimic the p_{T} cut on the leading jet in a signal region, the p_{T}^{cut} parameter of the generator is set to that of a specific signal region. The effect of truncation gets larger for higher values of n, as the signal acceptance is higher. Consequently more events are in the high-$\hat{s}$ part of the phase space, resulting in a larger difference between the complete and truncated cross sections. The large difference between complete and truncated cross sections in some regions indicates that the limits obtained from the model considered are highly dependent on the actual calculations of the effective theory, and do not reflect genuine constraints imposed by data on the existence of extra dimensions in these regions of the parameter space of the theory.

QCD higher order corrections on the LED model predictions are important and can increase the cross section by $\sim 10 - 20$ % in higher signal regions. This consequently affects the limits on M_D. While these limits have been obtained from an effective Lagrangian based on a non–renormalisable theory, it is still interesting to see how the limits increase when corrections for Next-to-Leading-Order (NLO) QCD effects are applied to the cross section. Using these NLO QCD corrections to the graviton production cross section, and the corresponding reduced scale uncertainties, the resulting M_D limits are shown in Fig. 11.8, and listed in Table 11.17, with the corresponding truncation effects in Table 11.18 for the fourth signal region. Additional limit plots based on other signal regions, as well as comparisons between LO and NLO limits are presented in Appendix D.

	Expected [pb]	Observed [pb]
Region1	1.82	1.92
Region2	0.18	0.17
Region3	0.024	0.030
Region4	0.0079	0.0069

Table 11.13: The 95% CL model-independent expected and observed upper limits on $\sigma \times A \times \epsilon$ [pb] in each of the 4 signal regions, using the combination of Z$\nu\nu$ predictions from the four channels: W$\mu\nu$, Z$\mu\mu$, W$e\nu$, and Zee, corresponding to BG (4) with simple weights in Table 10.1.

11.5 Limits on M^*

The same procedure can be applied to constrain Dark Matter pair production at the LHC. The same constraints on the possible number of new physics events in the observed data, corresponding to an upper limit on $\sigma \times A \times \epsilon$ of the WIMP pair production can then be converted to limits on the fundamental scale M^* of the theory (Sec. 2.3). The systematic

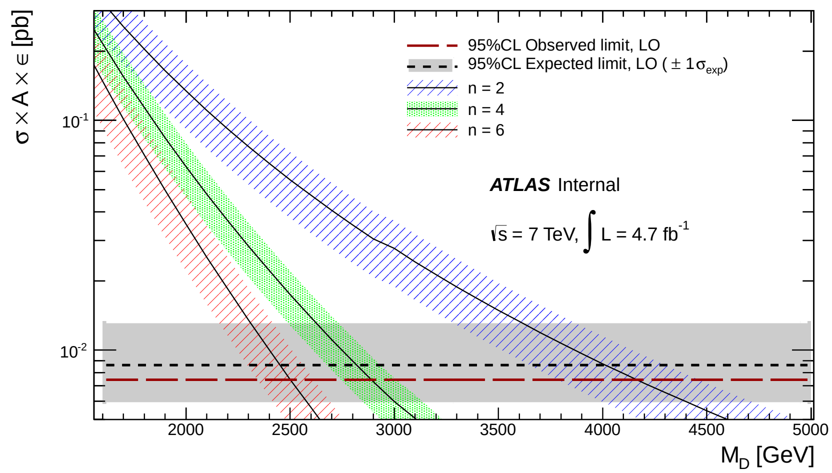

Figure 11.6: The 95% CL expected and observed upper limits on $\sigma \times A \times \epsilon$ [pb] (red and blue dashed horizontal lines), along with the ADD signal $\sigma \times A \times \epsilon$ for 2, 4, and 6 extra dimensions, in signal region 4. The error bands on the theoretical curves are the total theoretical uncertainties (PDF, ISR/FSR, and Scale Q uncertainties). The horizontal lines are obtained after taking into account the JES uncertainty correlation between signal and background, as well as luminosity, trigger, and simulation statistical uncertainties on the signal yields. The grey $\pm 1\sigma$ band around the expected limit is the variation expected from statistical fluctuations and experimental systematic uncertainties on the Standard Model and signal processes.

uncertainties considered are theoretical uncertainties on the choice of Parton Distribution Functions, Initial and Final State Radiation, and choice of the renormalisation and factorisation scale. The experimental systematic uncertainties on JES/$E_{\mathrm{T}}^{\mathrm{miss}}$, luminosity, and trigger are also considered [8]. The lower limits are set on the suppression parameter M^*, as shown for operator D11 in Fig. 11.9. The green relic line is taken from [24] and corresponds, for a given WIMP mass value, to the value of M^* at which annihilation of WIMPs exclusively via the given operator to quarks or gluons result exactly in the thermal relic density observed with WMAP [58]. The light-grey region, taken from [24], are the regions where the effective field theory approach breaks down; the effective field theory is only valid if the mediator mass is larger than the energy transfer in the event.

The lower bounds on M^* for a given m_χ can further be converted to upper limits on

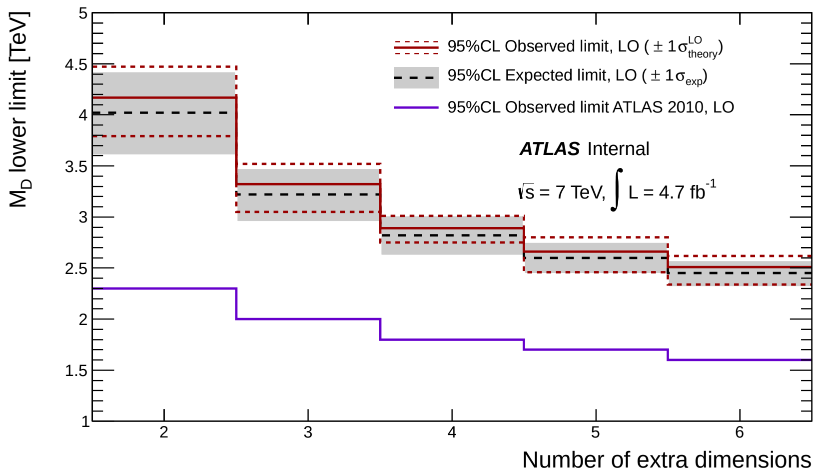

Figure 11.7: The 95% CL LO observed and expected lower limits on M_D [TeV] in signal region 4. The red dashed error bands around the observed limit show the impact of the total signal theoretical uncertainties (PDF, ISR/FSR, and Scale Q uncertainties) on the limits. The grey $\pm 1\sigma$ band around the expected limit is the variation expected from statistical fluctuations and experimental systematic uncertainties on the Standard Model and signal processes.

the WIMP–nucleon scattering cross sections [24], which are probed by direct dark matter detection experiments. The limits on M^* can also be converted to the upper limits on the annihilation rate of WIMPs to four light quark flavours [12]. The resulting limits are comparable to those from Fermi-LAT [59].

	Region 1		Region 2		Region 3		Region 4	
n	exp [TeV]	obs [TeV]	exp [TeV]	obs [TeV]	exp [TeV]	obs [TeV]	exp [TeV]	obs [TeV]
2	2.65 +0.23 -0.21	2.62 +0.15 -0.18	3.46 +0.32 -0.30	3.55 +0.24 -0.30	4.14 +0.39 -0.27	3.90 +0.28 -0.34	4.02 +0.41 -0.42	4.17 +0.30 -0.38
3	2.12 +0.14 -0.15	2.09 +0.11 -0.13	2.72 +0.20 -0.18	2.78 +0.13 -0.17	3.25 +0.24 -0.23	3.10 +0.18 -0.14	3.22 +0.26 -0.27	3.32 +0.20 -0.27
4	1.88 +0.11 -0.11	1.86 +0.09 -0.11	2.38 +0.15 -0.14	2.42 +0.11 -0.13	2.81 +0.17 -0.17	2.70 +0.11 -0.14	2.82 +0.20 -0.20	2.89 +0.12 -0.14
5	1.75 +0.10 -0.10	1.74 +0.08 -0.10	2.19 +0.11 -0.12	2.23 +0.10 -0.14	2.56 +0.14 -0.14	2.47 +0.12 -0.18	2.60 +0.16 -0.16	2.66 +0.14 -0.20
6	1.66 +0.09 -0.10	1.65 +0.07 -0.10	2.06 +0.09 -0.11	2.09 +0.08 -0.11	2.41 +0.12 -0.13	2.33 +0.11 -0.15	2.45 +0.13 -0.14	2.51 +0.11 -0.17

Table 11.14: The 95% CL expected and observed lower limits on M_D [TeV] for each number of extra dimensions, and in each signal region, using the combination of Z($\nu\nu$)+jets predictions from the four channels: W($\mu\nu$)+jets, Z($\mu\mu$)+jets, W($e\nu$)+jets, and Z(ee)+jets, corresponding to BG (4) in Table 10.1 with simple weights. The LO signal cross sections are used. The impact of one standard deviation theoretical uncertainties on the observed limits, as well as $\pm 1\sigma$ errors on the expected limits are also presented.

n	Region1	Region2	Region3	Region4
2	8.1×10^{7}	4.5×10^{7}	3.8×10^{7}	3.3×10^{7}
3	1.1×10^{3}	7.2×10^{2}	6.2×10^{2}	5.6×10^{2}
4	4.2	2.8	2.4	2.1
5	1.4×10^{-1}	10.0×10^{-2}	8.8×10^{-2}	8.0×10^{-2}
6	1.5×10^{-2}	1.1×10^{-2}	9.4×10^{-3}	8.5×10^{-3}

Table 11.15: The 95% CL LO observed upper limits on the size of the extra dimensions R [pm], for each number of extra dimensions and in each signal region, derived from the 95% CL observed lower limits on M_D presented in Table 11.14, excluding the effect of signal theoretical uncertainties.

(n, M_D [TeV])	Relative truncation effect (in %)
(2, 4.17)	0.02
(3, 3.32)	1.87
(4, 2.89)	11.82
(5, 2.66)	29.46
(6, 2.51)	49.13

Table 11.16: Relative difference (in %) between truncated and complete ADD signal cross sections, for $p_{\mathrm{T}}^{cut} = 500$ GeV at the generator level, corresponding to signal region 4. The values of M_D used are the ones corresponding to the LO observed limits, as listed in Table 11.14.

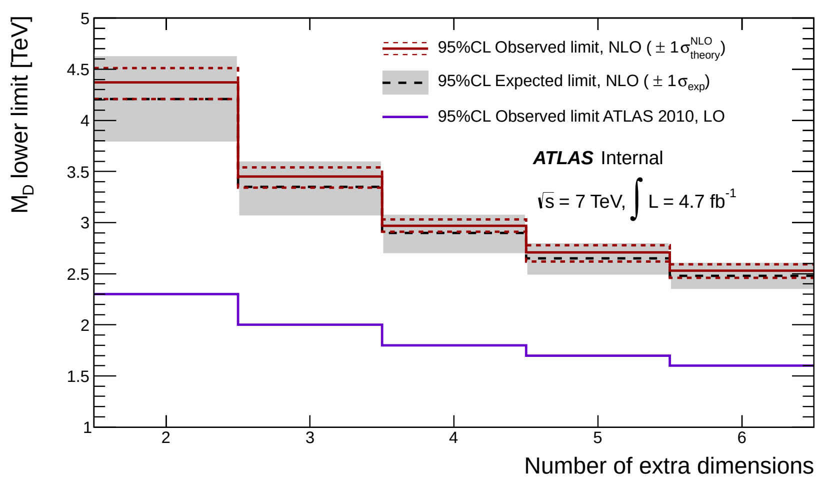

Figure 11.8: The 95% CL NLO observed and expected lower limits on M_D [TeV] in signal region 4. The red dashed error bands around the observed limit show the impact of the total signal theoretical uncertainties (PDF, ISR/FSR, and Scale Q uncertainties) on the limits. The grey $\pm 1\sigma$ band around the expected limit is the variation expected from statistical fluctuations and experimental systematic uncertainties on the Standard Model and signal processes.

	Region 1		Region 2		Region 3		Region 4	
n	exp [TeV]	obs [TeV]	exp [TeV]	obs [TeV]	exp [TeV]	obs [TeV]	exp [TeV]	obs [TeV]
2	2.80 +0.27 -0.23	2.76 +0.07 -0.08	3.65 +0.34 -0.31	3.74 +0.09 -0.10	4.41 +0.41 -0.39	4.16 +0.23 -0.28	4.21 +0.43 -0.43	4.37 +0.14 -0.16
3	2.14 +0.15 -0.14	2.12 +0.04 -0.05	2.80 +0.20 -0.20	2.85 +0.07 -0.07	3.37 +0.25 -0.24	3.22 +0.07 -0.09	3.35 +0.26 -0.29	3.45 +0.09 -0.11
4	1.85 +0.12 -0.11	1.84 +0.04 -0.06	2.40 +0.15 -0.14	2.45 +0.05 -0.05	2.87 +0.17 -0.18	2.75 +0.05 -0.05	2.90 +0.19 -0.21	2.97 +0.06 -0.06
5	1.68 +0.10 -0.10	1.66 +0.07 -0.07	2.18 +0.13 -0.12	2.22 +0.04 -0.06	2.58 +0.15 -0.14	2.49 +0.06 -0.05	2.65 +0.16 -0.17	2.71 +0.07 -0.09
6	1.55 +0.09 -0.09	1.54 +0.05 -	2.03 +0.11 -0.10	2.06 +0.06 -0.07	2.42 +0.12 -0.14	2.34 +0.04 -0.06	2.48 +0.14 -0.14	2.53 +0.06 -0.07

Table 11.17: The 95% CL NLO expected and observed lower limits on M_D [TeV] for each number of extra dimensions, and in each signal region, using the NLO QCD corrections. The combination of Z($\nu\nu$)+jets predictions from the four channels W($\mu\nu$)+jets, Z($\mu\mu$)+jets, W($e\nu$)+jets, and Z(ee)+jets, corresponding to BG (4) in Table 10.1, with simple weights, is used. The impact of one standard deviation theoretical uncertainties on the observed limits, as well as $\pm 1\sigma$ errors on the expected limits are also presented.

(n, M_D [TeV])	Relative truncation effect (in %)
(2, 4.37)	0.01
(3, 3.45)	1.26
(4, 2.97)	9.89
(5, 2.71)	27.17
(6, 2.53)	47.94

Table 11.18: Relative difference (in %) between truncated and complete ADD signal cross sections, for $p_{\mathrm{T}}^{cut} = 500$ GeV at the generator level, corresponding to signal region 4. The values of M_D used are the ones corresponding to the NLO observed limits, as listed in Table 11.17.

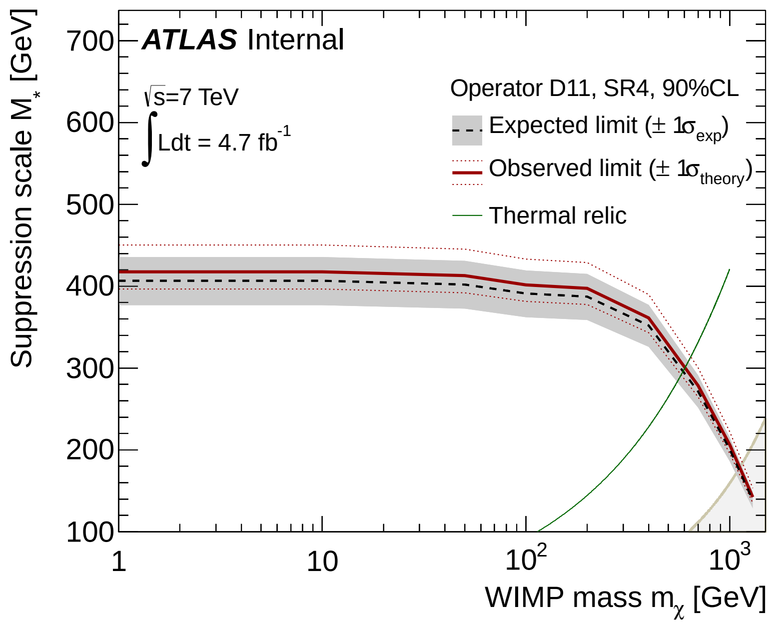

Figure 11.9: The 90% CL lower limits on M^* for different WIMP masses, m_χ. Observed and expected limits including all but the theoretical signal uncertainties are shown as thick black and red dashed lines, respectively. The grey $\pm 1\sigma$ band around the expected limit is the variation expected from statistical fluctuations and experimental systematic uncertainties on the Standard Model and signal processes. The impact of the theoretical uncertainties is demonstrated with the thin red dotted $\pm 1\sigma$ limit lines around the observed limit. The M^* values at which WIMPs of a given mass would result in the required relic abundance are shown as green lines, assuming annihilation in the early universe proceeded exclusively via the given operator. The shaded light-grey region indicate where the effective field theory approach breaks down.

Chapter 12

Measurement of the Invisible Width of the Z Boson

12.1 Introduction

The Z boson can decay to a pair of neutral weakly-interacting particles, resulting in missing energy in the detector. The sum of all such partial decay widths of the Z is referred to as the invisible width of the Z, $\Gamma_Z(inv)$. In the Standard Model, such decays only correspond to the decay of the Z to a left-handed neutrino anti-neutrino pair $(\nu_e, \nu_\mu, \nu_\tau)$, as explained in Sec. 1.1. However if there exist decays of the Z to weakly interacting exotic particles, or if the Z decay is sensitive to non–standard couplings of the Standard Model neutrinos to the Z boson, they also contribute to the invisible decay width of the Z. Therefore, this measurement provides means of testing the Standard Model.

The $\Gamma_Z(inv)$ has been independently measured in the LEP experiments. In such measurements, the charged leptonic $\Gamma_Z(\ell\ell)$ and the hadronic $\Gamma_Z(had)$ decay widths of the Z were measured, and subtracted from the total Z width obtained from the lineshape [60–63]. This gave $\Gamma_Z(inv) = 499.0 \pm 1.5$ MeV. However, the indirect method is not sensitive to the existence of new neutral weakly interacting exotic particles to which the Z boson can decay, as the total decay width of the Z expected from Standard Model was input. The direct measurement of $\Gamma_Z(inv)$ has also been performed in LEP [18–21], using photon plus $E_{\mathrm{T}}^{\mathrm{miss}}$ events, resulting in $\Gamma_Z(inv) = 503 \pm 16$ MeV. A direct measurement was also made by the CDF experiment [64] resulting in $\Gamma_Z(inv) = 466 \pm 42$ MeV.

In this section, the results of the direct measurement of $\Gamma_Z(inv)$ based on the results of the mono-jet search presented in the chapters 5 - 10 is presented. The measurement used the same mono-jet signal regions, and the results from the data-driven determination of the background in these regions (Table 10.1). The strategy was based on the exploitation of the ratio of Z+jets events in the $\nu\nu$ channel (mono–jet events) to Z+jets events in the $\ell\ell$ channel (mono–jet control region), to provide a measurement of the ratio of branching ratios as can be seen in Eq. 12.2 :

$$\frac{\Gamma_Z(inv)}{\Gamma_Z(\ell\ell)} = \frac{\sigma^{phase-space}(Z \to inv + \text{jets})}{\sigma^{phase-space}(Z \to \ell\ell + \text{jets})} = \frac{\sigma_{Tot}^{phase-space}(Z + \text{jets}) \times BR(Z \to inv)}{\sigma_{Tot}^{phase-space}(Z + \text{jets}) \times BR(Z \to \ell\ell)} \tag{12.1}$$

$$\frac{\Gamma_Z(inv)}{\Gamma_Z(\ell\ell)} = \frac{(N_{obs}^{phase-space} - N_{bkg})/\mathcal{L}_{\texttt{JetTauEtmiss}} \times \frac{1}{C_{jetE_{\mathrm{T}}^{\mathrm{miss}}}}}{[(N_{\mathrm{Z}(\to\ell\ell)+jets}^{Data} - N_{QCD})^{phase-space} \times (1 - f_{EW})]/(A_\ell \times \epsilon_\ell \times \mathcal{L}_{\texttt{JetTauEtmiss}})}, \tag{12.2}$$

where $phase - space$ is a given phase space, such as the mono-jet phase space. The first equality of Eq. 12.1 holds only if the acceptances of the "+jets" cuts, as well as the Z p_{T} (equivalent to $E_{\mathrm{T}}^{\mathrm{miss}}$ in the case of Z($\nu\nu$) events) are the same for the two processes Z($\nu\nu$) and Z($\mu\mu$). The second equality of Eq. 12.1 holds due to the narrow width approximation. The term N_{bkg} in Eq. 12.2 is the number of background events in each mono–jet signal region, excluding Z($\nu\nu$) events. The factor $C_{jetE_{\mathrm{T}}^{\mathrm{miss}}}$ corrects for the differences in the jets and $E_{\mathrm{T}}^{\mathrm{miss}}$ phase spaces of the two processes Z($\nu\nu$)+jets and Z($\ell\ell$)+jets, as explained later. The value of the leptonic width of the Z on the left hand side of Eq. 12.2, $\Gamma_{Z(\ell\ell)}$, was taken from the Particle Data Group (PDG), and equals 83.984 ± 0.086 MeV. Multiplying the measured ratio by this value gives the $\Gamma_Z(inv)$.

The Z($\nu\nu$)+jets cross section was obtained from mono-jet events according to $(N_{obs}^{mono-jet} - N_{bkg})/\mathcal{L}_{\texttt{JetTauEtmiss}}$. The values of $(N_{obs}^{mono-jet} - N_{bkg})$ were taken from Table 10.1 and are listed in Table 12.2. The estimation of systematic uncertainties are explained in Sec. 12.3. To ensure that the first equality of Eq. 12.1 holds, a correction factor, $C_{jetE_{\mathrm{T}}^{\mathrm{miss}}}$, was applied to the Z($\mu\mu$)+jets events in the full lepton phase space, to account for the differences in the jets and $E_{\mathrm{T}}^{\mathrm{miss}}$ phase spaces between Z($\nu\nu$) and Z($\mu\mu$) processes due to the presence of the leptons (see Sec. 8.2.2). This correction factor was obtained by dividing the values of $\frac{N^{SR}_{\mathrm{Z}(\to\nu\nu)+jets}}{N_{\mathrm{Z}(\to\mu\mu)+jets}}$ from simulation listed in Table 8.10, by the ratio of branching ratios of Z($\nu\nu$) to Z($\mu\mu$), BR, as shown in Eq. 12.3, with the corresponding values listed in Table 12.1.

$$C_{jetE_{\mathrm{T}}^{\mathrm{miss}}} = \frac{\left(\frac{N^{SR}_{\mathrm{Z}(\to\nu\nu)+jets}}{N_{\mathrm{Z}(\to\mu\mu)+jets}}\right)_{\mathrm{Simulation}}}{\mathrm{BR}} \tag{12.3}$$

The quantity BR was estimated from simulation by taking the ratio of Z($\nu\nu$) events without any cuts, to Z($\mu\mu$) events after only the invariant mass cut $m_{\mu\mu}$ at the truth. This reduces the γ^* contribution in the Z/γ^*($\mu\mu$) simulated samples. This ratio is 5.947.

Control region	$\frac{N^{SR}_{\mathrm{Z}(\to\nu\nu)+jets}}{N_{\mathrm{Z}(\to\mu\mu)+jets}}$	$C_{jetE_{\mathrm{T}}^{\mathrm{miss}}} \pm$ (stat.)
region 1	7.46 ± 0.06	1.254 ± 0.011
region 2	8.32 ± 0.23	1.399 ± 0.039
region 3	9.44 ± 0.88	1.587 ± 0.148
region 4	7.32 ± 1.66	1.231 ± 0.279

Table 12.1: Values of $\frac{N^{SR}_{\mathrm{Z}(\to\nu\nu)+jets}}{N_{\mathrm{Z}(\to\mu\mu)+jets}}$ from simulation in each Z($\mu\mu$) control region, and the corresponding jets/$E_{\mathrm{T}}^{\mathrm{miss}}$ phase space correction factors. Uncertainties are statistical only.

The cross section of the leptonic decay of the Z, $\sigma(Z\ell\ell + \mathrm{jets})$, was taken from the already available pseudo-cross section of Z($\mu\mu$)+jets in the muon control regions (Sec. 8.2.2). This pseudo-cross section is equal to:

$$\sigma(Z \to \ell\ell + \mathrm{jets}) = \frac{(N^{Data}_{\mathrm{Z}(\to\mu\mu)+jets} - N_{QCD})^{mono-jet} \times (1 - f_{EW})}{A_{\mu} \times \epsilon_{\mu_1} \times \epsilon_{\mu_2} \times \mathcal{L}_{\texttt{JetTauEtmiss}}} \times C_{jetE_{\mathrm{T}}^{\mathrm{miss}}} \tag{12.4}$$

Signl region	$N_{obs}^{mono-jet}$	$(N_{obs}^{mono-jet} - N_{bkg}) \pm$ (SR data stat.) $\pm$ (syst.)
region 1	124703	$63740 \pm 178.47 \pm 2396.6$
region 2	8631	$5197 \pm 56.13 \pm 264.0$
region 3	785	$538 \pm 19.21 \pm 47.99$
region 4	77	$52 \pm 5.93 \pm 10.28$

Table 12.2: Total number of data events in each mono-jet signal region, before and after subtraction of the background.

The reconstruction efficiency of the invariant mass cut was corrected for by applying the cut at the reconstructed level in the numerator of the acceptance, and at truth level in the denominator. The correction for the truth acceptance of the cut is almost 1, as the γ^* contamination in the mass range 66 - 116 GeV is almost the same as the contamination from Z bosons outside this window.

If the measured invisible width of the Z is in agreement with the Standard Model expectation, the ratio of widths in Eq. 12.2 can also be used to get a measurement of the number of light neutrino families in the Standard Model. This was done by dividing $\frac{\Gamma_{Z(inv)}}{\Gamma_{Z(\ell\ell)}}$ by value of $\frac{\Gamma_{Z(\nu_\ell\nu_\ell)}}{\Gamma_{Z(\ell\ell)}}$ in the Standard Model, 1.999 ± 0.001, taken from the PDG:

$$\frac{\Gamma_Z(inv)}{\Gamma_Z(\ell\ell)} \times \frac{\Gamma_Z(\ell\ell)}{\Gamma_Z(\nu_\ell\nu_\ell)} = \frac{\Gamma_Z(inv)}{\Gamma_Z(\nu_\ell\nu_\ell)} = n_\nu \tag{12.5}$$

12.2 Measurement of Z($\mu\mu$)+jets Pseudo cross section

The number of data events in each Z($\mu\mu$)+jets control region before background subtraction, and also in the full lepton phase space are listed in Table 12.3, based on the results of Sec. 8.2.2. The estimation of systematic uncertainties are explained in Sec. 12.3.

Dividing the total number of events in the full lepton phase space in each control region

Control region	Before background subtraction	Full μ space $\pm$ (data stat.) $\pm$ (syst.) (after the jets/$E_{\mathrm{T}}^{\mathrm{miss}}$ phase space correction)
region 1	4816	11149.56 $\pm$ 160.68 $\pm$ 392.78
region 2	445	956.08 $\pm$ 45.35 $\pm$ 62.00
region 3	45	102.52 $\pm$ 15.30 $\pm$ 11.84
region 4	6	11.94 $\pm$ 4.90 $\pm$ 2.74

Table 12.3: Total number of data events in each Z($\mu\mu$)+jets control region before background subtraction, and after applying all the correction factors to recover the full lepton phase space, and the additional factor to account for the differences in the jets and $E_{\mathrm{T}}^{\mathrm{miss}}$ phase spaces.

by $\mathcal{L}_{\texttt{JetTauEtmiss}} = 4703.65 \pm 183.44 \;\; pb^{-1}$ gives the pseudo cross section of Z($\mu\mu$)+jets in each control region, as listed in Table 12.4.

Control region	pseudo cross section [pb] $\pm$ (Total uncertainty)
region 1	2.37 $\pm$ 0.13
region 2	0.203 $\pm$ 0.018
region 3	0.022 $\pm$ 0.004
region 4	0.0025 $\pm$ 0.001

Table 12.4: Pseudo cross section of Z($\mu\mu$)+jets [pb] in each control region.

12.3 Systematic Uncertainties

The systematic uncertainties are evaluated on the two following terms:

- $T_1 = N_{obs}^{mono-jet} - N_{bkg}$
- $T_2 = \frac{N_{\mathrm{Z}(\rightarrow\mu\mu)+jets}^{Data} \times (1-f_{EW})}{A_\mu \times \epsilon_{\mu_1} \times \epsilon_{\mu_2}} \times C_{jetE_{\mathrm{T}}^{\mathrm{miss}}}$

The uncertainties on T_1 are due to the statistical uncertainty in the data signal region on $N_{obs}^{mono-jet}$, as well as systematic and data statistical uncertainties on N_{bkg}, due to the data regions used to determine N_{bkg}. All the uncertainties were taken from Sec. 10 after excluding the uncertainties on Z($\nu\nu$), and are listed in Table 12.5. The term T_1 has two components: the one which has correlated systematic uncertainties to a part of term T_2, corresponding to the data–driven electroweak backgrounds, N_{bkg}^{EW}, due to the simulated – based correction factors used, and a part which is completely uncorrelated, corresponding to the data events in the signal regions, as well as the rest of the backgrounds including the top, di–boson, multi-jet QCD, and non-collision backgrounds, $N_{obs}^{mono-jet} - N_{bkg}^{non-EW}$. The total uncertainty on T_1 from a source can then be written as:

$$\Delta^2 T_1 = \Delta^2 N_{obs}^{mono-jet} + \Delta^2 N_{BG}^{non-EW} + \Delta^2 N_{BG}^{EW} \tag{12.6}$$

$$\delta^2 T_1 = \frac{1}{T_1^2} \times [\Delta^2 N_{obs}^{mono-jet} + \Delta^2 N_{BG}^{non-EW}] + \frac{1}{T_1^2} \times \Delta^2 N_{BG}^{EW} \tag{12.7}$$

$$\delta^2 T_1 = \frac{1}{T_1^2} \times [N_{obs}^{mono-jet} + \delta^2_{non-EW} \times (N_{BG}^{non-EW})^2] + \frac{1}{T_1^2} \times \delta^2_{EW}.(N_{BG}^{EW})^2, \tag{12.8}$$

where ΔT_1 is the absolute error on T_1, and δT_1 is its relative error. The error on $N_{obs}^{mono-jet}$ is statistical only, and equals $\sqrt{N_{obs}^{mono-jet}}$ for the absolute error. The values of δ_{non-EW} and δ_{EW}, equal to $\frac{\Delta_{non-EW} N_{BG}^{non-EW}}{N_{BG}^{non-EW}}$ and $\frac{\Delta_{EW} N_{BG}^{EW}}{N_{BG}^{EW}}$ respectively, were taken from the mono-jet results already presented.

The uncertainties on T_2 include the data statistical uncertainty in the Z($\mu\mu$) control region, the systematic uncertainties on $1 - f_{EW}$, the muon scale and resolution (estimated to be negligible), and JES and $E_{\mathrm{T}}^{\mathrm{miss}}$ uncertainties on A_μ and $C_{jetE_{\mathrm{T}}^{\mathrm{miss}}}$, the uncertainties of the scale factors on the muon identification maps, and the MC modelling uncertainties on $C_{jetE_{\mathrm{T}}^{\mathrm{miss}}}$. These uncertainties were estimated from those on the data-driven determination of Z($\nu\nu$) from the Z($\mu\mu$) control region. This is due to the fact that all the factors in T_2 are the same as those used in the determination of Z($\nu\nu$) from the Z($\mu\mu$) data control region. In other words:

Systematic source	Region1	Region2	Region3	Region4
JES-$E_{\mathrm{T}}^{\mathrm{miss}}$	1.36%	1.83%	1.74%	2.23%
μ energy scale and resolution	0.03%	0.005%	0.04%	0.51%
SF (muon and electron)	0.39%	0.43%	0.35%	0.48%
MC modelling	2.72%	1.88%	1.29%	1.43%
$1 - f_{EW}$	0.86%	0.60%	0.41%	0.48%
MC stat uncertainty	0.49%	1.01%	1.99%	6.19%
non-EW systematics	1.53%	1.26%	1.51%	0.39%
data CR statistical uncertainty	0.47%	1.10%	2.35%	6.64%
Total systematic uncertainty	3.60%	3.36%	4.10%	9.50%
data SR stat uncertainty	0.55%	1.79%	5.21%	16.84%

Table 12.5: Relative systematic and statistical uncertainties on $(N_{obs}^{mono-jet} - N_{bkg})$, in each of the four regions.

$$T_2 = \frac{N^{Data}_{\mathrm{Z}(\to\mu\mu)+jets} \times (1 - f_{EW})}{A_\mu \times \epsilon_{\mu_1} \times \epsilon_{\mu_2}} \times C_{jetE_{\mathrm{T}}^{\mathrm{miss}}} = \frac{N^{SR}_{data-driven}(Z\nu\nu + jets)}{BR} \tag{12.9}$$

$$\delta^2 T_2 = \delta^2 N^{Data}_{\mathrm{Z}(\to\mu\mu)+jets} + \delta^2_{systematics}(N^{SR,Z\nu\nu}_{data-driven}) \tag{12.10}$$

$$\delta^2 T_2 = \frac{1}{N^{Data}_{\mathrm{Z}(\to\mu\mu)+jets}} + \delta^2_{systematics}(N^{SR,Z\nu\nu}_{data-driven}), \tag{12.11}$$

where $\delta^2 N^{Data}_{\mathrm{Z}(\to\mu\mu)+jets}$ is only the statistical error of the Z($\mu\mu$) control region, and $\delta^2_{systematics}(N^{SR,Z\nu\nu}_{data-driven})$ corresponds to all the systematic uncertainties on the Z($\nu\nu$) determination from the Z($\mu\mu$) data control region. This latter term is the one in correlation with the correction factors used to determine the N_{BG}^{EW} term in T_1.

The determination of $N^{SR}_{data-driven}(Z\nu\nu + jets)$ was explained in Sec. 8.2.2, and the corresponding systematic uncertainties are listed in Table 8.20. The systematic uncertainties of T_2 are listed in Table 12.6.

Systematic source	Region1	Region2	Region3	Region4
JES-$E_{\mathrm{T}}^{\mathrm{miss}}$	0.98%	4.28%	8.51%	6.58%
SF (muon)	0.80%	2.97%	0.36%	0.75%
MC modelling	3%	3%	3%	3%
$1 - f_{EW}$	1%	1%	1%	1%
MC stat uncertainty	0.86%	2.48%	7.12%	21.62%
Total systematic uncertainty	3.51%	6.47%	11.54%	22.83%
data stat uncertainty of Z($\mu\mu$) CR	1.44%	4.74%	14.91%	40.82%

Table 12.6: Relative error on $\sigma(Z\ell\ell + jets)$, in each of the four mono-jet regions.

The correlations between the systematic uncertainties of the two terms are on the uncertainties on $1 - f_{EW}$, muon scale factors only for those backgrounds determined from the muon control regions, JES and $E_{\mathrm{T}}^{\mathrm{miss}}$, and MC modelling uncertainties between $C_{jet-E_{\mathrm{T}}^{\mathrm{miss}}}$ and N_{bkg}. There is also a correlation due to the Z($\mu\mu$) data control region statistical error between T_1 and T_2, as the Z($\mu\mu$) and Z($\tau\tau$) backgrounds in T_1 were determined from the same Z($\mu\mu$) data control region. Finally, there is a correlation between simulation statistical uncertainties of $C_{jet-E_{\mathrm{T}}^{\mathrm{miss}}}$ in T_2 and the simulation–based correction factors used to determine the Z($\mu\mu$) and Z($\tau\tau$) backgrounds in T_1, as they used the same Z($\mu\mu$) simulated samples. However, the two latter correlations have negligible impact on the total uncertainty, as the Z($\mu\mu$) and Z($\tau\tau$) backgrounds contribute to less than 1% of the total background in the signal regions.

For a function $g = g(T_1, T_2) = \frac{T_1}{T_2}$, the error on g is:

$$(\frac{\Delta g}{g})^2 = (\frac{\Delta T_1}{T_1})^2 + (\frac{\Delta T_2}{T_2})^2 - 2.\frac{cov(T_1, T_2)}{T_1.T_2}, \tag{12.12}$$

where $cov(T_1, T_2)$ is the covariance term. Moreover, for two functions $f_1 = f_1(x_1, ..., x_n)$ and $f_2 = f_2(x_1, ..., x_n)$, the covariance equals:

$$cov(f_1, f_2) = \sum_i \sum_j (\frac{\partial f_1}{\partial x_i}).(\frac{\partial f_2}{\partial x_j}).cov(x_i, x_j) \quad (12.13)$$

Five variables x_i can be considered as follows:

$$x_1 = N_{obs}^{mono-jet} - N_{BG}^{non-EW} \quad (12.14)$$

$$x_2 = N_{data}^{CRs} \quad (12.15)$$

$$x_3 = \frac{N_{data}^{Z\mu\mu CR}}{BR} \quad (12.16)$$

$$x_4 = C_1(= \frac{N_{BG}^{EW}}{x_2}) \quad (12.17)$$

$$x_5 = C_2(= \frac{N_{data-driven}^{SR,Z\nu\nu}}{N_{data}^{Z\mu\mu CR}}), \quad (12.18)$$

where N_{data}^{CRs} is the number of events in a data control region used to determine backgrounds in the mono–jet signal regions, and C_1 represents the corresponding correction factors to get the determination of N_{BG}^{EW} from the control region. The factor C_2 corresponds to the correction factors needed for correcting the Z($\mu\mu$) data control region to resemble the Z($\nu\nu$) phase space. In terms of these five variables, the ratio $\frac{T_1}{T_2}$ can be written as[1]:

$$\frac{T_1}{T_2} = \frac{x_1 - x_2 \times x_4}{x_3 \times x_5} \quad (12.19)$$

Using Eq. 12.13, and considering the fact that for $i, j = 1, 2, 3$, and $i \neq j$: $cov(x_i, x_j) = 0$, as these three variables refer to orthogonal data regions, and their uncertainties are statistical only, and that $\frac{\partial T_1}{\partial x_3} = \frac{\partial T_1}{\partial x_5} = 0$, and $\frac{\partial T_2}{\partial x_1} = \frac{\partial T_2}{\partial x_2} = \frac{\partial T_2}{\partial x_4} = 0$, the covariance term

[1] In principle, the variables x_2 and x_4 should be separated for various background channels, as they are not all derived from the same control region, and different correction factors are used to determine them. The more correct way is to define T_1 in terms of 8 variables such that:
$T_1 = x_1 - N_{data}^{WelectronCR} \times C_1^{We\nu} - N_{data}^{WmuonCR} \times (C_1^{W\mu\nu} + C_1^{W\tau\nu}) - N_{data}^{ZmuonCR} \times (C_1^{Z\mu\mu} + C_1^{Z\tau\tau})$.

$cov(T_1, T_2)$ equals:

$$cov(T_1, T_2) = \frac{\partial T_1}{\partial x_4}.\frac{\partial T_2}{\partial x_5}.cov(x_4, x_5) = \frac{\partial T_1}{\partial x_4}.\frac{\partial T_2}{\partial x_5}.\rho_{4,5}.\Delta x_4.\Delta x_5 \tag{12.20}$$

As $T_1 = x_1 - x_2 \times x_4$ and $T_2 = x_3 \times x_5$, the covariance equals:

$$cov(T_1, T_2) = -x_2.x_3.\rho_{4,5}.\Delta x_4.\Delta x_5 = N_{data}^{CRs}.\frac{N_{data}^{Z\mu\mu CR}}{BR}.\rho_{C_1,C_2}.\Delta C_1.\Delta C_2 \tag{12.21}$$

where $\rho_{4,5} = 1$ for the fully correlated systematic sources. Putting this back to Eq. 12.12, and summing over all systematic uncertainties, the total error on the ratio $\frac{T_1}{T_2}$ is:

$$(\frac{\Delta(\frac{T_1}{T_2})}{\frac{T_1}{T_2}})^2 = (\frac{\Delta T_1}{T_1})^2 + (\frac{\Delta T_2}{T_2})^2 + 2 \times \frac{1}{T_1.T_2} \times N_{data}^{CRs} \times \frac{N_{data}^{Z\mu\mu CR}}{BR} \times \sum_a \rho^a_{C_1,C_2} \times \Delta^a C_1 \times \Delta^a C_2, \tag{12.22}$$

where $\Delta^a C_i$ is the absolute error on C_i due to systematic source a. The formula can also be written in terms of the relative errors:

$$\delta^2(\frac{T_1}{T_2}) = \delta^2(T_1) + \delta^2(T_2) + 2 \times \frac{1}{T_1.T_2} \times N_{data}^{CRs} \times \frac{N_{data}^{Z\mu\mu CR}}{BR} \times \sum_a \Delta^a C_1 \times \Delta^a C_2, \tag{12.23}$$

As the systematic uncertainties are not applied to data control regions (N_{data}^{CRs}, $N_{data}^{Z\mu\mu CR}$), this can also be written as:

$$\delta^2(\frac{T_1}{T_2}) = \delta^2(T_1) + \delta^2(T_2) + 2 \times \frac{1}{T_1.T_2} \times \frac{1}{BR} \times \sum_a \rho^a_{C_1,C_2} \Delta^a(N_{data}^{CRs}.C_1) \times \Delta^a(N_{data}^{Z\mu\mu CR}.C_2), \tag{12.24}$$

where $\delta^2(T_1)$ and $\delta^2(T_2)$ are the total relative errors on T_1 and T_2, taken from Tables 12.5 and 12.6. The terms $\Delta^a(N_{data}^{CRs} \times C_1)$ and $\Delta^a(N_{data}^{Z\mu\mu CR} \times C_2)$ were also taken from these tables, only considering the systematic uncertainties which have correlations between C_1 and C_2. The corresponding relative errors were then multiplied by the central values of

$N_{data}^{CRs} \times C_1$ and $N_{data}^{Z\mu\mu CR} \times C_2$, which equal N_{BG}^{EW} and $N_{data-driven}^{SR,Z\nu\nu}$, respectively, as defined in Eq. 12.17 and 12.18, to get the absolute errors. Therefore, Eq. 12.24 can also be written as:

$$\delta^2_{Total}(\frac{T_1}{T_2}) = \delta^2_{Total}(T_1)+\delta^2_{Total}(T_2)+2\times\frac{1}{T_1.T_2}\times\frac{1}{BR}\times\sum_a \rho_a\times\Delta^a(N_{BG}^{EW})\times\Delta^a(N_{data-driven}^{SR,Z\nu\nu}), \tag{12.25}$$

where $\delta_{Total}(T_i)$ is the total relative uncertainty on T_i, obtained from the quadratic sum of its total systematic and statistical uncertainties, and N_{BG}^{EW} includes the background contributions from W($\tau\nu$), W($\mu\nu$), W($e\nu$), Z($\tau\tau$), and Z($\mu\mu$) in the signal regions. The individual error from source a is:

$$\delta^2_a(\frac{T_1}{T_2}) = \delta^2_a(T_1) + \delta^2_a(T_2) + 2\times\frac{1}{T_1.T_2}\times\frac{1}{BR}\times\rho_a\times\Delta^a(N_{BG}^{EW})\times\Delta^a(N_{data-driven}^{SR,Z\nu\nu}) \tag{12.26}$$

Using the formula of Eq. 12.25, the resulting uncertainties on $\frac{\Gamma_Z(inv)}{\Gamma_Z(\ell\ell)}$ are listed in Table 12.7.

Systematic source	Region1	Region2	Region3	Region4
JES-$E_{\mathrm{T}}^{\mathrm{miss}}$	0.53%	2.74%	7.00%	4.17%
MC modelling (fully correlated)	4.05%	3.54%	3.27%	3.32%
μ energy scale and resolution	0.03%	0.005%	0.04%	0.51%
SF (muon and electron)	0.89%	3.00%	0.50%	0.89%
$1 - f_{EW}$	1.32%	1.17%	1.08%	1.11%
MC stat uncertainty (from `ALPGEN`)	0.99%	2.68%	7.39%	22.49%
non-EW systematics	1.53%	1.26%	1.51%	0.39%
data *CR* statistical uncertainty	1.51%	4.87%	15.09%	41.36%
data *SR* stat uncertainty	0.55%	1.79%	5.21%	16.84%
Total uncertainty	5.01%	8.13%	19.31%	50.31%

Table 12.7: Total relative uncertainties on $\frac{\Gamma_Z(inv)}{\Gamma_Z(\ell\ell)}$ in each of the four mono-jet regions.

Defining additional variables for T_1 in order to separate different background channels, since they have different correction factors, the more correct formula is:

$$
\begin{aligned}
&(\frac{\Delta(\frac{T_1}{T_2})}{\frac{T_1}{T_2}})^2 = (\frac{\Delta T_1}{T_1})^2+(\frac{\Delta T_2}{T_2})^2+2\times\frac{1}{T_1.T_2}\times(C_1^{\mu\mu}+C_1^{\tau\tau})\times C_2\times\rho_{T_1,T_2}^{Z(\mu\mu),dataCR}\times\Delta^2(N_{data}^{Z\mu\mu,CR}) \\
&+2\times\frac{1}{T_1.T_2}\times\sum_a[\rho^a_{C_1^{e\nu},C_2}\times N_{data}^{We\nu,CR}\times\Delta_a C_1^{e\nu}+N_{data}^{W\mu\nu,CR}\times(\rho^a_{C_1^{\mu\nu},C_2}\times\Delta_a C_1^{\mu\nu}+ \\
&\rho^a_{C_1^{\tau\nu},C_2}\times\Delta_a C_1^{\tau\nu})+N_{data}^{Z\mu\mu,CR}\times(\rho^a_{C_1^{\mu\mu},C_2}\times\Delta_a C_1^{\mu\mu}+\rho^a_{C_1^{\tau\tau},C_2}\times\Delta_a C_1^{\tau\tau})]\times\frac{N_{data}^{Z\mu\mu,CR}}{BR}\times\Delta_a C_2,
\end{aligned}
\tag{12.27}
$$

where $N_{data}^{Y,CR}$ is the number of events in a data control region corresponding to process Y used to determine backgrounds in the mono–jet signal regions, C_1^X is the correction factor required to determine background X in the mono–jet signal regions, C_2 is the correction factor to get the Z($\nu\nu$) phase space from Z($\mu\mu$) control region, and $\rho^a_{C_1^X,C_2}$ is the correlation of systematic source a between C_1^X and C_2.

12.4 Results

Using the results of Table 12.2 and Table 12.3, and final uncertainties of Table 12.7, Table 12.8 summarises the final results in each of the four signal regions, along with the LEP and CDF results.

The result, taken from the first signal region, is consistent with the LEP indirect measurement of 5.942 ± 0.019 within uncertainties:

$$\frac{\Gamma_Z(inv)}{\Gamma_Z(\ell\ell)} = 5.72 \pm 0.29 \tag{12.28}$$

$$\Gamma_Z(inv) = 480.14 \pm 24.02 \text{ MeV} \tag{12.29}$$

$$n_\nu = 2.87 \pm 0.14 \tag{12.30}$$

Signal region	$\frac{\Gamma_Z(inv)}{\Gamma_Z(\ell\ell)} \pm$ (syst.)	$\Gamma_Z(inv)$ [MeV] $\pm$ (syst.)	$n_\nu \pm$ (syst.)
region 1	5.717 ± 0.286	480.14 ± 24.02	2.87 ± 0.14
region 2	5.436 ± 0.442	456.20 ± 37.10	2.73 ± 0.22
region 3	5.248 ± 1.013	440.41 ± 85.01	2.64 ± 0.51
region 4	4.335 ± 2.181	363.90 ± 183.08	2.18 ± 1.10
LEP indirect	5.942 ± 0.019	499.0 ± 1.5	2.984 ± 0.008
LEP direct		$503. \pm 16.$	2.92 ± 0.06
CDF	5.546 ± 0.506	$466. \pm 42.$	2.79 ± 0.25

Table 12.8: $\frac{\Gamma_Z(inv)}{\Gamma_Z(\ell\ell)}$, $\Gamma_Z(inv)$, and number of light neutrinos, obtained using each of the 4 mono-jet signal regions.

Chapter 13

Conclusion

Among the fundamental problems of the Standard Model of particle physics is that it does not include a description of gravity, and does not account for the dark matter and dark energy content of the universe. Various models, providing partial or complete solutions to some of these problems, predict – among other things – final states including one hard jet and a large amount of $E_{\mathrm{T}}^{\mathrm{miss}}$. For example, in the ADD scenario the graviton propagates in the (4 + n)-dimensional bulk of space-time, resulting in large missing transverse energy in the event. These models can have different rates and populate different parts of the mono–jet phase space, but they may produce an excess of mono–jet events at the LHC, compared to what is expected by the Standard Model. In an attempt to find if such an idea corresponded to physical reality, a search for any significant deviation with respect to the Standard Model predictions in the $E_{\mathrm{T}}^{\mathrm{miss}}$ distribution of mono–jet events was performed. If a deviation was observed, it would be a discovery and a compelling argument for models leading to solution to the problems mentioned. If no excess is found, the results can be used to constrain these new physics theories. Moreover, in case of no excess, the couplings of the Z boson to neutrinos can be probed through a direct measurement of the invisible decay width of the Z. Finally, since there is a wide variety of Standard Model physics and beyond the Standard Model that can be studied with such a mono–jet search, the analysis was made as model–independent as possible, with no optimisation for a particular exotic signature. This avoids biases toward one of the many possible scenarios.

In order to perform such a search for signatures beyond the Standard Model with a central energetic jet and high $E_{\mathrm{T}}^{\mathrm{miss}}$, the 2011 proton – proton collision data with the ATLAS detector, corresponding to 4.7 fb^{-1} of integrated luminosity, was used. The model–dependence relies on the choice of the phase space in which the search was performed. In order to minimise any bias and thus keep the model–independence of the search, four inclusive signal regions with symmetric lower thresholds on the leading jet p_{T} and $E_{\mathrm{T}}^{\mathrm{miss}}$, from 120 GeV to 500 GeV, are defined. In all the regions, the rate of the expected signal is much smaller than the expected Standard Model background. Therefore, in order to maximise the sensitivity to new physics which could lead to a discovery, the precision at which the Standard Model background is estimated must be optimised. To achieve this, data–driven techniques were used to determine the contributions of most of the backgrounds, resulting in a reduction of systematic uncertainties, by factors of 2 to 5, depending on the kinematic region, compared to the predictions obtained by simulation only. In order to reduce the statistical limitation of such methods, four statistically independent regions have been used and combined to get the final background predictions, which also adds robustness to the predictions.

A good agreement is observed between data and Standard Model expectation in each signal region, with the observed data being within one standard deviation of the Standard Model expectation (Table 10.1). Therefore, model-independent 95% CL upper bounds on $\sigma \times A \times \epsilon$ have been set, corresponding to 1.92, 0.17, 0.30, and 0.0069 pb in each of the four signal regions, respectively. These limits can be applied to any existing and yet–to–be invented theory predicting a mono–jet signal, provided an acceptance and efficiency calculation exist for that theory. Examples of the acceptance and efficiencies have been computed for two different new physics scenarios, constraining the fundamental parameters of these models: ADD and the effective theory approach to the WIMP pair production. The results are then interpreted in the contexts of these ADD LED and WIMP pair production scenarios. Lower limits on the scale of the ADD model M_D are set, corresponding to 4.17, 3.32, 2.90, 2.66, and 2.51 TeV for n = 2 – 6, respectively, without considering the signal theoretical uncertainties. This results in an increase on the limits on M_D compared to previous limits [7], and to date constitutes the best limits on the scale M_D. This however does not yet exclude the possibility of a quantum gravity model at the weak scale. Nor does it exclude a solution to other Standard Model problems. However, it starts to put relatively severe constrains on the model parameters.

In the WIMP scenario an effective field theory is used, and limits are set on a mass suppression scale M^*. These limits can further be converted to upper limits on WIMP–nucleon spin-dependent and spin-independent scattering cross sections to be compared to the results of the so called direct detection experiments. They also give limits on the WIMP annihilation cross sections to four light quarks in the early universe, to be compared to the results determined by high energy gamma–ray observations by the Fermi-LAT experiment [59]. Considering the assumptions that the effective field theory approach is valid, WIMPs interact with Standard Model quarks or gluons, and they can be pair–produced at the LHC, some of the limits are competitive or substantially stronger than limits set by these direct and indirect dark matter detection experiments, particularly at small WIMP masses of $m_\chi < 10$ GeV. For masses of $m_\chi \geq 200$ GeV, the ATLAS sensitivity gets worse compared to the results from the Fermi-LAT experiment [59]. This will improve when the LHC starts operations at higher centre of mass energies. Depending on the type of interaction assumed for the SM-WIMP contact vertex, 95% CL limits on M^* range from 28 to 600 GeV.

As no deviation from the Standard Model expectation is observed, the results have also been used to probe the Z to neutrino coupling from the direct measurement of the decay width of the Z boson to a pair of weakly-interacting neutral particles. The measured invisible width is 480.14 ± 24.02 MeV, corresponding to a measured number of light neutrino pairs of 2.87 ± 0.14, consistent with the Standard Model expectations and the LEP and CDF measurements. This measurement is at the 5% precision level, comparable to the results of the L3 experiment at the 3% precision level [20]. It is better than all other LEP direct measurements. This measurement is completely independent of the LEP measurement, both experimentally and on the theoretical assumptions made, and so can be directly combined with the LEP results to improve the precision of the world average results. As an example, using the BLUE method [54] with the assumption of no correlation between total uncertainties of LEP direct (503 ± 16 MeV) and ATLAS direct measurements, a value of 496.0 ± 13.3 MeV is obtained. This new world average result from the direct measurement is consistent with the more precise indirect measurements.

The new physics search performed in this thesis can also be used for searches such as Higgs invisible searches [65], or search for unparticles [66, 67]. The techniques used in this thesis to determine the backgrounds result in high precision for a measurement in a hadronic state, enough to compete with the electroweak measurements performed at LEP. This search has also been performed at the centre of mass energy of 8 TeV in LHC. This corresponds to 10.5 fb^{-1} of integrated luminosity, and the corresponding upper limits on M_D have been updated (Appendix E), as no excess of data beyond the Standard Model expectation is observed. However, high sensitivity to very heavy states will be achieved once the centre of mass energy reaches 14 TeV.

Appendix A

List of Simulation Event Samples

Simulation event samples used in this analysis, along with their corresponding cross sections and the generator used to produce them, are presented in Tables A.1, A.2, A.3, A.4, A.5, A.6, and A.7.

Sample ID	Name	Generator	Cross Section [pb]	k–factor	N_{gen}
107680	WenuNp0_pt20	Alpgen Jimmy	6932	1.1955	3458883
107681	WenuNp1_pt20	Alpgen Jimmy	1305	1.1955	2499645
107682	WenuNp2_pt20	Alpgen Jimmy	378	1.1955	3768632
107683	WenuNp3_pt20	Alpgen Jimmy	101.9	1.1955	1008947
107684	WenuNp4_pt20	Alpgen Jimmy	25.7	1.1955	250000
144018	WenuNp5_excl_pt20	Alpgen Jimmy	5.81	1.1955	979197
144022	WenuNp6_pt20	Alpgen Jimmy	1.55	1.1955	144998
144196	WenuNp1_pt20_susyfilt	Alpgen Jimmy	7.38	1.1955	180899
144197	WenuNp2_pt20_susyfilt	Alpgen Jimmy	6.24	1.1955	134998
144198	WenuNp3_pt20_susyfilt	Alpgen Jimmy	3.47	1.1955	139999
144199	WenuNp4_pt20_susyfilt	Alpgen Jimmy	1.45	1.1955	75000
107690	WmunuNp0_pt20	Alpgen Jimmy	6932	1.1955	3462942
107691	WmunuNp1_pt20	Alpgen Jimmy	1305	1.1955	2499593
107692	WmunuNp2_pt20	Alpgen Jimmy	378	1.1955	3768737
107693	WmunuNp3_pt20	Alpgen Jimmy	101.9	1.1955	1008446
107694	WmunuNp4_pt20	Alpgen Jimmy	25.7	1.1955	254950
144019	WmunuNp5_excl_pt20	Alpgen Jimmy	5.82	1.1955	979794
144023	WmunuNp6_pt20	Alpgen Jimmy	1.54	1.1955	144999
144200	WmunuNp1_pt20_susyfilt	Alpgen Jimmy	7.08	1.1955	171000
144201	WmunuNp2_pt20_susyfilt	Alpgen Jimmy	6.14	1.1955	139900
144202	WmunuNp3_pt20_susyfilt	Alpgen Jimmy	3.42	1.1955	139899
144203	WmunuNp4_pt20_susyfilt	Alpgen Jimmy	1.44	1.1955	70000

Table A.1: Vector boson + jet simulation samples used in the mono-jet analysis including cross section times branching ratio, the k–factors and the number of generated events of the sample. The k–factors are the NNLO/LO scaling factors calculated with `FEWZ`, used to scale the overall cross section for $W \to \mu\nu$ and $W \to e\nu$ to the total NNLO inclusive cross section. "susyfilt" samples refer to the higher–statistics samples compared to the normal ones. In order to merge the two, an upper cut of 100 GeV at the truth level is applied to the $E_{\mathrm{T}}^{\mathrm{miss}}$ and the leading jet p_{T} in the lower–statistics samples.

Sample ID	Name	Generator	Cross Section [pb]	k–factor	N_{gen}
107700	WtaunuNp0_pt20	Alpgen Jimmy	6932	1.1955	3418296
107701	WtaunuNp1_pt20	Alpgen Jimmy	1305	1.1955	2499194
107702	WtaunuNp2_pt20	Alpgen Jimmy	378	1.1955	3750986
107703	WtaunuNp3_pt20	Alpgen Jimmy	101.9	1.1955	1009946
107704	WtaunuNp4_pt20	Alpgen Jimmy	25.7	1.1955	249998
107705	WtaunuNp5_excl_pt20	Alpgen Jimmy	5.82	1.1955	989595
144024	WtaunuNp6_pt20	Alpgen Jimmy	1.54	1.1955	149999
144204	WtaunuNp1_pt20_susyfilt	Alpgen Jimmy	10.9	1.1955	265000
144205	WtaunuNp2_pt20_susyfilt	Alpgen Jimmy	9.25	1.1955	204999
144206	WtaunuNp3_pt20_susyfilt	Alpgen Jimmy	5.10	1.1955	209900
144207	WtaunuNp4_pt20_susyfilt	Alpgen Jimmy	2.10	1.1955	104999

Table A.2: Vector boson + jet simulation samples used in the mono-jet analysis including cross section times branching ratio, the k–factors and the number of generated events of the sample. The k–factors are the NNLO/LO scaling factors calculated with `FEWZ`, used to scale the overall cross section for $W \to \tau\nu$ to the total NNLO inclusive cross section. "susyfilt" samples refer to the higher–statistics samples compared to the normal ones. In order to merge the two, an upper cut of 100 GeV at the truth level is applied to the $E_{\mathrm{T}}^{\mathrm{miss}}$ and the leading jet p_{T} in the lower–statistics samples.

Sample ID	Name	Generator	Cross Section [pb]	k–factor	N_{gen}
107650	ZeeNp0_pt20	Alpgen Jimmy	669.6	1.24345	6617284
107651	ZeeNp1_pt20	Alpgen Jimmy	134.6	1.24345	1334897
107652	ZeeNp2_pt20	Alpgen Jimmy	40.65	1.24345	809999
107653	ZeeNp3_pt20	Alpgen Jimmy	11.26	1.24345	220000
107654	ZeeNp4_pt20	Alpgen Jimmy	2.84	1.24345	60000
107655	ZeeNp5_pt20	Alpgen Jimmy	0.76	1.24345	20000
116250	ZeeNp0_Mll10to40_pt20	Alpgen Jimmy	3054.7	1.24345	994949
116251	ZeeNp1_Mll10to40_pt20	Alpgen Jimmy	84.9	1.24345	299998
116252	ZeeNp2_Mll10to40_pt20	Alpgen Jimmy	41.2	1.24345	939946
116253	ZeeNp3_Mll10to40_pt20	Alpgen Jimmy	8.35	1.24345	149998
116254	ZeeNp4_Mll10to40_pt20	Alpgen Jimmy	1.85	1.24345	40000
116255	ZeeNp5_Mll10to40_pt20	Alpgen Jimmy	0.46	1.24345	10000
107660	ZmumuNp0_pt20	Alpgen Jimmy	669.6	1.24345	6615230
107661	ZmumuNp1_pt20	Alpgen Jimmy	134.6	1.24345	1334296
107662	ZmumuNp2_pt20	Alpgen Jimmy	40.65	1.24345	404947
107663	ZmumuNp3_pt20	Alpgen Jimmy	11.26	1.24345	110000
107664	ZmumuNp4_pt20	Alpgen Jimmy	2.84	1.24345	30000
107665	ZmumuNp5_pt20	Alpgen Jimmy	0.76	1.24345	10000
116260	ZmumuNp0_Mll10to40_pt20	Alpgen Jimmy	3054.9	1.24345	999849
116261	ZmumuNp1_Mll10to40_pt20	Alpgen Jimmy	84.78	1.24345	300000
116262	ZmumuNp2_Mll10to40_pt20	Alpgen Jimmy	41.13	1.24345	999995
116263	ZmumuNp3_Mll10to40_pt20	Alpgen Jimmy	8.34	1.24345	150000
116264	ZmumuNp4_Mll10to40_pt20	Alpgen Jimmy	1.87	1.24345	39999
116265	ZmumuNp5_Mll10to40_pt20	Alpgen Jimmy	0.46	1.24345	10000

Table A.3: Vector boson + jet simulation samples used in the mono-jet analysis including cross section times branching ratio, the k–factors and the number of generated events of the sample. The k–factors are the NNLO/LO scaling factors calculated with `FEWZ`, used to scale the overall cross section for $Z \to e^+e^-$ and $Z \to \mu^+\mu^-$ to the total NNLO inclusive cross section.

Sample ID	Name	Generator	Cross Section [pb]	k–factor	N_{gen}
107670	ZtautauNp0_pt20	Alpgen Jimmy	669.6	1.24345	10613179
107671	ZtautauNp1_pt20	Alpgen Jimmy	134.6	1.24345	3334137
107672	ZtautauNp2_pt20	Alpgen Jimmy	40.65	1.24345	1004847
107673	ZtautauNp3_pt20	Alpgen Jimmy	11.26	1.24345	509847
107674	ZtautauNp4_pt20	Alpgen Jimmy	2.84	1.24345	144999
107675	ZtautauNp5_pt20	Alpgen Jimmy	0.76	1.24345	45000
116940	ZtautauNp0_Mll10to40_pt20	Alpgen Jimmy	3054.8	1.24345	41500
116941	ZtautauNp1_Mll10to40_pt20	Alpgen Jimmy	84.88	1.24345	79950
116942	ZtautauNp2_Mll10to40_pt20	Alpgen Jimmy	41.28	1.24345	34500
116943	ZtautauNp3_Mll10to40_pt20	Alpgen Jimmy	8.35	1.24345	15000
116944	ZtautauNp4_Mll10to40_pt20	Alpgen Jimmy	1.83	1.24345	5000
116945	ZtautauNp5_Mll10to40_pt20	Alpgen Jimmy	0.46	1.24345	2000
107710	ZnunuNp0_pt20	Alpgen Jimmy	39.62	1.2604	54949
107711	ZnunuNp1_pt20	Alpgen Jimmy	451.5	1.2604	909848
107712	ZnunuNp2_pt20	Alpgen Jimmy	196.5	1.2604	169899
107713	ZnunuNp3_pt20	Alpgen Jimmy	59.89	1.2604	144999
107714	ZnunuNp4_pt20	Alpgen Jimmy	15.51	1.2604	309899
144017	ZnunuNp5_excl_pt20	Alpgen Jimmy	3.57	1.2604	185000
144021	ZnunuNp6_pt20	Alpgen Jimmy	0.92	1.2604	114999
144192	ZnunuNp1_pt20_susyfilt	Alpgen Jimmy	12.86	1.2604	499898
144193	ZnunuNp2_pt20_susyfilt	Alpgen Jimmy	10.14	1.2604	399999
144194	ZnunuNp3_pt20_susyfilt	Alpgen Jimmy	5.40	1.2604	299998
144195	ZnunuNp4_pt20_susyfilt	Alpgen Jimmy	2.18	1.2604	184998

Table A.4: Vector boson + jet simulation samples used in the mono-jet analysis including cross section times branching ratio, the k–factors and the number of generated events of the sample. The k–factors are the NNLO/LO scaling factors calculated with `FEWZ`, used to scale the overall cross section for $Z \to \tau^+\tau^-$ and $Z \to \nu\bar{\nu}$ to the total NNLO inclusive cross section.

Sample ID	Name	Generator	Cross Section [pb]	N_{gen}
105200	T1	MC@NLO Jimmy	90.6	14983835
105204	TTbar_FullHad	MC@NLO Jimmy	76.2	1198875
108346	st_Wt	MC@NLO Jimmy	14.37	899694
108340	st_tchan_enu	MC@NLO Jimmy	6.83	299998
108341	st_tchan_munu	MC@NLO Jimmy	6.82	299999
108342	st_tchan_taunu	MC@NLO Jimmy	6.81	299999
108343	st_schan_enu	MC@NLO Jimmy	0.46	299948
108344	st_schan_munu	MC@NLO Jimmy	0.46	299998
108345	st_schan_taunu	MC@NLO Jimmy	0.46	299899

Table A.5: Top simulation samples used in the mono-jet analysis including cross section times branching ratio, and the number of generated events of the sample. The cross sections are given at the NLO with a next-to-next-leading logarithmic correction (NNLL).

Sample ID	Name	Generator	Cross Section [pb]	N_{gen}
125950	Ztoee2JetsEW2JetsQCD15GeVM40	Sherpa	0.447	199999
125951	Ztomm2JetsEW2JetsQCD15GeVM40	Sherpa	0.446	181200
125952	Ztott2JetsEW2JetsQCD15GeVM40	Sherpa	0.444	199899
125956	Ztoee2JetsEW2JetsQCD15GeVM7to40	Sherpa	0.477	100000
125957	Ztomm2JetsEW2JetsQCD15GeVM7to40	Sherpa	0.477	100000
125958	Ztott2JetsEW2JetsQCD15GeVM7to40	Sherpa	0.469	99900
128810	WWlnulnu	Sherpa	2.983	1999697
128811	WZlllnu	Sherpa	0.362	299950
128812	WZlllnuLowMass	Sherpa	1.021	299949
128813	ZZllll	Sherpa	0.267	100000
128814	ZZllnn	Sherpa	0.238	349900
143062	WZlnnn	Sherpa	0.719	100000
143063	WZqqnn	Sherpa	1.425	99900
143064	Wtolnu2JetsEW1JetQCD	Sherpa	24.54	99900
143065	Ztonunu2JetsEW1JetQCD	Sherpa	1.337	99999

Table A.6: Diboson simulation samples used in the mono-jet analysis including cross section times branching ratio and the number of generated events of the sample.

Sample ID	Name	cross section [pb]
145318	qqbar-delta2_MD_3500	0.09149
145319	qg-delta2_MD_3500	0.9751
145320	gg-delta2_MD_3500	1.159
145333	qqbar-delta3_MD_2500	0.1972
145334	qg-delta3_MD_2500	1.153
145335	gg-delta3_MD_2500	1.379
145342	qqbar-delta4_MD_2500	0.1262
145343	qg-delta4_MD_2500	0.4804
145344	gg-delta4_MD_2500	0.5877
145351	qqbar-delta5_MD_2500	0.08668
145352	qg-delta5_MD_2500	0.2447
145353	gg-delta5_MD_2500	0.3098
145360	qqbar-delta6_MD_2500	0.06143
145361	qg-delta6_MD_2500	0.1419
145362	gg-delta6_MD_2500	0.185

Table A.7: ADD signal samples for various (δ, M_D) phase space points, with p_{T} cut = 80 GeV at the generator level. CTEQ6.6 PDF set is used, and cross sections are quoted at the leading order.

Appendix B

ExoGraviton Generator

As there was no official graviton code available in the official ATLAS software Athena, a generator for producing graviton final states had to be written and included in Athena.

In the following the `ExoGraviton`[1] package used for the production of ADD gravitons in the official ATLAS software Athena, is described. It was discussed in Section 2.2 how to choose the free parameters of the generator when generating ADD samples in a region of phase space for which the calculations of the effective theory are valid. In this appendix the procedure of setting these parameters in the code is detailed. Section B.1 explains the package structure and its sub-directories, as well as the procedure of performing numerical integration to get the cross sections, and generating events, while Section B.2 includes the generator validation plots.

B.1 Package Structure

The `ExoGraviton` package includes the following sub-directories:

- `cmt`: for compilation.
- `ExoGraviton`: which contains the required header file.

[1] https://svnweb.cern.ch/trac/atlasoff/browser/Generators/ExoGraviton_i

- `share`: which contains the jobOption file to set the free parameters of the generator, generate events, and make the output pool file.

- `src`: which contains the main Fortran codes and a C++ code to interface between Fortran and `PYTHIA`.

Figure B.1 summarises the package sub-structure and what each sub-directory does. In the following sections the content of each sub-directory is explained in more details.

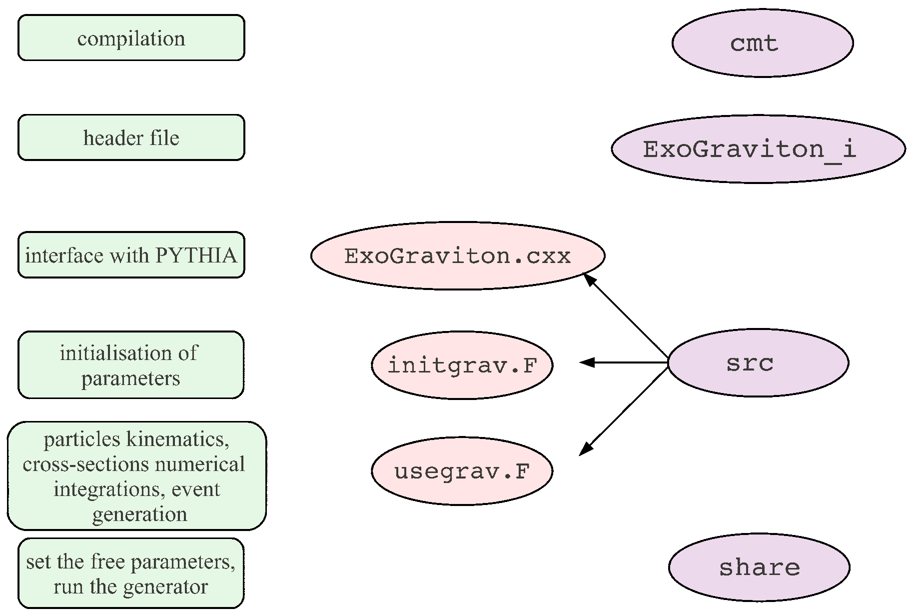

Figure B.1: Summary of the `ExoGraviton` package structure.

B.1.1 `cmt` Directory

This sub-directory includes a requirement file with the package dependencies, including a list of all Athena packages that are needed by the `ExoGraviton` package, and also a list of all source codes used by the package. The hadronisation, fragmentation, underlying events, and ISR/FSR settings are done elsewhere in `PYTHIA`, and not within the `ExoGraviton` package.

The requirement file contains the following:

```
use AtlasPolicy AtlasPolicy-*
use GeneratorModules GeneratorModules-* Generators

private
use Pythia      Pythia-*      External

library ExoGraviton_i *.cxx *.F
apply_pattern installed_library

apply_pattern declare_joboptions files="*.py"
```

B.1.2 ExoGraviton Directory

This sub-directory contains the header file, `ExoGraviton.h`, with the declaration of all the functions used in `src/ExoGraviton.cxx`. Three functions are defined, and will be explained in section B.1.3:

```
extern void WriteGravParam(int,int,double);
extern "C" void readgravparamint_(int*,int*);
extern "C" void readgravparamdbl_(int*,double*);
```

B.1.3 src Directory

This sub-directory contains two Fortran codes: one for initialising the generator's parameters, which are set in the jobOption by the user as explained in section B.1.4, and one for calculating the cross sections and kinematics of the particles. These Fortran codes are the interfaced with `PYTHIA` via `ExoGraviton.cxx`.

`ExoGraviton.cxx` This source code defines two functions that act as interfaces between `PYTHIA` and `ExoGraviton` Fortran codes: one for reading the values of the parameters from the jobOptions file (`readgravparamint`), and one for writing them to `initgrav.F` for initialisation (`WriteGravParam`, which is called from `initgrav.F`).

`initgrav.F` Initialisation of the free parameters is done here, by calling the `readgravparamint` function defined in `/src/ExoGraviton.cxx`. Types of the two incoming beams, proton beams here, are also specified in this code via:

```
IDBMUP(1)=2212
IDBMUP(2)=2212
```

A weight is assigned to each sampled point in the allowed phase space, equal to the differential cross section evaluated at that point. The numerical integration of these weights converge to the total cross section of the process. In `PYTHIA` this weight is called `XWGTUP` :

```
XWGTUP=sigev
```

where `sigev` is the differential cross section evaluated at each sampled phase space point, as explained in Sec. B.1.3.

Events are accepted, i.e. generated, if $\frac{\text{event weight}}{\text{maximum differential cross section}}$ is greater than a random generated number. The value of the maximum differential cross section is set in the jobOption file by the user[2] (Sec. B.1.4). If for a phase space point the weight is larger than the chosen maximum differential cross section, the maximum will be replaced by that weight. Events generated before this replacement would be incorrectly distributed. Therefore, a bad choice of the maximum differential cross section may require re-generating events with a better starting value. On the other hand if a very large

[2] In the case of running the Fortran codes in a stand-alone mode, it is directly set in the `initgrav.F`.

value is chosen, the speed of generation will be low due to small values of the ratio of the event weight to the maximum differential cross section.

For a Monte Carlo generator with the generation procedure as explained, the weighting strategy [3] - specified via `IDWTUP` - is equal to unity:

```
IDWTUP=1
```

This means all accepted (generated) events will be assigned a weight of one.

`usegrav.F` This is the main code that performs the sampling of the phase space, calculates the differential cross section of each phase space point, and generates events [4], as is schematically shown in Figure B.2.

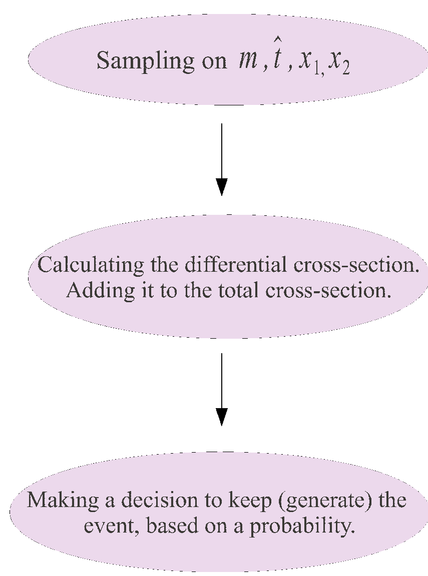

Figure B.2: General procedure of event generation and cross section calculations in the `ExoGraviton` package.

[3]The strategy used to mix different processes.

[4]This code has first been written in Fortran by "Georges Azuelos" and "Pierre-Hugues Beauchemin". In this section only the general procedure is explained. The reader is referred to the code: https://svnweb.cern.ch/trac/atlasoff/browser/Generators/ExoGraviton_i/trunk/src/usegrav.F, for further details.

The fraction of protons momenta carried by each of the two incoming partons is set by using the PYTHIA random function[5] PYR(0), generating random numbers between XMIN[6] $= \frac{\hat{s_{min}}}{E_{cm}^2}$ and 1 which corresponds to when the two incoming partons carry all the energy of the protons :

```
X1=XMIN**PYR(0)
X2=XMIN**PYR(0)
SHAT=X1*X2*ECM**2
```

where SHAT is the $\hat{s}$ of the process. The reason for using the random number generator as a power of XMIN instead of using a linear form is to sample mainly in the high x1-x2 region and increase the speed of generation. $\hat{s}_{min}$ is specified by equations of momentum conservation and noting that the p_{T} of the outgoing parton is above p_{T}^{Cut}, with p_{T}^{Cut} being set in the jobOption file.

The maximum mass of the graviton, set in the jobOption file, is chosen to be equal to M_D, above which the calculations of the effective field theory are not reliable. Also a maximum mass is calculated considering the event kinematics, momentum conservation, and assuming $p_{\mathrm{T}}^{parton} > p_{\mathrm{T}}^{Cut}$. The mass of the graviton cannot be larger than this value, which equals : $m_{max}^2 = \hat{s} - p_{\mathrm{T}}^{Cut}\sqrt{\hat{s}}$. The minimum value of these two is set as the maximum mass of the graviton :

```
am1 = shat-2*ptcut*sqrshat
ammax2=min(am1,amgravmax**2)
```

where am1 is the square of the maximum mass from kinematic constraints, and amgravmax is the maximum mass set in the jobOption by the user, usually chosen to be equal to M_D.

[5]This function generates a random number uniformly in the range]0,1[, excluding the endpoints.
[6]The term $\hat{s}_{min}$ corresponds to the $\hat{s}$ of the process when $p_{\mathrm{T}}^{\mathrm{parton}} = p_{\mathrm{T}}^{Cut}$.

Once the minimum (which has been set to zero[7]) and maximum masses of the graviton are specified, a random value between the two is generated for the graviton mass [8]:

```
AMGRAV2=ammin2+(ammax2-ammin2)*PYR(0)
```

where `ammin2` and `ammax2` are the square of the minimum and maximum masses of the graviton. The square form is chosen in order to have the F_i functions (Eq. 2.10 - 2.12) linear in the mass variable, once the variable of the mass integral is changed.

The sampling on $\hat{t}$, the 4-momentum transfer, is done by generating a random number in the interval $[th1, th2]$, where $th1$ and $th2$ are the two solutions of the quadratic equation obtained from the definition of $\hat{t}$ [9], by setting $p_{\mathrm{T}}^{parton} = p_{\mathrm{T}}^{Cut}$. They correspond to the minimum and maximum values $\hat{t}$ can have[10] in a given event, i.e. given a choice of x_1, x_2, and m. Putting `PYR(0)` in the power samples mainly in the high-$\hat{t}$ phase space.

```
that = th1 * (th2/th1)**pyr(0)
```

In order to get the full kinematics, the direction in the transverse plane ϕ, should also be specified. It is calculated by generating a random value between 0 and 2π as is not constrained by any kinematic condition and the differential total cross section does not depend on it:

```
phi=2*paru(1)*PYR(0)
```

where `paru(1)` is the value of π in PYTHIA.

[7]Graviton can have a zero rest mass due to the fact that gravity is a longe-range force.

[8]The mass spacing between two kk graviton modes is small, and the mass distribution can be assumed to be continuous, corresponding to a continuous graviton momentum in the extra dimensions. Each event has a different generated graviton mass. Summing over the differential cross sections of all these different modes will give the total cross section, as explained in Section 2.2.

[9]$\hat{t} = (p_1^2 - p_3^2)^2$, where p_1 and p_3 are the 4-momenta of the incoming parton and the outgoing graviton. It can be written in terms of $\hat{s}$, m_G, and p_{T}.

[10]These minimum and maximum solutions are: $\frac{-(\hat{s}-m_G^2)\pm\sqrt{(\hat{s}-m_G^2)^2-4\hat{s}p_{\mathrm{T,Cut}}^2}}{2}$

Now that all the four variables (m, $\hat{t}$, x_1, x_2) are sampled, the differential cross section in each of the Equations 2.7-2.9 can be calculated, which is called `sig0` later in the text. To get the full weight, some additional factors related to the parton distribution functions (PDF), and Jacobians of the transformations need to be included as explained below.

PDFs are specified by a call to the PYPDFU function in `PYTHIA`, which takes as input the flavour of the probed particle, and the values of `xi` and Q^2 at which the PDFs are evaluated. An array of dimension XP:(-25:25) [11] which contains the evaluated PDFs[12] is produced as the output. This is done via:

```
CALL PYPDFU(2212,X1,Q2,XP1)
```

for each proton beam. `Q2` is the momentum transfer set to $\frac{1}{2}m_{kk}^2 + p_{\mathrm{T}}^2$, equivalent to `mstp(32) = 2` in `PYTHIA`, where m_{kk} is the mass of the graviton mode, and p_{T} is the transverse momentum of the outgoing parton. The term `X1` is the fraction of proton's momentum carried by the parton, and sampled earlier.

For each of the three graviton production sub-processes, a sub-routine has been written to calculate the corresponding differential cross section at a sampled phase space point. The contribution of all possible parton scatterings are taken into account considering their corresponding evaluated PDFs. As an example, in the process $qg \to qG$ the dominant contribution to the cross section is from an up or a down valence quark, but sea quarks and anti–quarks can also contribute. This is taken into account by looping over different quark and anti–quark flavours and adding their contributions to the cross section[13]. In the case of $qg \to qG$:

```
sigev=0.
sigi(0,0)=0.
```

[11]The array components are ordered according to the standard particle KF codes, and the gluon corresponds to position 0 as well as 21.

[12]For each parton j carrying the fraction x_i of the proton's momentum, $x_i f_j(x_i, Q^2)$ will be returned.

[13]This is done for $q\bar{q} \to gG$ and $qg \to qG$.

```
do i1=-5,5
  if(i1.ne.0)then
    i2=21
    sigi(i1,0)=sig0*xp1(i1)*xp2(i2)
    sigi(0,i1)=sig0*xp1(i2)*xp2(i1)
    sigev=sigev+sigi(i1,0)+sigi(0,i1)
  end if
end do
```

where 21 is the gluon standard KF code, `sig0` is quoted in Eq. 2.8 in Sec. 2.2.2, and `xpi` are the evaluated PDFs.

In order to have events mostly populated in part of the allowed phase space with high differential cross sections a change in the integration variables has been done; integration variables of $\hat{t}$, x_1, and x_2 integrals are transformed to exponential forms. The Jacobians of these transformations and the phase space volumes should also be included in the weight. Therefore the final differential cross section at the sampled phase space point is:

```
sigev=sigev * wgt1 * wgt2 * conv * phspv
```

where `wgt1` is the volume of the mass phase space obtained from integration, after changing the integration variable in order to have the F_i functions linear in mass. The term `wgt2` is the Jacobian of the transformation in the $\hat{t}$ integral, multiplied by the volume of the allowed $\hat{t}$ phase space, `log(th1/th2)`.

The terms `wgt1` and `wgt2` are equal to :

```
wgt1=ammax2-ammin2
wgt2 = (-that) * log(th1/th2)
```

where `that` is the $\hat{t}$ of the process.

`conv` is a conversion factor to convert GeV^{-2} to pb, and `phspv` is the allowed volume of the phase-space in the $x1$-$x2$ plane, obtained by integrating over the allowed $x1$-$x2$ plane after change of the integration variables to exponential forms, equal to:

```
PHSPV=LOG(XMIN)**2/2
```

The output of PYPDFU, the xpi, is $x_i f_j(x_i, Q^2)$ for each parton j carrying a proton momentum fraction x_i. This cancels the additional x_i factor in the Jacobian of the transformation. Hence only the logarithmic part remains [14]. The integral boundaries after change of variable will be log(XMIN) and 0, since : XMIN $< x_i < 1$.

Once `sigev` is calculated, it is assigned to the sampled point of the phase space as a weight, as has been explained in Section B.1.3 :

```
XWGTUP = sigev
```

The total cross section is the sum of the differential cross sections of all the trials[15], although not all of them will be included in the generated event sample:

```
sigtot=sigtot+sigev
```

where `sigtot` is the total cross section of the sub-process. This total cross section is more precise than the one obtained from the kinematic distributions of the generated events, since the former is obtained by considering all the trials, but the latter only includes the generated (accepted) events.

Once $\hat{s}$, $\hat{t}$, and graviton mass are specified via the sampling procedure as explained, the 4-momenta of the outgoing particles in the lab frame can be calculated.

Particles pdgIDs are specified via `IDUP`. The graviton pdgID is chosen to be 39 in

[14] In fact the integration should be done over $x1$-$x2$ plane with weights equal to $f_j(x_1, Q^2)$ and $f_j(x_2, Q^2)$ which have already been taken into account when looping over various scatterings.

[15] The "accepted" events are a subset of the "tried" events (number of trials) in `PYTHIA`, accepted based on a probability as is explained in Section B.1.3.

PYTHIA6:

```
IDUP(3)=39
```

The status codes, being -1 for an incoming particle of the hard scattering process, and 1 for an outgoing particle in the final state, are specified in each sub-routine for each of the four particles via ISTUP:

```
ISTUP(1)=-1
ISTUP(2)=-1
ISTUP(3)=1
ISTUP(4)=1
```

Positions of the first and last mothers[16] of the outgoing particles are specified via:

```
do i=3,4
  MOTHUP(1,i)=i-2
  MOTHUP(2,i)=0
end do
```

To specify the particles colour flow which is required for the parton showering, colour tags ICOLUP(1,i) and ICOLUP(2,i) are used. These are integer tags for the colour flow lines passing through the colour and anticolour of particle i, respectively. Any particle with colour (anti-colour) should have the first (second) ICOLUP non-zero. These tags can be any non-zero integer. For example for $gg \to gG$ one can set the colour flow as follows:

```
icolup(1,1)=101
icolup(2,1)=102
icolup(1,2)=102
```

[16] Decay products normally have only one mother. For the second mother, either MOTHUP(2,i) = 0 or MOTHUP(2,i) = MOTHUP(1,i).

```
icolup(2,2)=103
icolup(1,4)=101
icolup(2,4)=103
```

where `icolup(i,4)` is the colour or anti-colour tag of the outgoing gluon. In the sub-process $qg \to qG$ one has to set the same integer for the colour of the incoming quark as for the anti-colour of the incoming gluon. In the case of the ADD graviton, there is only one possible colour flows for all three channels of each of the three sub-processes. Hence they need to be set only once for each sub-process.

B.1.4 `share` Directory

This sub-directory contains the jobOption file in which the random seed and the free parameters of the generator are set by the user. Since the generator uses `PYTHIA`, it has to import the relevant module:

```
from Pythia_i.Pythia_iConf import Pythia
```

The maximum number of events to be generated can be set as follows:

```
from AthenaCommon.AppMgr import ServiceMgr
theApp.EvtMax = 100
```

The generator is called via:

```
Pythia.PythiaCommand = ["pyinit user exograviton"]
```

This requires adding the header file as well as a call to the function defined in `ExoGraviton.cxx`, to the source code `Pythia.cxx` in the `Pythia_i` package:

```
#include "ExoGraviton_i/ExoGraviton.h"
```

```
if (myblock == "grav")
{
::WriteGravParam(myint6, myint1, (double)myfl0);
}
```

This calls the `ExoGraviton` generator and initialises the generator parameters, as is explained is Sec. B.1.3.

ExoGraviton should also be added to `Pythia_i/src/upinit_i.F` and `Pythia_i/src/upevnt_py.F`:

```
IF(ATLASCHOICE.EQ.EXOGRAVITON) CALL INITGRAV
```

```
IF(ATLASCHOICE.EQ.EXOGRAVITON) CALL USEGRAV
```

The free parameters of the generator are set in the jobOption file via:

```
grav x value
```

where x = 1-7: there are 7 free parameters in the generator as listed below:

- grav 1 : number of extra dimensions. This should be an integer[17].
- grav 2 : sub-process number. This should be 1110, 1111, or 1112, corresponding to $q\bar{q} \to gG$, $qg \to qG$, and $gg \to gG$, respectively.
- grav 3 : centre of mass energy in GeV.
- grav 4 : value of M_D in GeV.
- grav 5 : value of p_{T}^{Cut} of the outgoing parton at the generator level, in GeV.

[17] Having one extra dimension is excluded since it results in deviations from the Newton's law of gravity at distance scales already explored.

- grav 6 : maximum mass of the graviton mode, usually set to M_D, since above this value the calculations of the low-energy effective field theory are not reliable: Sec. 2.2.

- grav 7 : maximum value of the differential cross section in mb. If this value is lower than that of a sampled point in the phase space, PYTHIA will update this value.

The name of the output pool file can be set in the jobOption file as the following:

```
from AthenaPoolCnvSvc.WriteAthenaPool import AthenaPoolOutputStream
Stream1 = AthenaPoolOutputStream( "StreamEVGEN" )
Stream1.OutputFile = "Pythia_Graviton.pool.root"
```

B.1.5 Event Generation

After setting up the Athena software, the ExoGraviton package should be checked out and compiled from the cmt directory.

To run the generator, after setting the values of the parameters and the maximum number of events to be generated in the jobOption file, as explained in Section B.1.4, the generator can be run from the share directory via:

```
athena.py jobOptions.pythiaExo.py > log&
```

This makes a pool file (Pythia_Graviton.pool.root) containing the generated events, as well as printing out the value of the total cross section in the log file.

The larger the number of generated events, the more precise the result of the numerical integration would be, since more points will be sampled in the allowed phase space for performing the numerical integration.

Once the pool file is made, it can be converted to ESD, AOD, or D3PD formats depending on the need of the user.

B.2 Generator Validation

In order to validate the ExoGraviton package, kinematic distributions at truth level have been compared to those obtained from running the stand-alone Fortran code. Figure B.3 shows the distributions of the leading jet and graviton p_{T} at truth level for $qg \to qG$ events at 7 TeV centre of mass energy, for $M_D = 2$ TeV, and $p_{\mathrm{T}}^{Cut} = 80$ GeV. CTEQ5L PDF set has been used for both the package and the stand-alone code. Good agreement is observed between the two distributions.

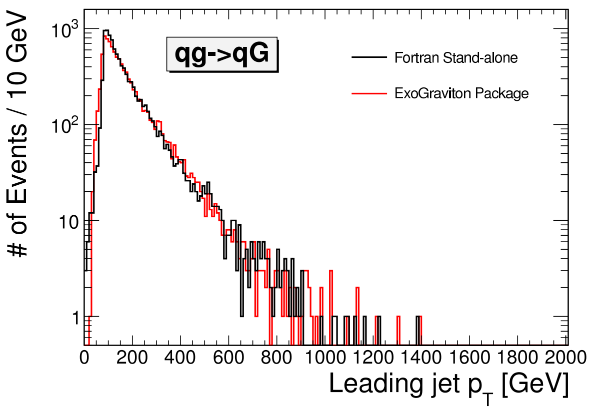

Figure B.3: Leading jet p_{T} (left) and graviton p_{T} (right) distributions at truth level for centre of mass energy of 7 TeV, from running both the ExoGraviton package and the stand-alone Fortran code, for the $qg \to qG$ sub-process.

Appendix C

Cosmic Background

C.1 Introduction

Energetic cosmic muons showering in the ATLAS calorimeter can result in high p_{T} jets and fake $E_{\mathrm{T}}^{\mathrm{miss}}$, mimicking the mono jet signature. The cosmic muon shower is an electromagnetic shower as it mostly contains electrons and photons. Therefore it has a smaller longitudinal length compared to hadronic showers, and is mostly contained either entirely in the Tile or Electromagnetic calorimeters depending on where the muon starts to shower. In the following the effect of four cleaning cut variables to remove this source of background is investigated.

Events are required to pass the following kinematic cuts specific to a mono-jet topology[1]:

1. Leading jet $p_{\mathrm{T}} > 80$ GeV, and $|\eta| < 2.5$
3. $E_{\mathrm{T}}^{\mathrm{miss}} > 80$ GeV
4. No second jet above 30 GeV in p_{T}
5. No fourth jet above 20 GeV in p_{T}

[1] This study was done in 2010. Therefore the selection cuts of the current mono-jet analysis were not applied.

C.2 Cleaning Cuts

Four cleaning cuts based on the characteristics of cosmic showers are defined, and are applied to the leading jet in the event.

C.2.1 Electromagnetic Fraction

Electromagnetic fraction (EMF) of a jet is defined as the ratio of the jet energy in the electromagnetic calorimeter to the total jet energy. Due to the shorter longitudinal length of the cosmic shower compared to the hadronic showers, it is mostly contained in either the electromagnetic or the hadronic calorimeters depending on where the cosmic muon starts to shower. Therefore the EMF of a cosmic shower is either close to zero or one, whereas the jets from the parton hadronisation have a wide range of values for EMF. Figure C.1 shows the EMF distribution of the leading jet for cosmic background events, ADD graviton signal, and the irreducible electroweak background $Z(\nu\bar{\nu})$+jets events[2]. A lower cut of 0.1 on EMF removes a large fraction of cosmic events with a negligible impact on the signal.

The efficiency of this cut, defined as the fraction of mono-jet events that pass this cleaning cut, is 99% for both the ADD signal and $Z(\nu\bar{\nu})$+jets events. The cosmic rejection is 47%, using Cosmic Run 92160.

C.2.2 Number of Topological Clusters

The number of topological clusters in the leading jet is lower in cosmic showers compared to the jets from the collision, as shown in Fig. C.2. A lower cut of 4 on the number of topological clusters has an efficiency of 98% and 99% for ADD signal and $Z(\nu\bar{\nu})$+jets,

[2]The $Z(\nu\bar{\nu})$+jets simulation sample considered here is a combination of two samples with a low and a high p_T cut at the generator level. An upper p_T cut of 400 GeV at the truth level is applied to the sample with the lower p_T cut, in order to avoid double counting of some events and to reduce the statistical fluctuations.

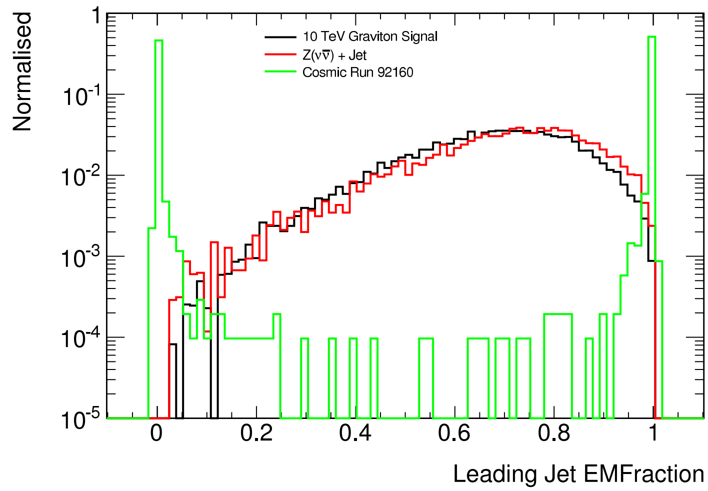

Figure C.1: Electromagnetic fraction of the leading jet for cosmics, ADD graviton signal, and Z($\nu\bar{\nu}$)+jet events.

respectively, with a cosmic rejection of 94% for Cosmic Run 92160.

There is a high correlation[3] between the two cuts for the ADD signal and Z($\nu\bar{\nu}$)+jets events. However, they are almost uncorrelated for cosmic events, with 10% and 21% correlation only, as estimated from the two cosmics runs 92160 and 139340, respectively. This ensures that applying both cuts will effectively remove cosmic events while having a negligible effect on the signal efficiency.

Figure C.3 shows the impact of correlation between the two cuts for cosmics Run 92160 and the ADD signal. As can be seen, a cut on the number of clusters removes cosmic events with a high EMF leading jet which had passed the EMF cut. Table C.1 shows the summary of the efficiencies and correlations for these two cuts.

C.2.3 Charge Fraction and Number of Tracks

When cosmic muons shower in the upper part of the calorimeter before entering the volume of the inner detector, the resulting jets have a low number of tracks as most of the electrons and photons of the shower lose large amount of their energy and stop before

[3]Defined as $\frac{\texttt{Number of events passed the kinematic, EMF, and number of clusters cuts}}{\texttt{Number of events passed the kinematic and EMF cuts}}$

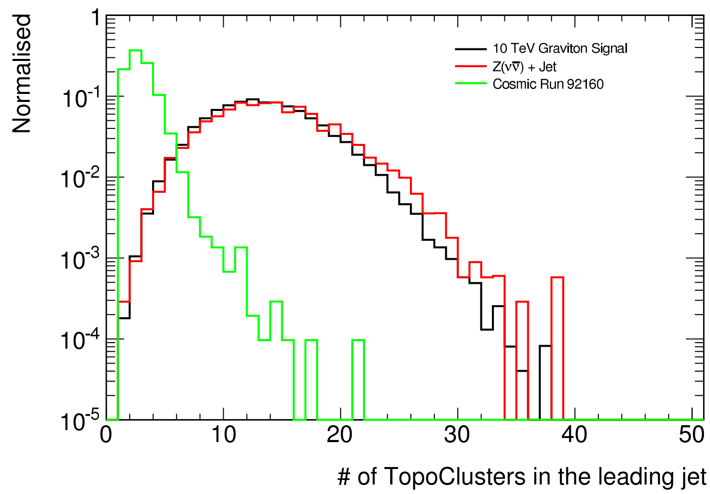

Figure C.2: Number of topological clusters in the leading jet for cosmics, ADD graviton signal, and Z($\nu\bar{\nu}$)+jet events.

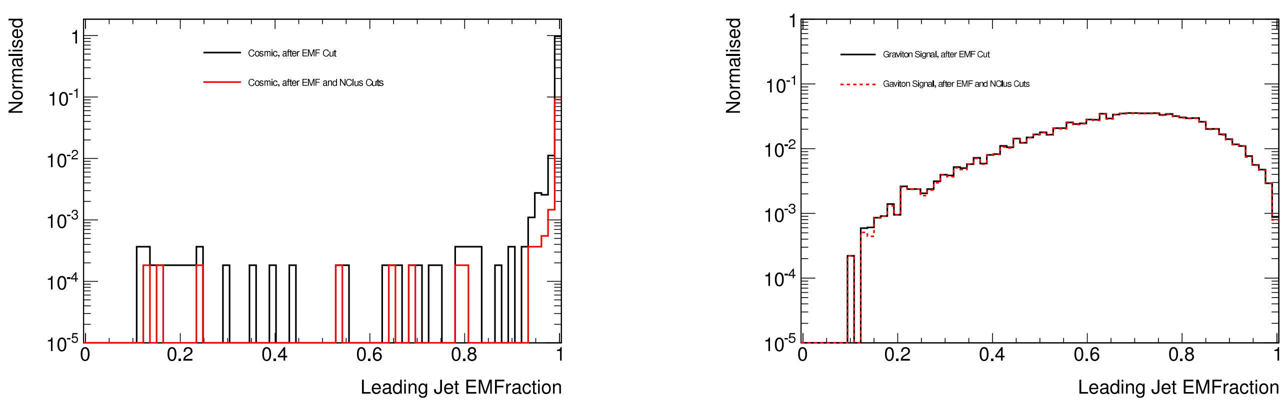

Figure C.3: Correlation between electromagnetic fraction and number of topological clusters in the leading jet for cosmic run 92160 and ADD graviton signal. Plots are normalised to the area of the black distribution.

Sample	EMF Cut	number Of Topoclusters Cut	Correlation
ADD signal	99%	98%	98%
Z($\nu\bar{\nu}$)+jet	99%	99%	99%
Cosmic run 92160 (rejection)	47%	94%	10%

Table C.1: Efficiencies and correlations of the two cleaning cuts - electromagnetic fraction and number of topological clusters- for the ADD signal, Z($\nu\bar{\nu}$)+jet and cosmic events. For cosmic events the rejections are given.

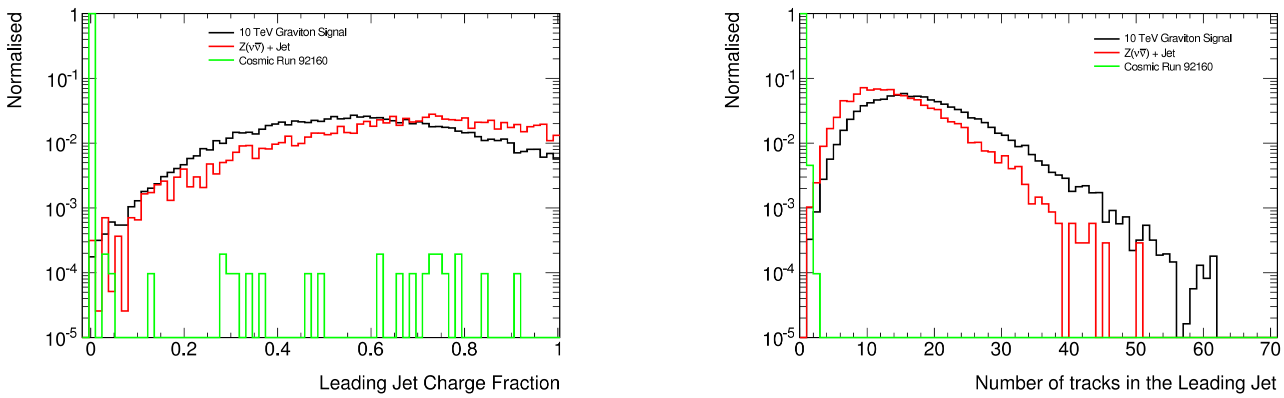

Figure C.4: Charge fraction and number of tracks associated to the leading jet for cosmics, ADD graviton signal, and Z($\nu\bar{\nu}$)+jet events.

Sample	Charge Fraction Cut	number Of Track Cut	Correlation
ADD signal	99%	99%	99%
Z($\nu\bar{\nu}$)+jet	99%	97%	97%
Cosmic run 92160(rejection)	99%	100%	10%

Table C.2: Efficiencies and correlations of the two cleaning cuts - charge fraction and number of tracks- for the ADD signal, Z($\nu\bar{\nu}$)+jet and cosmic events. For cosmic events the rejections are given.

reaching the inner detector. Based on this, two variables are defined: jet charge fraction, which is the ratio of the p_{T} sum of all the matched tracks[4] to the jet p_{T}, and the number of matched tracks to the leading jet. Both variables are expected to have small values for cosmic jets, as shown in Fig. C.4. A lower cut of 0.1 and 3 on the leading jet charge fraction and number of tracks, respectively, removes most of the cosmic events.

Figure C.5 shows the impact of the correlation between the two cuts for cosmics and the ADD signal respectively. The correlation is high for signal, and much lower for cosmic events. The efficiencies of the two cuts show that the cut on the number of tracks has a higher rejection power. Table C.2 is a summary of all the efficiencies and correlations for these two cuts.

[4]All tracks with p_{T} above 1 GeV, which have a ΔR less than 0.4 with respect to the jet axis are considered. The value of 0.4 is chosen based on the jet reconstruction method which was AntiKt4LCTopoJets.

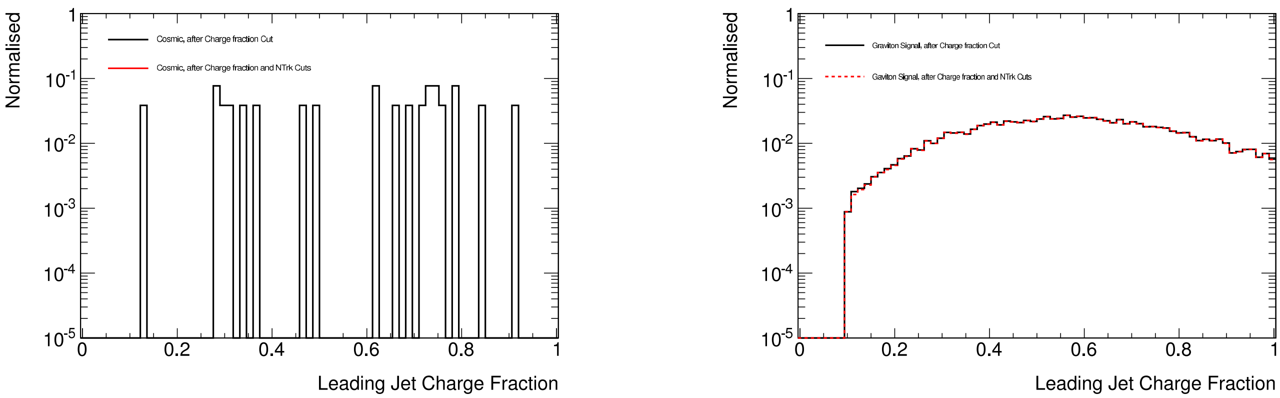

Figure C.5: Correlation between charge fraction and number of tracks in the leading jet for cosmic run 92160 and the ADD graviton signal events.

Figure C.6 shows the p_{T} and missing $E_{\mathrm{T}}^{\mathrm{miss}}$ distributions of the cosmic run after applying the following four cuts one by one:[5]

- Electromagnetic Fraction > 0.1
- Number of topo - Clusters > 4
- Charge Fraction > 0.1
- Number of tracks > 3

Table C.3 summarises the efficiencies of all the 4 cuts for the ADD signal, Z($\nu\bar{\nu}$)+jets, and cosmic events.

When a cosmic ray event overlays a low p_{T} QCD multi–jet event with pile-up, which is very frequent, the rejection power of the cuts slightly gets reduced. The method to estimate the residual non–collision background is explained in Sec. 9.2.

[5]The ADD signal and Z($\nu\bar{\nu}$)+jets distributions are normalised to an integrated luminosity of $100^{-}1pb$. For the cosmic run, the rate of the `L1Calo` data stream has been considered, as well as a rough estimate of the active ATLAS time corresponding to an integrated luminosity of $100^{-}1pb$, and an instantaneous luminosity of $10^{31}cm^{-2}s^{-1}$.

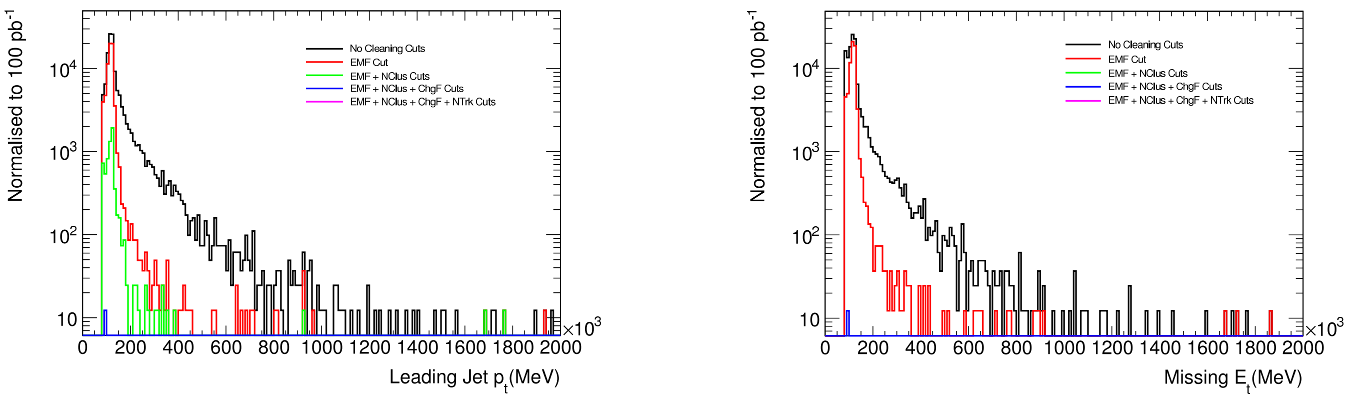

Figure C.6: Leading jet p_{T} and $E_{\mathrm{T}}^{\mathrm{miss}}$ distributions for cosmic Run 92160 after a step-by-step application of the four cleaning cuts.

ADD signal	Z($\nu\bar{\nu}$)+jet	Cosmic run 92160(rejection)
98%	96%	100%

Table C.3: Efficiencies of all the 4 cleaning cuts for signal, Z($\nu\bar{\nu}$)+jets and cosmic run 92160.

Appendix D

Additional Limit Plots with the 7 TeV Collision Data

The expected and observed upper limits on $\sigma \times A \times \epsilon$, and the resulting 95% CL expected and observed LO and NLO lower limits on M_D are shown in Figures D.1–D.3. A comparison between LO and NLO limits is also shown in Fig. D.4 for each signal region.

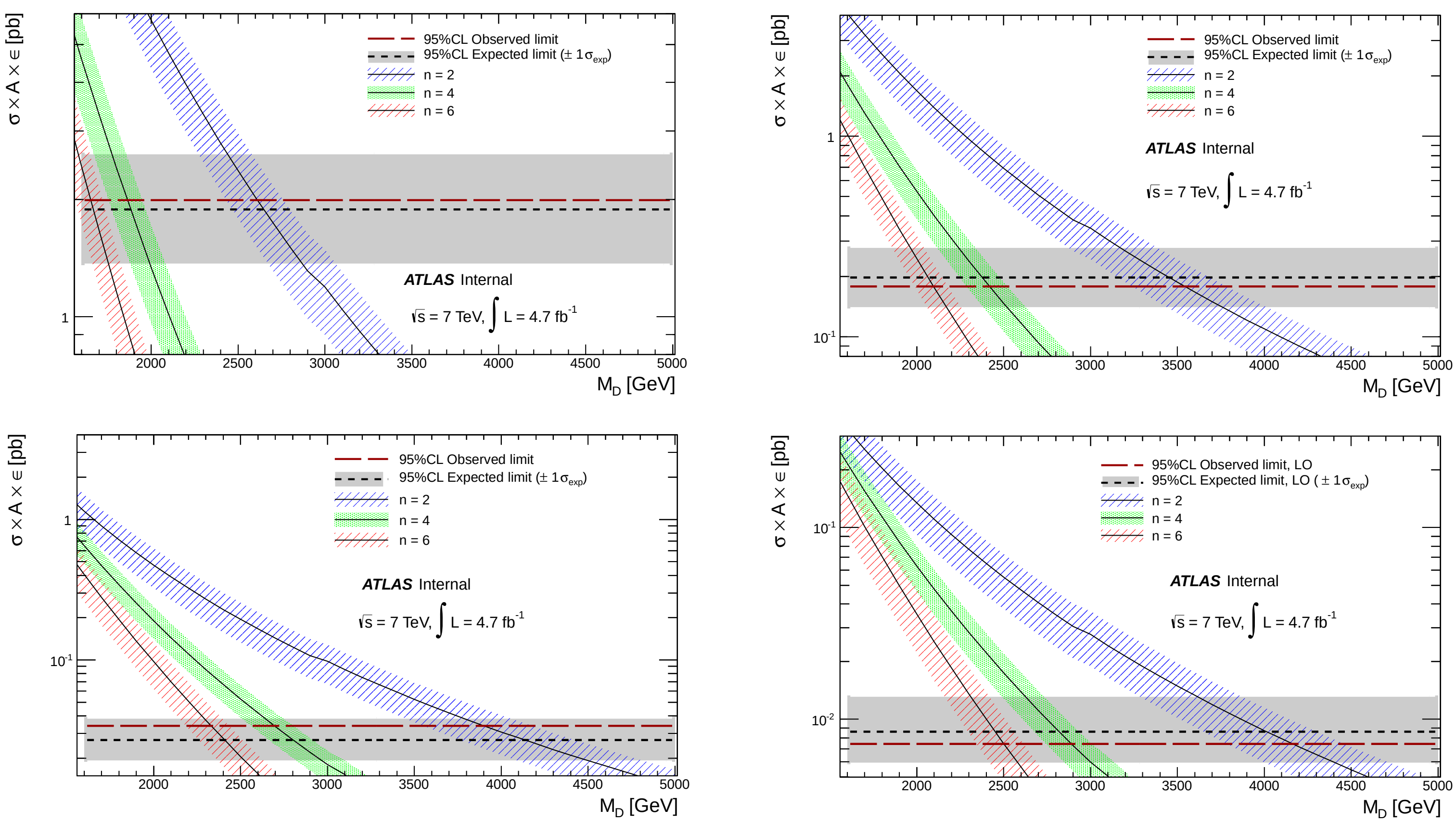

Figure D.1: 95% CL expected and observed upper LO limits on $\sigma \times A \times \epsilon$ [pb] (red and blue dashed horizontal lines), along with signal $\sigma \times A \times \epsilon$ for 2, 4, and 6 extra dimensions, in signal regions $1 - 4$. The error bands on the theoretical curves are the total theoretical uncertainties (PDF, ISR/FSR, and Scale Q uncertainties). The horizontal lines are obtained after taking into account the JES uncertainty correlation between signal and background, as well as luminosity, trigger, and MC statistical uncertainties on the signal yields. The grey $\pm 1\sigma$ band around the expected limit is the variation expected from statistical fluctuations and experimental systematic uncertainties on the Standard Model and signal processes.

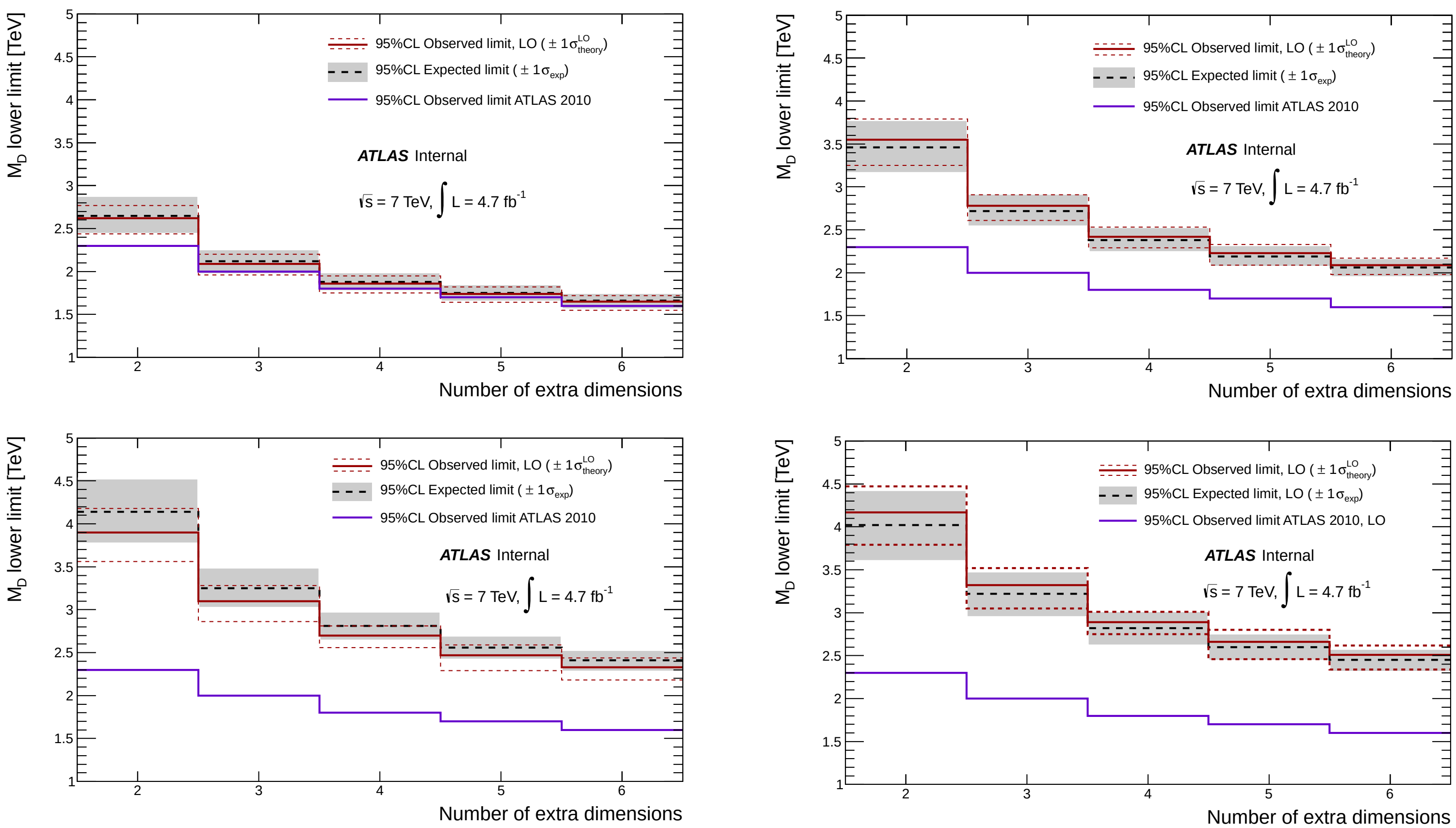

Figure D.2: 95% CL observed and expected lower LO limits on M_D [TeV] in signal regions 1–4. The red dashed error bands around the observed limit show the impact of the total signal theoretical uncertainties (PDF, ISR/FSR, and Scale Q uncertainties) on the limits. The grey $\pm 1\sigma$ error bands on the expected limits show the effect of the statistical fluctuations and experimental systematic uncertainties on the Standard Model and signal processes.

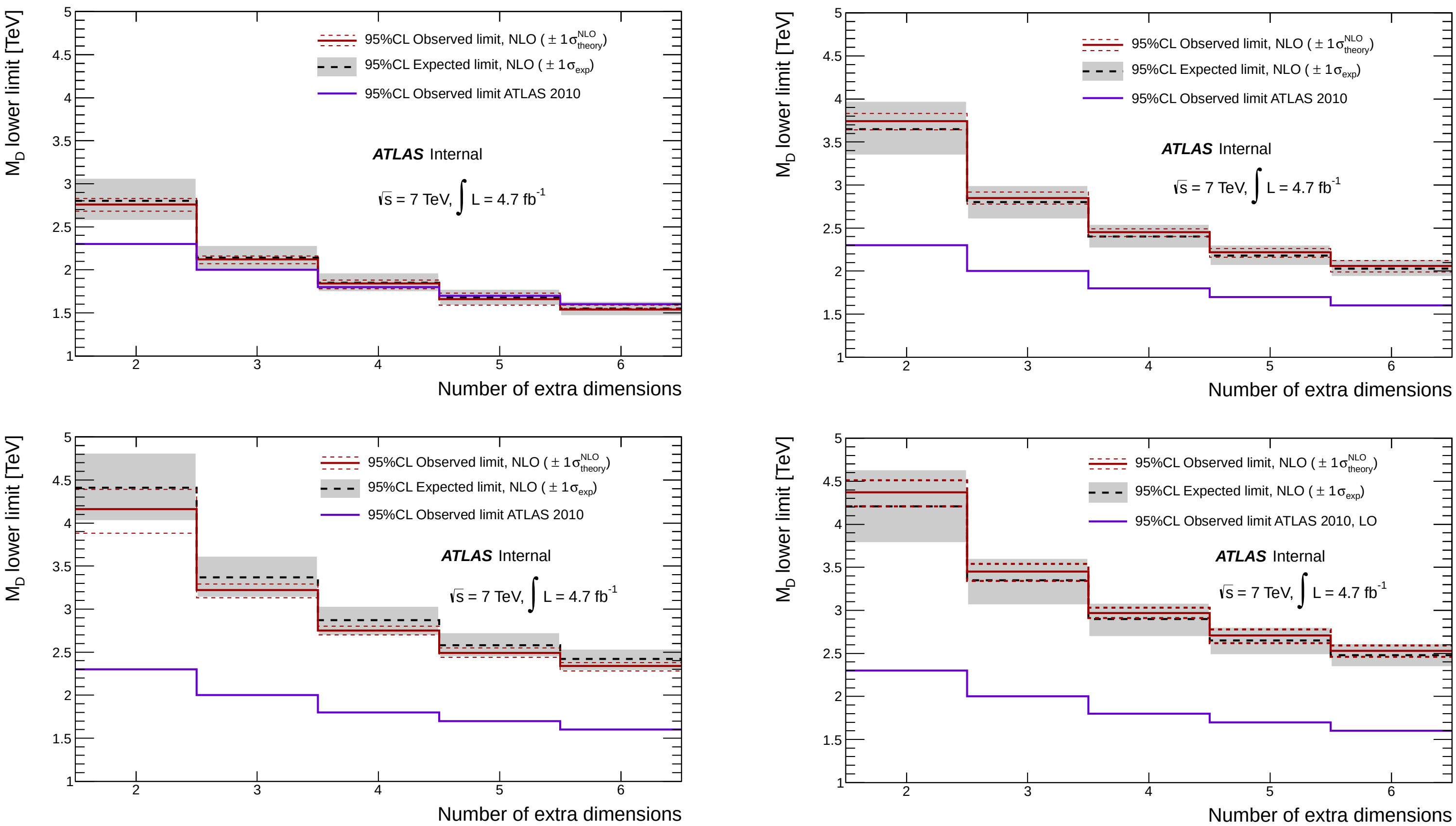

Figure D.3: 95% CL observed and expected lower NLO limits on M_D [TeV] in the signal regions 1–4. The red dashed error bands around the observed limit show the impact of the total signal theoretical uncertainties (PDF, ISR/FSR, and Scale Q uncertainties) on the limits. The scale uncertainties are reduced due to the inclusion of the NLO calculations. The grey $\pm 1\sigma$ error bands on the expected limits show the effect of the statistical fluctuations and experimental systematic uncertainties on the Standard Model and signal processes.

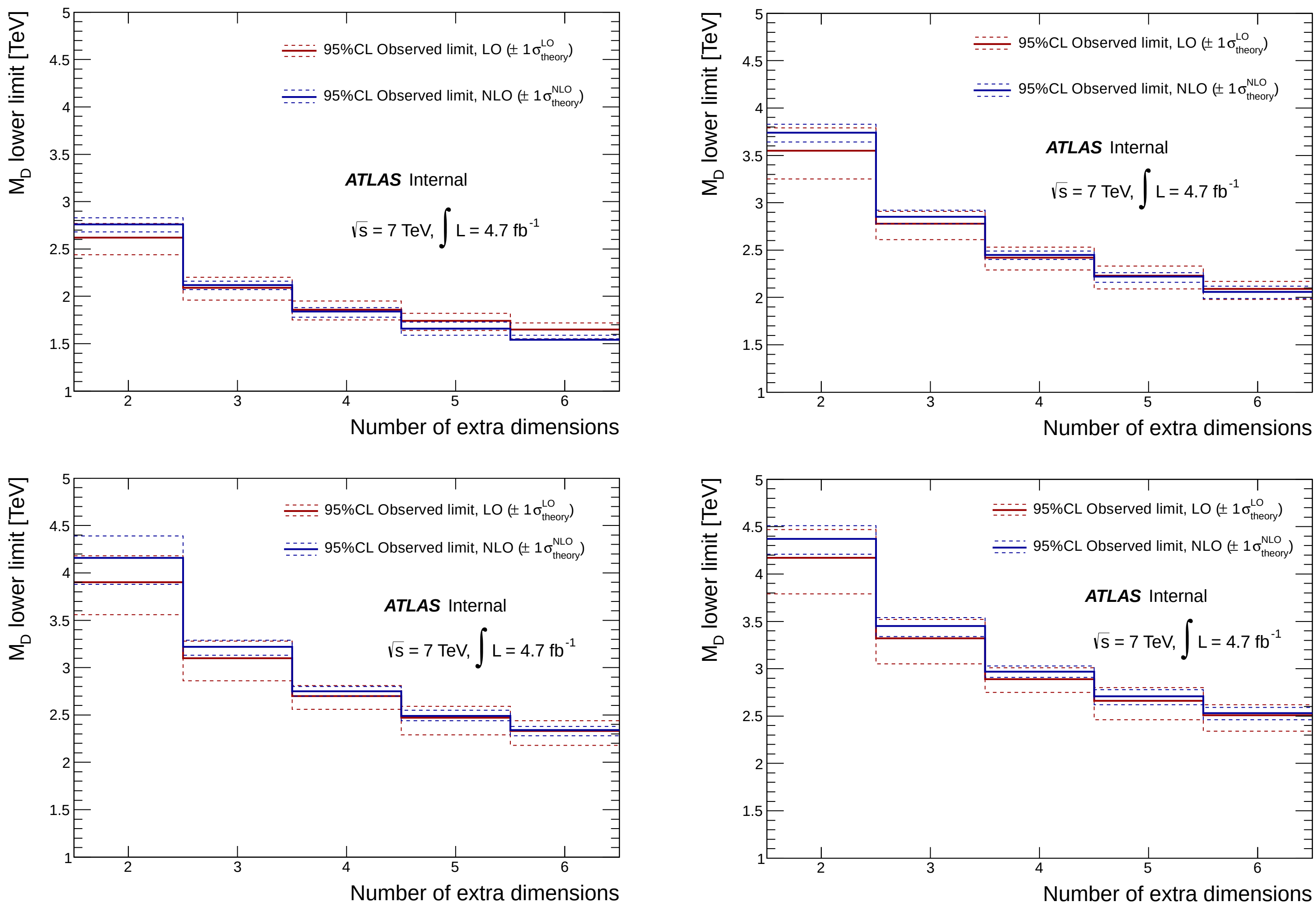

Figure D.4: Comparison between NLO and LO 95% CL observed and expected lower limits on M_D [TeV] in the signal regions 1–4, including the corresponding $\pm1\sigma$ theoretical uncertainties.

Appendix E

ADD Limits with the 8 TeV Collision Data

The 2012 data with the centre of mass energy of 8 TeV corresponding to 10.5 fb^{-1} of integrated luminosity has also been used to perform the mono-jet search. Preliminary results [68] indicate that no excess of events beyond the Standard Model expectations is found, and the limits on the scale M_D in the context of the ADD scenario can be updated. In Fig. E.1 the 95% CL expected and observed upper LO limits on $\sigma \times A \times \epsilon$ are shown, along with signal $\sigma \times A \times \epsilon$ for 2 and 6 extra dimensions, using the third signal region. The resulting lower limits on M_D are listed in Table E.1 along with their errors.

n	95% CL observed limit on M_D [TeV]			95% CL expected limit on M_D [TeV]		
	$+1\sigma$(theory)	Nominal	-1σ(theory)	$+1\sigma$	Nominal	-1σ
2	$+0.32$	3.88	-0.42	-0.36	4.24	$+0.39$
3	$+0.21$	3.16	-0.29	-0.24	3.39	$+0.46$
4	$+0.16$	2.84	-0.27	-0.16	3.00	$+0.20$
5	$+0.16$	2.65	-0.27	-0.13	2.78	$+0.15$
6	$+0.13$	2.58	-0.23	-0.11	2.69	$+0.11$

Table E.1: The 95% CL observed and expected limits on M_D for different number of extra-dimensions n for the third signal region, considering LO signal cross sections. The impact of one standard deviation theoretical uncertainties on the observed limits, as well as $\pm 1\sigma$ errors on the expected limits are also presented.

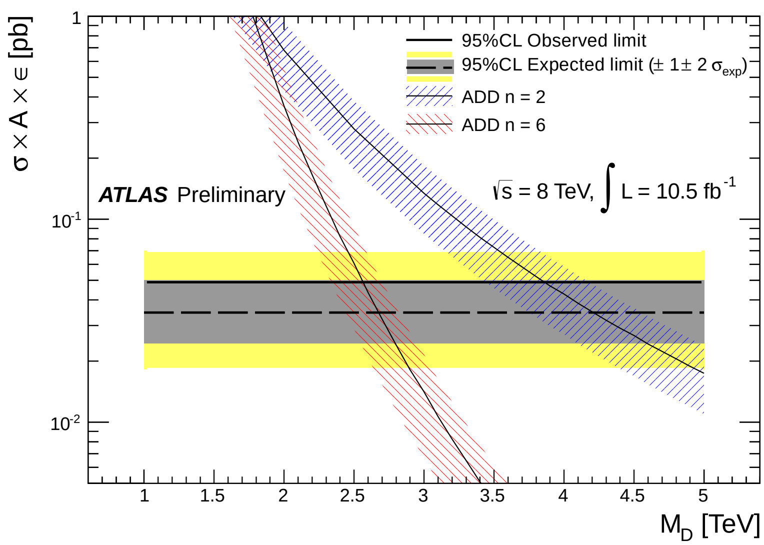

Figure E.1: The ADD $\sigma \times A \times \epsilon$ in the third signal region as a function of M_D for $n = 2$ and $n = 6$. The bands around the signal curves represent the total theoretical uncertainty. The model-independent observed (solid line) and expected (dashed line) 95% CL limits on $\sigma \times A \times \epsilon$ are also shown. The shaded areas around the expected limit indicate the expected $\pm 1\sigma$ and $\pm 2\sigma$ ranges of limits in the absence of a signal.

Appendix F

Event Display

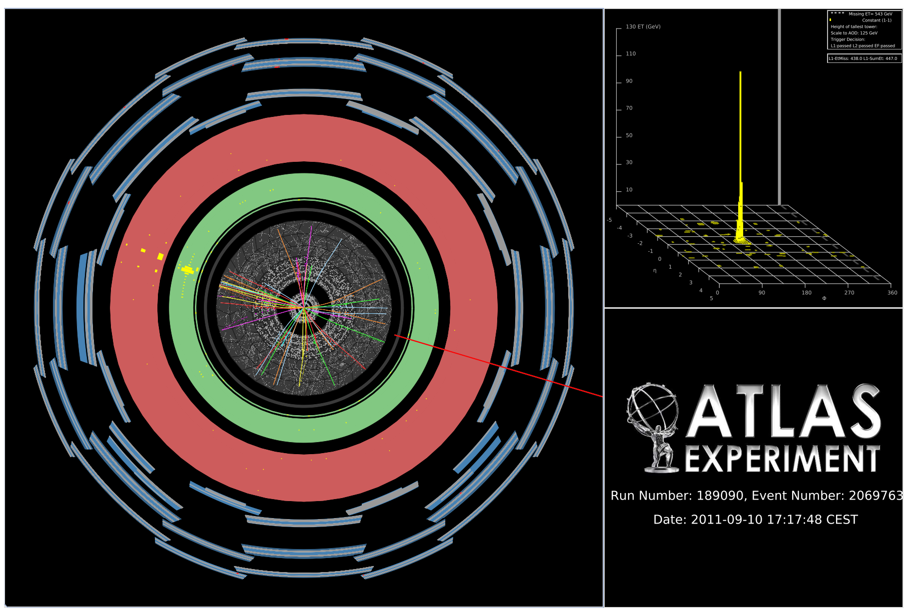

Figure F.1: Event display of a mono-jet event in signal region 4, with the leading jet $p_{\mathrm{T}} = 551$ GeV, $E_{\mathrm{T}}^{\mathrm{miss}} = 542$ GeV, and no additional jets with $p_{\mathrm{T}} > 30$ GeV.

Bibliography

[1] C. Quigg, *Gauge Theories Of The Strong, Weak, and Electromagnetic Interactions*, tech. rep., 1983.

[2] A. M. F. Halzen, *Quarks and Leptons: An Introductory Course in Modern Particle Physics*, tech. rep., 1984.

[3] ATLAS Collaboration, *Observation of a New Particle in the Search for the Standard Model Higgs Boson with the ATLAS Detector at the LHC*, Phys.Lett. **B716** (2012) 1–29, arXiv:1207.7214 [hep-ex].

[4] A.G. Riess *et al.*, *Observational Evidence from Supernovae for an Accelerating Universe and a Cosmological Constant*, arXiv:9805201v1 [astro-ph].

[5] B.C. Allanach, S. Grab and H.E. Haber, *Supersymmetric monojets at the Large hadron Collider*, arXiv:1010.4261v3 [hep-ph].

[6] ATLAS Collaboration, *Search for new phenomena with the monojet and missing transverse momentum signature using the ATLAS detector in $\sqrt{s} = 7$ TeV proton-proton collisions*, Phys.Lett. **B705** (2011) 294–312, arXiv:1106.5327 [hep-ex].

[7] ATLAS Collaboration, *Search for New Phenomena in Monojet plus Missing Transverse Momentum Final States using 1 fb-1 of pp Collisions at $\sqrt{s}$=7 TeV*

with the ATLAS Detector, Tech. Rep. ATLAS-CONF-2011-096, CERN, Geneva, July, 2011.

[8] ATLAS Collaboration, *Search for dark matter and large extra dimensions in events with a jet and missing transverse momentum with the ATLAS detector*, Tech. Rep. ATLAS-EXOT-2011-20-003, CERN, Geneva, August, 2012. arXiv:1210.4491 [hep-ex].

[9] N. Arkani-Hamed, S. Dimopoulos, and G. Dvali, *The Hierarchy problem and new dimensions at a millimeter*, Phys.Lett. **B429** (1998) 263–272, arXiv:hep-ph/9803315 [hep-ph].

[10] M. Beltran, D. Hooper, E. W. Kolb, Z. A. Krusberg, and T. M. Tait, *Maverick dark matter at colliders*, JHEP **1009** (2010) 037, arXiv:1002.4137 [hep-ph].

[11] A. Rajaraman, W. Shepherd, T. M. Tait, and A. M. Wijangco, *LHC Bounds on Interactions of Dark Matter*, Phys.Rev. **D84** (2011) 095013, arXiv:1108.1196 [hep-ph]. 20 pages, 11 figures.

[12] P. J. Fox, R. Harnik, J. Kopp, and Y. Tsai, *Missing Energy Signatures of Dark Matter at the LHC*, Phys.Rev. **D85** (2012) 056011, arXiv:1109.4398 [hep-ph]. 22 pages, 10 figures.

[13] C.P. Burgess, L. van Nierop, *Sculpting the Extra Dimensions: Inflation from Codimension-2 Brane Back-reaction*, arXiv:1108.2553 [hep-th].

[14] C.P. Burgess, L. van Nierop, *Large Dimensions and Small Curvatures from Supersymmetric Brane Back-reaction*, arXiv:1101.0152 [hep-th].

[15] H. Goldberg, *Constraint on the Photino Mass from Cosmology*, Phys.Rev.Lett. **50** (1983) 1419–1422.

[16] J. E. *et al.*, *Supersymmetric relics from the big bang*, Nucl. Phys. **B238** (1984) 453–476.

[17] A. Birkedal, K. Matchev, and M. Perelstein, *Dark matter at colliders: A Model independent approach*, Phys.Rev. **D70** (2004) 077701, arXiv:hep-ph/0403004 [hep-ph].

[18] R. Akert *et al.* Z. Phys **C 65** (1995) 47 – 65.

[19] P. Abreu *et al.* Z. Phys **C 74** (1997) 577 – 586.

[20] M. Acciarri *et al.* Phys. Lett **B 431** (1998) 199 – 208.

[21] D. Buskulic *et al.* Phys. Lett **B 313** (1993) 520.

[22] G. F. Giudice, R. Rattazzi, and J. D. Wells, *Quantum gravity and extra dimensions at high-energy colliders*, Nucl.Phys. **B544** (1999) 3–38, arXiv:hep-ph/9811291 [hep-ph].

[23] G. Steigman and M. S. Turner, *Cosmological Constraints on the Properties of Weakly Interacting Massive Particles*, Nucl.Phys. **B253** (1985) 375.

[24] J. Goodman, M. Ibe, A. Rajaraman, W. Shepherd, T. M. Tait, et al., *Constraints on Dark Matter from Colliders*, Phys.Rev. **D82** (2010) 116010, arXiv:1008.1783 [hep-ph].

[25] ATLAS Collaboration, *The ATLAS Experiment at the CERN Large Hadron Collider*, JINST **3** (2008) S08003.

[26] ATLAS Collaboration, *Expected performance of the ATLAS experiment – detector, trigger and physics*, Arxiv:0901.0512, 2009. arXiv:0901.0512.

[27] J. H. S. D. Ellis, M. Toennesmann, *On Building Better Cone Jet Algorithms*, eConf:C010630.

[28] W. Lampl *et al.*, *Calorimeter Clustering Algorithms: Description and Performance*, Tech. Rep. ATL-LARG-PUB-2008-002, CERN, Geneva, Apr, 2008.

[29] M. Mangano *et al.*, *ALPGEN, a generator for hard multiparton processes in hadronic collisions*, JHEP **07** (2003) , arXiv:hep-ph/0206293.

[30] G. Corcella *et al.*, *HERWIG 6: An event generator for hadron emission reactions with interfering 1255 gluons (including supersymmetric processes)*, JHEP **01** (2001) , arXiv:hep-ph/0011363.

[31] G. Corcella *et al.*, *HERWIG 6.5 release note*, arXiv:hep-ph/0210213.

[32] J. F. J. Butterworth, M. Seymour, *Multiparton interactions in photoproduction at HERA*, Z. Phys. **C72** (1996) , arXiv:hep-ph/9601371.

[33] J. Pumplin *et al.*, *New generation of parton distributions with uncertainties from global QCD analysis*, JHEP **0207** (2002) , arXiv:0201195 [hep-ph].

[34] K. Melnikov, F. Petriello, *Electroweak gauge boson production at hadron colliders through O(alpha(s)**2)*, Phys. Rev. **D74** (2006) , arXiv:hep-ph/0609070.

[35] R. Gavin *et al.*, *FEWZ 2.0: A code for hadronic Z production at next-to-next-to-leading order*, arXiv:hep-ph/:1011.3540.

[36] S. Frixione, B. Webber, *The MC@NLO 3.2 event generator*, arXiv:hep-ph/0601192.

[37] S. Frixione, B. Webber, *Matching NLO QCD computations and parton shower simulations*, JHEP **06** (2002) , arXiv:hep-ph/0204244.

[38] P. M. Nadolsky *et al.*, *Implications of CTEQ global analysis for collider observables*, Phys.Rev. **D78** (2008) , arXiv:0802.0007 [hep-ph].

[39] P.H. Beauchemin and R. Rezvani, *ExoGraviton_i Package; the ADD Graviton Generator in Athena Software*, Tech. Rep. ATL-COM-PHYS-2011-336, CERN, Geneva, March, 2011.

[40] *Performance of the ATLAS fast simulation ATLFAST*, Tech. Rep. ATL-PHYS-inT-2007-0-5, CERN, Geneva, January, 2007.

[41] T. Sjostrand, S. Mrenna and P. Skands, *PYTHIA 6.4 physics and manual*, JHEP **05** (2006) 026, arXiv:hep-ph/0603175.

[42] A. Sherstnev and R. Thorne, *Parton Distributions for LO Generators*, Eur. Phys. J. **C55** (2008) 553–575, arXiv:0711.2473 [hep-ph].

[43] ATLAS Collaboration, *Search for dark matter candidates and large extra dimensions in events with a photon and missing transverse momentum in pp collision data at $\sqrt{s}$ = 7 TeV with the ATLAS detector*, ATLAS-CONF-2012-085 . http://cdsweb.cern.ch/record/1460397.

[44] ATLAS Collaboration, *A measurement of the ratio of the W + 1 jet to Z + 1 jet cross sections with ATLAS*, Tech. Rep. ATL-COM-PHYS-2011-457, CERN, Geneva, May, 2011.

[45] ATLAS Collaboration, *Measurement of the production cross for W-bosons in association with jets in pp collisions at $\sqrt{s}$ = 7 TeV with the ATLAS detector*, Tech. Rep. ATL-COM-PHYS-2010-883, CERN, Geneva, December, 2010.

[46] ATLAS Collaboration, *Measurement of the cross section for jets produced in association with Z bosons*, Tech. Rep. ATL-COM-PHYS-2010-884, CERN, Geneva, December, 2010.

[47] ATLAS Collaboration, *Muon reconstruction efficiency in reprocessed 2010 LHC proton–proton collision data recorded with the ATLAS detector*, Tech. Rep. ATLAS-CONF-2011-063, CERN, Geneva, April, 2011.

[48] ATLAS Collaboration, *Determination of the muon reconstruction efficiency in ATLAS at the Z resonance in proton-proton collisons at $\sqrt{s} = 7$ TeV*, Tech. Rep. ATLAS-CONF-2011-008, CERN, Geneva, February, 2011.

[49] ATLAS Collaboration, *A measurement of the ratio of the W and Z cross sections with exactly one associated jet in pp collisions at $\sqrt{s} = 7$ TeV with ATLAS*, Phys.Lett. **B708** (2012) 221–240, arXiv:1108.4908 [hep-ex].

[50] ATLAS Collaboration, *Search for Supersymmetry with jets and missing transverse momentum and one lepton at $\sqrt{s} = 7$ TeV*, Tech. Rep. ATL-COM-PHYS-2010-1743, CERN, Geneva, March, 2012.

[51] ATLAS Collaboration, *Muon Momentum Resolution in First Pass Reconstruction of pp Collision Data Recorded by ATLAS in 2010*, Tech. Rep. ATLAS-COM-CONF-2011-003, CERN, Geneva, January, 2011.

[52] ATLAS Collaboration, *Search for Supersymmetry with jets and missing transverse momentum and one or more leptons at $\sqrt{s} = 7$ TeV*, Tech. Rep. ATL-COM-PHYS-2011-1743, CERN, Geneva, Dec, 2011.

[53] ATLAS Collaboration, D. Salek, D. Berge, J. Boyd, C. Chavez, L. Fiorini, and M. Huhtinen, *Beam background identification method*, 2012. ATLAS-COM-DAPR-2012-001.

[54] R. Nisius, *Combination of ATLAS Results on the Mass of the Top-Quark*, Tech. Rep. ATL-COM-PHYS-2011-714, CERN, Geneva, Jun, 2011.

[55] ATLAS Collaboration, G. Aad et al., *Luminosity Determination in pp Collisions at $\sqrt{s} = 7$ TeV Using the ATLAS Detector at the LHC*, Eur.Phys.J. **C71** (2011) 1630, arXiv:1101.2185 [hep-ex]. 24 pages plus author list (36 pages total). 9 Figures, 10 Tables, submitted to Journal EPJC.

[56] ATLAS Collaboration, *Luminosity Determination in pp Collisions at $\sqrt{s} = 7$ TeV Using the ATLAS Detector in 2011*, Tech. Rep. ATLAS-CONF-2011-116, CERN, Geneva, August, 2011.

[57] A. L. Read, *Presentation of search results: The CL(s) technique*, Tech. Rep. J.Phys.G G28 (2002) 2693 2704, 2002.

[58] WMAP Collaboration, *Seven-Year Wilkinson Microwave Anisotropy Probe (WMAP) Observations: Cosmological Interpretation*, Astrophys.J.Suppl. **192** (2011) , arXiv:astro-ph/1001.4538.

[59] Fermi-LAT Collaboration, *Constraining Dark Matter Models from a Combined Analysis of Milky Way Satellites with the Fermi Large Area Telescope*, Phys.Rev.Lett. **107** (2011) , arXiv:1108.3546 [astro-ph.HE].

[60] G. Abbiendi *et al.* Eur. Phys. J **C 19** (2001) 587.

[61] P. Abreu *et al.* Eur. Phys. J **C 16** (2000) 371.

[62] M. Acciarri *et al.* Eur. Phys. J **C 16** (2000) 1.

[63] R. Barate *et al.* Eur. Phys. J **C 14** (2000) 1.

[64] P.H. Beauchemin *et al.*, *Direct measurement of the invisible width of the Z boson using monojet events*, CDF8820 (2008) .

[65] ATLAS Collaboration, *Observing an invisibly decaying Higgs boson in ATLAS via vector boson fusion*, Tech. Rep. ATL-PHYS-2003-006, CERN, Geneva, October, 2002.

[66] H. Georgi, *Unparticle Physics*, Phys.Rev.Lett. (2007) , arXiv:hep-ph/0703260.

[67] K. Cheung, W. Y. Keung, T. C. Yuan, *Collider Phenomenology of Unparticle Physics*, Phys.Rev.D. **D76** (2007) , arXiv:hep-ph/0706.3155.

[68] ATLAS Collaboration, *Search for New Phenomena in Monojet plus Missing Transverse Momentum Final States using 10fb-1 of pp Collisions at* $\sqrt{s}$*=8 TeV with the ATLAS detector at the LHC*, Tech. Rep. ATLAS-CONF-2012-147, CERN, Geneva, November, 2012.